City Research Online

City, University of London Institutional Repository

This is the accepted version of the paper.

This version of the publication may differ from the final published version.

School of Mathematics, Computer Science & Engineering

In-nozzle Flow and Spray Characteristics in Gasoline Multi-hole Injectors

By

Milad Mirshahi

A thesis submitted in partial fulfilment of the requirement for the degree of

Doctor of Philosophy

London

28th August 2020

Table of Contents

Abstract

The current experimental research work is concerned to address different types of cavitation inside the multi-hole nozzle and their impact on the emerging spray stability and atomisation as the effect of cavitation on atomisation is not yet fully understood. The previous studies have provided experimental data addressing unresolved questions about string cavitation origin, area of formation, lifetime and influence on the nozzle hole flow [1] [2] [3] [4] [5] [6]. More importantly, it is aimed to fully characterize the spray structure generated from the new generation stepped multi-hole injectors [7] [8]. Thus, this experimental research work has been planned in four phases to address specific issues. The first phase of the experimental investigation was to visualise the in-nozzle flow and cavitation development inside a 15-times transparent enlarged model of a conventional multi-hole injector (6-holes symmetric) using high-speed visualisation (Mie Scattering) technique. A new enlarged model injector was designed that was geometrically similar to phase 1 model but 7-times larger than the real injector. In this regard, cavitation types and development at different flow conditions were visualised. It was found that the geometric and vortex cavitation can significantly affect the spray angle and can induce instability in the spray structure. The underlying mechanisms relating to the interaction of vortex and geometric cavitation and the resulting impact of the bubble pockets and their collapse in the erosion sites was obtained. Two counter rotating vortex cavitation found at the top and bottom of the nozzle inlet which can contribute to erosion at the erosion sites. The results also revealed that the hydraulic flip happens much earlier than expected and at lower cavitation numbers compared to the 15 times enlarged model. It also reveals that a stochastic ligament spray with much lower velocities is being formed at the vicinity close to the upper part of the nozzle exit where the air entrainment seems to be maximum. The wetting phenomena can happen inside the counter bore stepped-hole region of the nozzle or on the curved surface on the tip of the injector nose. In the third phase of the experiment, a real-size stepped injector

test rig was designed and manufactured. It also enabled the measurement of the spray tip penetration and cone angle from different viewing angles. It further allowed the visualisation of the overall spray behaviour and very near-nozzle exit spray. It was found that stepped-nozzle compared to straight nozzle injector may have flapping of the jets creating snake shape pattern. Unique A shaped with no visible jet boundary was also seen. Higher jet to jet interactions and higher air entrainment were observed compared to other injectors. Tip penetrations of 22mm at 0.25ms, 50mm at 0.75ms ASOI are almost similar to other injectors. Increasing the pressure from 50 bar to 100 bar increases the cone angle significantly from 64 degrees to 72 degrees. In the fourth phase of the experiment, a Fiberflow Dantec PDA measurement system was setup to measure spray characteristics including droplet diameters and velocities at the very near-nozzle area of the injector (1mm from it) up to distance of 35mm from injector tip, to investigate early breakup and spray characteristics. Velocities up to 120m/s at 1mm away from nozzle exit at 100bar are in good agreement with micro-PIV measurements of the in-nozzle flow of transparent model of a similar type of injector at the same injection pressure. Comparison of the average droplet diameter at 1mm away from nozzle exit of the current stepped multi-hole injector (7.5μm) with conventional straight multi-hole (15μm) and outward pintle-type (13μm) at same operation condition shows better atomization performance of this model. The improved atomization performance can be due to the stepped part of the current injector where the fuel undergoes through a sudden expansion process whereby the flow becomes 3-D and highly turbulent and becomes susceptible to earlier breakup and rapid atomization. It was also found that as Jet 1 is slightly contracted, the center of the jet moves slightly downward towards the axis of the spray during the main injection event. Also existence of 4 local peaks in the instantaneous velocity contour plot and the change in their location at different ASOI during the main injection event indicates that there are instabilities in the velocity. Maximum droplet mean diameter, SMD, and Weber number decreases during the main injection event. The injector has Weber number of 8 at 1mm from nozzle exit while outward pintle-type model had Weber number of 25 at 2.5mm away from nozzle exit.

List of Figures

11

15

16

List of Tables

Acknowledgements

First and foremost, I offer my sincerest gratitude to my supervisor, Prof Jamshid Nouri, who has supported me throughout my research with his knowledge and patience whilst allowing me the room to work in my way. Furthermore, I am grateful that he provided me with funding. I would also like to thank Dr Youyou Yan, who supported me along the way by her academic guidance. I would also like to thank the technicians' team at the workshop, including Mr Jim Ford, Mr Grant Clow, Mr Richard Leach and Rob. I also want to thank Prof Ahmed Kovacevic, Dr Sham Rane, Prof Keith Pullen, Prof Abdulnaser Sayma, Prof Raj Kumar for their educational guidance in any way during this journey of thought and soul. I also want to thank the university staff who supported me along this journey and my friends and colleagues at City University. I also thank my line manager Radmila. I want to thank my family members, including parents who supported me along the way emotionally and otherwise. Above all, I want to thank my wife, the better part of myself, who motivated me continuously not to give up with all the ups and downs of PhD life. I want to dedicate this work to my wife.

Declaration

This thesis is a presentation of my original research work. Wherever contributions of others are involved, every effort is made to indicate this clearly, with due reference to the literature and acknowledgement of collaborative research and discussions. The work was done under supervision of Professor Jamshid Nouri and Dr Youyou Yan at City University of London.

Date: 20/04/2021

List of Publications

Here are the list of publications during the course of this study:

1. Mirshahi, M., Yan, Y. and Nouri, J.M. (2015). *Influence of cavitation on near nozzle exit spray*. Journal of Physics: Conference Series, 656(1). doi:10.1088/1742-6596/656/1/012093.

2. Gavaises, E., Mirshahi, M., Nouri, J. M. & Yan, Y. (2013). *Link between in-nozzle cavitation and jet spray in a gasoline multi-hole injector*. Paper presented at the ILASS 2013 - 25th Annual Conference on Liquid Atomization and Spray Systems, 1-4 Sept 2013, Chania, Crete.

A 3rd paper will be submitted in MDPI, Fuels:

3. Mirshahi M, Nouri J M, Yan Youyou. '*Full PDA measurement of spray from a stepped multi-hole injector very close to the nozzle exit*'.

Nomenclatures

CIDI	Compression-ignition direct-injection
CO/CO_2	Carbon monoxide/dioxide
SIDI	Spark-ignition direct-injection
FIE	Fuel injection equipment
UBHC	Unburned Hydrocarbons
LDA	Laser Doppler Anemometry
LDV	Laser Doppler Velocimetry
LIF	Laser induced fluorescence
NO_x	Nitrogen oxides
PDA	Phase Doppler Anemometry
PIV	Particle Image Velocimetry
RMS	Root mean square
d	Distance from nozzle or length of the cone legs
SMD	Sauter mean diameter
SI	Spark-ignition
CN	Cavitation number
D	Injection hole diameter / Droplet diameter
L	Injection hole length
P_{back}, p_b	Chamber pressure

Pinj   Injection pressure

Re   Reynolds number

T   Temperature

Chapter 1: Introduction

1.1 Introduction

Since its invention, the internal combustion (IC) engine has been used extensively in the automobile industry over the last century. The compact size and efficiency of the internal combustion engine, combined with the benefit of storage of liquid fuel, have made it an effective power plant used in many other industries, including aviation, ship propulsion, and stationary power generation. From its early years of invention, the IC engine has been developed over the decades in order to increase its power to weight ratio. In this journey, the efficiency of the IC engine (power to fuel consumption ratio) was also improved. In addition, the power output (torque times speed) was also improved. However, with the rises in fuel costs over time, fuel economy was becoming a dominant issue. Due to the rise of the fuel costs per gallon for gasoline, diesel engine became an alternative solution for lowering the costs. That is because 1 litre of diesel has around 30% more power than 1 litre of gasoline. That is why gasoline engines run on higher rpm in order to produce same horsepower. In this situation, the spark ignition engine needed to improve its fuel economy to remain competitive. With recent environmental impacts of CO2 and other exhaust emissions, the race to develop engines with less harmful emissions became more intense. In this race, the diesel engine has experienced a big difficulty after 2015 news about the real level of Nox and the spark ignition engine (SIDI) is still at the forefront of this race.

1.2 IC engine emissions

Combustion of fossil fuels in IC engines produces carbon dioxide, which is contributing to global warming. It also produces NOx and CO and some other harmful gases. For these reasons, there is pressure over the transportation sector to reduce emissions of carbon dioxide and other pollutants from vehicles. This is due to the sharp increase in number of passenger cars and freight demand. Therefore, the current trend is towards replacing conventional IC engines with newer technologies. There are number of new technologies which will significantly contribute to the

reduction of carbon emission in the transportation sector. These engine technologies are: Electric cars, Hydrogen fuel cells, Hybrid vehicles, Bio fuels and Spark Ignition Direct Injection (SIDI) engine.

The last choice is the refinement of current technology of IC engines. Automotive engineers are trying to develop IC engines which can comply with the future emission requirements while simultaneously enhancing brake-specific fuel consumption (BSFC). Among conventional IC engines, diesel engines were believed to have lower CO_2 emissions compared to gasoline engines until a few years ago [9]. However an ICCT report in 2019 confirmed that the gasoline TSI (Turbocharged Stratified Injection) emitted lower CO2 levels than the TDI (Turbocharged Direct Injection), under similar laboratory conditions [10]. In addition, during on-road testing, CO2 levels of the gasoline TSI were found to be lower than of the TDI. [10] On the other hand, Diesel has more Nox emissions due to the higher compression ratios and it has less power output since it has more limited speed range. Hence, the trend has been to develop an internal combustion engine which has a combination of the characteristics of both diesel engines and gasoline engines with less CO2 emissions and more power output. Researchers have shown that a promising candidate for reaching this goal is a spark ignition direct injection (SIDI) engine. It is also referred to as gasoline direct injection (GDI) engines in the market.

1.3 Theory of Operation of SIDI Engines

The major advantages of a SIDI engine are increased fuel efficiency and high power output. Emissions levels can also be more accurately controlled with the SIDI system. The cited gains are achieved by the precise control over the amount of fuel and injection timings that are varied according to engine load. In addition, there are no throttling losses in some SIDI engines, when compared to a conventional fuel-injected or carburate engine, which greatly improves efficiency, and reduces 'pumping losses' in engines without a throttle plate. When fuel is injected directly into the combustion chamber, it evaporates and absorbs heat from the surroundings, therefore the temperature of the cylinder is reduced. Less temperature causes the engine to be less sensitive to engine knock. Hence the engine can have higher compression ratio and this will increase the engine efficiency [9] . Direct injection can also be combined with turbo-charging to

increase the specific power output of the engine [11]. This could be exploited to downsize the engine and to further increase the fuel economy.

On the other hand, direct injection also has drawbacks. The shorter time available for mixture preparation greatly increases the accuracy and precision requirement for injectors. In addition, it needs higher injection pressure for better atomization and mixture homogenization. Moreover, parasitic losses increase as the pressure can be up to 20 MPa (200 bar) , compared to PFI pressure of 0.3-0.7 MPa [9]. Furthermore, problems with soot emission may arise at full load operation. Besides all these, SIDI engines have more complex control systems with more complex fuel injection components. This is the main barrier for simple conversion of typical Port fuel injection to direct injection engine. The key question for engine manufacturing company is that adding complexity required to produce SIDI engine will be justify by fuel economy [12].

In SIDI engines, engine speed is controlled by the engine control unit/engine management system (ECU/EMS), which regulates fuel injection function and ignition timing, instead of having a throttle plate that restricts the incoming air supply [12].

In this engine, The engine management system continually chooses among three combustion modes: ultra lean burn, stoichiometric, and full power output. Each mode is characterized by the air-fuel ratio. The stoichiometric air-fuel ratio for gasoline is 14.7:1 by weight (mass), but ultra lean mode can involve ratios as high as 65:1 (or even higher in some engines, for very limited periods). These mixtures are much leaner than in a conventional engine and reduce fuel consumption considerably [13].

Ultra lean burn or stratified charge mode: This mode is used for light-load running conditions, at constant or reducing road speeds, where no acceleration is required. The fuel is not injected at the intake stroke but rather at the latter stages of the compression stroke. The combustion takes place in a cavity on the piston's surface which has a toroidal or an ovoidal shape, and is placed either in the center (for central injector), or displaced to one side of the piston that is closer to the injector. The cavity creates the swirl effect so that the small amount of air-fuel mixture is optimally placed near the spark plug. This stratified charge is surrounded mostly by air and residual gases, which keeps the fuel and the flame away from the cylinder walls. Decreased combustion temperature allows for lowest emissions and heat losses and increases air quantity

by reducing dilation, which delivers additional power. This technique enables the use of ultra-lean mixtures that would be impossible with carburetors or conventional fuel injection [4].

Stoichiometric mode: This mode is used for moderate load conditions. Fuel is injected during the intake stroke, creating a homogeneous fuel-air mixture in the cylinder. From the stoichiometric ratio, an optimum burn results in a clean exhaust emission, further cleaned by the catalytic converter [4].

Full power mode: This mode is used for rapid acceleration and heavy loads (as when climbing a hill). The air-fuel mixture is homogeneous and the ratio is slightly richer than stoichiometric, which helps prevent detonation (pinging). The fuel is injected during the intake stroke in this mode [4].

It is also possible to inject more than once during a single cycle. After the first fuel charge has been ignited, it is possible to add fuel as the piston descends. The benefits are more power and economy, but certain octane fuels have been seen to cause exhaust valve erosion.

1.4 Other Companion Technologies

Direct injection may also be accompanied by other engine technologies such as variable valve timing (VVT), variable length intake manifolding (VLIM), and turbocharging. Exhaust gas recirculation (EGR) may help reduce the high nitrogen oxides (NOx) emissions that can result from burning ultra lean mixtures. Modern turbocharged engines use continuous cam phasing in place of EGR.

Tuning up an early and precise direct injection event to generate higher power is difficult, since the only time it is possible to inject fuel is during the induction phase. Conventional port fuel injection engines can inject throughout the 4-stroke sequence, as the injector squirts onto the back of a closed valve. In SIDI engines, a direct injection is limited to the intake stroke of the piston. As the RPM increases, the time available to inject fuel decreases. Newer SIDI systems that have sufficient fuel pressure to inject even late in compression phase do not suffer to the same extent; however, they still do not inject during the exhaust cycle. Hence, all other factors being equal, a SIDI engine needs higher-capacity injectors to achieve the same power as a conventional engine [4].

1.5   SIDI Fuel Injection System

The fuel injection system in a SIDI engine is a key component that must provide the desired mixture cloud over the entire operating range of the engine. A well-atomized fuel spray must be produced for all operating conditions. Fuel injection systems must have the capability of providing both late injection for stratified-charge combustion at part load, as well as injection during the intake stroke for homogeneous-charge combustion at full load. At full load, a well-dispersed fuel spray or mixture plume is desirable to ensure a homogeneous charge for even the largest fuel quantities. At part load a well-atomized compact spray or mixture plume is desirable to achieve rapid mixture formation and controlled stratification. In addition, the fixed location of the ignition source makes it quite difficult to operate in the part load for other than full load. This imposes a critical additional requirement on the fuel mixture formation process of this type of engine. The mixture cloud that results from fuel vaporization must be controlled both spatially and temporally in order to obtain stable combustion. For part-load operation, the injection system should provide the capability for rapid injection late in the compression stroke into an ambient pressure of up to 1.0 MPa. The fuel injection pressure is very important for obtaining both effective spray atomization and the required level of spray penetration. A higher fuel injection pressure reduces the mean diameter of the spray approximately as the inverse square root of the pressure differential Pinj - Pcyl [13].The use of a high fuel injection pressure, such as 20 MPa, will enhance the atomization but will most likely generate an over-penetrating spray, resulting in fuel wall impingement. The fuel pressures that have been selected for most of the current prototype and production SIDI engines range from 4 to 12 MPa, which are quite low when compared with diesel injection system pressures of 50–200 MPa, but are relatively high in comparison with typical PFI injection pressures of 0.3–0.7 MPa [13].
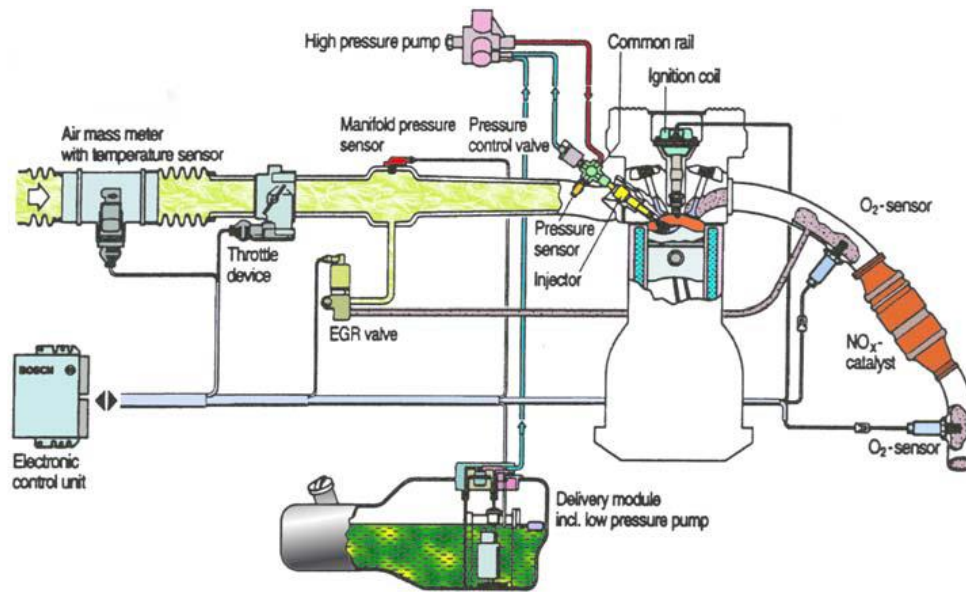
Figure 1-1 Typical direct-injection, spark-ignition engine system layout [13]

Based on recent researches, it has been concluded that common-rail injection systems can meet these exact requirements. As it is shown in Fig. 1-1 shows a low-pressure fuel pump delivers fuel to the high-pressure pump. The high pressure pump delivers the fuel to the common rail with more than 200bar pressure. A pressure sensor and regulator are installed on the common rail. Injection pressure and duration are controlled electronically from the electronic control unit (ECU). Other values such as intake air mass and temperature, throttle valve position, manifold pressure and oxygen concentration in the exhaust gases are all calculated by sensors. Following a certain evaluation of these data, the ECU then drives various actuators, and controls fuel injection pressure and duration and spark plug timing. Finally, the injector is responsible for the injection of the required amount of the fuel into the combustion chamber.

1.6   Combustion Systems in SIDI

The trend in the global automotive industry is toward small yet powerful engines. Manufacturers from Europe, the U.S., and even China are embracing downsizing concepts to build increasingly compact and economical low displacement engines which continue to offer equivalent levels of performance and driving enjoyment thanks to turbocharging. The fuel which the injectors spray into the combustion chamber is so finely atomized that it can be ignited directly without having to mix it in the combustion chamber. This enables higher engine compression, which translates into greater efficiency. The direct injection technology also makes a major contribution to improved cylinder cooling. All that flows through the open intake valve in the intake duct is fresh air. High-pressure injection valves inject the fuel directly into the combustion chamber. This cools the combustion chamber, making basic compression higher thanks to the decreased propensity to knock. The economical consumption and low emissions of gasoline direct injection are due to the precise metering, preparation, and distribution of air and fuel for each individual combustion cycle. In combination with downsizing and turbocharging, gasoline direct injection offers the potential to reduce consumption and CO2 emissions by some 15 percent. [14]

Three different combustion systems, i.e., spray-guided, wall-guided and air-guided, in the stratified operation SIDI engine have been proposed, as shown in Figure 1-2.
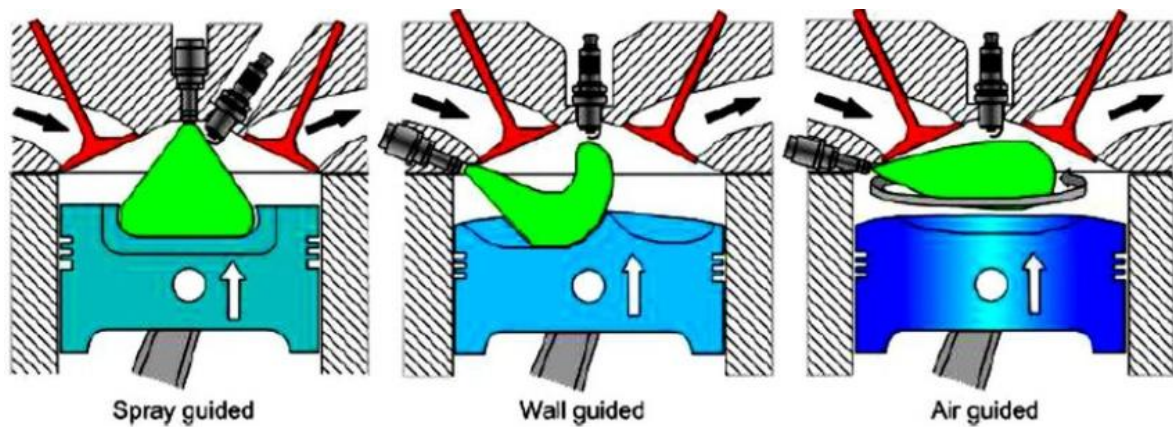
Figure 1-2 Spray guided, wall guided, air guided concepts in SIDI systems [15]

The SIDI engine mainly works using two different charge formation mechanisms, depending on the load and the engine speed: the homogeneous charge operating with stoichiometric mixtures, and the stratified charge with an overall lean AFR composition at low load and up to medium speed operation. Figure 1-3 shows the different mechanisms of mixture formation in homogeneous and stratified charge mode. Combining these two different charge formation mechanisms it is possible to take the maximum advantage in terms of fuel-economy. Figure 1-4 shows a diagram of the optimal charge formation mechanism as function of the engine load and speed: the SIDI engine runs with a stratified charge and with lean mixtures during low load/speed operation, and runs with a ''homogeneous'' charge at higher load/speed points. [15]
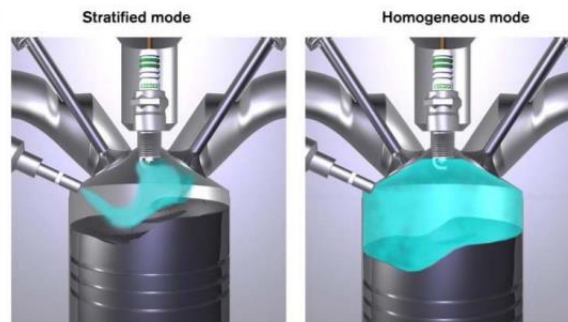
Figure 1-3 The different mechanisms of mixture formation in homogeneous and stratified charge mode. [15]
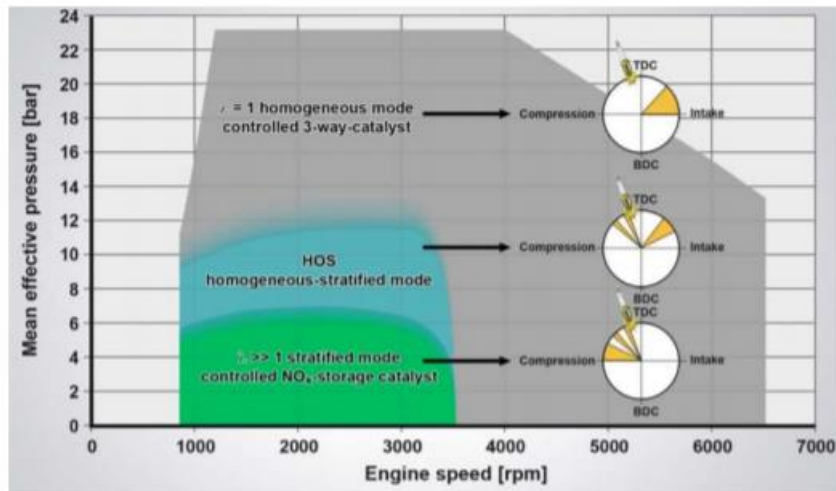
Figure 1-4 A diagram of the optimal charge formation mechanism as function of the engine load and speed [16]

1.7   SIDI injectors

During the development of the SIDI injector, the fuel injector gradually becomes a key component because the SIDI injector needs to provide the capability to operate on both homogenous and stratified charge combustion under different injection strategies. When the engine operates on homogenous charge conditions, a well-atomised and well-mixed dispersed fuel spray distribution is required under the conditions of early injection and low in-cylinder pressure. When the engine operates on stratified charge conditions, a well-atomised, compact and repeatable spray structure is required under higher in-cylinder pressure and late injection in order to obtain the fast mixture formation and controlled stratification. To fulfill the above requirements for the SIDI engine, three different standard types of SIDI injectors are widely used. [17]

The differences between the types of nozzle can be identified by the way in which they open and close as shown in figure 1-5. The injection mechanism for the outward-opening nozzle consists of liquid passing thorough the cross plane of the nozzle and producing a self-forming spray cone angle when the valve opens. The multi-hole and swirl nozzle are designed as the inward opening structure in order to generate swirl flow in the nozzle

upstream for a better mixture. The characteristics of the multi-hole nozzle can be identified by its sharp and individual jet structure. [17]

(a) Outward-opening nozzle   (b) Multi-hole nozzle   (c) Swirl nozzle
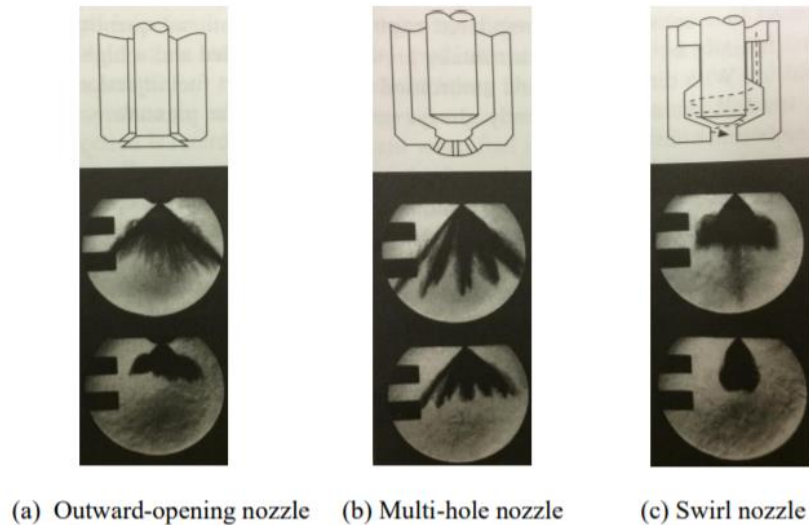
Figure 1-5 Three different standard types of SIDI injectors which are widely used [12]

By using the multi-hole nozzle, a partially homogenous mixture condition in the chamber can be established due to the insufficient spray atomisation quality. The distributions of the partially homogenous mixture contain an enriched mixture and lean mixture regions which result in different flame speeds during the combustion process. The flame speed accelerates in the enriched mixture region of each individual spray jet and then slows down in the lean region between each spray jet. To improve the lean mixture regions in the combustion chamber, increasing the number of nozzle holes and the hole's diameter are the common way to solve this issue. However, increasing the amount of hole numbers may result in a deposit formation and then cause higher hydrocarbon and soot emissions. [13]

To compare the outward-opening nozzle with the inward-opening nozzle, it can be seen that the advantage of the outward-opening lies in its production of a uniform structure of a hollow cone spray and also it is less affected from the chamber pressure for the spray angle. This allows the possibility of controlling the droplet size and injection mass flow rate by using multi-injection at a short injection duration time. [13]

1.8   Multi-hole Injectors

The main part of the injection system is the injector which produces an atomized spray inside the combustion chamber. Figure 1.6 shows the different parts of a typical multi-hole injector. [18]

The high-pressure injector and the high-pressure pump are designed for system pressures up to 200 bar. Up to seven individually positioned injection holes enable the spray pattern to be adapted flexibly to different combustion chambers. The engine control unit performs all the different functions that are required of an efficient engine management system. These include selecting the right injection pressure and the right moment to inject the fuel. To do this, the electronic control unit calculates thousands of times a minute exactly how the injection process should be performed. [19]

Solenoid
(off)

Fuel inlet

Needle valve
(closed)

Fuel flow

Fuel flows through 6
micro-nozzles each of
them inclined 45° with
respect to injector axis
(100 μm diameter)

Solenoid
(on)

Fuel flows through 6
micro-holes parallel to
each other on a circular
array pattern
(500μm diameter)

Fuel spray

Needle valve
(open)
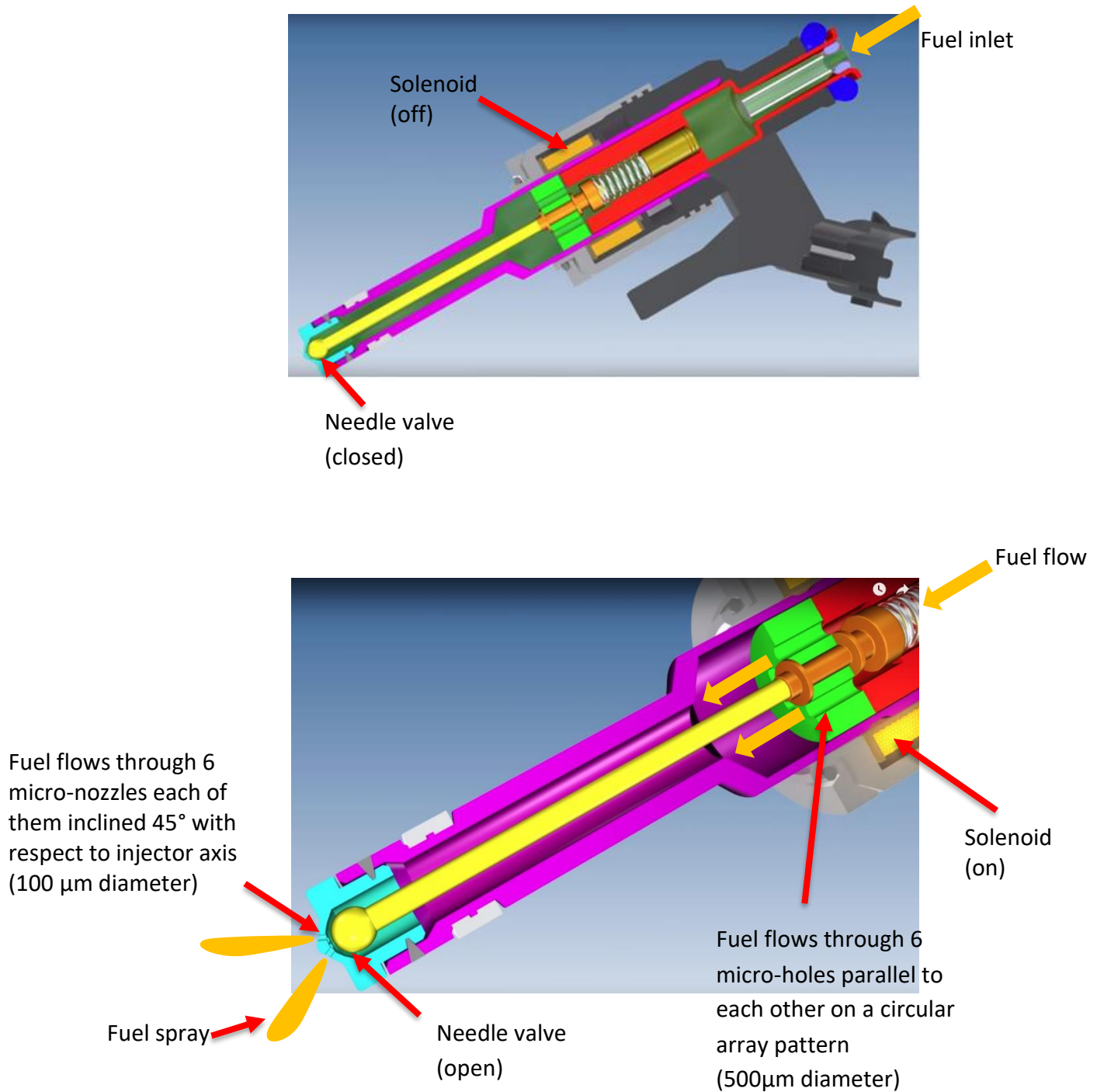
Figure 1-6 Cross-section of a multi-hole fuel injector [18]

The main requirements of the SIDI injector are [13]:

1. flexibility in adopting the spray pattern to the combustion chamber design

2. stability in spray characteristics in each cycle

3. minimal variation in spray characteristics from unit to unit

4. a small value of spray mean drop size (well atomized spray)

5. more spray penetration control

6. more control on the sac volume spray

7. more resistance to deposit formation

8. more resistant to cavitation erosion

9. ability to operate at higher temperatures

The SIDI injector should be designed to deliver a precisely metered fuel quantity with symmetric and highly repeatable spray geometry, and must provide a highly atomized fuel spray having a Sauter Mean Diameter (SMD) of generally less than 25 µm. In fluid dynamics, Sauter mean diameter (SMD, d_{32} or D[3, 2]) is an average of particle size. It is defined as the diameter of a sphere that has the same volume/surface area ratio as a particle of interest.

The sac volume within the injector tip is the volume of fuel, resulting from the previous injection, which is not at the fuel line pressure; therefore it reduces the acceleration of the injected fuel and degrades the fuel atomization. In general, the smaller the sac volume, the fewer large drops will be generated when the injector opens.

Another requirement is that needle bounce on closure should be avoided, as it results in uncontrolled atomization consisting of larger droplets. It also contributes to increases in the UBHC and particulate emissions. Needle bounce on opening is not nearly as important as that on closure, but should be controlled.

1.9   Multi-hole injector vs other injectors

This injector type has been utilised extensively in SIDI engines as well as diesel engines for many years. An important advantage of the multi-hole injector is the flexibility in terms of spray orientation and structure. There are typically two main types of multi-hole injectors: VCO which stands for valve covered orifice and mini-sac which is the model that is in our study. Figure 1-18 (a) shows inside section view of VCO multi-hole injector figure 1-18 (b) shows the spray from a mini-sac injector. The number of holes can be varied from 5 up to 12 holes. The holes are generally placed in a peripheral location with the extra possibility to

include holes in the centre as well. It was seen that the ratio of hole-length over hole-diameter (L/D) affects considerably the air entrainment, atomisation quality and penetration length of the emerging spray jet. Each jet presents a remarkable spray stability and cycle-to-cycle repeatability. All these advantages make the multi-hole injector a good candidate for the spray guided applications. Figure 1-7 shows a cross section of a multi-hole injector and the corresponding spray structure.

(a)   (b)
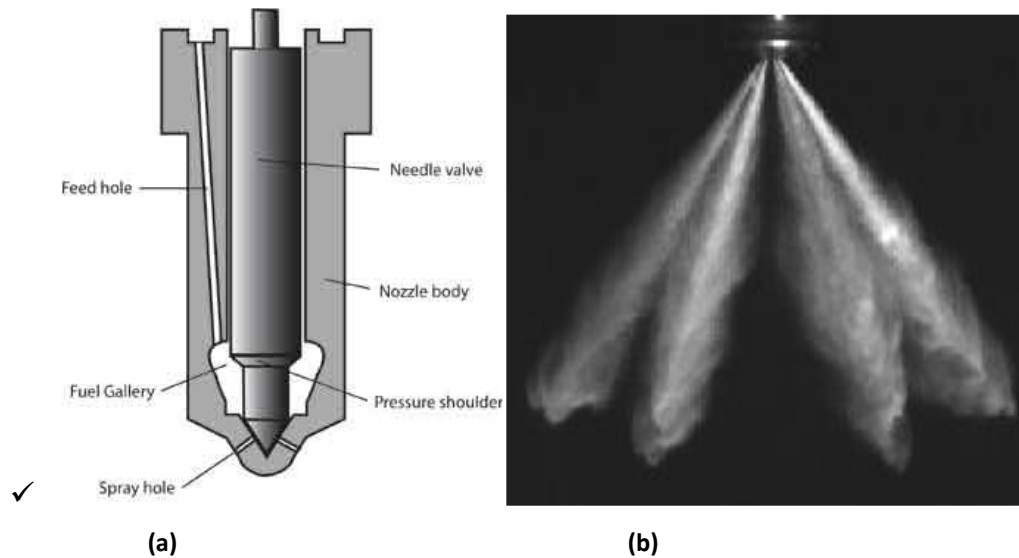
Figure 1-7 (a) Schematic model of a VCO (valve covered orifice) multihole injector , (b) Spray of 6-hole injector [20]

On the other hand, for a rail pressure of up to 100bar, multi-hole injector presents a poorer atomisation quality than the swirl atomizer. At higher pressure, atomisation improves at a satisfying level, However beyond 200 bar, the spray over penetrates leading to excessive wall impingement. The inward opening design of this injector implies the presence of an initial liquid mass trapped in the sac volume. Since this trapped fuel in the sac volume is isolated from the rail pressure, the atomisation at the start of the injection will be very poor and a significant amount of fuel entering the cylinder as large liquid droplets. In addition, the multi-hole atomiser has the problem of nozzle contamination by high temperature carbon soot due to its relatively small hole diameter (0.07-0.25mm) [9]. Another problem is associated with the cavitation erosion which will cause damage to the nozzle surface. Cavitation erosion of metals is characterised by local impacts of fluid against the metallic

surface due to collapse of bubbles, resulting in progressive loss of original material from the solid surface, in the vicinity of the active cloud within a liquid. Some problems related to cavitation are vibration in hydraulic machines, change in hydrodynamic flow, noise, thermal and light effects like luminescence, besides erosion wear. Erosion wear has demanded special attention of researchers and engineers in many applications eg. hydraulic machine components, high pressure injectors, etc. This is due to the high costs associated to preventive and corrective maintenance of the components, which are continually exposed to cavitation. For these reasons the design and the layout of this injector inside the cylinder has to be optimised not only for the best spray adaptability and stability but also to minimize the erosion wear inside the nozzle.

1.10 Controlled injector opening operation:

In this system, the electronic control unit records the triggering signal during the injection and determines the optimum timing for opening and closing the injector needles. This enables the electronic control unit to calculate the actual injection quantities of each individual injector and adjust this as required. This regulated control system allows even the tiniest quantities of fuel to be injected with minimal tolerances. The typical opening and closing event for the injector is 0.6 ms. [19]
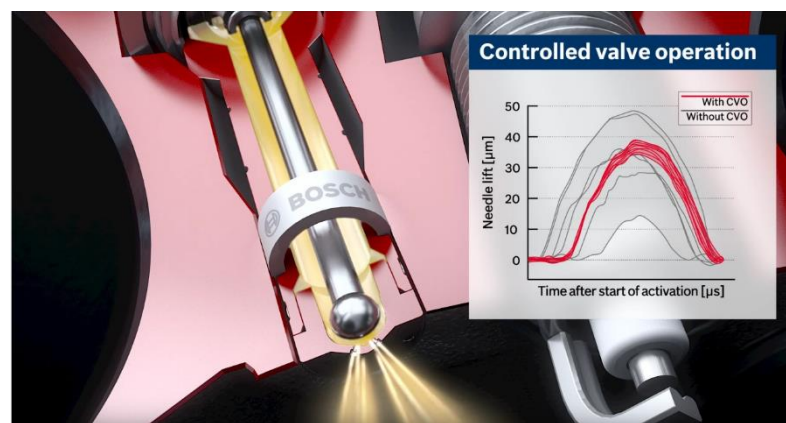
Figure 1-8 Controlled timing of the injector opening and closing events. The typical opening and closing event for the injector is 0.6 ms. [19]

1.11   Laser drilled holes

The high quality of the drilled holes in the injector helps ensure particularly good combustion of the fuel and helps reduce emissions at the same time. The gasoline is injected directly into the cylinder at high pressure (200 bar) through five to seven tiny laser-drilled holes. The sharp edges and smooth inner walls of the holes ensure that the fuel is atomized into extremely small droplets. The finer the spray achieved, the greater its surface area. This leads to particularly good contact with the oxygen in the air so that virtually all the gasoline is burned on ignition. For efficient, clean combustion, it is important to prevent droplets of injected fuel from being impinged and deposited on the walls of the cylinder or the surface of the piston. Such deposits result in poor-quality combustion. By drilling the five to seven holes in the injection nozzle with similar or different diameters, the best possible control over fuel distribution in the combustion chamber could be achieved. The diameters range from 0.25 millimeters down to 0.1 millimeters. The smallest openings allow less gasoline though, the larger ones slightly more. This creates a specific spray pattern in the cylinder, enabling the fuel to be used to maximum effect. [19]

Until recently, the technology for producing nozzle holes has been the Electrical Discharge Machining (EDM) technique. It has been developed to create close-spaced round holes with a taper. Limitations of EDM technology include long cycle times per hole, creation of molten metal, electrode consumption and the inability to create non-round holes. It also includes inability to create stepped-nozzles (counterbore) as shown in figure 1-9. [20]
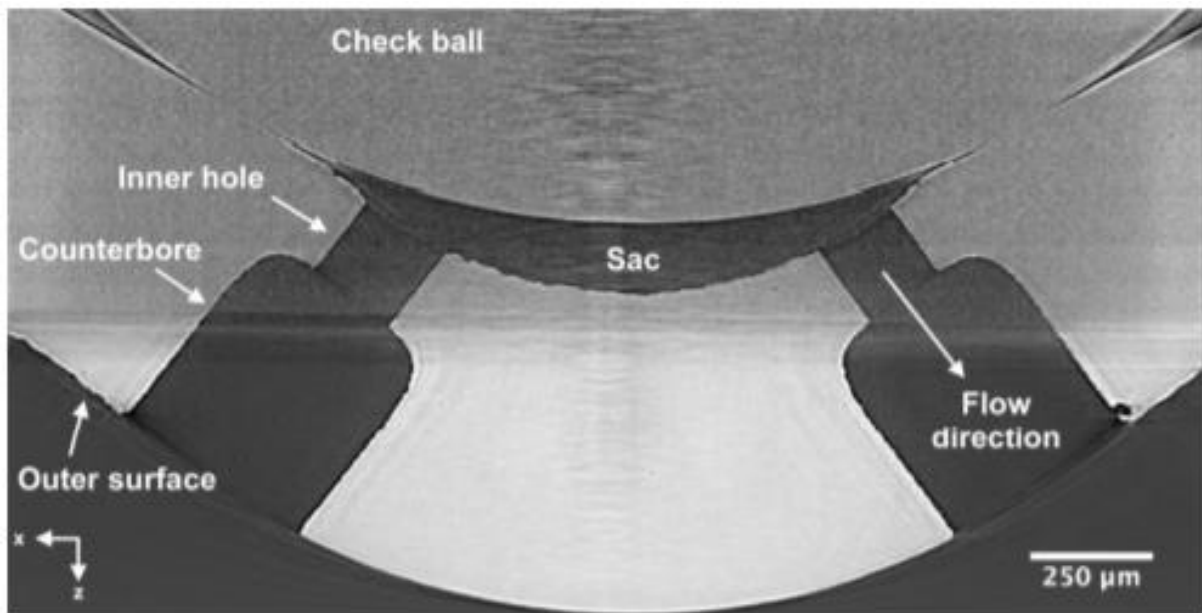
Figure 1-9 X-ray tomography of the tip of a multi-hole steeped injector. The inner hole and the counterbore are drilled using laser drilling technology. [21]

On the other hand, the development of femtosecond fiber lasers has made laser drilling viable for manufacturing injector nozzles including stepped-nozzle holes. Femto-second laser technology removes material at the molecular level without generating heat (ablation). This enables part machining to precise geometries with no thermal damage to the material (no melting, burrs, discoloration, recast, etc. Figure 1-10 compares femto-second laser drilling surface finish quality with EMD and pico-second laser drilling. [20]
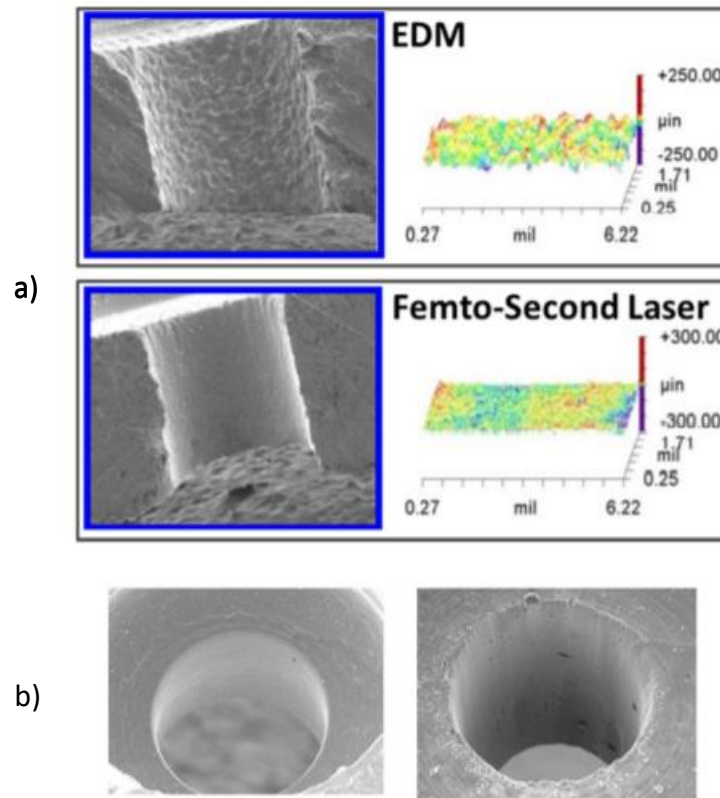
Figure 1-10 a) Comparison between EDM and femto-second laser surface finish b) femto-second laser hole (left) and pico-second laser (right) [20]

No post processing steps are required to achieve acceptable consistent hole geometry. As compared to the Pico-second laser the hole edge is more consistent and avoids spatter recast debris for the laser entrance side [22].

1.12   Injector tip wetting

Injector tip wetting – i.e. liquid fuel remaining on the tip of the injector after the end of injection – is a source of particulate emissions. The underlying fluid dynamics are poorly understood and, while it is known that changes in injector design can lead to significant improvements in particulate emissions, clear correlations have only been found for some injector design parameters. [23]

Figure 1-11 (a) shows high-speed visible light images of spray and tip wetting of a two-hole injector, field of view 1.5 × 1.5 mm^2 . Injection of n-heptane at 200 bar; the injection duration is 2ms.

(a)   (b)
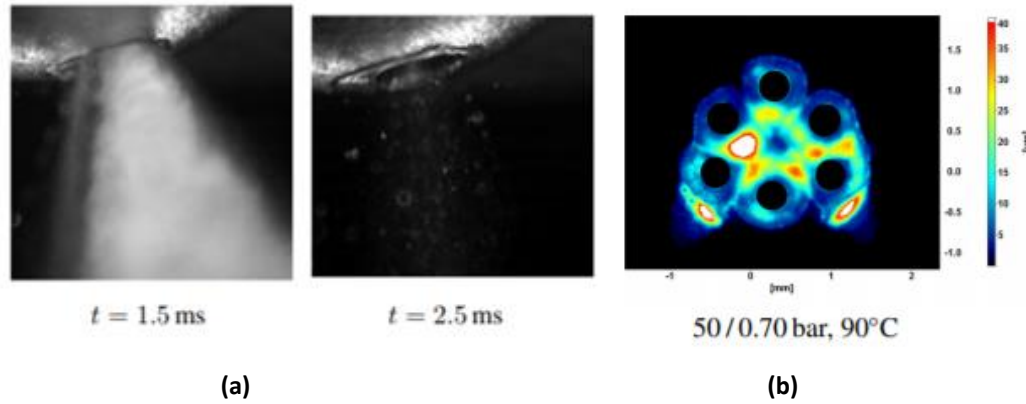
Figure 1-11 (a) High-speed visible light images of spray and tip wetting of a two-hole injector, field of view 1.5 × 1.5 mm^2 . Injection of n-heptane at 200 bar; the solenoid is energized for 1.5 ms and the injection ends at around 1.8 ms. (b) Fuel distribution and the wetted areas on injector tip, 4 ms AESOI, the white colored areas shown are saturated film formation, it is clear that the maximum film formation is inside the inner circle of the nozzles [23]

Figure 1-11 (b) shows Fuel distribution and the wetted areas on injector tip, 4 ms AESOI, the white colored areas shown are saturated film formation, it is clear that the maximum film formation is inside the inner circle of the nozzles closer to the injector axis shown by yellow arrow. It is not yet fully understood why the inner circle has higher film formation than the outer surface. [23]

1.13   Cavitation in multi-hole fuel Injectors

Cavitation is the phenomenon of vaporous pocket formation inside liquids, due to a drop in the local static pressure [24]; it commonly appears in hydraulic pumps, turbines, propellers, rudders, in high pressure fuel injection systems and in heart valves [25]. In general, cavitation causes flow blockage and choking and reduces the discharge coefficient of the nozzle, while the collapse of cavitation structures may lead to cavitation erosion damage with detrimental consequences on the reliability and maintenance of relevant devices.

Two main type of cavitation are recognized inside the nozzle of the injector including geometric and string cavitation.

(a)

(b)
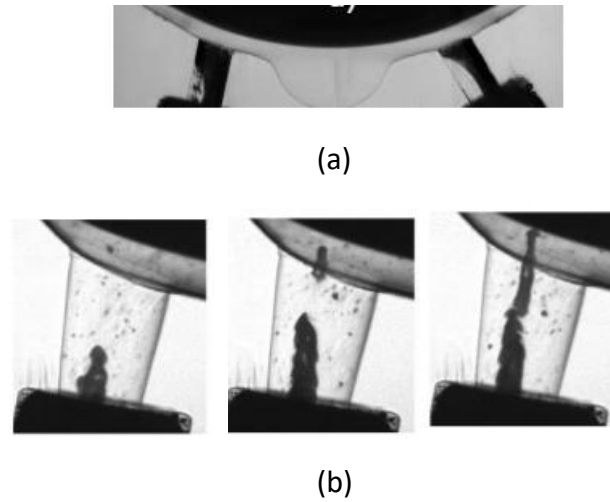
Figure 1-12 Different types of cavitation in transparent realsize models of SIDI injector: (a) Geometric cavitation (b) initiation and development of string cavitation [7]

It is believed that cavitation can enhance the turbulence inside the nozzle and the primary breakup and atomization of the spray. However it is also believed that cavitation can create instabilities in the nozzle flow and can affect the spray cone angle and ultimately can lead to misfire in the engine. In addition to this, cavitation causes erosion and material wear which will ultimately damage the internal geometry of the nozzle and can lead to poor performance in spray cycle to cycle stability [1] [2] [4] [7] [25].

Figure 1-13 shows the link between cavitation and erosion damage sites in a multi-hole injector. [26]
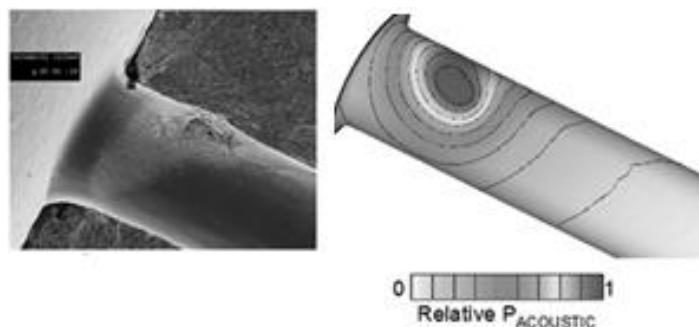
Figure 1-13 Link between nozzle erosion shown by SEM image of a cross-section of a nozzle (left) and the cavitation sites predicted by simulation of high acoustic pressure contour plots (right) [26]

Apart from the aforementioned effects, in the field of fuel injection systems, cavitation plays a detrimental role in jet formation, stability and atomization, affecting the combustion process and finally the performance and emissions of modern engines. For all the previous reasons, significant effort has been put in the investigation of cavitating flows and prediction/quantification of its related effects both with experimental and numerical/simulation techniques, in order to prevent negative aspects or harness any positive potential [25].

1.14   A critical review

Considering all factors discussed in this chapter, a short-term solution for CO_2 reduction that is viable more quickly is the hybridization of direct injection gasoline engines. A direct switch from gasoline to gasoline-mild-hybrid can deliver 11%, and a further 23% in reducing CO2 in moving to full hybrid. [27] As these numbers demonstrate, there are immediate-term options for significant fuel efficiency improvement and, hence, CO_2 reduction of the order of 30% or more. [28]

With regards to the emission problem with current IC engines, a critical review to mention is that a distinction should be made between pollutant emissions and the CO_2 emissions from combustion engines. CO_2 emissions necessarily accompany any hydrocarbon combustion. The CO_2 is directly proportional to the hydrocarbon fuel that is consumed, which is continually being reduced by technological improvements. [28]

In the medium-to-long term, there is even greater scope for improving engines by co-designing biofuel/engine systems for optimal performance. Considering all the facts that has been discussed from the beginning of this chapter, it is important to note that there are still no real alternatives that can compete with the SIDI engines over the entire range of applications that they cover and that, even today, SIDI engines are undergoing continuous further improvement. [29] These developments make it even more challenging for competing technologies to gain advantage over the SIDI engines.

Focusing on transport, the demand for energy is very large. There are around 1.2 billion light-duty vehicles (LDVs) and around 380 million heavy-duty vehicles in the world, and these numbers are growing. These numbers are not comparable with 5 million EVs sold worldwide today. In addition, the daily demand for liquid fuels exceeds 11 billion liters (23000 million tons oil equivalent per year). [28]

All alternatives, whether they are alternatives to IC engines or alternatives to petroleum-based liquid fuels, face very significant barriers to fast adoption. But, ill-informed mischaracterizations of combustion have led to the belief that the IC engines are experiencing its final years of its existence. [30] The conclusion obtained here is that, for the foreseeable future, road and off-road transport will be characterized by a mix of solutions involving internal combustion engines (ICEs) as well as battery and hybrid powertrains. Therefore it is necessary to continue researching on fundamental studies in direct injection systems used in IC engines in order to improve the design of fuel injectors and understand how different parameters in the injection system including design and operational parameters such as nozzle geometry, pressure, cavitation, erosion, etc can affect the in-nozzle flow and spray breakup and atomisation in order to achieve optimized combustion.

1.15   Aims and objectives

The importance of cavitation inside multi-hole injectors has been addressed in many previous investigations and they are given in next chapter. They have quantified the cavitation formation and its development and the spray characteristics and atomisation. Different types of geometrical and vortical cavitation have been identified and their advantages and disadvantages has been discussed. Among the advantages, cavitation can increases atomisation and therefore enhance fuel vaporisation, which lead to better engine performance with higher efficiency and lower emission. On the other hand, it is believed that uncontrolled cavitation can induce instability in the jet spray cone angle that may

change the spray plume directed towards the spark plug. This may cause misfire in the stratified charge mode combustion operation. In addition, the bubble collapses which resulted from intense cavitation clouds can produce shockwaves near the surface of the nozzle holes. The impact force of this shockwave is so much that it can cause surface erosion. All, in all, the influence of cavitation on the formation and stability of the emerging jet spray characteristics is not fully established and needs to be investigated further. Another important issue is the influence of the nozzle tip design and the stepped-hole nozzle on the internal flow and ultimately the performance of the injector and that it can influence the atomisation of the spray. Thus the spray from a new stepped-nozzle multi-hole injector will be fully characterised and compared with previous conventional injectors. Also the wetting of the tip of the nozzle which can cause unburned hydrocarbons should be minimised. Thus the main aims of the current research work are to address these outstanding issues through the following experimental investigation:

- The first phase of the experimental investigation was to visualise the in-nozzle flow and cavitation development inside a 15-times transparent enlarged model of a conventional multi-hole injector (6-holes symmetric) using high-speed visualisation (Mie Scattering) technique. The in-nozzle cavitation and near-nozzle exit jet spray were visualised simultaneously and were quantitatively analysed to stablish the link between the cavitation and emerging jet spray instability, and to enhance our understanding further. A new optical configuration has been designed for the injector model that allowed the visualization of up to 50,000 fps with high quality images; an improvement on imaging frame rate of up to 2.5 times compared to the previous works who used the same model and the same experimental equipment.

- In the second phase of the experimental investigation, a new enlarged model injector was designed that was geometrically similar to phase 1 model but 7-times larger than the real injector; the new model was manufactured in house utilising a Computer Aided Design software. The new model allowed an enhanced simultaneous visualisation of the in-nozzle flow and near-nozzle jet spray and a comparison between the two different enlarged models. In this phase, the new

transparent model was uniquely designed in SOLIDWORKS to provide almost the same viewing depth-of-the-field of the camera (DoF of less than 1mm) for the in-nozzle flow region and the near-nozzle exit jet spray, which allowed both flow regions to remain optically sharp, which, in turn, it helped to improve the image analyses greatly. The results revealed different stage of cavitation at different cavitation numbers. It was observed that cavitation and the string directionality can affect the spray jet axis. It also revealed that the hydraulic flip happens much earlier than expected and at lower cavitation numbers compared to the 15 times enlarged model. It also reveals that a stochastic ligament spray with much lower velocities is being formed at the vicinity close to the upper part of the nozzle exit where the air entrainment seems to be maximum which can ultimately result in stochastic tip wetting of the nozzle. The wetting phenomena can happen inside the counter bore stepped-hole region of the nozzle or on the curved surface on the tip of the injector nose

- In the third phase of the experiment, a real-size stepped injector test rig was designed and manufactured using SOLIDWORKS which enabled the injector to rotate along the axis of the needle 360⁰ freely and allowed high-speed visualization of the spray plume from different angles. A CAD model of the injector was also designed from scratch in SOLIDWORKS which allowed the assembly to be rotated and configured and enhanced the views of the stepped holes from different angles for visualization. It also enabled the measurement of the spray tip penetration and cone angle from different viewing angles. It further allowed the visualisation of the overall spray behaviour and very near-nozzle exit spray which is also important for PDA setup.

- In the fourth phase of the experiment, a Fiberflow Dantec PDA measurement system was setup to measure spray characteristics including droplet diameters and velocities at the very near-nozzle area of the injector (1mm from it) up to a distance 35mm from injector, to investigate early breakup. Due to the very closed-spaced compact arrangement of the nozzle holes located at the injector tip region, high

attention was given to the setup and location of the probe position at the edge of the injector tip. In order to do this, the zero point of the traverse reference system was carefully chosen using a novel technique which ensured that it was exactly located on the symmetric axis of the injector tip. In addition, one of the nozzle jet sprays was carefully isolated and the optical mounting was rotated and aligned in a specific direction that allowed the spray droplets to have maximum exposure to the PDA detector system while travelling through the probe region, and therefore minimising the attenuation of the transmitting beam and collecting scattered light; this was possible only by designing a new model of the injector that allowed 3D rotation of the assembly in CAD software in order to find the best possible arrangement for PDA measurement; this new arrangement was done accordingly in the real-size model which allowed full measurement of droplets diameter and velocity across the jet spray at 1mm away from the exit.

1.16   Outline of the thesis

The current thesis comprises of seven chapters. Chapter 1 presents an intoruction to the growing market of gasoline direct injection systems and the underlying reason behind why it is still a dominant market. The brief explanation comprises drawbacks, benefits and targets of the new direct injection systems including the multi-hole injection system and the technology involved. Chapter 2 contains a literature reviews of some of the most recent papers about gasoline direct injection. More specifically, it reports the review of literature about investigation on enlarged models, spray characterisation and publications on the multi-hole gasoline fuel injectors. Every paper or document reported includes the name of the corresponding authors, the description of experimental set up, Technique and the main findings and conclusion. Chapter 3 examines the breakup theory and some fundamentals of the experimental techniques used in the current research. Chapter 4 reports the methodology used in this research which is subdivided into 4 phases: phase one and two

which includes the visulisation of the in-nozzle flow and near nozzle spray in 15 times and 7 times transparent model of a 6 hole gasoline stepped multi-hole injector, respectively. Phase three involves visualization of the spray in a real-size gasoline stepped-hole multi-hole injector and reports on performance of the spray including analysis on structure, tip penetration, cone angle and some near-nozzle analysis of the spray. And finally phase four contains full analysis on PDA measurement of the spray in the real-size stepped multi-hole injector. Chapter 5, 6 and 7 presents the results of this research. Chapter 5 includes results from visulisation of the enlarged models of injectors (7 and 15 times enlarged models). In this chapter the link between geometric and string cavition and erosion of the nozzle is addressed. The influence of geometric and string cavitation and shedding on spray stability has been addressed too. The formation of stochastic ligament spray is also visualized. Chapter 6 presents the results of visulisation of real-size spray and comparison of the structure, tip penetrataion, cone angle of the current injector with two other models of multi-hole injectors which has been investigated in the group. Chapter 7 contains results of the full PDA measurement of the spray at different distances from the nozzle exit and the error analysis of the PDA measurement. Chapter 8 contains conclusion and recommendations for further work in the area of experimental research on the mult-hole injector. The bibliography of the references of publication and documentation cited throughout the thesis is then presented followed by the appendices.

Chapter 2 : Literature Review

2.1   Introduction

This chapter provides literature review of some of the most important papers for in-nozzle flow and spray characteristics of fuel injection systems which are focused on dense fuel sprays i.e high pressure gasoline fuel injection systems. Section 2.2 consists of a table with Part A, B and C.

Part A in section 2.2 presents the summarized tabular format of the papers in the literature on the subject of internal nozzle flow. This topic is primarily focused on SIDI injectors but also includes relevant diesel injector literature. Within this topic is any research focused on the internal flow upstream from the nozzle exit. The papers are in chronological order starting with the most recent papers. As the research on the near-nozzle atomistation of the stepped-nozzle multi-hole injector is relatively rare, there are currently very few paper on the characterisation of the spray in this region and also this type of injectors.

Part B in section 2.2 is focused on the spray characterisation of gasoline sprays. The bulk of this topic is experimental data from overall spray characterisations using either the Mie scattering or Phase Doppler Anemometry or Xray phase contrast imaging. Very few of the most recent papers are focused on characterization of stepped-nozzle while there is a lack of near-nozzle data for this type of injector. However, there is a small proportion of work which includes some data from the near nozzle spray region. Part C presents a few examples of miscellaneous papers related to this research.

Section 2.3 provides a summarized storytelling of the literature review for the relevant papers which have investigated the in-nozzle flow and and the jet spray.

Finally section 2.4 identifies the gaps in the literature review and identifies the key papers in this field.

2.2   Major findings in the literature review

Part A: In-nozzle flow	
paper	Major findings
Dimitri Mamaikin et al 2020 [7]	The velocity field upstream of the hole reveals a slightly faster flow on the outer side of the injector due to the impact of throttling in the needle seat. The static pressure distribution shows the minimum pressure region in the upper, inner side of the hole. This region was observed to be the recirculation area of the flow due to relatively high, local flow deflection. The outlet velocity was found to be around 120-130 m/s.
Tekawade et al. 2019 [31]	The cavitation layer arises from known azimuthal variations in the inlet corner radius and extends, at some angles, the full length to the exit of the nozzle potentially causing hydraulic flip. A flow blockage of up to 30% is observed at the nozzle exit. Simulations predict the asymmetric, strongly cavitating flow as shown by the experimental results
Torelli et al. 2019 [32]	Manufacturing tolerances and needle radial motion are responsible for orifice-to-orifice mass flow rate differences. Needle motion variability is responsible for shot-to-shot inconsistencies. Cavitation in the orifices and at the needle seat correlate strongly with radial needle motion. Cavitation within the orifices might increase shot-to-shot variability by reducing the orifice cross-sectional areas and discharge coefficients. Cavitation might lead to local erosion of the nozzle internal geometry, leading to even higher variability with time
Karathanassis et al. 2018 [6]	In geometrical layouts where wall curvature affects the flow, vortex cavitation is promoted over cloud cavitation. Frequency analysis of cavity radius allowed estimations on the recirculation intensity found to be in agreement with the cavitating-vortex theoretical model by Pennings et al. 2015. Measurements of the flow turbulence PTV

	demonstrating that turbulence is suppressed in the presence of well-established cavitation according to Koukouvinis et al. (2017)
Koukouvinis et al. 2017 [33]	Cavity shedding, collapse and vortex cavitation (string cavitation) has been visualized. Sheet cavity formed at the edge of the orifice entrance, oscillating at a Strouhal number of ~0.35-0.38, based on orifice diameter and average flow velocity (attached cavity shedding period of 78-95 µs for high and low cavitation number operation respectively. Attached cavity collapses at ~2 mm from nozzle inlet. Shed cavities collapse at 7-8 mm downstream the entrance. Existence of counter rotating vortices 2mm downstream of the nozzle entrance (with 95 micro second shedding period corresponding to CN=1.5) and 2.5 mm downstream of the nozzle entrance (with 78 micro seconds shedding period corresponding to CN=2.18). At *Cn* = 1.5 shows a peak of turbulent kinetic energy at ~ 2 mm downstream the orifice entrance. High cavitation number operation shows two peaks, one at ~ 1mm downstream the entrance and another at ~ 8 mm downstream the entrance. Experimental results indicate that the isosurfaces of 25%, 50% and 75% liquid reach ~ 6 mm, 7 and 8mm respectively. Liquid fraction distribution does not match very well with simulation rise and collapse of a cavitation structure at the trailing edge of the cavitation cloud from vapour pressure from ~0.172 bar to 200 bar within 2 µs. Single cavity collapse and collapse cascade are shown. Two distinct erosion sites relates to attached cavity collapse at length of 0-5mm and detached cavity at length of 5-10mm collapse.
N. Mitroglou et al 2014 [34]	At low needle lifts, string vapour structures were observed and found to be air entering the low pressure region of the nozzle flow and extending upwards towards the hole inlet, rather than cavitation extending down from the sac volume. Once these vortex structures reached the hole inlet and interacted with geometric cavitation, the spray cone angle was found to vary from approximately 20º to a

	maximum of 55º . At higher lifts there appears to be little change in the behaviour of the flow, other than the level of geometric cavitation being enhanced. It is stated that string cavitation, while promoting atomisation, is particularly unstable. However, geometric cavitation has been shown to be more stable and exhibiting a good balance between atomisation and stability.
Nouri et al 2012 [35]	General observations of cavitation with respect to needle lift show the same trends as the other extensive research done using large-scale models. Lower needle lifts were shown to exhibit reduced geometric and string cavitation occurrence and intensity. While the cavitation structures present in both nozzles were found to be the same (due to almost identical inlet conditions), the longer hole length nozzle was found to exhibit fewer and more stable cavitation structures at the nozzle exit. Higher fluid viscosities were found to slightly suppress the intensity of the cavitation, especially at the onset of cavitation within the nozzle. •The effect of fluid viscosity or L/D on the spray was not investigated.
Aleiferis et al 2010 [36]	The effects of back pressure, fuel type, nozzle diameter and injector body temperature on the cavitation number were demonstrated. Nozzle diameter was shown to have the greatest effect for a given fuel while at sub atmospheric back pressures a small increase in temperature was shown to have a marked effect on the cavitation number. Cavitation bubbles have been observed to exit the nozzle before conditions of choking are experienced in the nozzle. At the critical cavitation number the dominance of cavitation over chamber pressure is apparent with respect to the spray cone angle. The onset of cavitation rapidly increases the spray cone angle of the spray by 1.2º despite only a decrease of 0.15 MPa in chamber pressure. As expected, decreasing back pressure or increasing injection pressure reduces the spray cone angle. However, when crossing the region of

	the critical cavitation number, the spray cone angle rapidly increases before returning to the original trend. Film cavitation on the upper edge of the nozzle hole entry was observed under all conditions for all fuels and nozzles. Under most conditions the spray was found to be asymmetric due to the film cavitation at the top edge of the nozzle hole entry.
Tropea et al. 2009 [37]	For all nozzles, two counter rotating vortices were observed in the cross plane of the spray. One was found to exhibit four vortices in the near nozzle region that quickly broke up into two. As expected, higher turbulence levels in the spray improved breakup but it was observed that vortices in the cross plane retarded breakup.
Andriotis et al 2008 [38]	String cavitation structures were found to be present in all nozzles and inception was observed to both begin in the sac volume and through the mechanism of air being drawn into the centre of the nozzle exit due to the high vorticity of the nozzle flow. The frequency of string cavitation appearance was correlated to the Strouhal number of large scale vortices present in the nozzle hole. Two different flow regimes containing string cavitation structures have been observed within the nozzle. The first is where the cavitation string interacts with the geometric cavitation and the second where the string is confined to one half of the nozzle and doesn't interact with the geometric cavitation. Both have been observed in all nozzles in all injectors. It has been shown that the discharge coefficient of the nozzles increases at lower needle lifts due to the cavitation being less well developed and that the fewer the nozzle holes; the greater the discharge coefficient. It has been stated that relatively, tapered holes are more sensitive to variations in spray cone angle. This is because the suppression of geometric cavitation in these nozzle holes means that the minimum cone angle is lower yet the widening of the cone due to string cavitation (a maximum) is equal between tapered and non-

	tapered holes. The tapered nozzle design exhibits significantly lower spray cone angles than that of the cylindrical nozzle; particularly the bottom angle when in a non-cavitating state.
Gavaises et al 2009 [4]	With a tapered (converging) nozzle hole, it was found that string cavitation was the dominant cavitation structure observed while with a parallel hole both regimes were present. In both cases greater needle lifts resulted in more fully developed and reduced intensity cavitation. In the tapered hole it was observed that often the string cavitation would form from the nozzle exit where-as with a parallel hole it often formed at the hole entry as a result of geometrically induced cavitation bubbles appearing close to the hole axis. Contrary to previous research, the Reynolds number was shown to have an effect on the probability of the appearance of strings in the nozzle hole. However, the cavitation number and needle lift are the dominant factors.
Gavaises et al 2008 [26]	Shows similar erosion images to the previous paper in 2007. The use of a grooved VCO needle has been shown to significantly reduce cavitation intensity and collapse in these regions but the suppression of cavitation likely degrades the atomisation due to the increased emissions observed when using this nozzle. Experiment and simulation have suggested the discharge coefficient can be reduced by 8% as a result of cavitation at low needle lifts with increases as the needle lifts. AT low needle lifts string cavitation was observed in all nozzles regularly except the normal VCO nozzle with no groove. At all lifts the tapered nozzles only exhibited string cavitation while the cylindrical showed evidence of fully developed cavitation with strings at high needle lifts. All variations on the standard VCO showed much lower acoustic pressures and cavitation erosion after testing. It is thought that the needle groove allows the fluid to turn into the nozzle hole more easily, particularly at low lifts, while the tapered nozzle

	suppresses geometric cavitation. It is stated that string cavitation is unlikely to be the cause of surface erosion in injector nozzles because experimental evidence shows that they do not collapse near the surface but remain in the central region of the nozzle passage.
Andriotis et al 2007 [1]	String cavitation structures were found to originate at the cores of recirculation zones. It was also found that air sucked in at the exit of the nozzle holes could initiate cavitation. Cavitation strings were found to be a function of both needle lift and nozzle hole entrance shape. A variation of up to 10% in mass flow rate of the nozzles was recorded due to the presence of cavitation structures choking the nozzle flow. Through extrapolation string cavitation is expected to be present in shorter time scales than an injection event in a real size nozzle, showing that they are able to influence the hole-to-hole and cycle-to-cycle repeatability of the spray
Nouri et al 2007 [39]	The visualisation revealed that the flow into the nozzle holes originated either from the incoming annular flow above the six injection holes or from the deflected annular flow inbetween two adjacent injection holes. This flow regime was a possible cause for the formation of vortices in the sac volume between the needle face and the two adjacent injection holes. Needle strings first appeared in the multihole gasoline injector prior to the formation of geometric cavitation structures. The onset of cavitation was found to be when the cavitation number approached 0.7 - 0.9 and presented a well developed structure for CN higher than 1 when needle strings started to disappear. Following the disappearance of the needle strings another type of string cavitation known as vortex strings were found to appear.

Part B: Gasoline Spray Characterisitics	
Spencer et al. 2019 [40]	Under non-flash boiling conditions, it was found that the injection pressure dictates the length of the spray penetration before collapse occurs, with an increase in pressure resulting in an increase in this length. The mid-sized of the three-hole diameters tested there was found to produce a spray that more readily collapsed than that of the smaller or larger hole diameters under flash boiling conditions, the convergent hole had a greater propensity to exhibit spray collapse. The larger droplet size resulted in a lower level of droplet breakup in comparison to the smaller diameter holes, because of the lower fluid velocity of the large hole.
Battistoni et al. 2018 [41]	Comparison between experimentally measured and predicted interfacial area profiles reveals the potential of the USAXS measurement to distinguish regions of continuous liquid structures and finely atomized droplets. In central regions of the spray, the projected surface area profile may be related to the degree of atomization of the liquid jet; local minima may indicate regions of poorly atomized spray comprised of larger liquid structures and detached droplets, whereas local maxima may indicate regions of completely atomized spray.
Duke et al 2017 [8]	plume-to-plume variations in the mass fluxes from the holes can cause large-scale asymmetries in the entrainment field and spray structure. Both internal flow transients and small-scale geometric features can have an effect on the external flow. It is difficult to optically access individual plumes. Strong entrainment effects and persistent unsteadiness in the spray after the needle reaches full lift limit the usefulness of steady- state analysis. The sharp turning angle of the flow into the holes also causes an inward vectoring of the

64

	plumes relative to the hole drill angle, which increases with time due to entrainment of gas into a low-pressure region between the plumes. The plumes were found to have a decreasing targeting angle with increasing distance from the nozzle. PDA reveals a time-dependent motion of the plumes toward the nozzle centerline. Therefore the spray does not have a true 'steady state'. The x,y wobble does not cause any appreciable change in the flow area into the sac. However, the z motion may lead to asymmetric and time-varying inflow to the sac and to the nozzle hole flow. This points toward the need for transient simulation efforts which include the details of the internal nozzle geometry.
Moon et al. 2017 [42]	The fuel with lower surface tension promoted the spray atomization The effects of fuel property and injection pressure on spray atomization became saturated from a certain Weber number (critical We0). The critical We0 decreased as the nozzle hole length decreased. The relative velocity (ratio of spray center velocity at certain axial location to initial injection velocity) at the atomization termination location appeared almost identical (0.72) regardless of the injection condition. It indicated that the faster spray deceleration caused by the promoted initial flow breakup and dispersion brought the atomization termination location closer to the nozzle due to rapid attenuation of liquid-gas relative velocity, which is denoted as 'trade-off relationship between the degree of initial flow breakup and potential atomization distance
Zigan et al. 2012 [43]	The investigation shows that the viscosity of the fuel plays an important role in the breakup and spray characteristics of the emerging spray. Thus it is important to select the appropriate fuel when using working fluids other than gasoline in optical experiments. For a given Re, a reduced viscosity enhances turbulence within the nozzle and appears to result in a narrower spray cone angle with

	increased penetration over the resultant spray from a higher viscosity fluid. Elevating the temperature increases the Re and thus has the same effect. Using a higher viscosity fluid appears to enhance the spray breakup even at low Weber numbers. Thus it can be stated that the Reynolds number plays an important role, along with the Weber number, in spray breakup.
Zigan et al. 2011 [45]	Comparison of a range of alkanes showed that iso-octane, while being a good representative of gasoline, was inferior to n-heptane in terms of kinematic viscosity for example. The type of fuel used was found to have a big influence on the size of the recirculation zone at the outer edge of the spray with the biggest difference coming from the high volatility fuels, especially late in the injection. Axial fuel propagation was relatively unaffected by the fuel type while radial propagation showed high sensitivity to the fuel characteristics. As the volatility of the fuel reduced, the droplet sizes of the fuel increased as expected. with gasoline having an average droplet size about 50% great than iso-octane. In nearly all respects the in-house 3-component fuel was found to better represent gasoline than the single component fuels tested. This was especially true of the evaporation characteristics and its effect on fuel distribution.
Marchi [44]	According to the Weber number trend, the secondary breakup takes place up to an axial location of 20mm (27mm in jet direction). This result was in agreement with the mean diameter distribution which shows a reduction from 14μm to 7μm (50%) within 27mm from the injector tip. At axial location beyond 40mm, phenomena such as turbulence and recirculation could promote droplet collision and, therefore, coalescence represented in PDA plots by bimodal distribution corresponding to a group of very fine droplets and a group of agglomerated droplets.

Nouri et al 2007 [45]	The overall spray cone angle was found to be almost independent of injection pressure. A higher chamber pressure resulted in a reduced tip penetration length due to increased drag. Spatial velocity profiles were jet-like at all axial locations with the maximum residing along the spray cone axis. Temporal velocity profiles were shown to increase rapidly during the SOI, remain almost constant during the main part of the injection and then decrease during needle closing. The chamber pressure was shown to have a much larger effect on the droplet size than injection pressure. Higher rail pressures slightly reduced the droplet size where-as higher chamber pressures significantly increased the droplet size due to coalescence.
Mitroglou 2006 [46]	When the dwell time between the two injection events in a double injection strategy is longer than 0.5ms it was found that the second injection event was unaffected by the first. For dwell times under 0.5ms, it was observed that a significant amount of pre-spray preceded the second injection event. This was very dependent on the injection pressure. Higher injection pressures were found to result in an earlier SOI for the second injection event. Contrary to previous research, injection pressure was found to have an apparent effect on the needle opening rate. PDA results showed that the droplet velocities in the second injection event were higher, even with a 1ms delay. This implies that the flow inside the sac volume of the injector has still not stabilised after 1ms.

Part C: Mischellaneous papers	
Leicke et al. 2018 [23]	Increased injection pressure is consistently found to decrease tip wetting and particulate emissions and tip wetting is most pronounced when flash-boiling of the spray occurs. It is only in the front view configuration of the injector tip that the tip wetting can be quantified and this is only after the injection finishes while the side view visualisation highlight the temporal evolution of spray structure and liquid film formation and facilitate a distinction between films formed during the quasi-steady phase of the spray or deposited on the tip as the injection ceases. It is not yet fully understood why the inner circle has higher film formation than the outer surface
Reits et al 2019 [28]	IC engine research have a bright future, in contrast with some widely distribu. The power generation and the vehicle and fuel industries are huge, representing trillions of dollars per year, with a massive infrastructure. The power generation industry will not become fully renewable and transport will not become fully electric for several decades. Highly efficient ''fully flexible'' engines with hybridized solutions will be a big part of sought-after efficiency improvements, as well as emission/GHG reductions
Sivathanu et al. 2017 [47]	Higher ambient and injection pressure result in higher transient peak surface area which gradually decreases as we move toward lower ambient and injection pressure. This was attributed to fine spray at the higher injection and ambient pressures leading to higher drop surface area while a merging of plumes leading to smaller drop surface area.
Befrui et al 2016 [48]	VOF-LES analysis of the ECN spray G seat flow and the near-field primary atomization coupled to a Lagrangian stochastics simulation method adopting the discrete droplet model (DDM), found that there is notable interaction of spray with the counter-bore walls.

2.3   Summary of the literature review

Fuel injection methods and strategies have been developed extensively during the history of the IC engine [49] [50] . Multi-hole injectors are wildly used in both diesel and gasoline engines and have many advantageous such as their flexibility in terms of number of holes and their arrangements which can be fitted to different combustion cylinder head, their ability to produce stable spray which is critical for spray guided concept, and their ability to be used at high injection pressure to ensure enhanced atomization and evaporation [39] [51]. Successful fuel delivery depends on controlled, reliable and consistent injection events. The structure and stability of the fuel spray depends on the design of the injector, and the injection parameters such as the injection pressure and duration, ambient pressure and temperature, and fuel temperature [52] [53]. Experimental studies of in-nozzle flow characteristics, in particular, cavitation in enlarged transparent model multi-hole injectors and spray characteristics of real size multi-holes have been extensively investigated by City research group [1] [2] [3] [4] [5] [26] [38] [46] [54] [55] [56] [57] [58] [59] [60] [61] [62]. Different optical methods e.g. Mie scattering spray visualization using a high-speed camera, LDV, PDA, PIV and PLIF have been used to characterise in-nozzle flow, spray shape/cone angle/penetration, special distribution of droplets size/velocity and fuel mixture distribution at different operating condition. The results of in-nozzle flow of enlarged models showed that the dominant flow phenomenon within fuel injectors is the cavitation which, in turns, influences the spray liquid break up and plays a major role in spray stability. Arcoumanis et al. [63] showed that needle eccentricity was found to influence the internal annulus flow inside the injector and consequently affect the nozzle flow and local cavitation structures. Cavitation within the nozzle holes of multi-hole SIDI injectors can lead to significant spray instabilities which can cause problems in combustion when operating in stratified mode. Therefore knowledge of in-nozzle flow characteristics, in particular the cavitation formation, its development and its link with liquid break-up at the exit of the nozzle hole is essential. This call for a closer look into the details of the link between cavitation and emerging spray in order to establish how cavitation influence spray shape,

instability and break up. From previous researches, the high speed flow visualization was found to be the best method to start investigating the development of cavitation inside the nozzle injector as it identifies different type of cavitating flows, their mechanisms, their developments and the regions they occur; the results are detailed enough that can also be used to validate the in-nozzle flow calculation by CFD models. Imaging of the flow inside the injector nozzle has identified the formation of three different types of cavitation as a function of the cavitation number, CN [59]. The first is needle cavitation, in the vicinity of the needle, which penetrates into the opposite hole when it is fully developed. The second is the well-known geometric cavitation originating at the entrance of the nozzle hole due to the local pressure drop induced by the nozzle inlet hole geometry. Finally, and at the same time as the onset of geometric cavitation, string type cavitation can be formed inside the nozzle sac and hole volume having a strong swirl component as a result of the large vortical flow structures present there; these become stronger with increasing CN [59]. Its link with geometric cavitation creates a very complex two-phase flow structure in the nozzle holes which seems to be responsible for hole-to-hole and cycle-to-cycle spray variations [59]. Arcoumanis et al (2000) [64] showed that geometric and string cavitation structures were observed to occur at different cavitation and Reynolds numbers. It has been revealed that cavitation strings are found at the areas of flow circulation and they originate either from pre-existing cavitation sites forming at sharp corners inside the nozzle where the pressure falls below the vapour pressure of the flowing liquid, or even from suction of outside air downstream of the hole exit [60]. Arcoumanis et al (2001) identified two types of film cavitation; pre-film and film. In this study, string cavitation only appeared at high lifts in the real size injector but at all lifts in the enlarged model. Interaction between string cavitation and film cavitation was also observed [60]. The converging nozzle, coupled with greater nozzle inlet radius, was found to suppress cavitation under all test conditions. The highly cavitating cylindrical nozzle was found to have a greater individual spray cone angle, particularly at the start of injection [65]. The previous studies have provided experimental data with regards to the questions about string cavitation origin, area of formation, lifetime and influence on the nozzle hole flow [1] [4]. Information for their frequency of formation, time of development, frequency of appearance and size within the

injection hole has been also reported [1] [4]. The frequency of appearance of strings has been correlated with the Strouhal number of the large-scale vortices developing inside the nozzle volume [1]. Cavitation erosion has been observed at different locations within the nozzle. These have included the top surface inside the nozzle hole next to its entry, the 3o'clock and 9c'clock hole side-inlets as well as at the needle seat area [26]. The cavitating flow regimes associated with these erosion sites correspond to geometrically-induced hole cavitation, the string cavitation and the needle seat cavitation, respectively [26]. Large variations in the instantaneous fuel injection quantity of individual injection holes have been recorded when a cavitation string is observed inside them [1]. Combination with model predictions has revealed that the observed reduction in the individual hole flow rate is partially due to the increased vapor fraction inside the hole when a string is present; the vortex flow developing upstream of the hole entry is the main reason for the observed trend [1]. Extrapolation based on model predictions for real-size injectors operating at realistic injection pressure indicates that cavitation strings are expected to appear within the time scales of typical injection events [1]. Flow images indicate string cavitation, can be formed from outside air trapped in the core of recirculation zones persisting up to the exit of nozzle holes. The formation of cavitation strings is enhanced with increasing flow rate (and thus increasing cavitation number) while it is less sensitive to needle lift. Cavitation strings may travel upstream the injection hole entry well inside the nozzle's sac volume but with a reduced frequency of appearance compared to their presence inside the injection hole [38]. Nozzles with tapered holes also suppress formation of geometric cavitation and have also been proved erosion-free. However, experiments performed in enlarged transparent nozzle replicas have provided evidence of string cavitation structures formed inside the different nozzle designs. The nozzles with the grooved needle have been found to enhance formation of string cavitation, in an unsteady and non-repeatable mode. The formation of cavitation strings was maximized at lower lifts of the grooved needle in the tapered hole nozzle. Interestingly enough, the grooved nozzle designs dominated by string cavitation have been found to result in increased engine exhaust emissions, while nozzles with tapered converging holes have been found to satisfy both durability to surface erosion and engine exhaust emissions [2] [5]. The most recent study has provided a number of

experimental data for string cavitation regarding their origin and their immediate effect on spray instabilities [62]. Presence of such string structures is found to alter the spray dispersion angle significantly and induce random instabilities. At later stages during the injection event and at times when flow is fully developed inside the hole, string cavitation is identified to initiate at the hole entry [62]. The absence of string cavitation has been demonstrated stable effects on spray dispersion angle and subsequent atomisation quality. The location of cavitation strings relative to the geometric-induced cavitation inside the hole is strongly connected to the instability of upper or lower spray boundary [62]. The velocity field upstream of the hole reveals a slightly faster flow on the outer side of the injector due to the impact of throttling in the needle seat [7]. The cavitation layer arises from known azimuthal variations in the inlet corner radius and extends, at some angles, the full length to the exit of the nozzle potentially causing hydraulic flip with flow blockage of up to 30% is observed at the nozzle exit [31]. It was observed that manufacturing tolerances and needle radial motion could be responsible for orifice-to-orifice mass flow rate differences [32]. Measurements of the flow turbulence using particle tracking velocimetry (PTV) demonstrate that turbulence is suppressed in the presence of well-established cavitation according to Koukouvinis et al [6]. Sheet cavity formed at the edge of the orifice entrance were observed to oscillate at a Strouhal number of ~0.35-0.38, based on orifice diameter and average flow velocity. Here an attached cavity shedding period of 78-95 μs was observed for high and low cavitation number operation respectively. [33]

In the work of Mitroglou [46]., PDA results showed that the droplet velocities in the second injection event were higher, even with a 1ms delay. This implies that the flow inside the sac volume of the injector has still not stabilised after 1ms. In conventional multihole injector, spatial velocity profiles were jet-like at all axial locations with the maximum residing along the spray cone axis. Temporal velocity profiles were shown to increase rapidly during the SOI, remain almost constant during the main part of the injection and then decrease during needle closing. The chamber pressure was shown to have a much larger effect on the droplet size than injection pressure. Higher rail pressures slightly reduced the droplet size where-as higher chamber pressures significantly increased the droplet size due to coalescence [39]. In the work of Marchi [44] in piezo injector, according

to the Weber number trend, the secondary breakup takes place up to an axial location of 20mm (27mm in jet direction). This result was in agreement with the mean diameter distribution which shows a reduction from 14μm to 7μm (50%) within 27mm from the injector tip. At axial location beyond 40mm, phenomena such as turbulence and recirculation could promote droplet collision and, therefore, coalescence represented in PDA plots by bimodal distribution corresponding to a group of very fine droplets and a group of agglomerated droplets. Zigan et al [43] showed that he type of fuel used was found to have a big influence on the size of the recirculation zone at the outer edge of the spray with the biggest difference coming from the high volatility fuels, especially late in the injection. It was also shown that axial fuel propagation was relatively unaffected by the fuel type while radial propagation showed high sensitivity to the fuel characteristics.

Moon et al [42] showed that the critical We_0 decreased as the nozzle hole length decreased. It was also shown that the relative velocity (ratio of spray center velocity at certain axial location to initial injection velocity) at the atomization termination location appeared almost identical (0.72) regardless of the injection condition. It was also shown that the effects of fuel property and injection pressure on spray atomisation became saturated from a certain Weber number [42]. Duke et al. [8] showed that after PDA measurement, a time-dependent motion of the plumes appears toward the nozzle centerline. Therefore the spray does not have a true 'steady state'. Battistoni et al. [41] distinguishes the regions of continuous liquid structures and finely atomized droplets within the near-nozzle jet using Xray phase contrast. In central regions of the spray, the projected surface area profile may be related to the degree of atomization of the liquid jet; local minima may indicate regions of poorly atomized spray comprised of larger liquid structures and detached droplets, whereas local maxima may indicate regions of completely atomized spray. This shows the presence of multi-modal jet peaks inside the cross-section of the spray plume. Finally Spencer et al [40] shows that in a stepped-hole nozzle injector, the larger droplet size resulted in a lower level of droplet breakup in comparison to the smaller diameter holes, because of the lower fluid velocity of the large hole.

2.4   Identifying the Gaps in the Literature Review

The first gap identified in the literature, is that how and why complex cavitation structures form and their influence on the internal flow and resultant spray. Complex structures such as multiple cavitation strings in the same nozzle, interconnecting strings and interaction of different types of cavitation have been observed in enlarged models with some clarity. However, while it has been suspected that similar conditions are found within real injectors, there has been no progress in identifying the more complex of these due to the limitations of imaging inside real injectors.

The second gap is the difficulties of simultaneous visualisation of the internal nozzle flow and subsequent spray from either real size or enlarged optical models. Previous attempts have often tried to match internal flow imaging with spray structure by separate imaging of the two systems but this misses the proper correlation required to really make meaningful conclusions. In addition, the enlarged model used for simultaneous imaging were all x15 times or bigger and there is a need to use smaller enlarged models.

The third gap is the influence of the presence of stepped-hole which can affect the in-nozzle flow pattern and ultimately influence the breakup and atomization of the near-nozzle jet spray. In order to find the link between in-nozzle flow and near-nozzle spray, experimental investigation including high speed imaging and PDA needs to be conducted for the full spray to compare the spray characterisitcs with the conventional multi-hole injector. Most importantly, PDA experiments should be conducted in order to quantify the full spray characteristics for the overall spray and also the near-nozzle spray characteristics and obtain a better understanding of the performance of the stepped- injector and the influence of the design of the injector on atomisation of the near-nozzle jet spray compared to conventional multi-hole injectors. Besides this, the near-nozzle atomization should be quantified and compared with the previous results in other injectors.

The fourth gap which was one of the most important ones was the lack of presence of instantaneous 2-D contour plot of velocities and droplet sizes in the literature review. This should be quantified and obtained by means of a MATLAB code since the 2-D countor plots

presented by BSA software in PDA technique in the literature review are average quantities

over the whole duration of the spray. This was also not reported in the previous works.

Chapter 3: Breakup Theory & Experimental Techniques in Gasoline Fuel Sprays

3.1   Introduction

The internal flow and the spray structure of a new stepped multi-hole injector in an enlarged model injector and real size injector have been investigated in this thesis to have a better understanding of the in-nozzle flow structure within the stepped nozzle, especially cavitation formation and its development, the link between the vortical strings cavities and the formation of spray and its stability. Also, to map and characterise temporal and spatial fuel spray in terms of simultaneous droplets velocity and size measurement and to establish the spray-to-spray variation (flapping), the phenomena that have an important role in the behaviour of the overall spray-guided Spark Ignition Direct Injection (SIDI) system. These have been possible by the use of an in house designed transparent enlarged model injector and an optical fuel spray chamber. These helped to overcome the difficulties encountered in the observation (qualitative) of the internal flow and spray using Mie scattering high speed visualization, and also quantitative flow and spray analysis performed using PDA technique. In this chapter, the atomization and breakup theory will be first explained and then the experimental techniques used in this work will be covered.

3.2   Breakup Theory

'As soon as the liquid phase exits the nozzle, the surrounding gas and processes within the liquid phase – or more precisely the interplay between aerodynamic forces, surface tension and viscosity of the liquid – start to disintegrate the surface and break up the liquid core into ligaments, blobs and large droplets. This process is therefore called primary or liquid breakup' [66]. It is characterised by the following dimensionless numbers:

Weber number The Weber number describes the relation between inertial and surface tension forces. It is defined as:

$$We_l = \frac{\rho_l v_l^2 d_l}{\sigma} \quad \text{or} \quad We_g = \frac{\rho_g v_l^2 d_g}{\sigma}$$

With d_l as the diameter of the liquid droplet (or the nozzle), ρ_l and ρ_g as the density of the liquid (or the air), v_l the relative velocity between the droplet (or the liquid jet) and the surrounding air and σ as the surface tension of the liquid.

In a most recent paper in 2017 [67] Bonhoeffer et al categorised spray breakup processes into five different regimes as shown in figure 3-1: Dripping (I), Rayleigh breakup (II), First wind-induced breakup (III), Second wind-induced breakup (IV), and Atomization (V) [68]. The interface between different regimes can be defined by the corresponding Weber numbers.
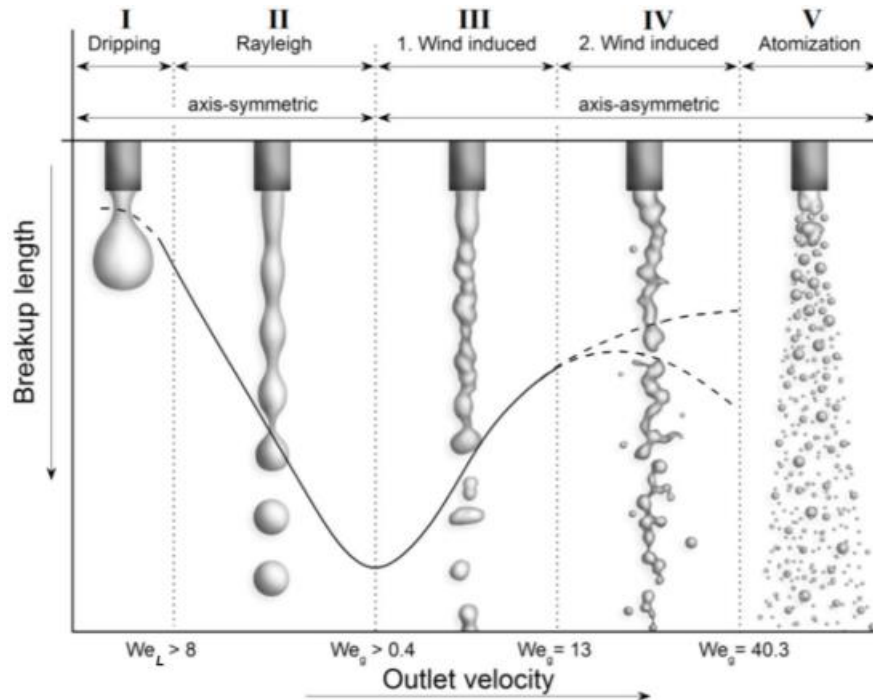
Figure 3-1 Illustration of the breakup regimes of round liquid jets in the quiescent air. Impact of outlet velocity on breakup length of injected liquid from a circular nozzle; I: Dripping; II: Rayleigh breakup; III: First wind-induced breakup; IV: Second wind-induced breakup; V: Atomization. [68]

Due to the contribution of the density of the surrounding gaseous medium, ρ_g in regimes III-V, the Weber number We_g affected by the surrounding gas is used for these regimes.

Different regimes in Fig. 3-1 are described by [68] as follows:

I: In the dripping regime, the outlet velocity is very low; therefore, the liquid accumulates at the nozzle tip until it drips from it.

II: In the Rayleigh regime, with increasing velocity, an axis-symmetrical jet is generated, which breaks up into single droplets of uniform size.

III: In the first wind-induced breakup, a further increase in outlet velocity leads to a decreasing breakup length, mainly caused by air friction.

IV: In the second wind-induced breakup, even higher velocities and increased air resistance lead to surface rupture and separation of single droplets from the jet.

V: At very high velocities, atomization occurs, where the separation into small droplets occurs right at the nozzle exit with the breakup length being close to zero.

It is possible that the droplets break up multiple times, if the momentum force is still sufficiently large compared to the surface tension force. The point when the droplet's momentum runs out and Weber number goes below the critical number is where its smallest diameter is achieved. This critical Weber number allows an estimation of the smallest droplets to encounter under the given parameters. For liquids with low viscosity this is Wecrit =12.5. This means if the Weber number is below 12.5, there is no further atomization and the spray is fully atomized. [66]

Reynolds number Another non-dimentional number associated with spray atomization characteristics is the Reynolds number which is the ratio of inertial forces to the viscous forces as follows:

$$Re = \frac{\rho_l v_l d_l}{\mu}$$

Ohnesorge number The Ohnesorge number (Oh) describes the relation between the damping characteristics of the viscous forces and the surface tension. Oh is depending on the fluid properties and geometric conditions, only [66]

$$Oh = \frac{\eta}{\sqrt{\sigma \rho d}} = \frac{\sqrt{We}}{Re}$$

Beyond a certain point the Rayleigh capillary instability no longer exists and Kelvin– Helmholtz instabilities become more dominant. At higher velocities of the jet, aerodynamic forces starts to affect the atomization and also the turbulence level in the liquid jet starts influencing the atomization. These effects were first characterized by Ohnesorge (1936).

According to Yarin, Tropea [69] "The process of atomization involves the generation of drops from bulk fluid, achieved using a wide variety of atomization concepts, depending on the desired local drop number, size and velocity flux densities, as well as on the bulk fluid and its properties, e.g. pure liquids, dispersions, suspensions, emulsions, etc."

Different mode of breakup regimes according to Yarin, Tropea are shown in figure 3-2 as a function of Reynolds and Ohnesorge number. It is used to estimate whether the atomization is poor or strong. For example, the strong atomization of gasoline and diesel injectors lies in the Oh of range 0.01<Oh<0.1, and Re>10000.

The equations shown in the figure:

$$Re = \frac{\rho_L U D}{\mu_L}$$

$$Oh = \frac{\mu_L}{\sqrt{\sigma_L \rho_L D}}$$
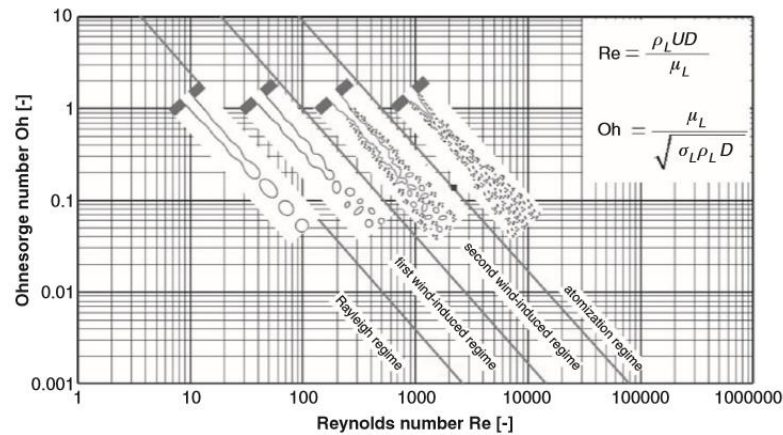
Figure 3-2 shows different modes of breakup according to Ohnoserge and Reynolds number (Yarin, Tropea, 2017) [69]

The Ohnesorge diagram can only reflect the properties of the liquid phase or fuel. However, studies have shown the additional and nonnegligible influence of gas density on the atomization process. Increasing gas density leads to higher inertial force in the gas phase and, hence, accelerated atomization. Figure 3-3 shows the three-dimensional diagram, including the ratio of the gas / fluid density.
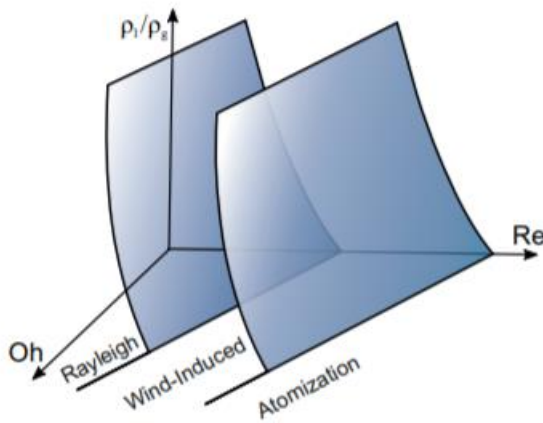
Figure 3-3 shows the three-dimensional diagram of the Ohnesorge/Reynolds atomisation, including the ratio of the gas / fluid density.

The disintegration of a liquid sheet into drops is an important part of primary atomization. The droplet sizes occurring from the sheet disintegration depends on two factors: First is the mode of disintegration and second is the sheet thickness; Three modes of liquid sheet disintegration have been identified: rim, wave instabilities and sheet perforation.

Under equilibrium conditions, the internal pressure at any point on the drop surface, P_I, is just sufficient to balance the external aerodynamic pressure P_A and the surface tension pressure $P\sigma$ so that

$$P_I = P_A + P_\sigma$$

"A drop can remain stable as long as a change in air pressure at any point on its surface can be compensated by a corresponding change in pσ such that pI remains constant. However, if pA is large compared with pσ, then any appreciable change in pA cannot be compensated by a corresponding change in pσ to maintain pI constant." [66]

"When a liquid jet emerges from a nozzle as a continuous body of cylindrical form, the competition set up on the surface of the jet between the cohesive and disruptive forces gives rise to oscillations and perturbations. Under favorable conditions, the oscillations are amplified, and the liquid body disintegrates into drops. This process is sometimes referred to as primary atomisation". [66]

If the size of the droplets that are formed from primary breakup exceed the critical size, they further disintegrate into drops of smaller size. This process is known as secondary atomization. Normally if the Weber number is higher than 13 the secondary atomization is still taking place.

The instability that occurs at the interface between two horizontal parallel streams of different velocities and densities is called Kelvin-Helmholtz instability. This is also when there is velocity shear in a single continuous fluid. The Kelvin-Helmholtz type instabilities trigger the appearance of axisymmetric modulations on the surface of the liquid. This is caused by shear forces induced between the slow moving liquid and the fast moving gas stream. These axisymmetric waves then undergo transverse azimuthal modulations once the gas velocity reaches a critical value.The Rayleigh–Taylor instability, or RT instability, is an instability of an interface between two fluids of different densities which occurs when the lighter fluid is pushing the heavier fluid. At azimuthal wave crests, ligaments are formed and then stretched but the fast moving gas relative to the liquid. Eventually they are stretched beyond a stable length and they are broken into droplets through capillary instability. It is suggested that Rayleigh-Taylor instability is the cause of the azimuthal perturbation [70]. The underlying effects in droplet disintegration and atomization are the Kelvin-Helmholtz (KH) and Rayleigh-Taylor (RT) instabilities, as well as boundary layer stripping due to the gas force acting on the droplet that causes secondary atomisation. The gas-liquid interface experiences unstable wave growth (KH instabilities), while the surface tension counteracts this. Hence, smaller droplets disintegrate from the surface and a slow reduction in the number of droplets occurs. RT instabilities cause the droplets to break into fragments, as illustrated in Figure 3-4. [71]
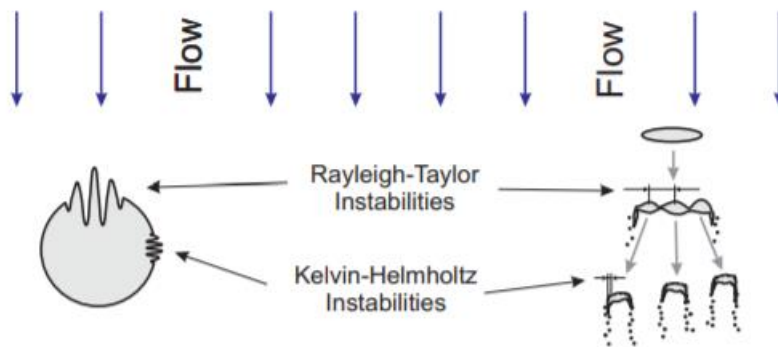
Figure 3-4 Rayleigh Taylor and Kelvin Helmholtz instabilities [71]

Haenlein [72] identified four distinct regimes of breakup in the disintegration of a liquid jet:

1. Drop formation without the effect of air. This is the same mechanism investigated by Rayleigh. It is also called varicose regime.

2. Drop formation with the influence of air. In this mode, when the jet velocity goes up, the aerodynamic forces of the gas come into effect and tend to accentuate the waves formed under regime 1

3. Drop formation because of the waviness of the jet. This regime is linked with the increased influence of aerodynamic forces and lessened influence of surface tension. It is also called sinuous regime

4. Complete disintegration of the jet, that is, atomisation. In this regime, the liquid is broken up at the nozzle in a chaotic and irregular manner.

(a)

Oscillations cause jet breakup. No air friction.

(b)

Oscillations with air friction.

(c)

Wave-like breakup caused by air friction.
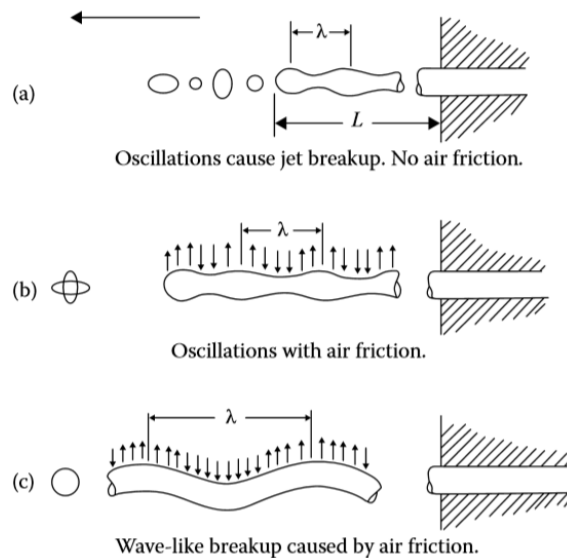
Figure 3-5 Breakup regime according to Haenlein [66]

In the current study, the emphasis is on the 4th regime which is atomisation. From practical point of view, the atomisation regime is not easily described and is still subject to research. [66]

Ohnesorge classified the data according to the relative importance of gravitational, inertial, surface tension, and viscous forces.

"At low Re the jet disintegrates into large drops of fairly uniform size. This is the Rayleigh mechanism of breakup"

"At intermediate Re, the breakup of the jet is by jet oscillations with respect to the jet axis. The magnitude of these oscillations increases with air resistance until complete disintegration of the jet occurs. A wide range of drop sizes is produced"

"At high Re, atomization is complete within a short distance from the discharge orifice."
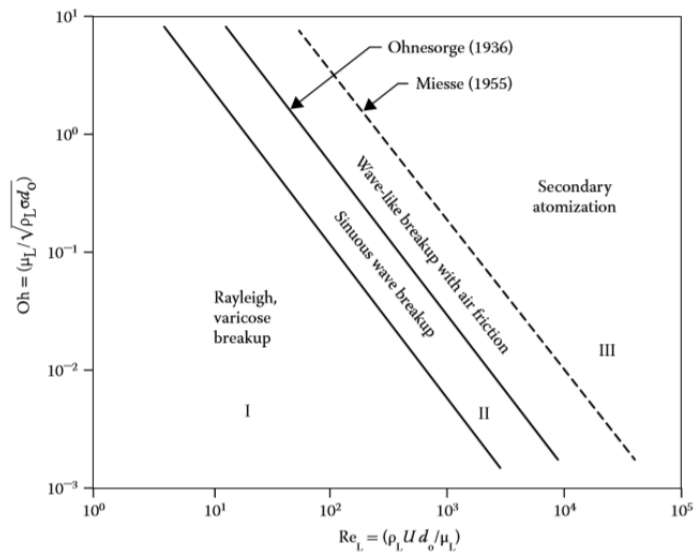
(a)
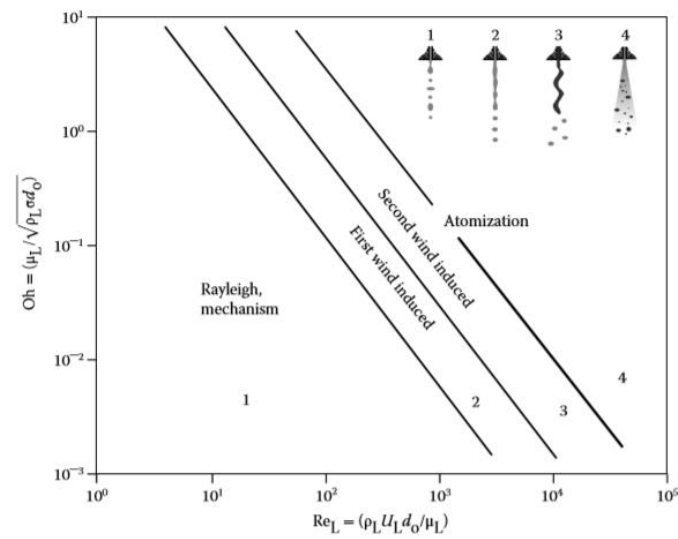
(b)

Figure 3-6 Breakup regime according to (a) Ohnesorge [66] and (b) Reits [30]

In a key study, Reitz attempted to resolve some of the uncertainties surrounding the Ohnesorge chart.

According to Reitz [30], the following four regimes of breakup are encountered as the liquid injection velocity is progressively increased.

1. Rayleigh jet breakup. This is caused by the growth of axisymmetric oscillations of the jet surface, induced by surface tension. Drop diameters exceed the jet diameter.

2. First wind-induced breakup. The surface tension effect is now augmented by the relative velocity between the jet and the ambient gas, which produces a static pressure distribution across the jet, thereby accelerating the breakup process. As in regime 1, breakup occurs many jet diameters downstream of the nozzle. Drop diameters are about the same as the jet diameter.

3. Second wind-induced breakup. Drops are produced by the unstable growth of short wavelength surface waves on the jet surface caused by the relative motion of the jet and the ambient gas. This wave growth is opposed by surface tension. Breakup occurs several diameters downstream of the nozzle exit. Average drop diameters are much less than the jet diameter.

4. Atomization. The jet disrupts completely at the nozzle exit. Average drop diameters are much less than the jet diameter.

Table 3-1 Classification of breakup regime according to Reitz [30]

Regime	Description	Predominant Drop Formation Mechanism	Criteria for Transition to Next Regime
1	Rayleigh breakup	Surface tension force	$We_A > 0.4$ $We_A > 1.2 + 3.4 Oh^{0.9}$
2	First wind-induced breakup	Surface tension force; dynamic pressure of ambient air	–
3	Second wind-induced breakup	Dynamic pressure of ambient air opposed by surface tension force initially	$We_A > 40.3$ $We_A > 13,$
4	Atomization	Unknown	–

Source: Reitz, R.D., Atomization and Other Breakup Regimes of a Liquid Jet, Ph.D. thesis, Princeton University, Princeton, New Jersey, 1978.

According to Miesse [73] and Reitz [30], the regime starts to form at We g > 40 and We g > 13, respectively.

Stability Curve:

Many investigators have characterized jet behavior by determining experimentally the relationship between jet velocity and breakup length. The latter is defined as the length of the continuous portion of the jet, measured from the nozzle to the breakup point where drop formation occurs. [66]
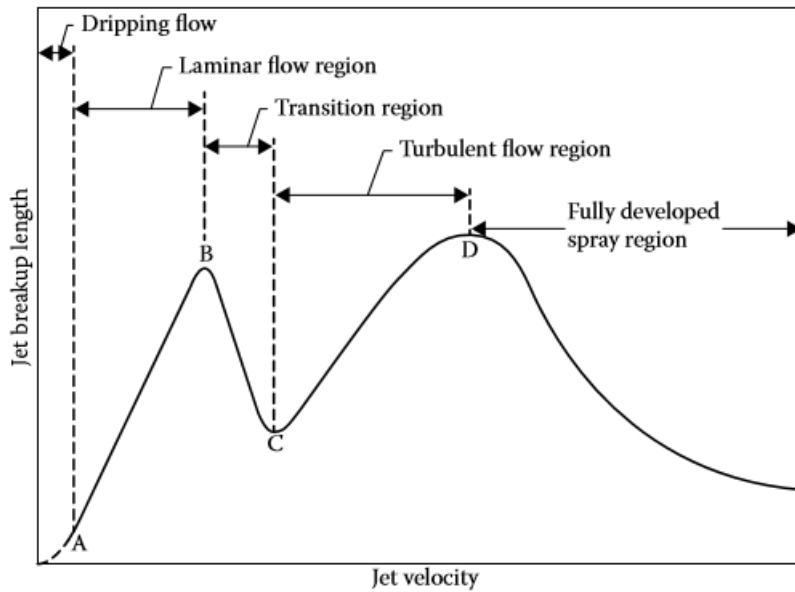
Figure 3-7 Jet stability curve indicating change of breakup length with jet velocity.   [66]

Laminar Flow Region:

The general shape of the length–velocity curve is shown in Figure 3-7. The initial dashed portion of this curve below A corresponds to drip flow. Point A shows the lower critical velocity where the drip flow changes to jet flow. From A to B, the breakup length L increases linearly with velocity. This part of the curve corresponds to disintegration of the jet due to surface forces as studied by Rayleigh and Weber.

Upper Critical Point:

According to Haenlein [72] point B on the stability curve corresponds to the change in the breakup mechanism from varicose to sinuous.

Influence of lo/do Ratio:

Hiroyasu et al studied the breakup of high-velocity water jets under conditions similar to those occured in diesel engines. Figure 3-8 (a) shows the measured values of breakup length obtained for several nozzle lo/do ratios at jet velocities up to 200 m/s when injecting into air at normal atmospheric pressure. This figure shows breakup length increasing with injection velocity up to a maximum at around 60 m/s. After this point, any further increase in jet velocity causes breakup length to decline. The influence of lo/do on breakup length shows no clear trend. In the range of

jet velocities of most practical interest, that is, >50 m/s, it is of interest to note that for lo/do ratios of 10 and 20, breakup length may be increased by either reducing the lo/do ratio to 4 or increasing it to 50. [66]
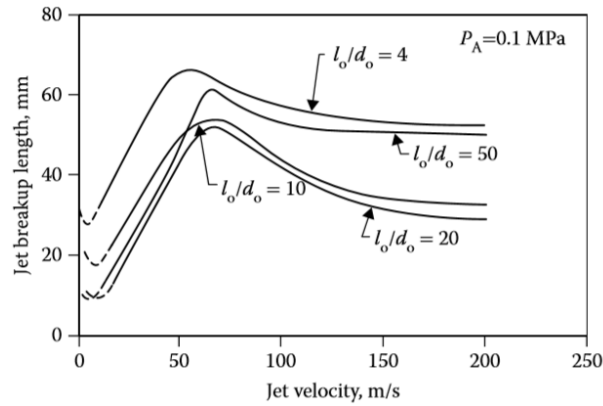
(a)
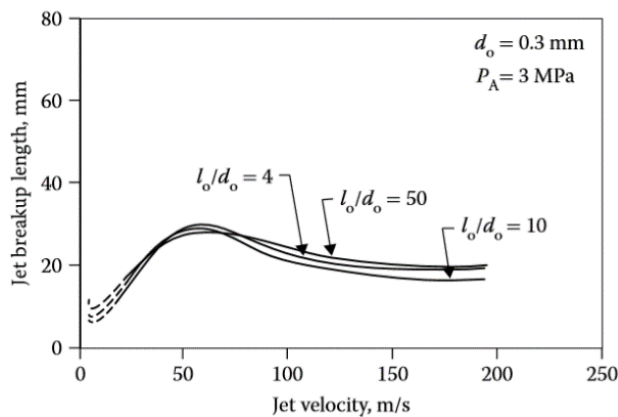
(b)

Figure 3-8 (a) Effect of L₀/D₀ ratio and jet velocity on breakup length for low ambient pressure P = 0.1 MPa. (b) Effect of L₀/D₀ ratio and jet velocity on breakup length for high ambient pressure P = 3 MPa. [66]

Similar data on the effect of L_0/D_0 on L, obtained at an ambient air pressure of 3 MPa (30 atm) are shown in Figure 3-8 (b). At this high pressure, the influence of L_0/D_0 is clearly much less pronounced, presumably because the aerodynamic effects on the jet surface now far outweigh the hydrodynamic instabilities generated within the liquid upstream of the nozzle exit.

Influence of ambient pressure and coflowing air and transverse airflow on the breakup length has also been studied but these factors and their relationship with breakup length is outside the scope

of this work. Another factor that is believed to affect the breakup is cavitation which is discussed in the section 3.3.

The quality of atomization can be characterized by a number of representative droplet diameters. The use of mean diameters instead of the complete droplet distribution simplifies the calculations of mass transfer and flow processes. The notation of mean diameters has been initially developed by Mugele and Evans (1951).

The "geometrical" or arithmetic mean diameter D (or D10), is the mean diameter. Several additional mean diameters providing other useful information are respectively, the "surface area" mean diameter, D20, the "volume mean diameter", D30 and the "Sauter Mean Diameter" (SMD), D32. A list of mean diameters and their related field applications are given in table 3-2. These mean diameters can be expressed differently based on the droplet diameter exponents p and q in the equation below:

$$D_{pq} = \left[\frac{\sum_{i=1}^{\infty} ni \cdot D_i^p}{\sum_{i=1}^{\infty} ni \cdot D_i^p} \right]^{\frac{1}{(p-q)}}$$
                                                                                Equation 1

Di: Diameter of the ith droplet:

ni: Number of the ith droplet

p and q : Values 0, 1, 2, 3, or 4

Table 3-2 Mean diameters and their field of application [68]

Definition	Mean diameter	Field of application
D_{10}	Arithmetic mean diameter	Evaporation rate
D_{20}	Surface area mean diameter	Monitoring surface applications
D_{21}	Area-length mean diameter	Absorption studies
D_{30}	Volume mean diameter	Hydrology and mass flux applications
D_{31}	Mean evaporative diameter	Evaporation and diffusion applications
D_{32}	Volume/surface mean diameter or Sauter mean diameter	Mass transfer and reaction
D_{43}	Mean diameter over volume or De Broukere diameter	Combustion applications

SMD corresponds to values of p = 3 and q = 2 in the above equation due to volumetric and surface dependence. Using the example in figure 3-9, different mean diameters are deduced from the calculations for the histogram of spherical droplet distribution. Due to volumetric and surface area dependence, D32 and D43 are strongly representative of the large droplets even if their number density is less in numbers in comparison with the small droplets.
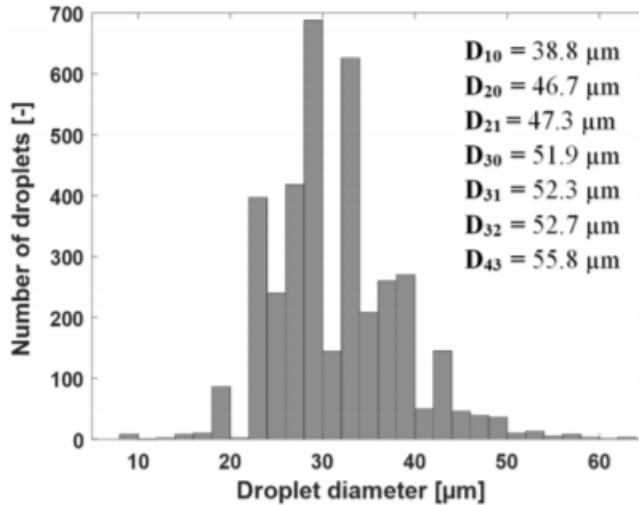
Figure 3-9 Example of different mean diameters calculated using Eq. 1. It is deduced from the histogram of droplet size distribution. [68]

3.3   Experimental techniques for investigation of cavitating flows

Cavitation in micro-nozzles have been extensively investigated utilising high-speed shadowgraphy and other optical techniques. Mauger et al. [74] has discussed a summary of optical visualization techniques, involving Schlieren, shadowgraphy and interferometry in the field of cavitation in a simplified, high pressure 2D channel. Mitroglou et al [34] investigated the in-nozzle flow and near-nozzle spray in a real size diesel injector. In this study, the metallic tip of the injector was replaced with a transparent material made of quartz. The experiment was conducted under realistic operation conditions of the injector i.e. a pressure pulse up to 600 bar, while observing cavitation formation in the sac and nozzles of the injector. The authors focused on the formation of cavitating vortices which are also termed as "string cavitation" in the fuel injection industry. It is known that string cavitation increases spray cone angles [43]. Similarly, Hult et al [75] examined the cavitating flow patterns in a marine diesel injector utilising high-speed shadowgraphy. In this

study, the vortical structures formed at the nozzle was visualized and their influence on the near nozzle jet behavior was investigated.

Although optical methods provides valuable knowledge in understanding cavitation structures, it should be noted that the intensity of the elastic forward scattering from cavitation clouds does not correlate with the actual density of the liquid/vapour mixture [33]. Additionally, cavitation may block the optical path which prevents further observation of the cavitation structures along the optical path. For this reason, quantitative experimental techniques have been developed and employed to study and gain insight in the density distribution of cavitating flows. Such techniques rely on the attenuation of powerful photon or particle beams due to the presence of sample material along their path. [33]. Notable examples are X-ray absorption and X-ray phase contrast imaging methods.

3.4   Experimental techniques for studying sprays

According to Lefebvre [76], there are different experimental techniques available for studying sprays like mechanical, electrical and optical methods. In this classification, Xray methods are considered to be a part of optical methods. However according to Linn [77] for dense sprays such as gasoline fuel sprays a few of these optical techniques are used. In this chapter some of the optical techniques are reviewed and the benefits and drawbacks are discussed.

3.4.1   Lorenz-Mie light scattering

In general, large particles scatter more light than smaller ones. It should be also noted that particle sizes affect the spatial distribution of the scattered light as shown in Figure 3-10.
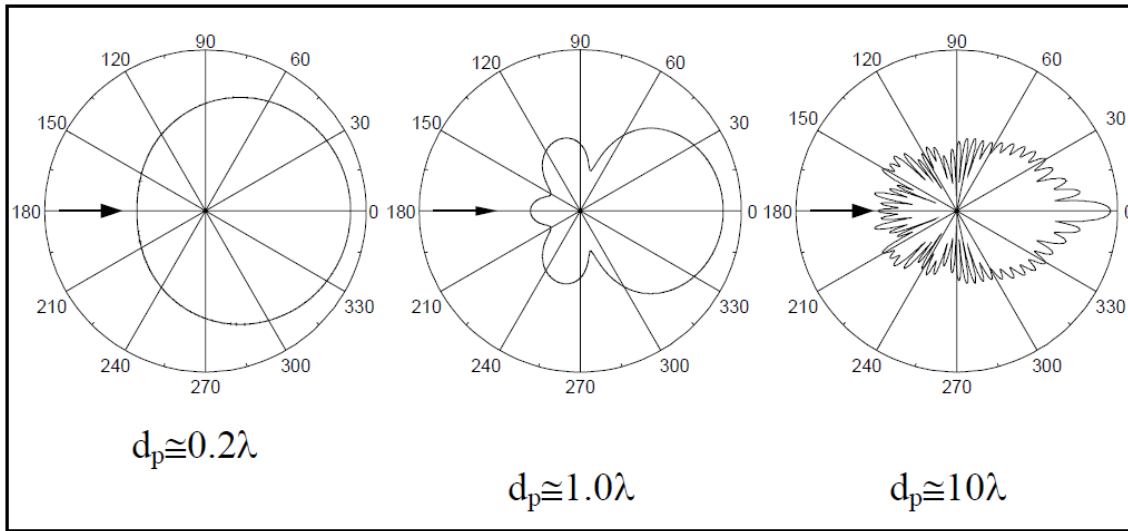
Figure 3-10 Spatial distribution of the scattering light intensity emmited from droplets/particles with different diameter compared to the wavelength of the incident beam. [78]

For large particles the ratio of forward to backward scattered light can be in the order of 102 to 103, while smaller particles scatter more evenly. For large particles direct surface reflection generally dominate the scattered light, and the intensity is thus roughly proportional to the square of the particle diameter For smaller particles diffraction play a major role in the light scattering, and polarisation of the incident light has significant influence. [78]

When a particle is illuminated with an electromagnetic light wave, the electric field of the wave will cause the electrons and protons (electric charges) to oscillate. The acceleration caused by the oscillation of these electric charges results in radiation of electromagnetic energy in all directions. This radiation is called scattered radiation. If a particle is divided into small regions in such a way that each of these regions are characterized by a dipole moment, the incident wave will cause each of these dipoles to oscillate. These oscillations will create scattered wavelets that are emitted by each region of the particle in all directions. Scattering is thus the result of the sum of all these wavelets. [79]

The size of a scattering particle can be represented with the non-dimensional parameter χ defines as:

$$\chi = 2\pi r / \lambda$$ **Equation 2**

where r is the particle radius and λ is the light wavelength. Based on the value of χ, the three main scattering regimes are then characterized as negligible scattering, Rayleigh scattering, Mie scattering and geometric scattering as shown in figure 3-13. [80].

χ <0.002 : Negligible scattering

0.002< χ <0.2 : Rayleigh scattering

0.2 <χ<2000 : Mie scattering

χ >2000: Geometric Scattering

As it could be seen from figure 3-11, the fuel spray droplet sizes are normally within the Mie scattering regime when studies by laser light and white light.
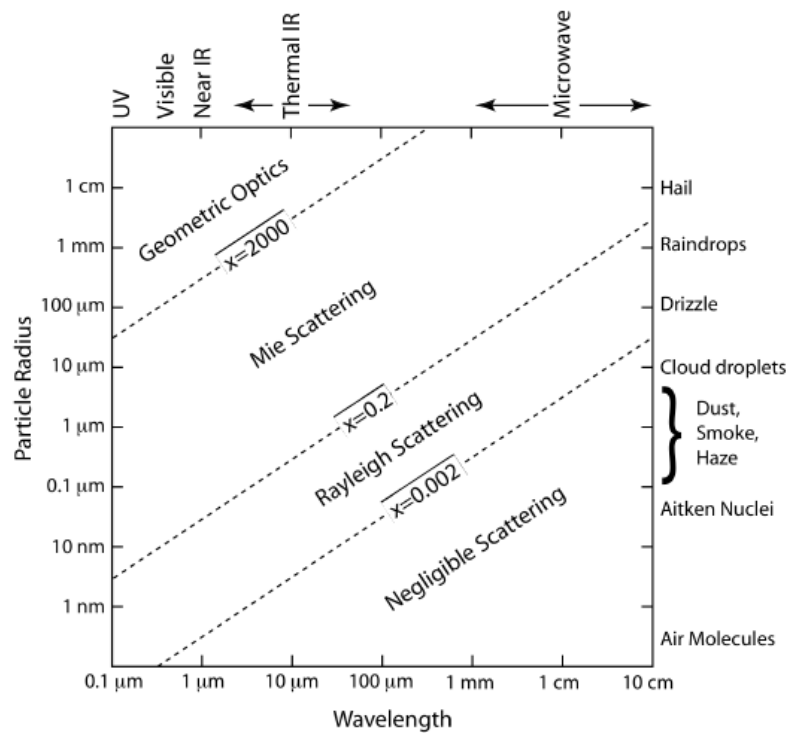
Figure 3-11   Scattering regimes related to the Particle size and Wavelength [80]

Figure 3-12 compares Mie scattering and Rayleigh scattering regimes and the spatial intensity of the light that is emitted from a particle in different directions in each of these regimes. It can be seen that if the particle is smaller the intensity of the forward scattering (refracted light) reduces while the intensity of the backward scattering (reflected light) increases.

Mie scattering:

Rayleigh scattering:
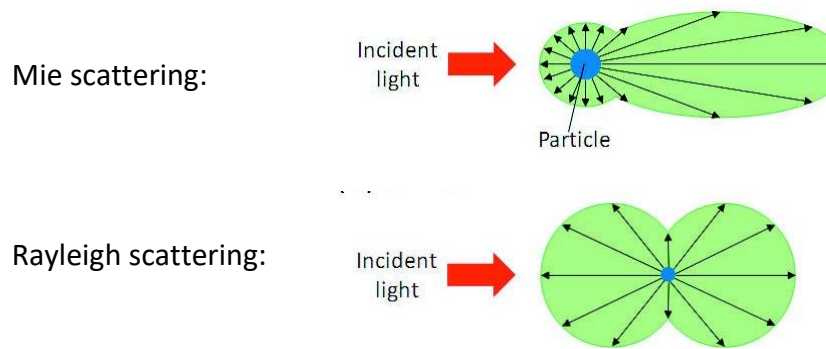
Figure 3-12: Scattering regimes related to the Particle size and Wavelength.

Figure 3-13 shows an incident ray of light with a spherical droplet and the scattering orders which happens consequently after the incident beam interacts with sphere. It is obvious from the figure that there are different modes of scattering. The order of scattering is shown by P. When P=0, the beam is partially reflected and partially transmitted (refracted) into the sphere. The part of the beam that is reflected is known as P=0. When the transmitted light penetrates inside the sphere, it will have another scattering which is referred to P=1. Here part of the beam is reflected inside the sphere and part of it is refracted outside the sphere. The refracted light outside the sphere is called first order refracted P=1. This continues in a similar manner until 2nd order and 3rd order refracted lights are formed consequently as shown in figure 3-13.
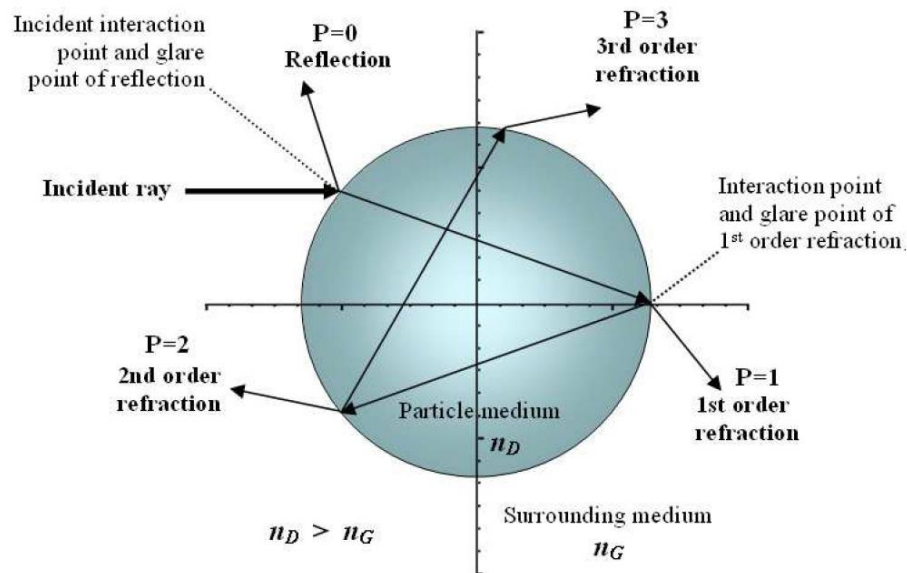
Figure 3-13 Shows an incident ray of light with a spherical droplet and the scattering orders which happens consequently after the incident beam interacts with sphere [78]

93

3.4.2   Laser Doppler Velocimetry (LDV)

Laser doppler velocimetry measures the velocity of small particles or droplets that are moving in the fluid of interest. The velocimeter can provide local velocity measurements of every particle moving through a very small egg-shaped region, usually called control or measuring volume. Since fluid is usually have droplets by itself or seeded with thousands of particles, the laser Doppler technique samples the flow velocity at discrete times corresponding to the passage of particle through the measuring volume.

To perform its task, for a single velocity component, LDV need two laser beams crossing at one point as it is shown on Figure 3-14.

When these two beams intersect with each other, they create an ellipsoidal measuring volume which has got fringe patterns due to interference effect of electromagnetic waves. This 3D fringe pattern is shown in figure 3-15. The separation distance of the fringes is

$$\mathbf{df} = \lambda/2\sin\left(\frac{\theta_b}{2}\right) \hspace{4cm} \textbf{Equation 3}$$

Using the seperation distance one can obtain the velocity of the droplet. This method is called Laser Doppler Velocimetry. This technique was first developed in early 70's by Durst 1971 and Farmer 1972.

Assuming one particle moves through the measuring volume, it scatters light when it reaches a bright fringe, and scatters no light as it passes a dark fringe. This result in a fluctuating pattern of scattered light intensity which produce an oscillating signal, named Doppler burst, similar to the one shown in Figure 3-17. The frequency of this signal v_D (known as Doppler frequency) is proportional to the speed of the particle. If the distance d_f between two neighbouring fringes is known, the speed u of the transient particle can be state using the following equation:

$$\mathbf{u} = V_D \cdot \mathbf{df} \hspace{4cm} \textbf{Equation 4}$$

When a droplet passes over the interference fringes, it scatters light proportional to its intensity according to figure 3-16. This light signal is collected by a lens and focused onto a photo-detector which converts the light intensity fluctuations into voltage fluctuations as shown in figure 3-17. When a droplets moves from one bright point to the next, the voltage signal creates a peak to peak curve. The rate of intensity variation ie the number of peaks per seconds is called the Doppler frequency. The time for a droplet to travel the distance between two fringes has an

inverse relationship with the doppler frequency. If the frequency is higher, that means the time that it takes for one droplet to move from one peak to the next peak is shorter which means its velocity is higher.
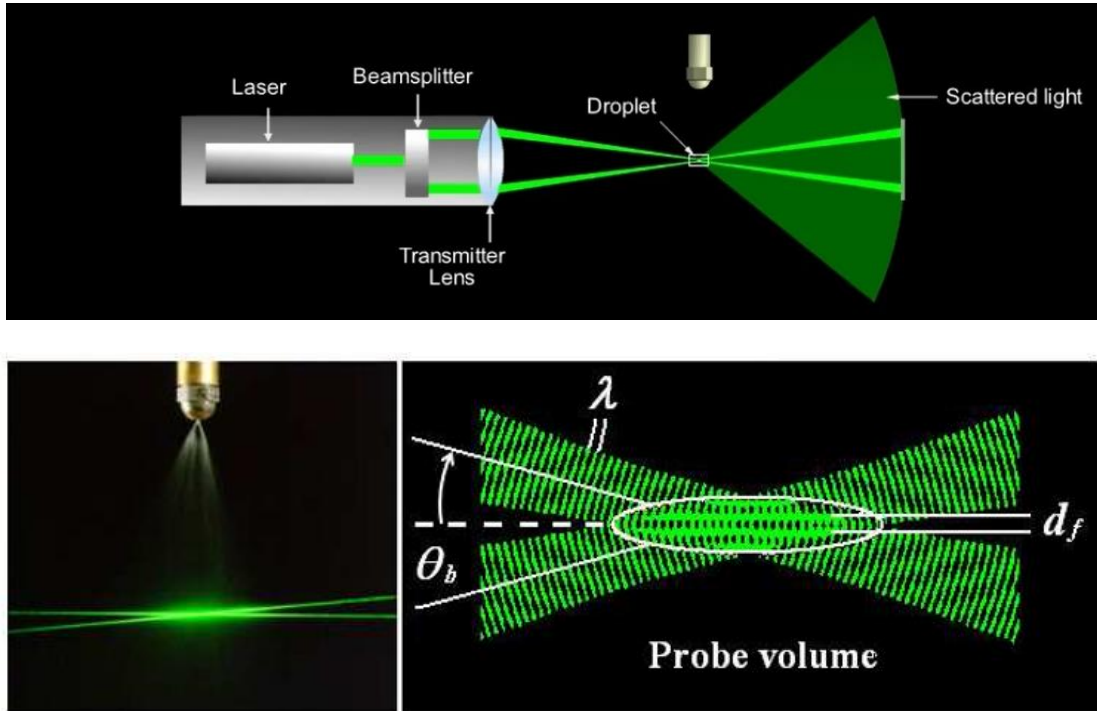
Figure 3-14 Configuration of the LDV transmitter: Two gaussian laser beams with wavelength of λ intersecting with each other and creating an ellipsoidal probing volume with horizontal planes referred to as fringe pattern (shown in brighter color) [81]

| (a) | (b) |
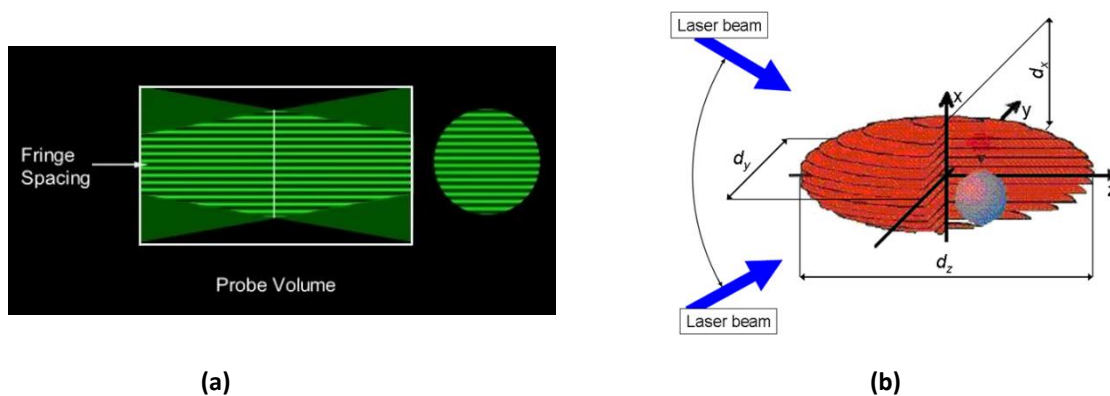
Figure 3-15 Top: shows side view and section view of an ellipsoidal fringe patterns, Middle: 3D view of the ellipsoidal fringe pattern and the corresponding lengths dx, dy and dz. Bottom: A spherical droplet passing through the probing volume and the refracted light pattern created by the droplet **[54] [81]**

When a spheric droplet passes the probing volume it will reflect light according to figure 3-16 (a) and (b). Here a droplet with a diameter of 30 microns is shown as an example. If the intensity of the light over the surface of the droplet is projected onto xy plane in a polar coordinate, the resulting figure could be shown in figure 3-16 (c).

(a)   (b)

(c)
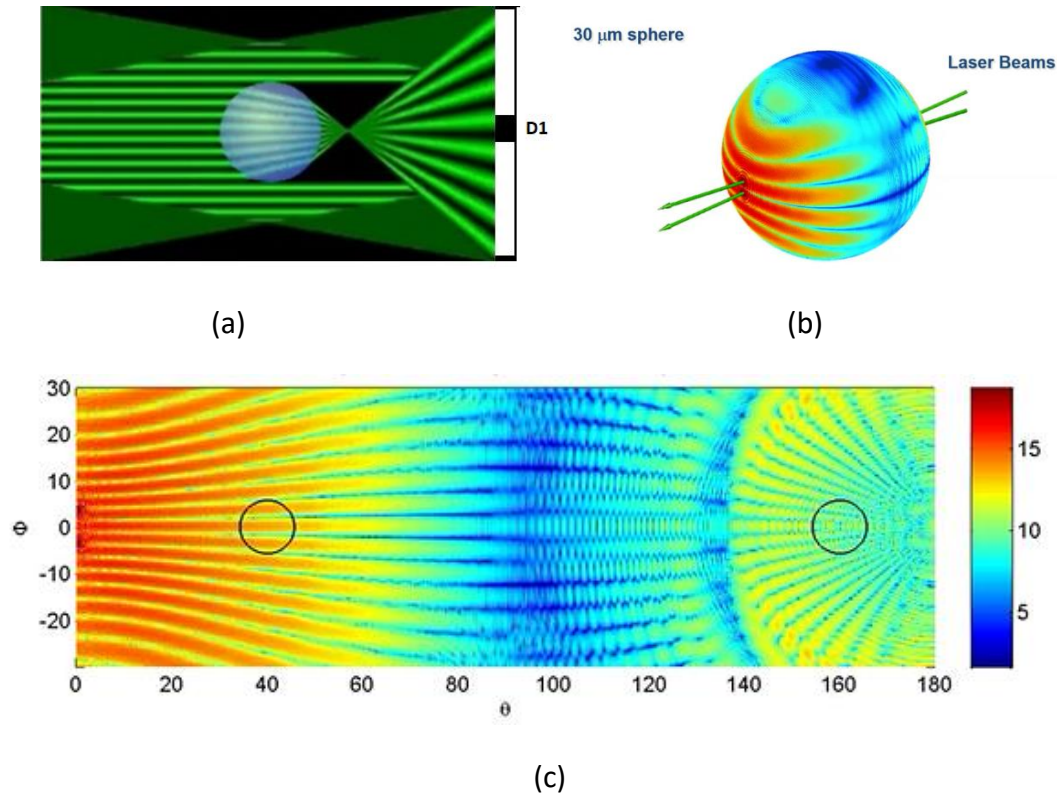
Figure 3-16 (a): A spherical droplet passing through the probing volume and the reflected light pattern from its surface on the receiver detector (LDA1 signal). (b): A 3D droplet with 30 μm diameter and the 3D light intensity contour plots shown on the surface of the droplet. (c) : The 2D contour plot of light intensity on the droplet surface with 100μm diameter while moving through the probing volume [81]

3.4.2.1 SIGNAL PROCESSOR UNIT

To obtain the needed information and accuracy for LDV experiments, consideration must be given to the electronic equipment necessary to transform the raw signals from the detector into velocity information. In the interest of this thesis, the method analysed is a BSA flow software signal processing that includes as well frequency spectra analysis. The features of this technique are summarised in Figure 3-17 and 3-18. The basic working principle can be explained in three steps:

First, the processing unit is supplied with the continuous random amplitude signal illustrated in Figure 3-17 that occur when there are many particles moving through the scattering volume. Signals of this type are characterized by amplitude and phase fluctuations. The processor has to separate every particle burst from the others and check the SNR; only burst enough with acceptable signal to noise ratio are validated and sent to the next step.

Second, using a set of high pass filters adjustable by external PC, the processing unit filters out the accidental noise from the true signal.

Finally, assuming particle velocity constant during its permanence in the control volume, the processor uses the low pass filter and calculates the doppler frequency v_D applying spectral analysis of the burst signal as shown in figure 3-17.
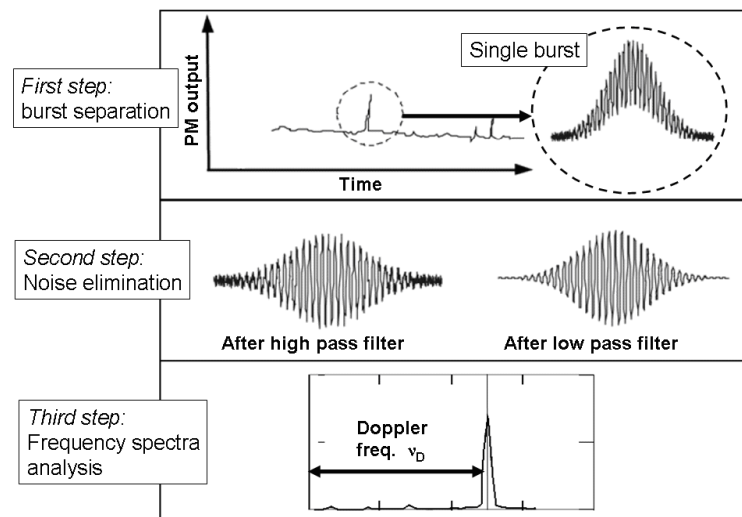
Figure 3-17 BSA software signal processing steps [82]

Since the velocity is carried by the frequency v_D of the signal, directional information cannot be determined by a stationary fringe system. In fact, if a particle is now assumed to traverse the fringes with the same velocity but in opposite direction, it will also induce a signal with the same frequency v_D (blue curve Figure 3-18). The solution is to shift the frequency of one or both the laser beams, this result in fringes that are essentially moving inside the control volume.
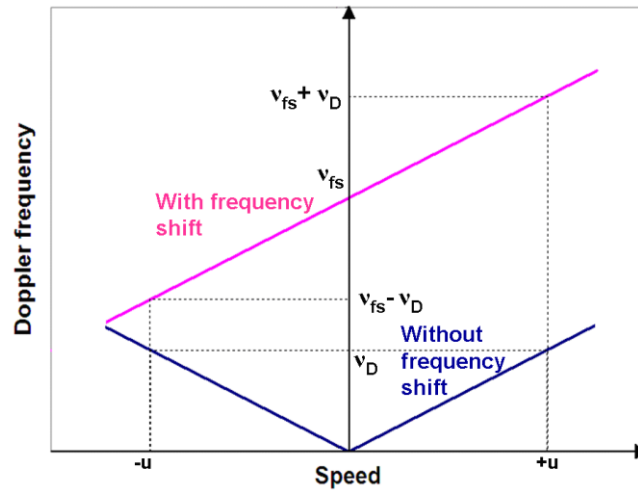
Figure 3-18 Schematic representation of frequency shift [82]

Now consider the situation in which the laser is operated with a frequency shift v_{sf}. A particle travelling with speed **+u** that, in stationary fringe system, produces a Doppler frequency v_D will now experience a total shift of the sum of v_{sf} and v_D. Vice versa, if the flow is moving in the opposite direction, a particle travelling at the speed **-u**, that with no frequency shift, generates the same frequency v_D, will now produce a signal of total shift of the difference between v_{sf} and v_D. This is shown by the violet curve of Figure 3-18. It is worth noting that laser wave length λ has no effects on the movement of the travelling fringes.

Signal processing unit not only provide the speed of the particle but also compare the signal with other detectors and provides other data such as, droplet diameter, the particle transient time, count numbers, etc. The method by which the droplet diameter would be calculated is explained in PDA technique in the next section.

3.4.3 **Phase Doppler Anemometry (PDA)**

Using a second photo-detector, the LDV system can be modified in order to measure not only the droplet velocity but also the droplet diameter. This method is called Phase-Doppler Anemometry (PDA). When two detectors are placed at slightly different scattering angles and record the Doppler signal, the phase of the two signals will slightly be different than each other. This changes of phase $\Delta\Phi$ is shown in figure 3-19. It could be shown that this phase change is linearly proportional to the diameter, D, of spherically homogeneous (constant index of refraction)

particles when the signal detected is dominated by only one scattering mode. Illustration of the

PDA principle is shown in figure 3-19. [78]
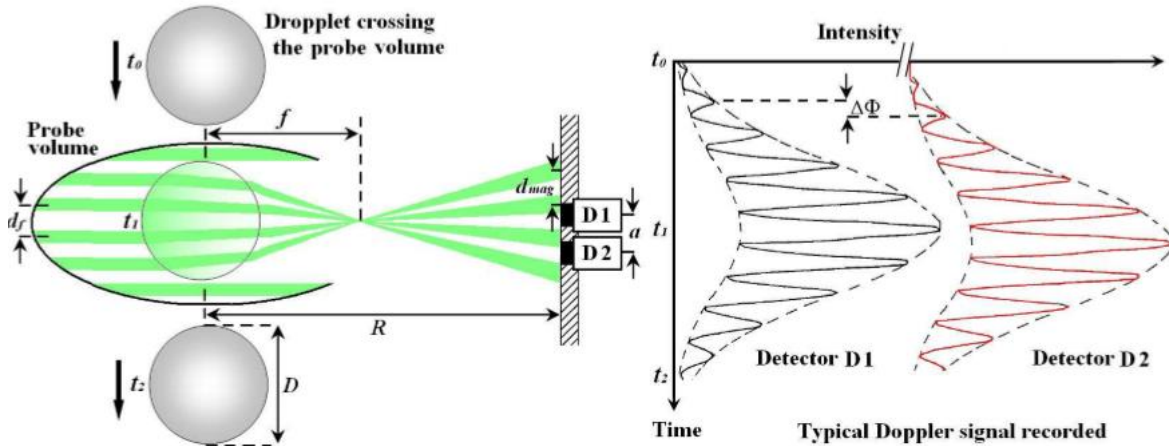
Figure 3-19 Left - Illustration of the PDA principle where a droplet is crossing the probing volume and the refracted light which is turned into an electric signal in the detectors – Right : Two consecutive signals recorder with phase shift of ΔΦ [78]

In figure 3-20, the phase shift $\Delta\Phi$ is shown to be directly related to the droplet diameter D. A

consideration could be made that the droplet is a thick lens with diameter of D and focal length

f. Therefore a small droplet with small D will act as a small lens with small f and a large droplet

with larger values of D will act as a large lens with longer focal length as shown in figure 3-20.
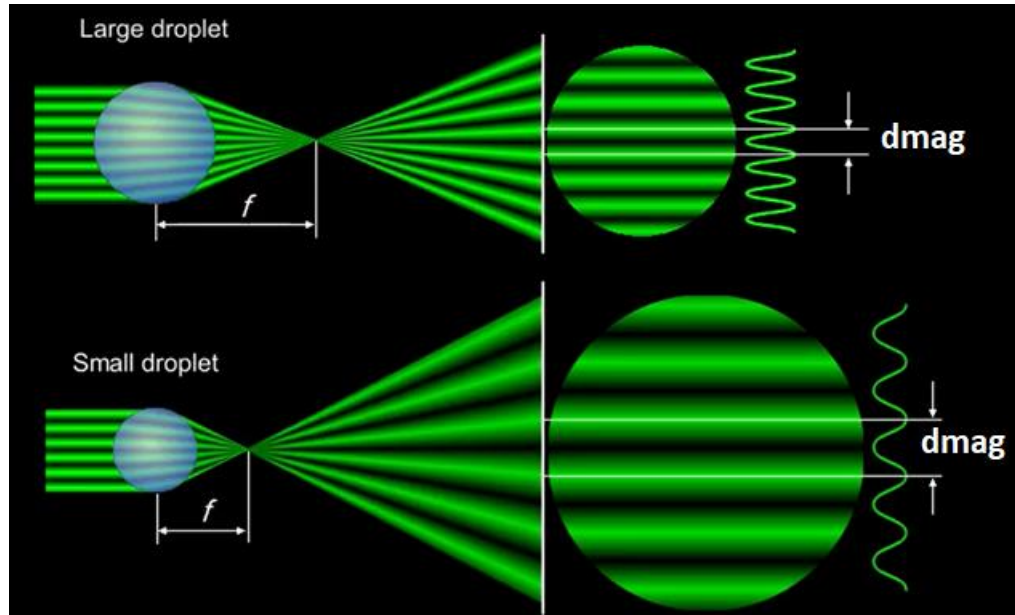
Figure 3-20 shows that a small droplet with small D will act as a small lens with small f and a large droplet with larger values of D will act as a large lens with longer focal length [81]

Therefore as shown in the figure 3-20 and 3-21, dmag which is the magnified distance between the two refracted light beams could be mathematically shown as:

$$\mathbf{dmag} \ = \ (\mathbf{R} - \mathbf{f}).\,\mathbf{df}/\mathbf{f}$$ **Equation 5**

And since R>>f then it could be written as

$$\mathbf{dmag} \ = \ \mathbf{R}.\,\mathbf{df}/\mathbf{f} \sim \mathbf{R}.\,\mathbf{df}/\mathbf{D}$$ **Equation 6**

which means the distance between the two reflected beams is inversly proportional to the diameter of the droplet.

Figure 3-21 shows the configuration of 2 detector PDA system. Here θ_b is the angle between the two beams and Ψ is the angle of detector 1 (and 2) with respect to YZ plane and θ_s is the angle of receiver axis with respect to Z axis.
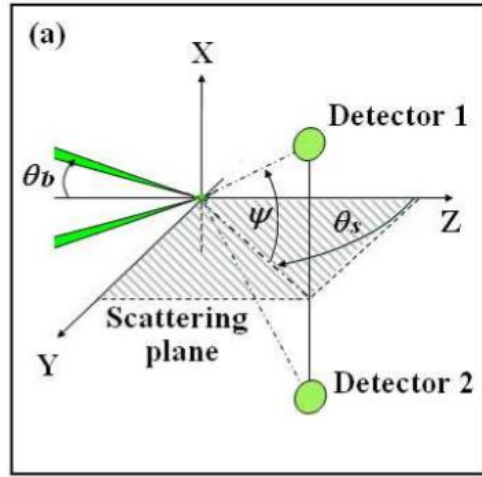
Figure 3-21 configuration of the simple 2 detector Phase Doppler Anemometry system. [78]

It should be noted that when the medium is transparet the first order refraction is normally used which is the case in our experiment. Here is the formula:

$$\Delta\emptyset = \frac{-2\pi D}{\lambda} \frac{n_r sin\theta_b \sin\psi}{\sqrt{2(1 + cos\theta_s \cos\psi \cos\theta_b)(1 + n_r^2 - n_r\sqrt{2(1 + cos\theta_s \, cos\psi \, cos\theta_b)})}}$$

Equation 7

where n_r is the real part of the droplet refractive index. Since fuel sprays are transparent, first order refraction is used and the best possible answer will be obtained when the receiver is positioned at the Brewster's angle with respect to Z axis (which is the transmitter axis) ie

$$\theta s = tan^{-1}2(1/n_r)$$

Equation 8

This angle is generally between 30° and 80°. For water droplet of refractive index n = 1.33 in air and for parallel polarized light this angle equals 70° (Saffman 1986, Wigley 1994). In this experiment the angle of 70° has been used for PDA measurement.

3.4.3.1 PDA technique errors

PDA technique has been corrected from several sources of errors. The first one, known as "Gaussian beam defect", is related to the detection of unwanted scattering modes, and explained as follows:

As shown in figure 3-22, the reflected light from the top droplet and refracted light from the bottom droplet may have roughly equal intensities . This problem occurs also for laser beams with approximately uniform intensity profile or for top hat intensity profiles but the problem is much more difficult to control for Gaussian beams (Bachalo 2000). This is shown in figure 3-22 where depending on the position of the droplet, reflected (P=0) and first order refracted (P=1) light can have similar intensities.
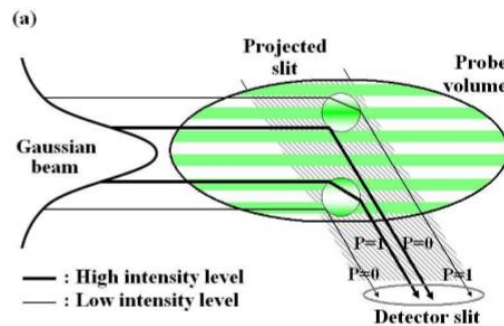
Figure 3-22 Gaussian beam defect: depending on the position of the droplet, reflected (P=0) and first order refracted (P=1) light can have similar intensities. [78]

The second source of error, also related to the detection of unwanted scattering modes, is "the slit effect". It occurs when the droplets traverse an edge of the detection volume. This is shown in figure 3-23. Here the non-detection of the beams is the source of error since some information is missing.
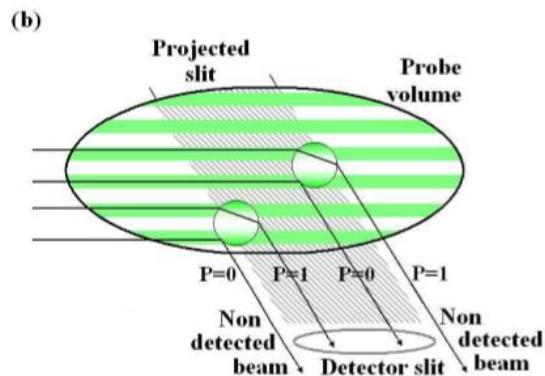
Figure 3-23 Slit effect: for particle trajectories at one edge of the slit projection, unwanted scattering mode dominates. [78]

The third source of errors is the detection of phase shifts greater than 360°. This occurs when measuring sprays with high variations in droplets size ie gasoline fuel sprays. To avoid this problems, a third detector is used in practice as shown in figure 3-24 providing a second determination of the phase shift and serves to place the measurement in its appropriate cycle [78].
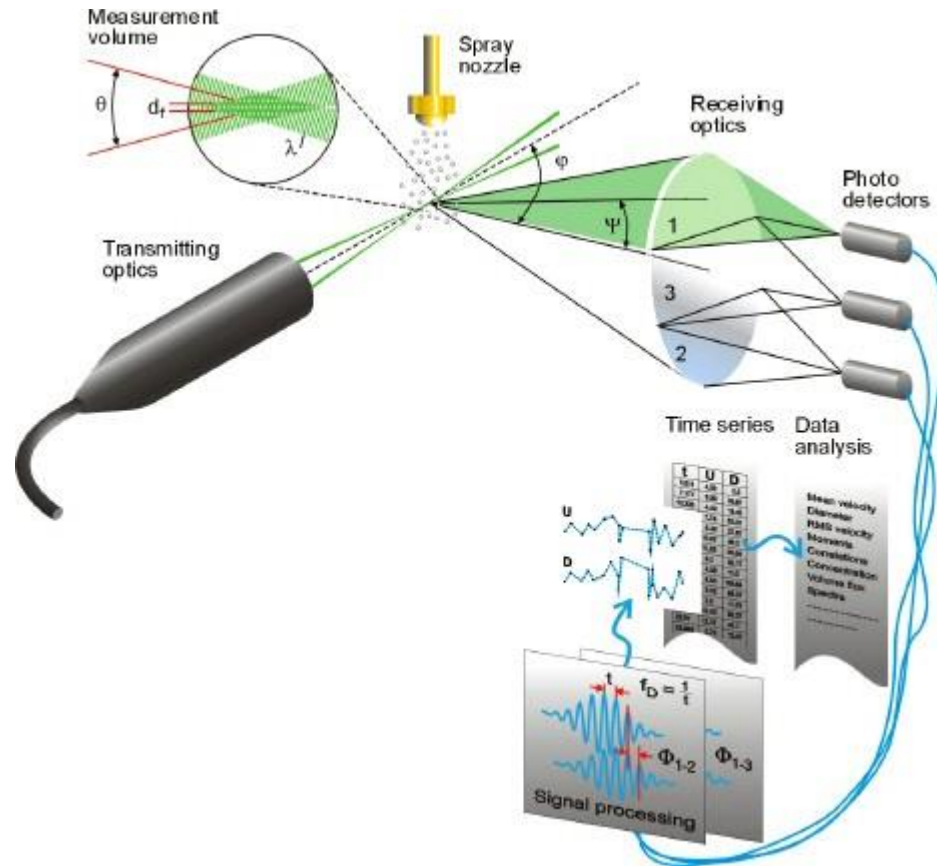
Figure 3-24, 3 detector PDA system which is also referred to as PDPA [83]

The maximum particle size that can be unambiguously measured with two detectors corresponds to the inverted blue graph of Diameter as a function of Φ_{1-2} from which D_{max} is obtained when $\Phi_{1-2}=360$ as depicted in figure 3-25. Reducing the distance between the detectors can extend the particle size range. This however, will also reduce the measurement resolution. Using three detectors provides a large measurable size range which corresponds to the red graph of Diamater as a function of Φ_{1-3} from which D_{max} is obtained when $\Phi_{1-3}=360$. This combination will provide both a high measurement range (Φ_{1-3} graph shown in red) and a high measurement resolution (Φ_{1-2} graph shown in blue colour).
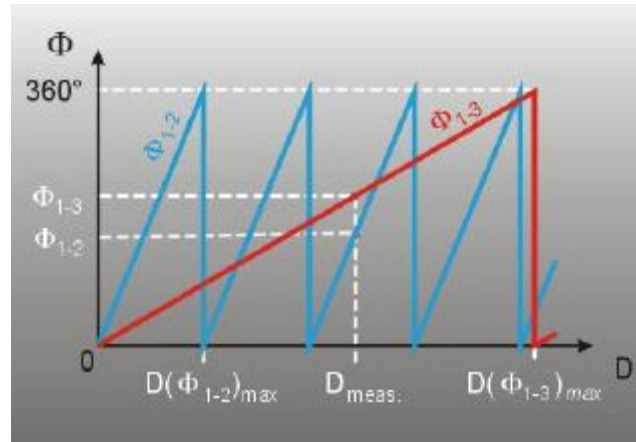
Figure 3-25 Resolving the Φ ambiguity issue in a two detector system (Φ 1-2) is achieved by using a third dectector and calculating Φ 1-3 which can enable the system to measure droplets with higher diameter values [83]

Another limitation in PDA measurements is known as "droplet shape effects". When probing non-spherical particles, errors related to the non-sphericity are introduced in the measurement. These errors can result in overestimation of droplet diameters up to 45%. [78] In modern PDA instruments, the sphericity validation is performed by comparing the phase differences measured from two pairs of detectors and rejecting the detected sample whose deviation exceeds a certain amount as shown in figure 3-26.
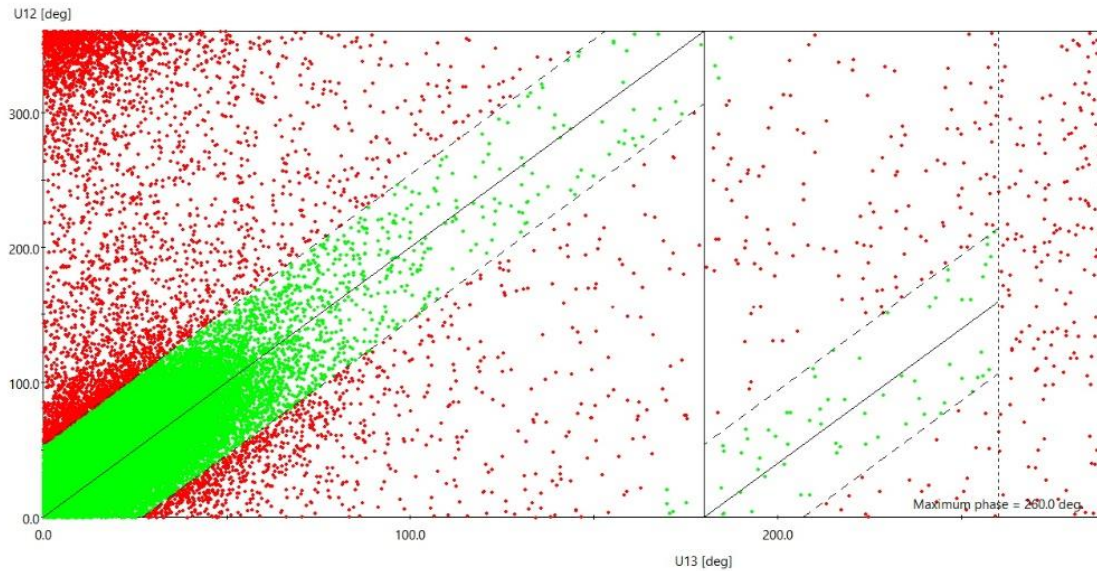
Figure 3-26 The sphericity validation in 3 detector system is performed by comparing the phase differences measured from two pairs of detectors Φ 1-2 and Φ 1-3 and rejecting the detected sample whose deviation exceeds a certain amount. [84]

The fifth source of error is referred to "multiple occupancy" and appears when several droplets occupy the probe volume. The last source of error introduced in PDA measurements is caused by multiple scattering and attenuation processes.

3.5   Planar and Dual PDA for measurement of fine particles

For the measurements of fine particles (D<=10µm), another optical arrangement called the "Planar configuration" has been developed by Naqwi (1991) which has higher precision compared to standard configuration. The planar PDA positions the two laser beams, their electric vector and the two detectors all on the same plane (XY plane in figure 3-27).
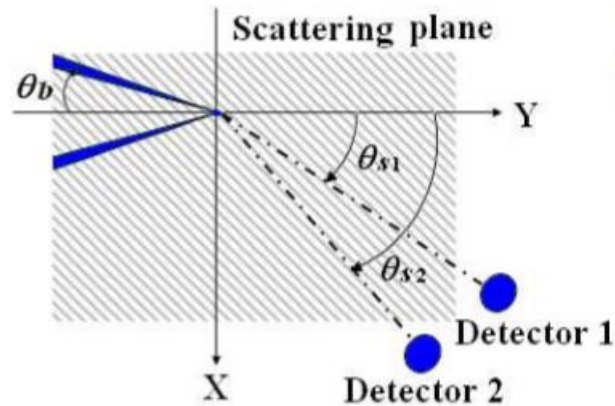
Figure 3-27 Planar configuration of the 2 detector PDA system [78]

The most advanced PDA system has been developed by Tropea et al. (1995) as shown in figure 3-28. It is called Dual-PDA which has been used in the current study. It combines the standard PDA (figure 3-21) with the planar configurations (figure 3-27). In order to differentiate in the same setup each configuration, two laser wavelengths λ = 514.5 nm (green) and λ = 488 nm (blue) are generated from an argon-ion laser and the emitted signal detected by two pairs of photo-detectors (one pair for each wavelength). By means of this arrangement, the system is able to reduce the Gaussian beam defect and the slit effect allowing considerable improvements in the measurement accuracy of mass flux and droplet concentration. [79]
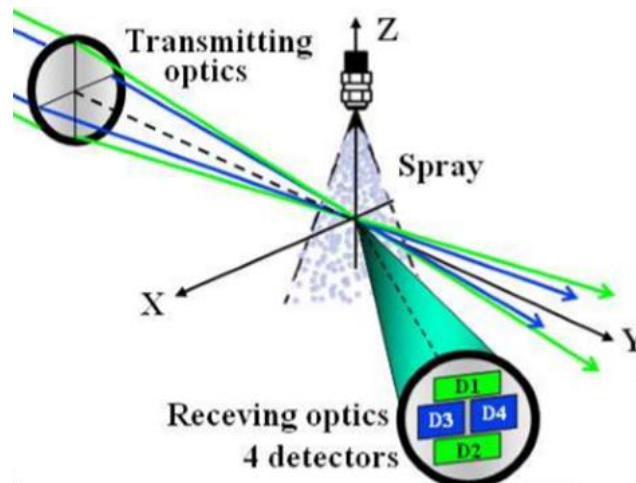
Figure 3-28 Dual PDA configuration with 4 detectors, two for vertical velocity measurement (D1 and D2) and 2 for horizontal measurement (D3 and D4) [79]

A comparison with other PDA instruments given by Dullenkopf et al. (1998) demonstrates the high performances and accuracy of the technique. The Dual-PDA is actually the most reliable instrument for spray characterization and offers simultaneous measurements of droplet size, velocity, flux, number density and time-of-arrival statistics. However, in phase-Doppler measurements, only local information is extracted, and the complete characterizations of sprays is time consuming.

Chapter 4: Methodology

4.1   Introduction

In this chapter, the methodology and the experimental techniques that were utilised during the current research will be explored and further discussed.

4.2   High-Speed Visualisation (Mie Scattering) of 15-times Transparent Enlarged Model of injector Test Rig (Low-pressure)

The first set of experiments involved high speed imaging of 15 times enlarged model of a conventional Bosch mutli-hole injector. The experimental rig which has been used in this experiment has been developed in the group at City University as shown in figure 4-1. [85]

A multistage centrifugal pump was used to provide upstream pressure for water as the working fluid in the transparent 15-times enlarged model of SIDI multi-hole injector. The flow-rate was measured by an ultrasonic flow-meter. The injection pressures were varied from 1bar to 5bar and the spray which was formed out of each nozzle was injected into the atmosphere and was collected by 6 hoses. Water was collected in a tank and was pumped again into the enlarged model which was fixed on the test rig. The enlarged injector assembly has a needle lift mechanism accompanied by a micrometer to set the exact needle height. The needle will be fixed at a given position and it will remain in that position during the measurements. The flow inside the nozzles is continuous, i.e. steady state flow condition; This means that transient nature of the flow and the influence of the needle opening and closing processes are absent.
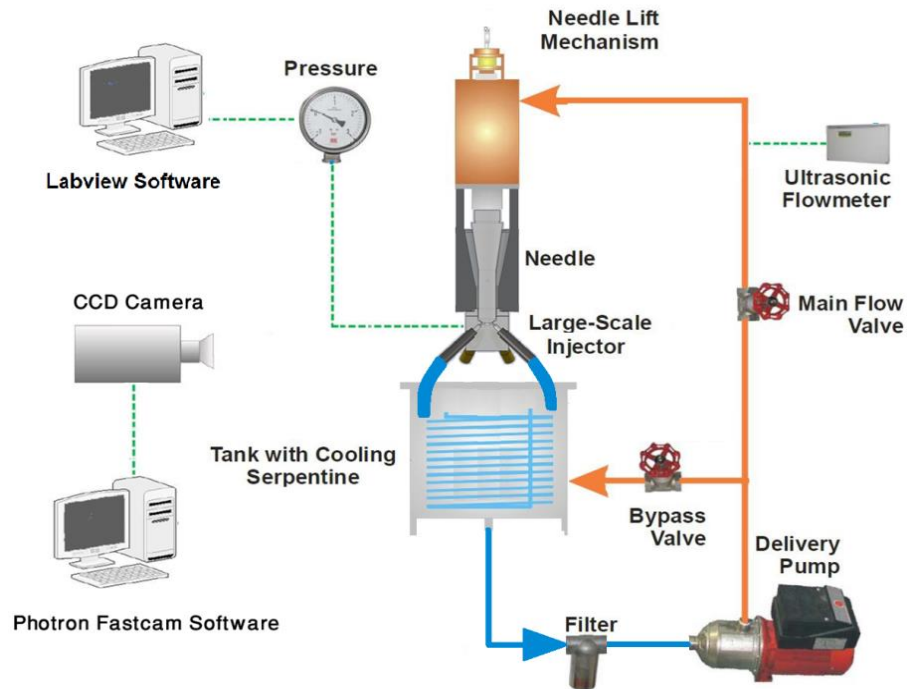
Figure 4-1 The schematic diagram of the closed loop steady-state flow rig of the transparent large-scale injector showing the flow circuit and the CCD camera

4.2.1 15-times enlarged model of the injector

The use of an enlarged 3-D transparent model of the nozzle injector is essential to examine the flow through scaled up injectors with geometry similar to those of real-size production or prototype injectors. Figure 4-2 show the real size and the enlarged model of a six-hole mini sac type nozzle for gasoline direct injection. Figure 4-2 shows the six holes in the prototype real-size injector that are symmetrically positioned in the nozzle tip at an angle of 45° to the injector axis forming an overall spray cone angle of 90°. Figure 4-2 also shows a section view and an isometric view of Perspex nozzle. All the dimensions of the prototype real-size multi-hole nozzle were enlarged by a factor of 15 with nozzle hole diameter and full lift height being 2.1mm and 1.05mm, respectively. Although a novel method has been developed at the group [86] for matching refractive index of the working fluid and the Perspex (refractive index 1.49), due to the hazardeous nature of the working fluid, water was used as a working fluid with refractive index of 1.33. Although some light distortion at the liquid-solid interfaces was expected, but this would not affect the conclusion of the present investigation since the objective of this work was to

visualise and image the cavitation processes and the near-nozzle cone angle under different operating conditions and under continuous light source.
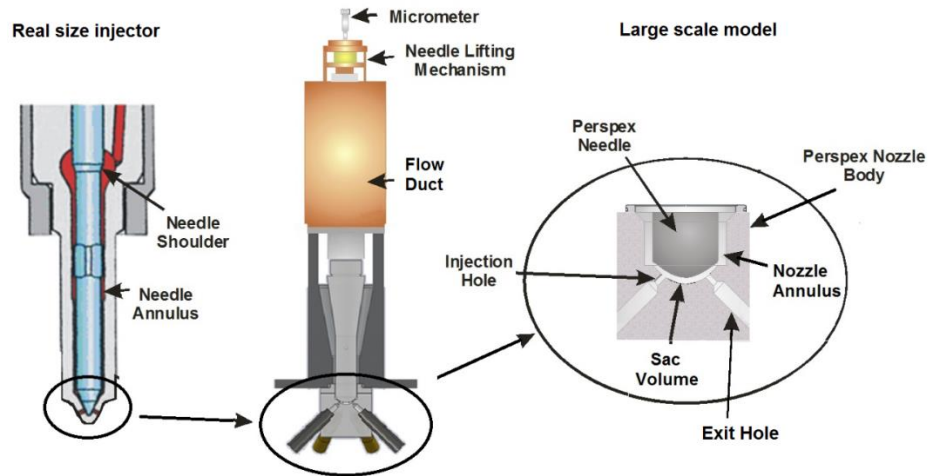
Figure 4-2 Real-size and large-scale injector.

The enlarged transparent nozzle has a diameter (D) of 2.1mm and length (L) of 5.7mm (corresponding to the diameter of $140\mu m$ for the real-size nozzle. The needle lifts were set to a quarter (0.26mm), half (0.52mm), three-quarters (0.78mm), and full lift (1.04mm) respectively.
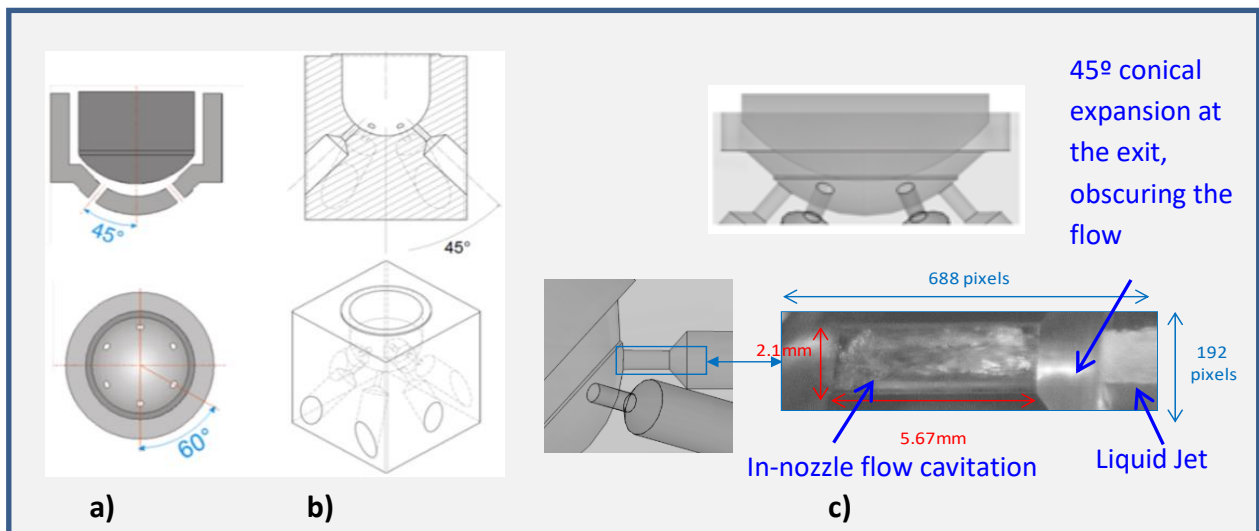
Figure 4-3 Three-dimensional models of the real size injector prototype and the large-scale 6-hole nozzle: (a) geometry of the symmetric injection nozzles (b) Schematic of imaging nozzle area and the actual image of in-nozzle flow.

At the exit holes, the flow is expanded initially before entering into another pipe with diameter six times bigger than that of the nozzle holes which direct the exit flow into the tubes leading to the tank; the exit hole configuration can also be seen in figures 4-3.

Figure 4-4 shows the configuration of the needle seat area and the minimum distance between the needle and the sac volume when the needle valve is closed. The radius of the needle was designed to be 18mm which corresponds to 15-times enlarged model of that in a real-size injector.
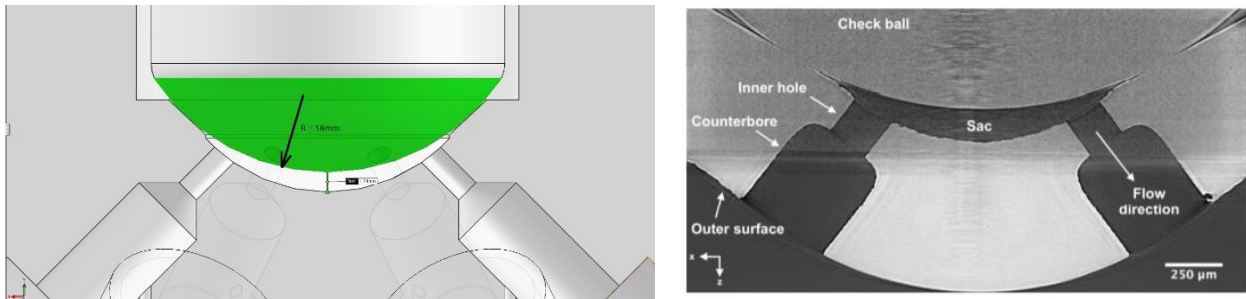
Figure 4-4 Needle seat and sac geometry: (a) Cross-section of the 15-times enlarged model of the conventional injector (b) X-ray tomography of the sac volume of a SIDI Spray G stepped-nozzle injector [21]

4.2.2 Measurement of 15-times enlarged model

Measurements with this model have been carried out at different injection pressures and needle lifts which are listed in tables below.

Table 4-1 Experiment Conditions

L/D=2.7		Needle Lift			
		¼ lift	½ lift	¾ lift	Full lift
Injection Pressure (bar) And CN Number	CN=1.04	Re=13700	Re=23300	Re=25200	Re=26100
	CN=2.09	Re=22300	Re=32900	Re=34800	Re=35700

CN=3.12	Re=27100	Re=39600	Re=406000	Re=40600
CN= 4.15	Re=31000	Re=48200	Re=50200	Re=50200
CN=5.22	Re=31700	Re=49700	Re=50700	Re=50700

The needle lift was set using a micrometre with uncertainty of ±0.005mm. To achieve the full lift condition, the needle was raised 1.05mm above the fully closed position. This means the uncertainty in the full lift position used for this experiment was ±0.48% which is acceptable for this study. The flow rate was measured by the ultrasonic flow meter with a resolution of ±0.002 l/s giving a maximum error of 1% at the lowest flow rate. The pressure upstream of the nozzle was measured using a pressure transducer with an accuracy better than 1 %. The cavitation number, C_N, and the Reynolds number, Re, are calculated in the Labview program based on the following definitions:

$$C_N = \frac{P_{inj} - P_{back}}{P_{back} - P_{Vapour}}$$
(1)

$$Re = \frac{D \cdot U_{inj}}{\nu} = \frac{D}{\nu}\left(\frac{Q_t}{n A_h}\right) = \frac{4Q_t}{\pi \nu n D}$$
(2)

where P_{inj}, P_{back} and P_{vapour} are the injection pressure upstream of the nozzle, back pressure downstream of the nozzle and vapour pressure, respectively. Since the spray is injected into the atmosphere, P_{back} is the atmospheric pressure. D is the nozzle hole diameter, U_{inj} is the nozzle hole mean velocity, n is the number of holes (6), Q_t is the total flow rate through the injector, A_h is the cross section area of an individual nozzle hole and n is the liquid kinematic viscosity. Although the experiment runs at steady state conditions, but due to highly turbulent flow structure through the nozzles and, in particular, the cavitation phenomena at injection holes, the

flow is expected to behave transiently and to have short time scales. This behaviour is virtually impossible to capture with conventional imaging (CCD camera) techniques. Since it is important to gain knowledge about the dynamics of cavitation inception and formation processes, high-speed digital video technique was the primary method used for this study. Many of the previous experiment to visualise the cavitations inside the nozzle holes were done using the shadowgraphy technique. In this study, the cavitations were visualised by means of Mie-scattering technique using a high speed camera and the lighting set up. The images were captured with Photron Fastcam SA1-1 camera with a frame rate of 50,000 fps for a resolution of 198x688 pixels and a shutter speed of $1/177000s^{-1}$. Two continuous ARRI M8 light sources was used which provided 16,200 lux per area of Ø 1.3m circle at 5m distance to provide sufficient light for the non-intensified CCD imaging chip [87]. The directions of the light sources were obtained through trial and error with chosen angles of about 15 and 60 degrees, for left and right lights, respectively
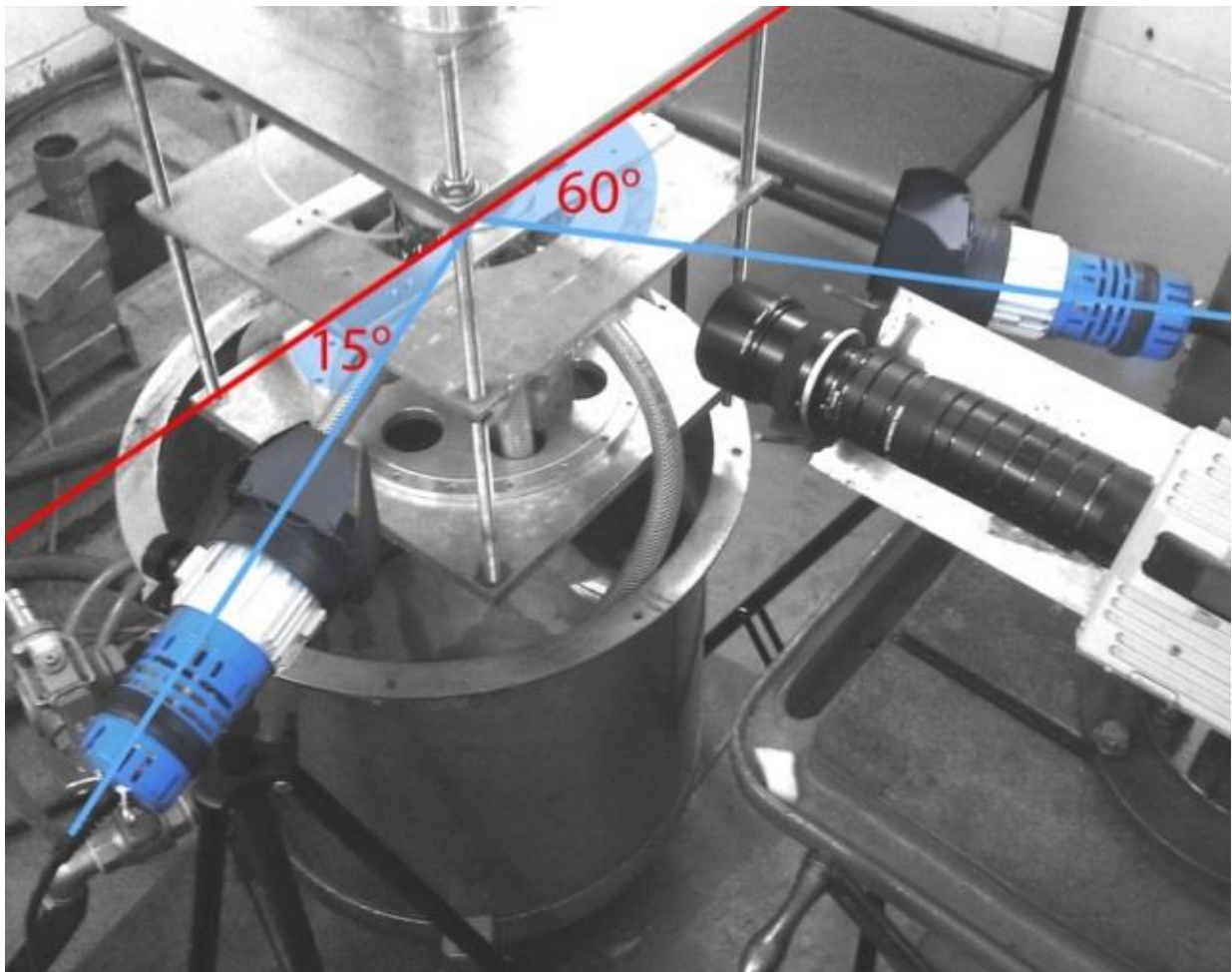
Figure 4-5 Photograph of the lighting set up

In such position reflection from surfaces of injector nozzle is minimised and reflection from the cavitating region and bubbles is maximised. To gain desired magnification, extension tubes were placed before the main NIKKOR 135mm lens. A black coating was placed on the rear face of injector model to have a uniform and consistent black colour in the background of images and to minimize background light noise which helped to obtain images with much better definition. Therefore, the bubbles appear brighter than background and can be tracked and analysed easier. Moreover, this will allow measuring the spray cone angle due to clear boundary between the liquid jet and the surrounding air. An in-house Matlab image-processing software was modified which was previously used for real-size spray angle measurement using polyfit function of the threshold boundary curve. In this mode, the small effect of ligaments at the spray edge is not being taken into consideration because the resolution of the real-size spray is not high enough for this purpose. After modification, the Matlab code was able to measure the angle of the near-nozzle spray for enlarged model which included the effect of spray ligament creation and separation from the nozzle exit (The code is presented at the appendix).

Further analysis was done on spray cone angle using Matlab programme. The definitions used for spray cone angles are shown in Figure 4-6 which shows an individual jet spray with the overall cone angle, top and bottom half angle, nozzle axis and jet spray axis; the latter may move above or below the nozzle axis depending on in-nozzle geometrical and vortex cavitation. The nozzle axis has been used as the reference 0 degree angle for the presentation of the results. The cone spray angles were measured at different CN numbers for different needle lifts. There were 40 different cases and limited samples of the results are presented here. Different angles of each individual spray were measured including upper angle, lower angle, spray axis angle and the cone angle for all the cases. The spray edges were calulated using the polyfit function in Matlab. At first, a point with maximum brightness (ie 200) will be chosen with a default threshold value (i.e 40%). Using this threshold, the boundary of the spray where the points have the value of 80 (200* 40%) will be detected and highlighted in green colour. The x and y values of these points are then calculated by the code. Then a polyfit will be obtained for the x and y values and the angle of the spray edge will be ultimately calculated. The original code is given in the appendix. Figure 4-6 shows the region where the near-nozzle angles were measured in Matlab by detecting the upper

and lower edges of the spray. A linear fit will then be applied to the jet boundary and the angle is mearued based on the horizontal
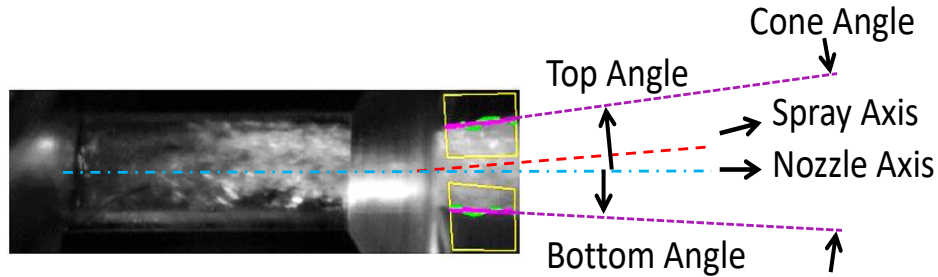
Figure 4-6. Top angle, bottom angle, spray axis angle, and the overall cone angle as measured by Matlab Software; nozzle axis angle is used = 0)

4.3 High-Speed Visualisation (Mie Scattering) of 7-times Transparent Enlarged Model of injector Test Rig (Low-pressure)

In another set of experiments, a 7-times transparent enlarged model was manufactured and assembled on the enlarged model test rig and the internal flow characteristics of the flow was visualised using high speed video imaging. The advantage of this model compared to the 15-times model was the possibility of visualising the in-nozzle flow and the near-nozzle spray simultaneously.

The experimental set up for this configuration is shown in figure 4-7. Due to the fact that the size of the nozzle was half of that of the previous investigation, A long telescopic extension tube was used on the CCD camera to maximise the magnification ratio of the screening area that can yield acceptable results. A multistage centrifugal pump provides the upstream pressure in the transparent enlarged model. Working fluid is water at 25°C. The injection pressure was varied from 0.5 bar to 3bar and the sprays from each nozzle hole were injected into the atmosphere and were collected back into the supply tank. A 100mm diameter focusing lens with the focal length of 300mm was used to increase the light intensity around the nozzle area to more than 2 million Lux. Three set of 45° hot mirrors were used to filter out infrared wavelength in order to protect the Perspex nozzle from high temperatures. To ensure capturing high quality images, 2 set of cooling fans were used to decrease the temperature further around the nozzle and also to remove the water mists of the spray away from the near nozzle towards the suction collector to avoid

fouling the imaging window. The injector assembly has a needle lift mechanism adjusted by a micrometre to set the exact needle height. The flow inside the nozzles is continuous, i.e. steady state flow condition, which means that transient nature of needle during its opening and closing processes is absent. The enlarged transparent model is geometry similar to the real-size injector and operates at similar Reynolds numbers.
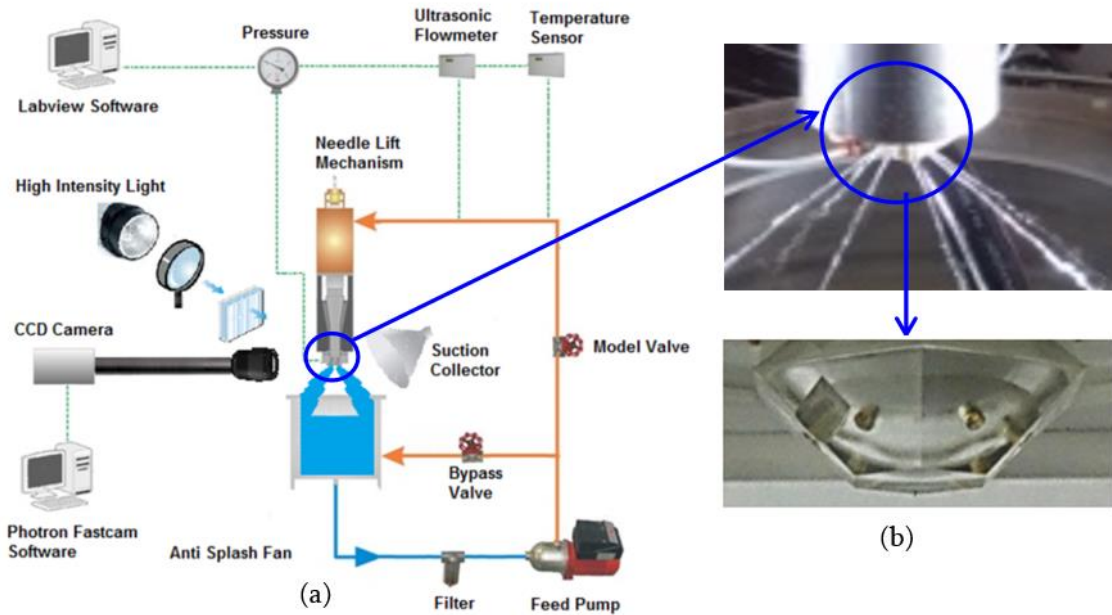
Figure 4-7 Experimental setup of the 7-times enlarged model of injector with the schematic diagram of flow circuit (left); (b) Close-up of transparent nozzle injector assembly.
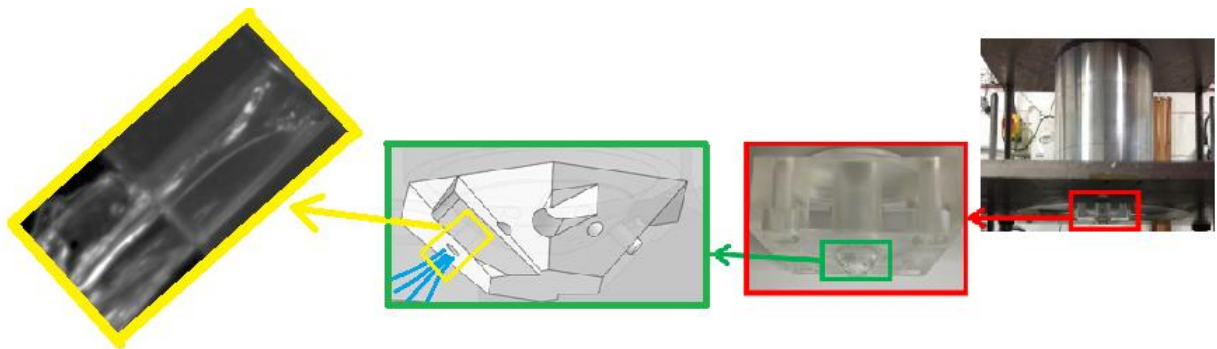
Figure 4-8 Close-up of the in-nozzle flow and the very near-nozzle jet spray (as it emerges into the stepped-nozzle)

Figure 4-8 shows step-by-step magnification of the in-nozzle flow and the very near-nozzle jet spray as it emerges into the stepped-nozzle.
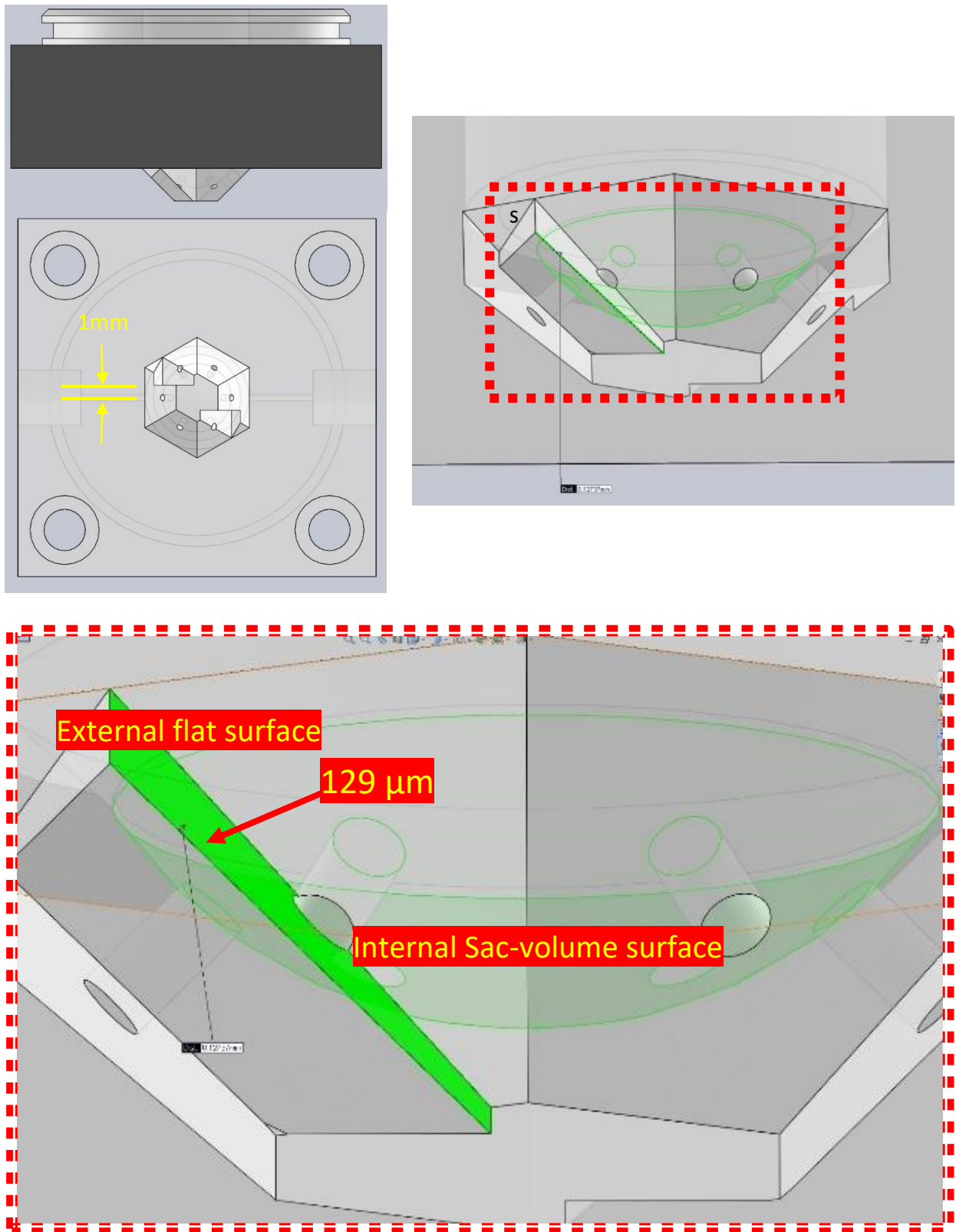
Figure 4-9 Different orthographic and 3D zoom views of a novel design of the transparent model

Figure 4-9 shows different orthographic and 3D zoom views of a novel design of the transparent model which allowed simultaneous in-nozzle flow and near-nozzle spray visualization using CAD, the machining of the nozzle were done in a manner that the minimum distance between the inner edge of the viewing window and the curved surface of the sac volume is around 100 μm.

(a)   (b)
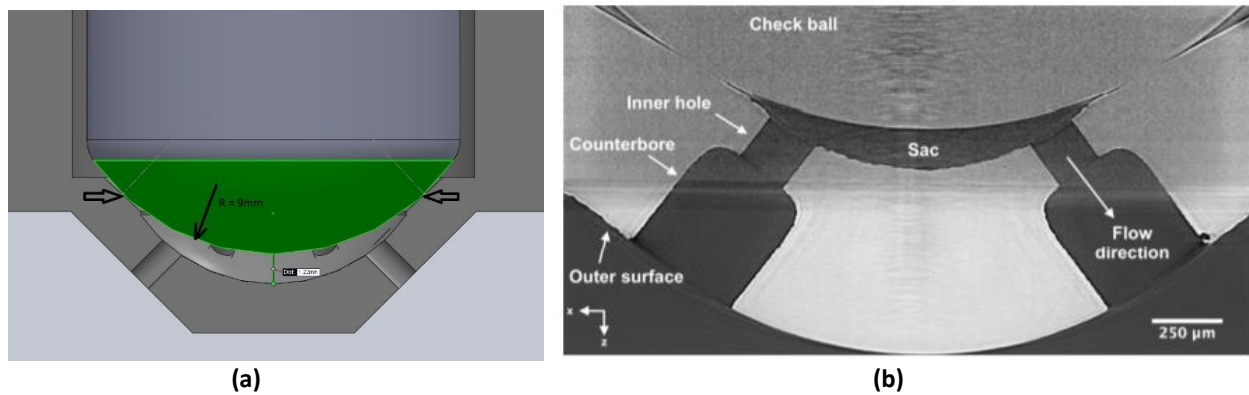
Figure 4-10 Needle seat and sac geomety: (a) Cross-section of the 7-times enlarged model of the conventional injector (b) X-ray tomography of the sac volume of a SIDI Spray G stepped-nozzle injector [21]

Figure 4-10 shows the needle seat and sac geometry. On the left side, the cross-section of the 7-times enlarged model of the conventional injector (b) X-ray tomography of the sac volume of a SIDI Spray G injector [21]

4.4 Spray visualization in real-size high pressure injector

In this part of the experiment, a closed loop system of continuous recirculating fuel flow was used, which consisted of all the necessary components needed to meet the optimum conditions for a successful injection. The experiments were performed in a laboratory that was specifically designed for investigations on engines and fuel injection system. The whole experimental setup can be divided into two system. On one hand, the fuel injection system with its different parts for providing repeatable injections and on the other the high-speed imaging system for capturing and saving the images at the same time. The fuel which was used was iso-octane HPLC grade (99.9% purity). Table 4-2 shows the physical properties of the fuel which was used and compare it with other fuel properties.

Table 4-2 shows the physical properties of the fuel which was used (Iso-octane) and compare it with other fuel properties.

	n-Hexane	n-Heptane	iso-Octane	n-Decane	Three-component	Gasoline
0.1 MPa at 25°C						
Density (kg/m^3)	656	664	694	717	705	720 - 740*
Normal boiling point (°C)	66	99	100	174	66 to 174	35 - 200*
Surface tension (mN/m)	17.89	19.65	18.33	23.37	–	22
Kinematic viscosity x10^{-6} (m^2/s)	0.446	0.583	2.874	1.21	0.568	0.53
Vapour pressure (kPa)	19.9	6.06	6.58	1.71	–	50 - 60*
Refraction index	1.375	1.388	1.391	1.409	1.385	1.427
Heat of evaporation (kJ/kg)	360.3	357.6	303	350.3	–	420
1.5 MPa at 70°C						
Density (kg/m3)	618	630	659	690	638	695
Vapour temperature (°C)	190	226	233	321	–	–
Surface tension (mN/m)	13.27	15.24	14.33	19.23	15.35	17.6
Kinematic viscosity x10^{-6} (m^2/s)	0.337	0.405	2.427	0.73	–	–
Vapour pressure (kPa)	104	40.4	40.8	2.38	–	210
Refraction index	1.352	1.365	1.37	1.395	1.37	1.41
Heat of evaporation (kJ/kg)	328.3	330.2	280.3	329.9	–	–

* Non-aromatic compounds

A stepped-nozzle (injector 3) has been investigated in this thesis and was compared with two other previous models - a non-step injector model (injector 1) – and a stepped-nozzle (injector 2) which has been investigated in the group before.

Table 4-3 A comparison of the two previous injectors in previous works [88] and [89]

	Injector 1	Injector 2	Injector 3
Injector	Bosch	Magneti Marelli	Bosch
Type	6-Hole Multi-Hole	6-Hole Multi-Hole	7-Hole Multi-Hole
Arrangement	Symmetric Nozzle Configuration	Asymmetric Nozzle Configuration	Asymmetric Nozzle Configuration
Nozzle	Parallel Cylindrical (Staright)	Parallel Cylindrical with Stepped Exit	Parallel Cylindrical with Stepped Exit
Hole Diameter	140 μm	180 μm	190 μm

A Photron FASTCAM SA1.1 was used to take the spray images. This high-speed camera provides megapixel resolution to 5400 fps and reduced resolution to 675000 fps. The camera needed to be set up with detailed accuracy to capture the injection sprays with the best quality. The figure 4-11 shows the schematic of the configuration of the real-size injection test rig. [90]
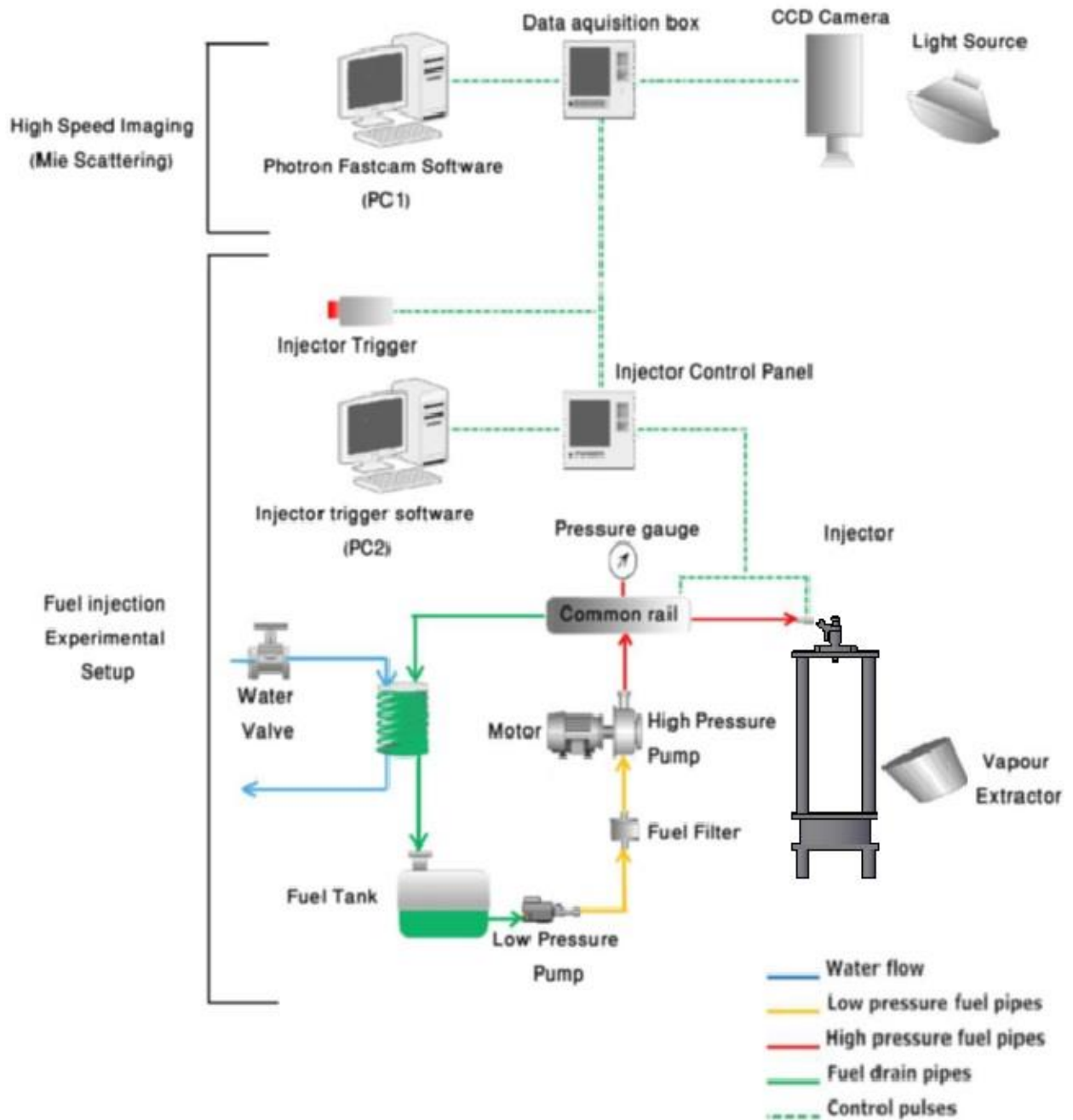
Figure 4-11 Schematic diagram of the test rig for spray visualization of high pressure injector [90]

Injector:

The injector used for this project was a Bosch multi-hole step-nozzle injector. It consisted of 7 holes each with stepped nozzle exit design. Figure 4-12 shows the magnified tip of the injector under microscope.

(a)   (b)
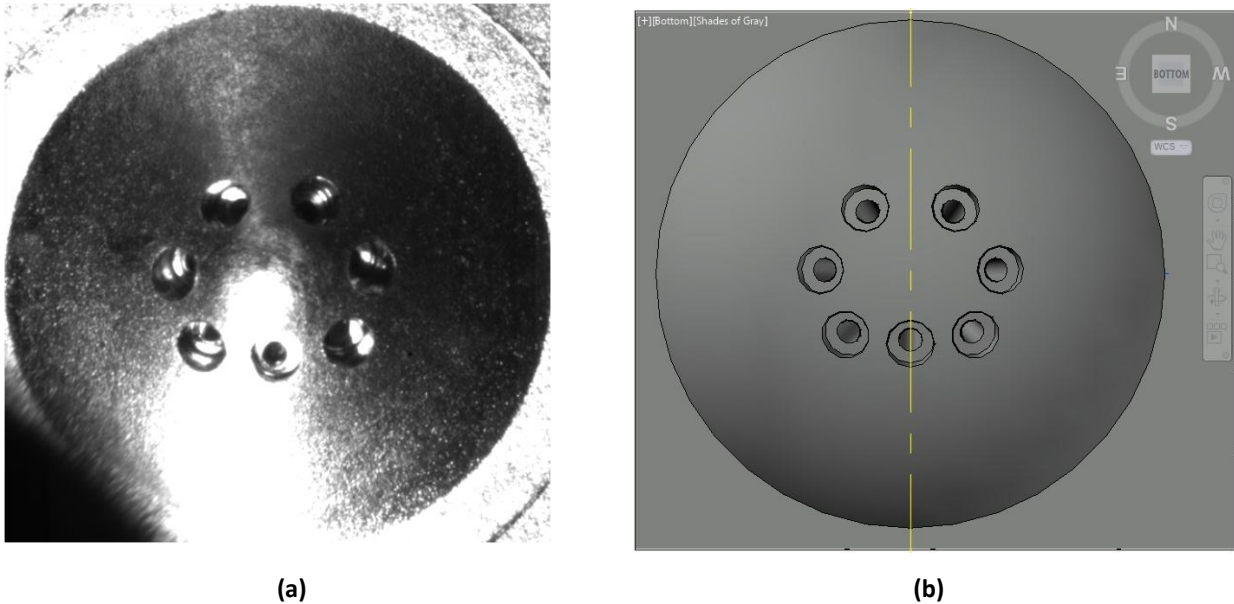
Figure 4-12 The tip of the injector under examination (a) magnified image of the tip of the injector under microscope. (b) the injector design in CAD

The exact geometry of the tip of the injector and the hole configuration could be obtained using figure 4-12 a. It is then used to create the 3D conceptual design on the right. Although the dimensions of these holes were not provided, it was possible to calculate them thanks to the very close up high-resolution image. The captured image clearly shows the step nozzle; thus, it was possible to calculate the diameter of the step. Through manual calculation by using the pixel size and the injector tip diameter, it was found that the step size of the nozzle is approximately 380±5 μm and the actual nozzle size is approximately 190±5 μm. Thus, the ratio between the step and the actual nozzle is around 0.5. This suggest the diameter of actual nozzles is half the step nozzle diameter. Figure 4-12 b shows that the injector has a symmetry plane which is shown by the yellow centre line. It should be noted that each of the stepped-nozzle in this injector is directed in a specific angle, this is to maximise the effectiveness of the spray. The injector was investigated at 0° and 90° rotational configuration.
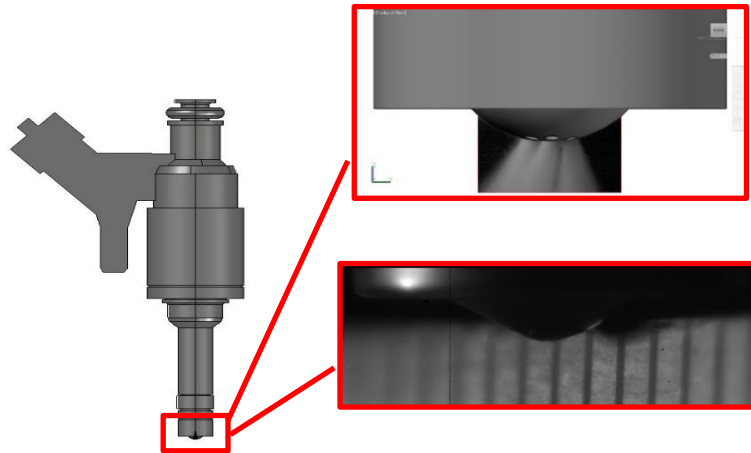
Figure 4-13 Side view of the CAD model of the injector under investigation – magnified tip of the injector and a real photo of the injector tip showing the relative size of the tip of the injector

Figure 4-13 shows the side view of the CAD model of the injector 3. The position of the stepped holes are shown on the magnified tip of the injector which is overlapped with a real photo of the near-nozzle spray.
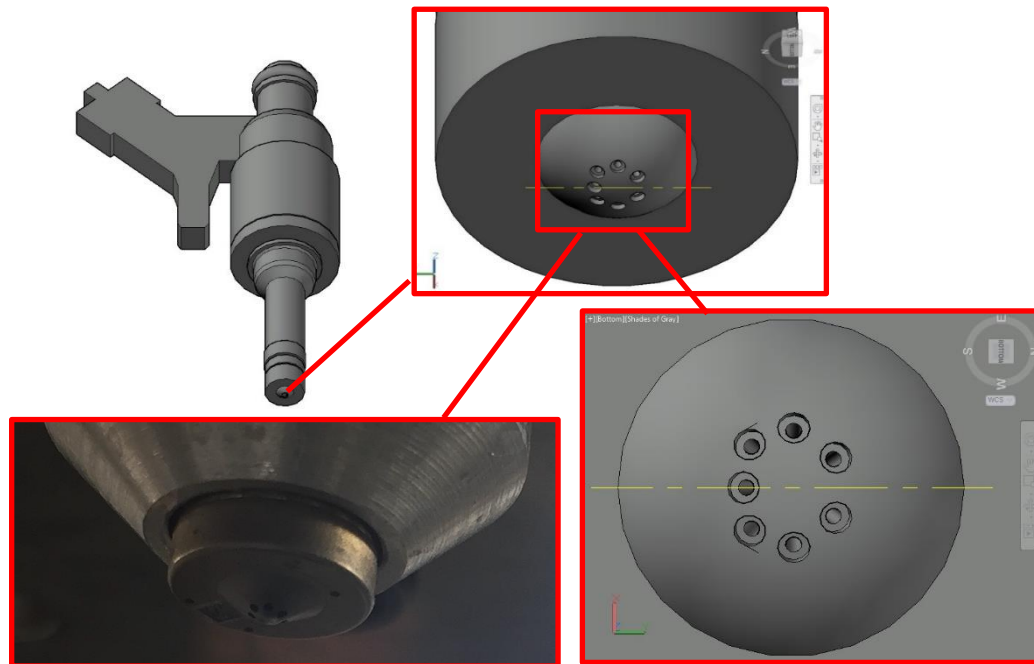
Figure 4-14 3D view of the the injector: designed in CAD and the whole configuration from the bottom view

Figure 4-14 shows the bottom view of the CAD model of the injector 3. The position of the stepped holes are shown on the magnified tip of the injector.

The overall injection system consists of several parts which could produce pressurised fuel spray such that of inside of a combustion chamber. Although inside an actual combustion chamber there would be presence of chamber pressure, this parameter was not considered for this measurement. The fuel was injected into the atmospheric condition. To allow the injector to be mounted stably on the optical table while allowing rotation, a base was designed and manufactured utilising dual axial roller bearings to allow smooth rotation with zero axial movement under vibrational input, the base was mounted on four pillars and included a ceramic insulating spacer. [88]

(a)   **(b)**
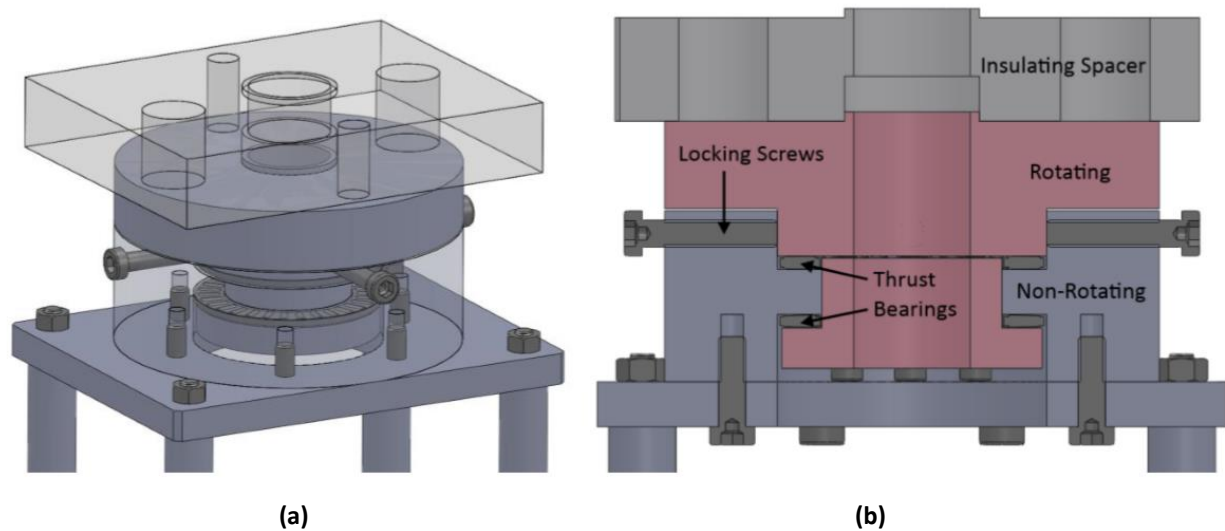
Figure 4-15 Mounting designed for rotation of the injector (a) 3-D view of the mounting design (b) side view of the mounting design showing the non-rotating and the rotating parts [88]

The injector was bolted onto the metal plate which mounted onto a secure structure, which can rotate 360° (shown on Figure 4-15), and this structure was bolted onto the table surface so that there is no vibration produced, as this could affect the fuel spray characteristics. For this experiment the injector was rotated to 90° for symmetrical spray configuration. The view of the different sprays produced at different injector rotation angle is shown in figure 6-3 in chapter 6. Figure 4-16 shows the assembly of the injector on the rotating platform.
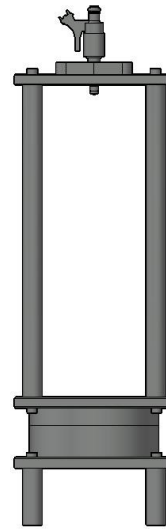
(a)   (b)

Figure 4-16 The injector mounting which can rotate 360 degrees (a) an image of the injector mounted on the rotating platform fitted with a suction tube (b) 3D design of the injector fitted on the rotating platform

Figure 4-17 shows the camera setup and the lighting setup for visualization of the spray under investigation.
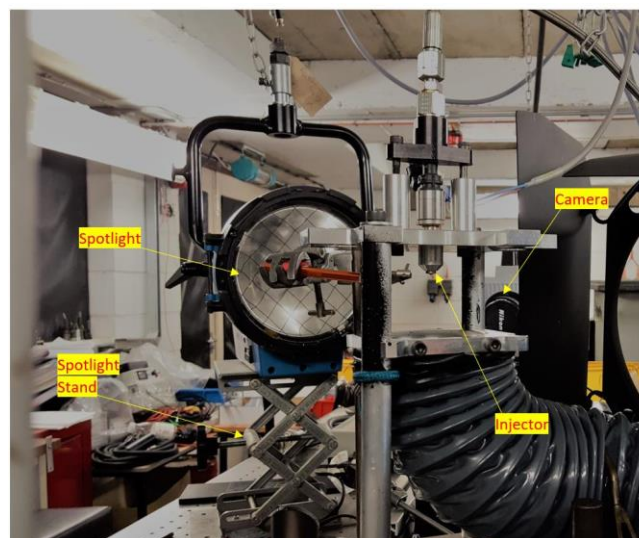
Figure 4-17 The camera setup and lightning for recording images

The macroscopic characteristic of the spray is one which can be analysed through physical analysis either qualitatively or quantitively. The quantitative characteristics of the spray can be

analysed in the software defined with the following physical parameters: Spray tip penetration, Spray cone angle as shown in figure 4-18. The focus of the visualization of the spray was to find the spray tip penetration and cone angle in order to prepare the test rig for PDA measurement.
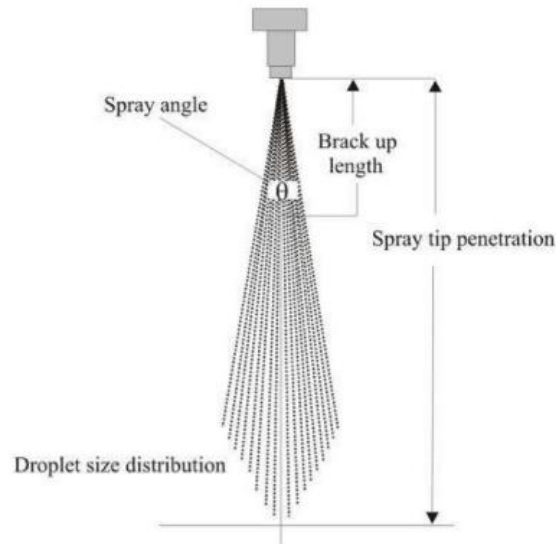
Figure 4-18 A schematic of the spray breakup length and spray angle. [91]

Figure 4-19 shows the Matlab interface and the spray tip penetration and cone angle analysis. The first image in the row from left shows the initial regions chosen to calculate these parameters before running the Matlab software. The second image shows an instance of the Matlab programme running and calculating the spray cone angle profile (green curve which is not visible due to overlap with the pink line), and the linear fit of the polyfit (pink line), the spray edge profile (blue dots) and the spray maximum tip penetration (purple line). For the edge detection, the images were first changed to binary mode. Then the single pixels were removed and the boundary was found using bwmorph filter. This boundary is shown on the image in green colour which is not visible due to overlap with the pink line. After this step, a linear fit was applied to the boundary using Polyfit in Matlab.

(a)   (b)
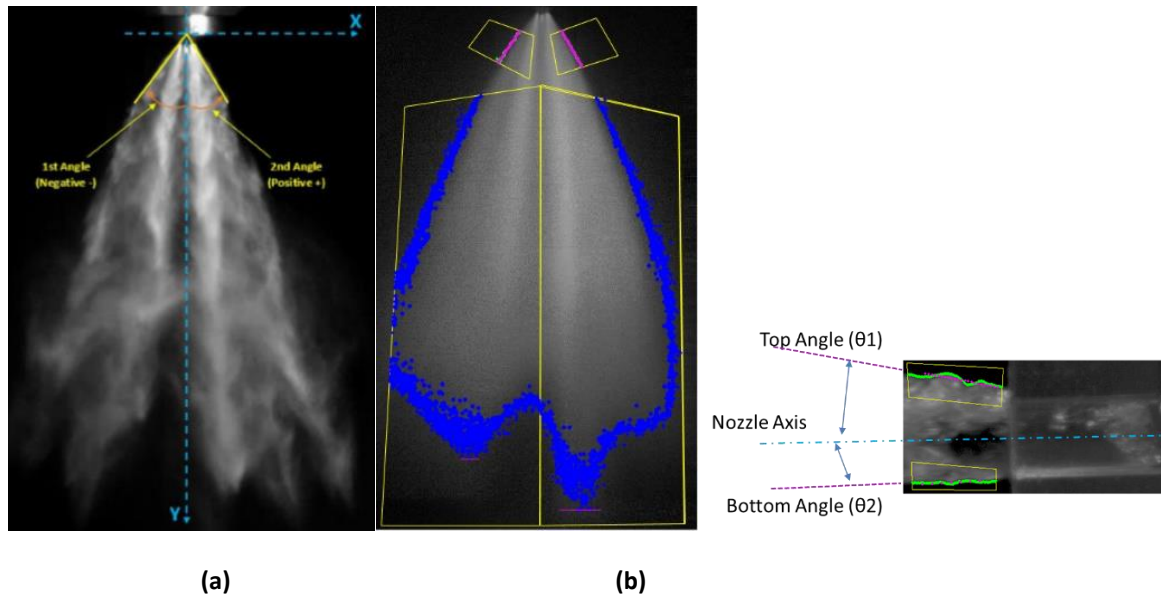
Figure 4-19 An in-house Matlab code which was developed to measure near-nozzle spray cone angle and penetration for different individual jets

An effort was also made to calculate the near-nozzle angle of the spray according to the length scales introduced in Hiroyasu & Array (figure 4-20). It was assumed that the liquid core of the spray is fully atomized in the step region and therefore the angle region started very close to the nozzle exit. The maximum deviation of the spray edge angles was 7 degrees, which gives a maximum angle intensity of 7/8.83=0.79, which means that the statistical error in mean cone angle for 2000 images would be 2 x $0.79/\sqrt{2000}$ = 0.018 or 1.8% with 95% confidence level and the corresponding standard deviation would be 2 x $1/\sqrt{2 \times 2000}$ = 0.032 or 3.2% according to Yanta estimation.
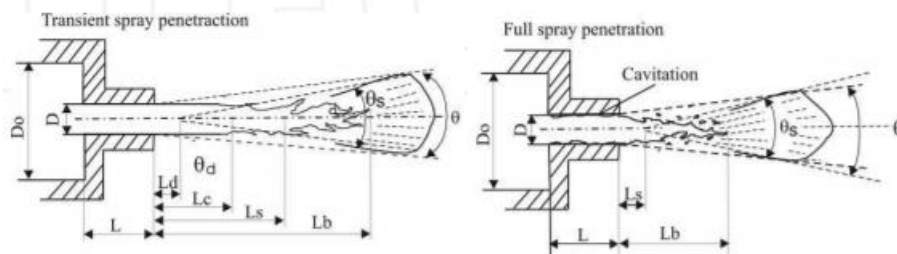
Figure 4-20 Internal structure of complete and incomplete spray [92]

4.5   PDA measurement of real-size high pressure injector

The first step of the PDA measurement involved the setup of the nebuliser and the PDA transmitter and receiver configuration. A nebuliser with average droplet size of 5μm was used in for the setup according to figure 4-21.
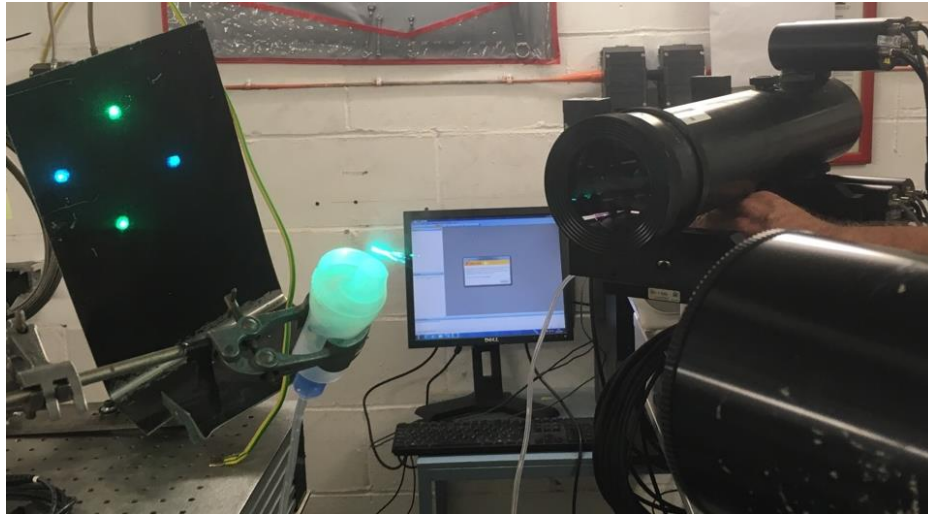
Figure 4-21 A nebuliser used for setup of the PDA system

The probe volume has an elliptic shape with dx= 0.04767mm , dy = 0.04734mm and dz = 0.3989mm. The fringe spacing is 2.168 μm. The beam half angle is 6.815 degrees which means the total beam angle is 13.68 degrees.

Firstly the main laser beam was setup on maximum and the output was measured to be around 100 units. The power of the laser in the probing volume is much lower than the main beam due to the losses in the system. An eye-piece was used to locate the probing volume below the injector while the spray was being injected at high pressure. In order to gain accurate measurement the final setup was made available by using BSA flow software. This was done after tuning the PDA receiver detectors by changing the high voltage (LDA1 = 850 volts, LDA2 = 900 volts, LDA3 = 910 volts, LDA4 = 910 volts, to get maximum data rate and validation and spherical validation.

The angles for the PDA setup was chosen to be 70 degree which is common in PDA measurement of fuel spray droplet. This is due to the maximum refraction that is produced at this angle from droplets.
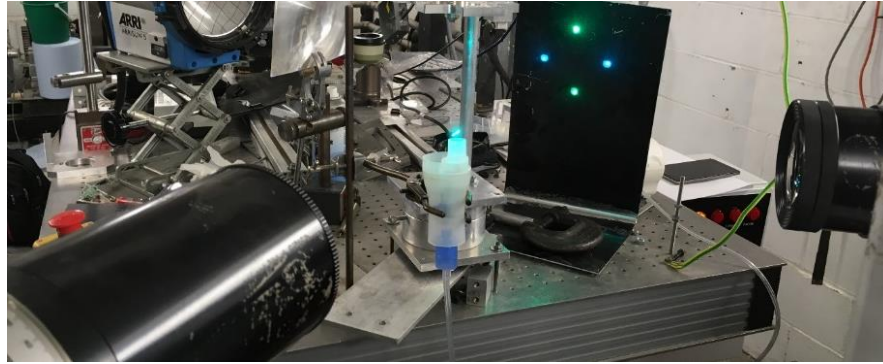
Figure 4-22 Setting the distance between the measurement volume and the transmitter/receiver

In the next step the validation and spherical validation of the LDA signals for the nebuliser were checked using the BSA software. The results were 98% validation for LDA1 signal and 99% validation for LDA4 signal. The spherical validation was also 98% which shows a very high accurate mesaurement. The criteria for accurate measurement of the droplet size was the ratio between the measured volumetric flow rate and the actual volumetric flow rate. The measured volumetric flowrate can be obtained by the total volumetric flux of the droplets at the probing volume. This value could be approximated using the equation below considering 100% sphericity and detection.

$V = \sum n_i \left(1/8 \, \pi D_i^3 \right)$

In the next step, the nebuliser was removed and the PDA system was directed on to the injector test rig using the traverse as shown in figure 4-23. The PDA set up at this stage of the experiment was set where the transmitting and receiving optics are also shown. Firstly the injector was rotated 110 degree according to figure 4-24 (a) and (b) in order to isolate one of the sprays which is mostly vertical and can offer maximum exposure for the laser light and the reciever. The angle of the receiver and the transmitter was set to 70 degrees.
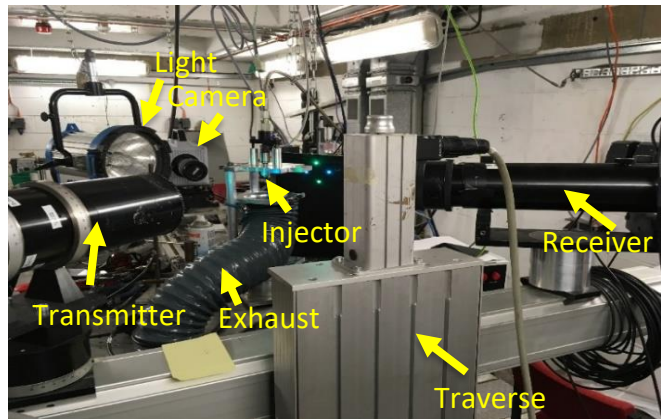
Figure 4-23 Shows the configuration of the PDA system

As can be seen in the figure 4-24 (a) and (b), the spray has been rotated 110 degrees in order to provide better exposure for laser experiment. The transmitting laser beams and the receiving optics were set up to minimize the effect of beam and scattered light attenuation to collect full spray signal near the injector exit where the spray is very dense. The data were collected continuously during the injection process and up to 100000 samples were collected over many injection cycles for each measuring location.

The measurements were done continuously for each location until a fixed sample of data was reached or a maximum sampling time is passed whichever occurred sooner. The data were then changed to cyclic ensembles using Matlab functions. This was done for short duration of start of the injection (ASOI) up to 2ms ASOI up to axial distance of 35 mm from the injector tip. The collected information of time, velocity and the size were resolved over a time interval of 0.05 ms to obtain the ensemble-averages. The number of validated samples in 0.05 ms time interval varied from 1000 to 8000 samples with maximum statistical uncertainty of ~2.5% in the mean velocity value.
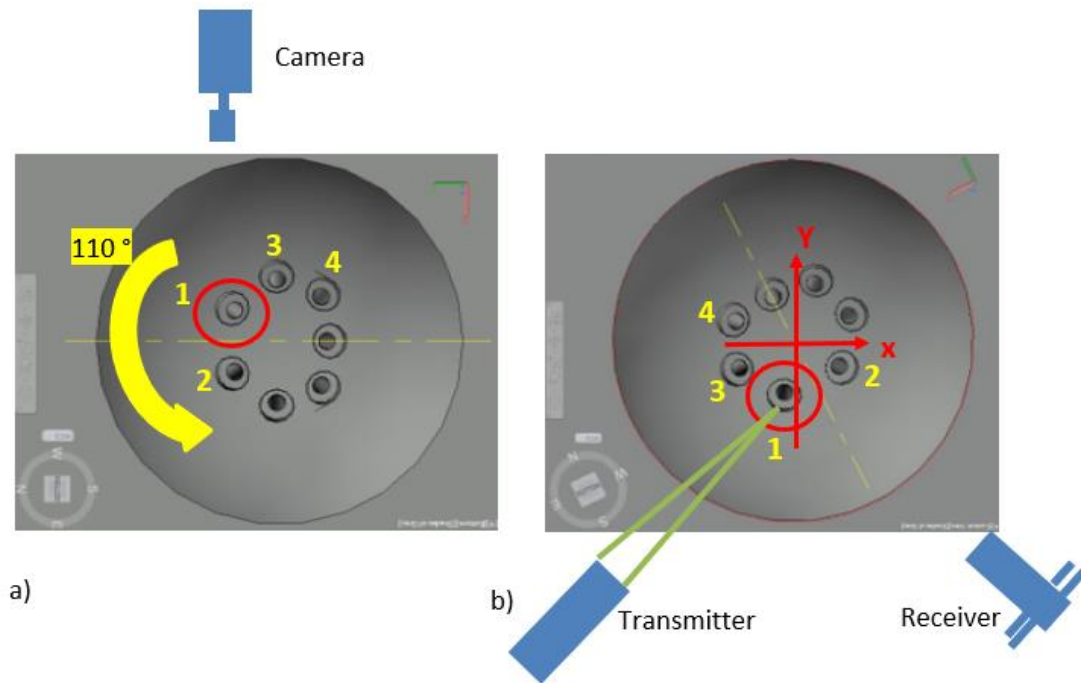
Figure 4-24 a) shows the 0 angle configuration of the spray for visualization of jet 1 , 3 and 4. b) The injector was rotated 110° to isolate jet 1 for the PDA measurement

The PDA experimental set-up is also shown in Figure 4-24 including transmitter and receiver. The laser transmitting and receiving optics were mounted on a traverse with resolution of 0.05mm (50µm), which allowed the control volume to be located to any positions within the spray. Before starting the PDA measurement acquisition, it was necessary to set up the experimental rig and to align the instrumentation. The optical receiver and the transmitting optics were set up according to angle of 70 degree and focal distance of 310mm. Adjustment were then carried out by traverse in order to achieve the highest burst signal possible. After the optics were set, the zero reference point was aligned with the control volume, which was chosen on the centre of the injector exit. Once the center of the injector and nozzle exit had been determined, the traverse was set to zero reference point by a optically aligning the traverse in the same location. This process is further explained in the next section. It is very difficult to isolate other sprays due to compact nature of the hole arrangements, however the injector axis was rotated 110 degree which allowed the favourite spray under examination to be as isolated as possible.

Figure 4-25 The PDA setup from another view

4.6 Setting up the reference point for PDA measurement

In the next step, the zero reference point was setup according to figure 4-26. It could be seen

from the figure 4-27 that at x=0,y=0, z=0 mm the laser beam has a mostly symmetric gaussian

distribution. When the laser beam was moved up to x=0, y=0 and z=0.1mm (as in figure 4-27),

the gaussian distribution is decreased to almost Full Width Half Maximum (FWHM) and the

beam is still visible. By moving the laser beam even upper to X=0, Y=0, Z=0.1, as shown in figure

c, the gaussian distribution of the beam disappears, however a small arc is still visible in the

images. Figures e and f shows the position of the arc which is moved in the X direction when X=

0.5 and X = -0.5 respectively.
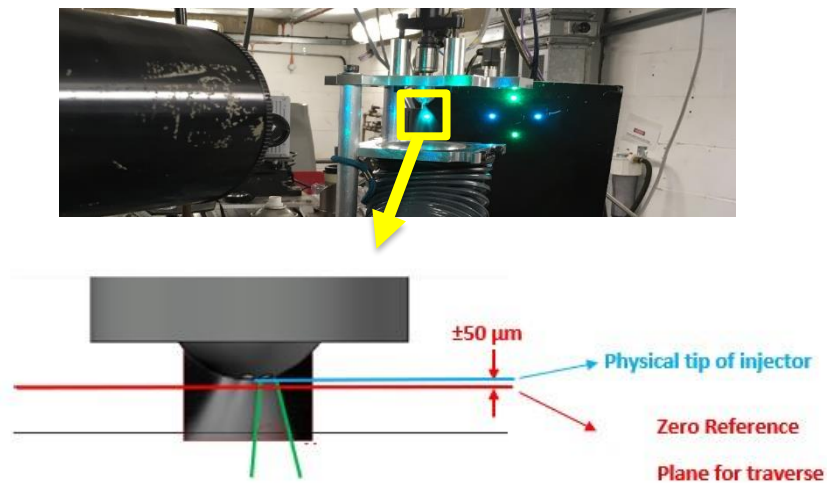
Figure 4-26 Setting up the reference point for PDA measurement at the distance of ±50μm below the physical edge of the injector tip.
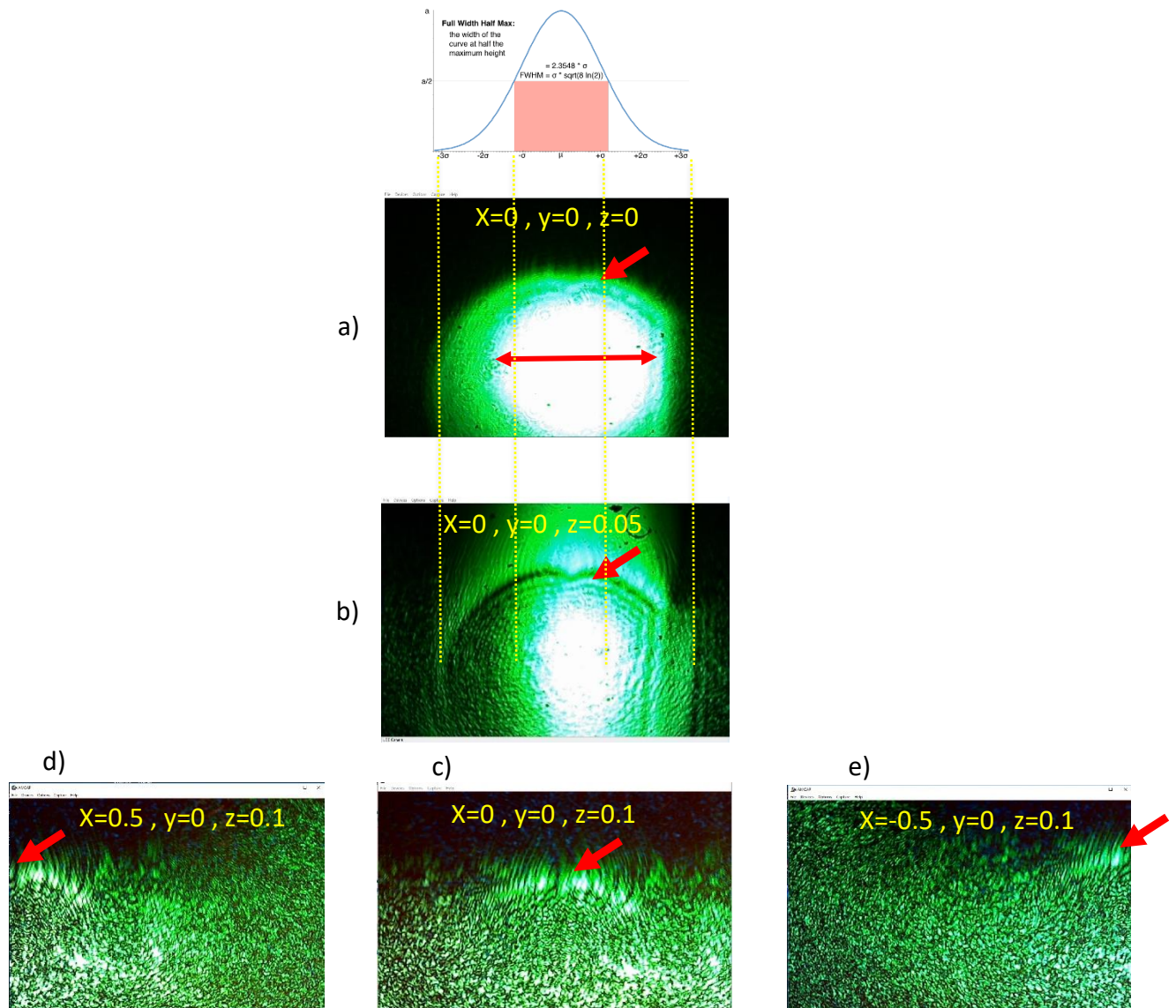
Figure 4-27 Setting up the zero reference point on the tip of the injector axis using a high magnification camera and the traverse system

Ensuring that the reference point remains the same between each round of the experiment.

(a)   (b)
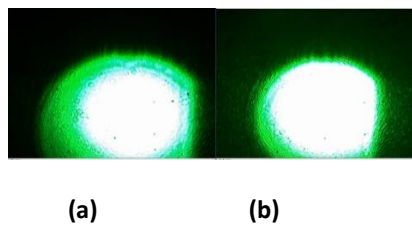
Figure 4-28: (a) The image of the laser beam taken by a fixed camera located closed to the reference point, (b) an image of the reference point in another round of measurement

A common source of uncertainty in the near-injector region of dense sprays was reported by [93], [94] and although it had no effect on size measurement accuracy [93], the effect of high droplet density can be considerable which may cause the system to fail in detecting droplets during the main injection period. In order to achieve good results, it was necessary to minimise attenuation of the laser beam and the most appropriate way of achieving this was to turn the injector at 110º angle. This allowed the isolated jet spray to be exposed fully to the laser light coming from the transmitter and to be visible by the receiver without any obstruction by any other jet spray.

4.7   Measurement strategy for 100 bar:
The measurement was done at the axial distance of 1, 2.5, 5, 10, 15, 20, and 35mm from the nozzle tip.
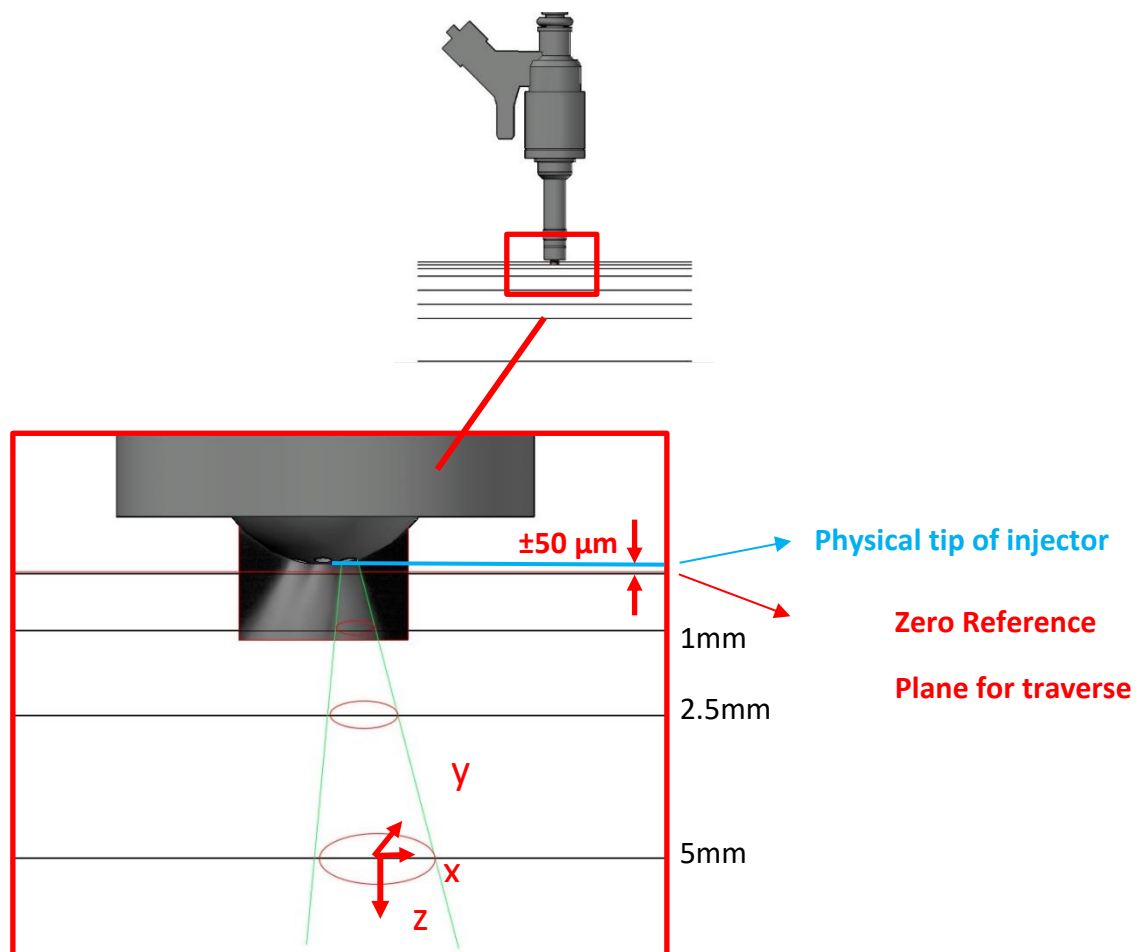
Figure 4-29 Different distance along z direction at which the measurement were done

In order to start with the PDA measurement, a particular mesh needs to be specified in the BSA software with x and y limits at a specific height of z. In order to choose the distance needed for coarse grid measurement of x and y of the isolated spray, mean grayscale image of 10 photos of the isolated pair of jet 1 captured at 1.5 ms ASOI shown for 20 bar and 100 bar from 0 angle side view according to figure 4-30 (a) . This was necessary in order to guide the traverse during measurement according to the mesh specified in BSA software.

a) 20 bar (mean)

b) 100 bar (mean)
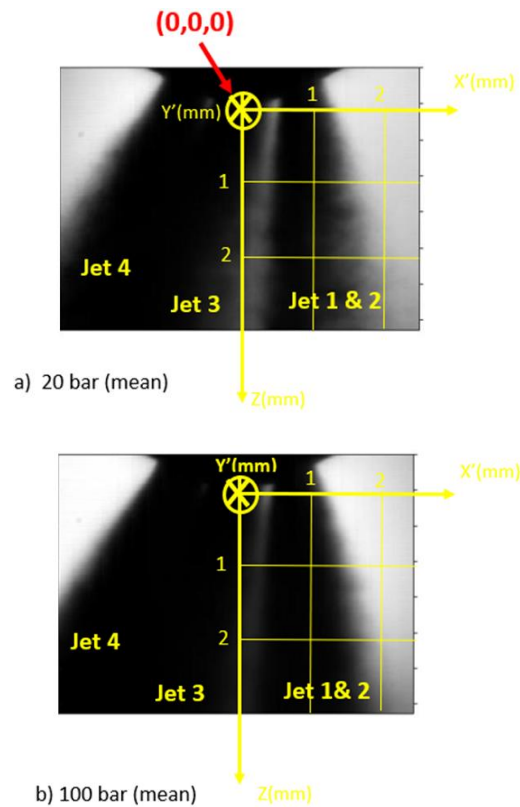
Figure 4-30 a) Mean grayscale image of 10 photos of the isolated pair of jet 1 captured at 1.5 ms ASOI shown for 20 bar and 100 bar from 0 angle side view.

Figure 4-30 a) shows 3D and 2D Front view of jet 1 and the coordinate system x,y,z for the movement of the traverse. It also demonstrates the velocity of the jet 1 by Vz which is along z direction. The radial velocity Vr is negligible and is one order of magnitude smaller and therefore is not included in the calculations. The angle of transmitter and receiver with respect to the X direction is also shown in the figure 4-31 which is 70 degrees.
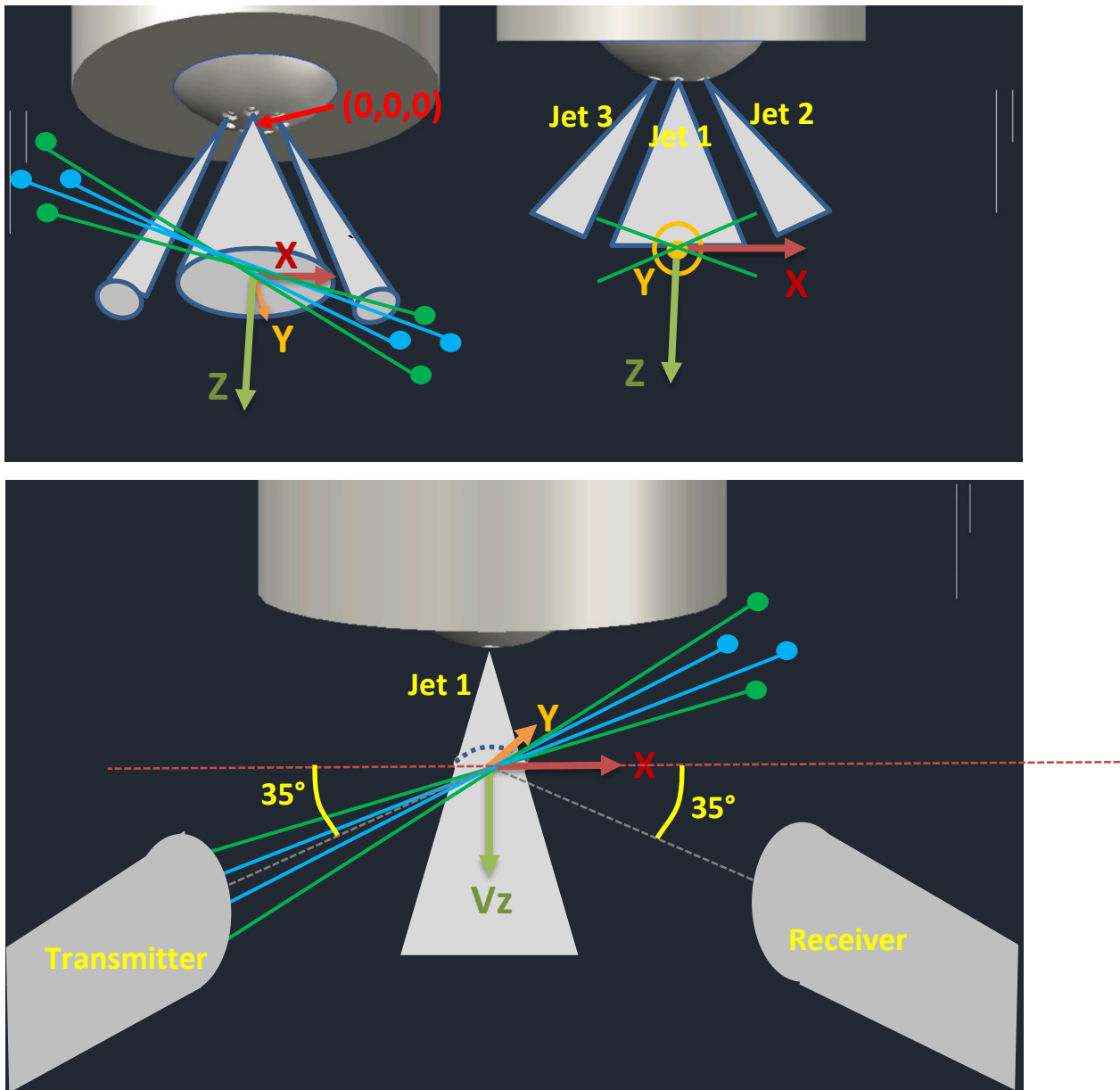
Figure 4-31 Top: 3D and 2D Front view of jet 1 and the coordinate system x,y,z for the movement of the traverse.

The data were collected for injection duration of 2ms at the pressure of 100 bar and up to 100000 samples were collected over many injection cycles for each measuring location.

4.8   Coarse grid measurement at z = 1mm

The first round of the measurement involved setting up the traverse for rough grid measurement of an area of 2mm x 4mm (this area is called region 1) for the below the nozzle exit at the height of 1mm away from the nozzle with grid length of 0.4mm in both X and Y direction. Region 1 is shown in figure 4-32. It was necessary to obtain this figure to find the approximate location and the contour plots of velocities of the isolated jet 1. It was also necessary to find the relative position of jet 2 and 3 as shown in figure 4-32.
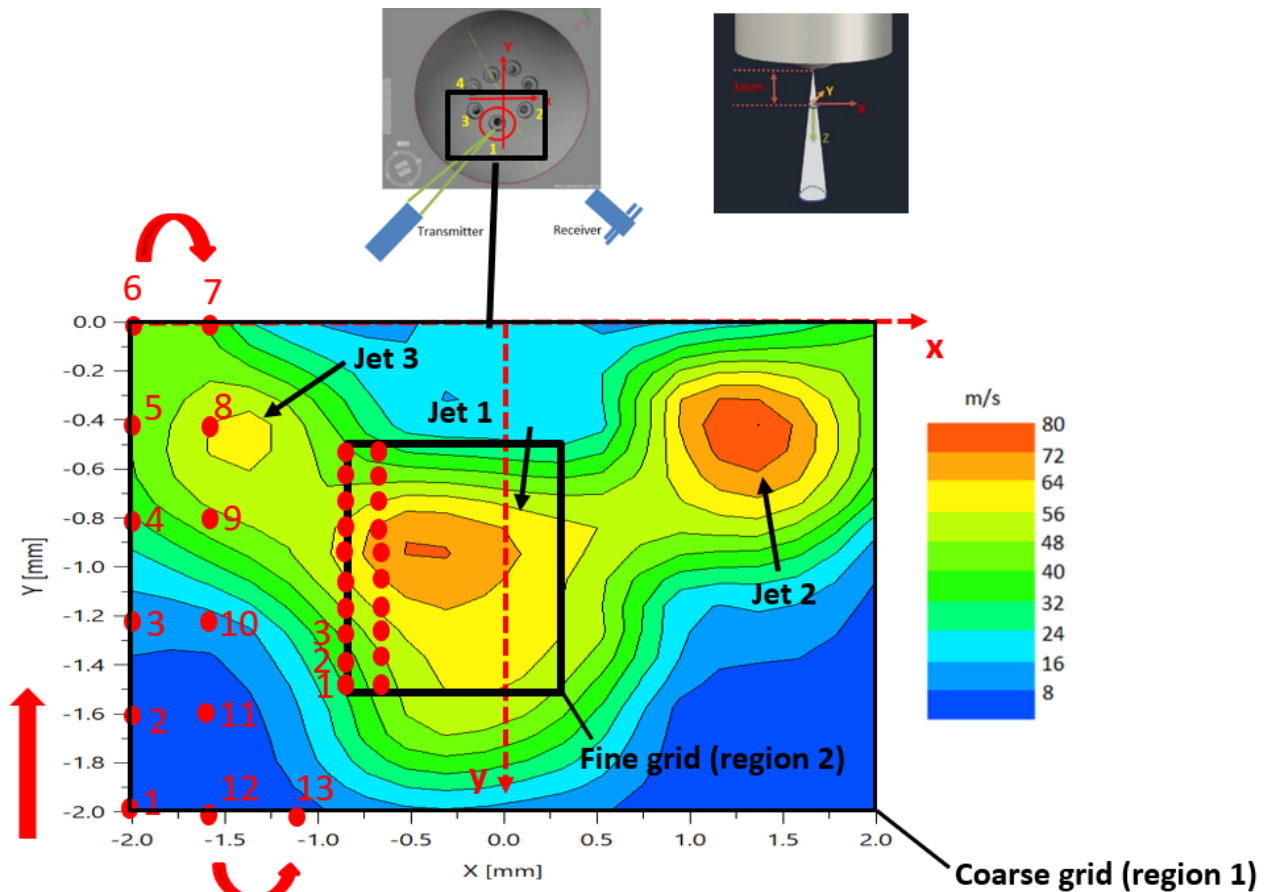
Figure 4-32 An example of rough grid measurement of jet velocities contour plots at the distance of 1mm below the nozzle exit, the black square shows the fine grid (region 2) measurement obtained based on the count numbers of data collected

In figure 4-32, the traverse started to measure from the point of (-2,-2) at the bottom left corner and finished the measurement at the point of (2,0) at the top right corner. In this configuration, the PDA system was able to measure up to 66 points with minimum count number of 1 sample and maximum count number of 10000. It was observed that the number of counts for point 1, 2,

and 3 are very low which are referring to the dark blue part of contour plot in figure 4-32. This clearly shows that point 1, 2 and 3 are not representing enough information on the core or the edge of the jet. It also shows that the mesh is too big to resolve the distribution with enough precision. Therefore, the area of the measurement was reduced to a smaller window and the grid size was reduced from 0.4 mm to 0.1 mm in the next step in order to obtain better resolution and velocity profiles.

The coarse grid measurement were done for all z values of 1mm, 2.5mm, 5mm, 10mm, 15mm, 20mm, and 35mm in order to present the contour plots of velocities and to obtain the location of the center of jet 1. The estimated center of the jet 1 were then used as a reference point for more precise measurement of finer grid contour plots of velocities for each case.

Looking at figure 4-32, one can realize that the peak velocity (red zone) of the jet 1 is located approximately at the position of (-0.5, -1). The next step was to use the information already obtained as a reference to create a finer grid region #2 with smaller grid of 0.1 mm which covers a smaller area of a 1mm x 1mm square around the approximate center of the jet with coordinated of (-0.5, -1). Therefore, it was concluded that the region 2 for finer grid measurement could be selected in such a way that x changes from 0 to -1 and y changes from -0.5 to -1.5. This area can confidently present the 2D contour plot of jet 1 at the distance of 1mm away from the nozzle. This could be verified by near-nozzle shadowgraph in figure 4-30.

Figure 4-33 shows the velocity contour plot for the fine mesh region (#2) (also shown in figure 4-33 in the black box). Here the grids are 0.1mm x 0.1mm. The measurement starts from point 1 (-1,-1.5) at the left bottom corner and ends at the point 121.

Using with grid distance of 0.1 mm. It can be seen from figure 4-33 that due to the finer meshing, the values of velocity measurements are more precise and can resolve up to mean velocities of around 90 m/s at the center of the jet compared to 80 m/s in the case of rough meshing. From figure 4-33, it will be concluded that the center of the jet 1 approximately point (-0.2, -1)
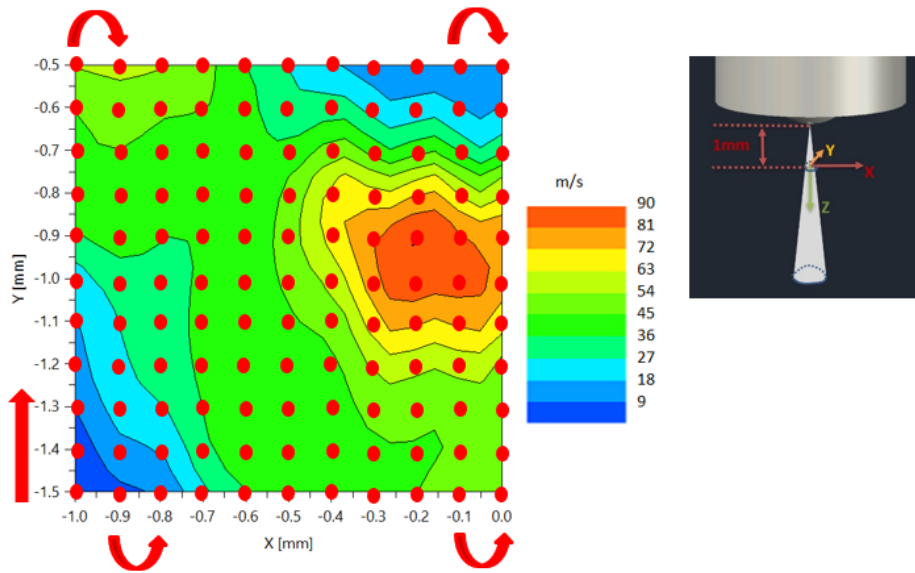
Figure 4-33 velocity contour plot for the fine mesh region (#2).

Therefore it is concluded to change the location of the region (#2) to a new region (#3) with same size and resolution in a manner that the center of jet 1 will be overlapped with the geometric center of the region (#3) ie the middle of the square. The new region 3 will be a new area of 1mm x 1mm in which X values changes from 0.3 to -0.7 and Y values changes from -0.5 to -1.5 as shown in figure 4-34.
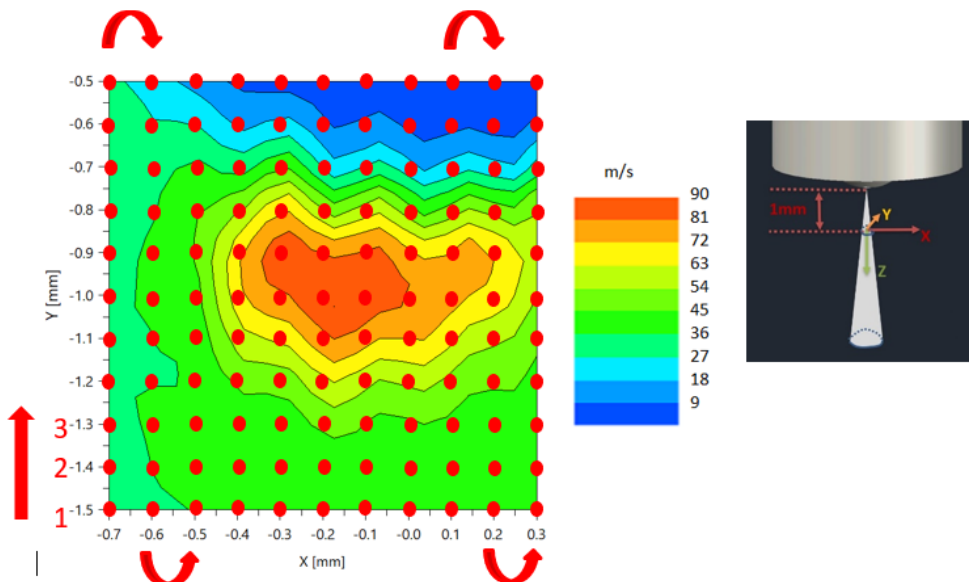
Figure 4-34 Velocity contour plot for the fine grid measurement region #3 at the distance of 1mm below the nozzle exit. The grid minimum distance is 0.1 mm.

In figure 4-34, traverse started to measure from the point of (-0.7, -1.5) at the bottom left corner and finished the measurement at the point of (0.3, -0.5) at the top right corner. In this configuration the PDA system was able to measure up to 121 points with maximum count number of 10000 samples and minimum count number of around 2500. After examination of the data, it was found that the limits of the mesh have enough number of samples (20000). It was concluded that the length chosen for the grid which is 1mm x 1mm is acceptable and therefore the next step of the measurement was carried out using this information. In the next section, the very fine measurement of the velocity profile of jet 1 is explained.

4.9   Very fine grid measurement at z= 1mm (50 microns grid)

In this section, the very fine measurement of the velocity profile of jet 1 is explained.
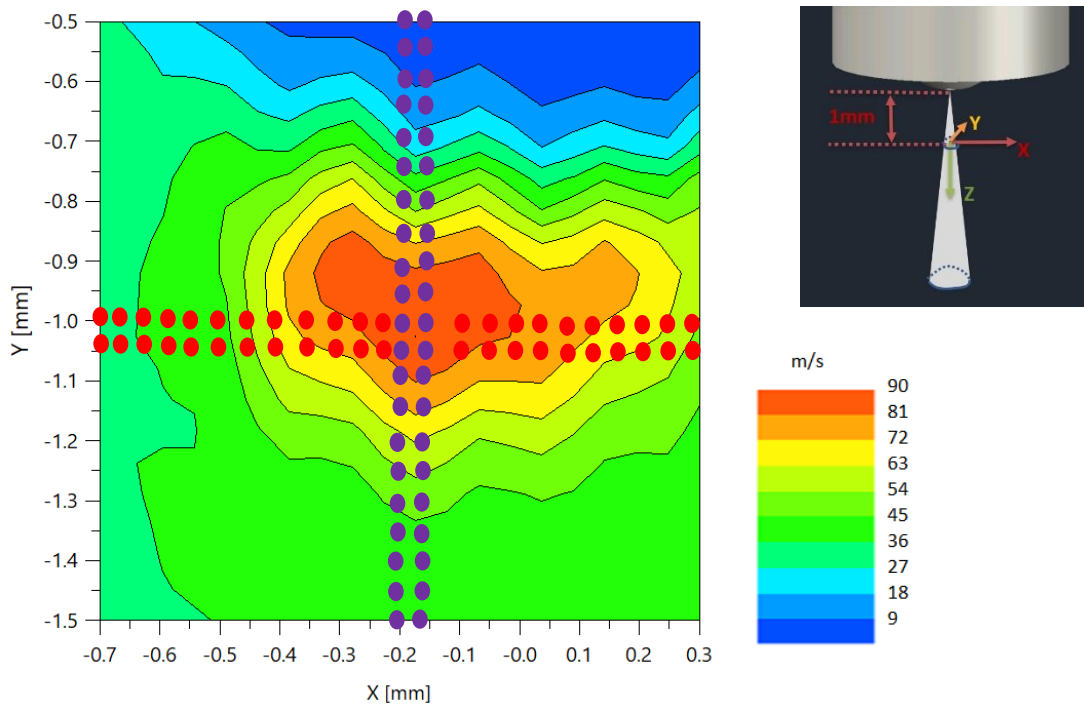
Figure 4-35 In the very fine mesh grid, there are 42 points from top to the and 21 points from right to left for measurement of the velocity profiles along x direction. Also there are 20 points from bottom to the top and 20 points from top to the bottom for measurement along y axis. The distance between each point is 0.05 mm.

In this configuration, the grid minimum distance is 0.05 mm (50 μm). Here there are 20 points from left to right and another 20 points from right to left for measurement of the velocity profiles along x direction. Also there are 20 points from bottom to the top and 20 points from top to the bottom for measurement along y direction.

4.10 Average Velocity distribution at height of 1mm along y axis
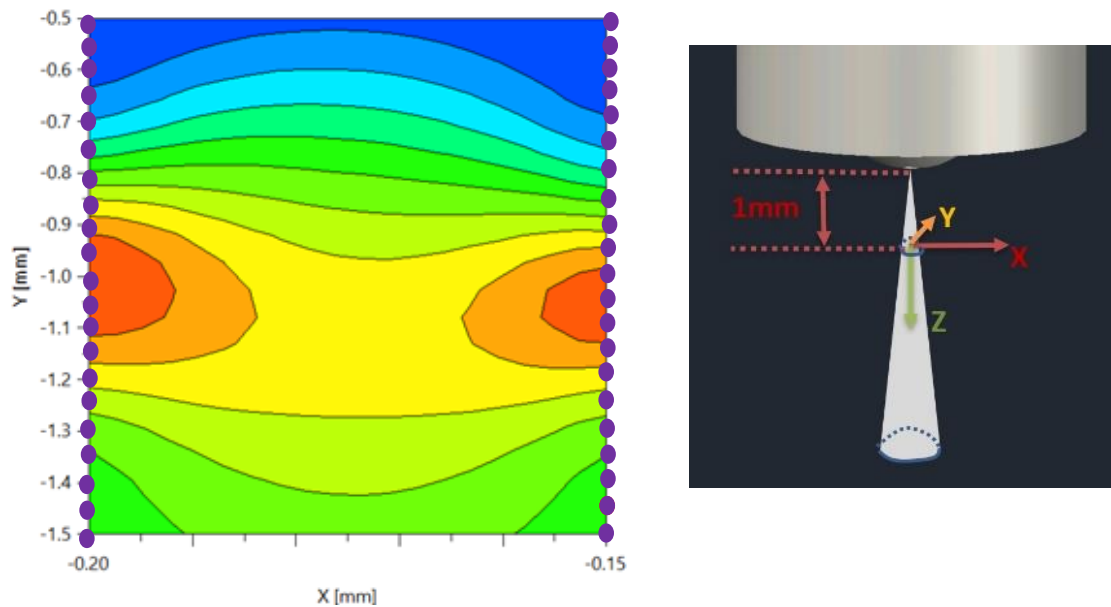
Figure 4-36 Contour plot of velocities for the very fine mesh measurement along y axis at the height of 1mm. The traverse started moving along y from (-0.2, -1.5) to (-0.2, -0.5) and then move right along x for 0.05 mm to (-0.15, -0.5) and then move down to (-0.15, -1.5). The x axis has been exaggerated.

Table 4-4 A list of data in the measurement while the traverse moves from point 1 to point 7 the number of samples were maintained at 100,000.

	X [mm]	Y [mm]	Z [mm]	Date_Time	Count{1}	Count{2}	Data Rate{1} [#/s]	Data Rate{2} [#/s]	Validation {1} [%]	Validation {2} [%]	LDA1-Mean [m/s]	D-Mean [μm]
1	-0.20	-1.50	1.00	11:11:46	100000	10000	1908.41	1785.56	66.41	69.01	49.46	5.5
2	-0.20	-1.45	1.00	11:12:41	100000	10000	1988.09	2173.61	59.06	55.35	49.29	5.3
3	-0.20	-1.40	1.00	11:13:34	100000	10000	1883.24	2499.02	51.63	42.78	48.91	5.2
4	-0.20	-1.35	1.00	11:14:29	100000	10000	1642.04	2438.31	45.17	49.54	49.22	5.0
5	-0.20	-1.30	1.00	11:15:32	100000	10000	1353.20	2222.10	38.34	53.67	50.86	4.9
6	-0.20	-1.25	1.00	11:16:48	100000	10000	1146.80	1886.39	34.39	30.53	54.55	5.0
7	-0.20	-1.20	1.00	11:18:18	100000	10000	1012.16	1612.60	33.28	27.44	61.00	5.4
8	-0.20	-1.15	1.00	11:19:59	95411	10000	955.05	1234.50	36.36	24.15	69.60	5.9
9	-0.20	-1.10	1.00	11:21:41	91621	10000	917.13	1020.31	38.60	26.42	76.81	6.3
10	-0.20	-1.05	1.00	11:23:24	83900	9098	839.84	918.65	43.46	24.43	82.08	6.7
11	-0.20	-1.00	1.00	11:25:06	70544	8616	706.15	869.74	47.47	22.25	85.41	7.1
12	-0.20	-0.95	1.00	11:26:52	52611	9499	526.64	959.22	51.67	25.73	85.06	7.5
13	-0.20	-0.90	1.00	11:28:34	39589	10000	396.29	1110.96	54.35	40.66	79.34	7.5
14	-0.20	-0.85	1.00	11:30:16	29957	10000	299.87	1369.56	58.59	40.08	69.12	7.2
15	-0.20	-0.80	1.00	11:31:59	24686	10000	247.11	1538.27	60.30	55.35	56.24	6.6
16	-0.20	-0.75	1.00	11:33:41	21978	10000	220.00	1753.80	64.09	46.56	41.96	5.9
17	-0.20	-0.70	1.00	11:35:23	20548	10000	205.68	1851.31	65.21	65.83	31.96	5.3
18	-0.20	-0.65	1.00	11:37:05	20364	10000	203.84	1959.98	64.25	64.24	25.62	5.0
19	-0.20	-0.60	1.00	11:38:47	20844	10000	208.65	1999.34	62.09	65.45	22.41	4.9
20	-0.20	-0.55	1.00	11:40:30	21880	10000	219.02	1723.94	60.47	51.45	19.91	4.9

4.11 Velocity profile at height of 1mm along x axis
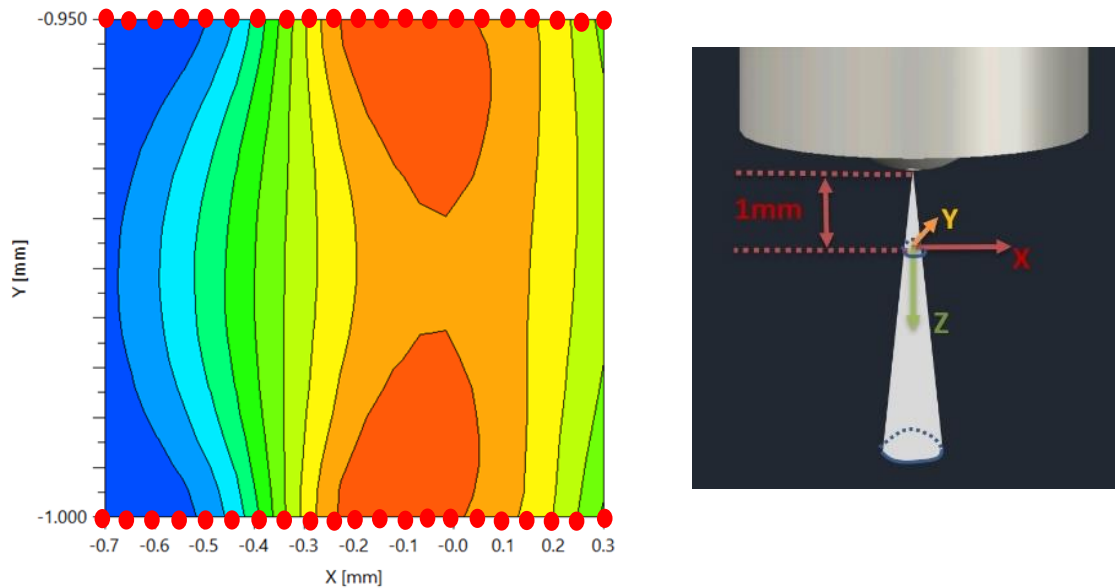
Figure 4-37 Contour plot of velocities for the very fine mesh measurement along x axis at the height of 1mm. The traverse started moving along a zig-zag pattern. The y axis has been exaggerated.

Table 4-5 A list of data for the velocity measurement in very fine mesh configuration at the distance of 1mm along x axis.

	X [mm]	Y [mm]	Z [mm]	Date_Time	Count{1}	Count{2}	Data Rate{1} [#/s]	Data Rate{2} [#/s]	Validation {1} [%]	Validation {2} [%]	LDA1-Mean [m/s]	D-Mean [µm]
1	-0.70	-1.00	1.00	09:55:25	100000	10000	2150.54	2173.20	66.94	55.87	43.92	4.3
2	-0.70	-0.95	1.00	09:56:14	100000	10000	2164.51	2127.23	68.74	44.09	43.32	4.3
3	-0.65	-0.95	1.00	09:57:02	100000	10000	2164.47	2272.02	67.31	61.09	43.51	4.2
4	-0.65	-1.00	1.00	09:57:51	100000	10000	2141.31	2272.31	64.39	62.06	43.93	4.2
5	-0.60	-1.00	1.00	09:58:40	100000	10000	1999.98	2222.18	57.93	57.64	44.45	4.2
20	-0.25	-1.00	1.00	10:19:32	65965	7754	660.31	783.11	46.13	19.67	84.36	6.6
21	-0.20	-1.00	1.00	10:21:18	64949	7760	650.14	783.70	47.70	19.82	87.13	6.9
22	-0.20	-0.95	1.00	10:23:01	57500	7986	575.58	806.54	49.47	20.79	87.20	7.0
23	-0.15	-0.95	1.00	10:24:43	56307	8034	563.64	811.39	48.90	22.05	88.09	7.2
24	-0.15	-1.00	1.00	10:26:25	65294	8294	653.60	837.45	47.65	26.72	87.23	7.0
39	0.25	-0.95	1.00	10:52:08	78797	8517	788.76	860.14	43.28	30.55	72.61	6.4
40	0.25	-1.00	1.00	10:53:51	97010	9607	971.08	970.25	41.23	34.21	67.81	5.9
41	0.30	-1.00	1.00	10:55:33	100000	10000	1090.53	1063.81	40.70	35.86	64.03	5.6
42	0.30	-0.95	1.00	10:57:07	93336	9162	934.30	925.28	41.58	25.62	67.39	6.0

4.12 Diameter profile at distance of 1mm along y axis

Figure 4-38 shows the contour plot of the diameter of the droplets measured for jet 1 at the distance of 1mm along the y axis of the jet. It should be mentioned that the axis has been exaggerated. It can be observed that the range is from 4μm to around 7μm.
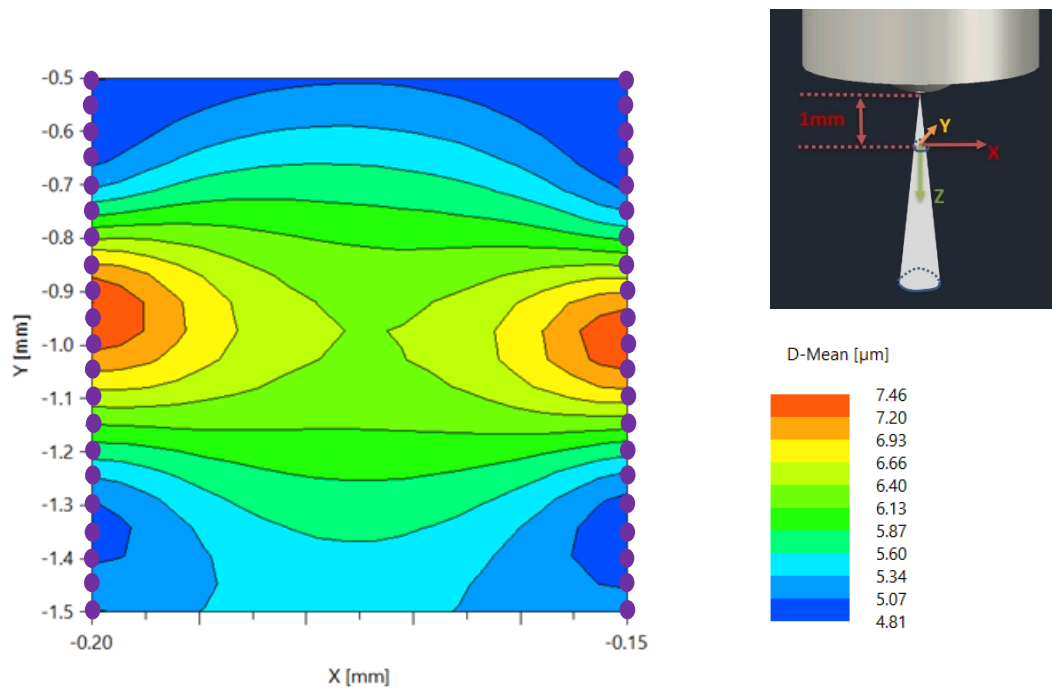
Figure 4-38 shows the contour plot of the diameter of the droplets measured for jet 1 at the distance of 1mm along the y axis of the jet.

Table 4-6 The data for the droplet statistics in very fine mesh configuration at the distance of 1mm along y axis.

	X [mm]	Y [mm]	Z [mm]	Counts	Spherical Validation [%]	D10 [μm]	D20 [μm]	D21 [μm]	D30 [μm]	D31 [μm]	D32 [μm]	D43 [μm]	Concentration [#/cm³]	U Flux [cm³/cm²/s]
1	-0.20	-1.50	1.00	100000	86.19	5.5	6.1	6.8	6.8	7.7	8.6	12.5	25945	0.0049
2	-0.20	-1.45	1.00	100000	86.09	5.3	6.0	6.7	6.8	7.8	9.0	13.9	21271	0.0047
3	-0.20	-1.40	1.00	100000	84.90	5.1	5.9	6.7	6.8	7.8	9.2	14.4	13248	0.0043
4	-0.20	-1.35	1.00	100000	80.59	5.0	5.8	6.8	7.0	8.2	9.9	16.0	19838	0.004
9	-0.20	-1.10	1.00	91621	55.53	6.1	7.6	9.4	9.5	11.8	14.9	22.6	13554	0.0064
10	-0.20	-1.05	1.00	83900	50.50	6.5	8.1	10.0	10.1	12.5	15.6	23.0	28146	0.0084
11	-0.20	-1.00	1.00	70544	47.33	6.9	8.6	10.7	10.6	13.3	16.5	23.8	9596	0.0082
12	-0.20	-0.95	1.00	52611	44.40	7.1	9.0	11.2	11.1	13.9	17.1	24.3	20269	0.0078
17	-0.20	-0.70	1.00	20548	70.86	5.1	6.8	8.9	8.9	11.7	15.5	23.5	26893	0.0012
18	-0.20	-0.65	1.00	20364	74.48	4.9	6.4	8.4	8.4	11.0	14.5	22.3	22965	0.00081
19	-0.20	-0.60	1.00	20844	76.01	4.8	6.3	8.2	8.2	10.8	14.1	21.9	36620	0.00076
20	-0.20	-0.55	1.00	21880	74.52	4.9	6.4	8.5	8.5	11.2	14.8	22.4	40603	0.00091

It should be mentioned that the y axis has been exaggerated. It can be observed that the range is from 4µm to around 7µm. This is important to note since it shows that the validated droplets are atomised to a good level.

4.13 Diameter profile at distance of 1mm along x axis
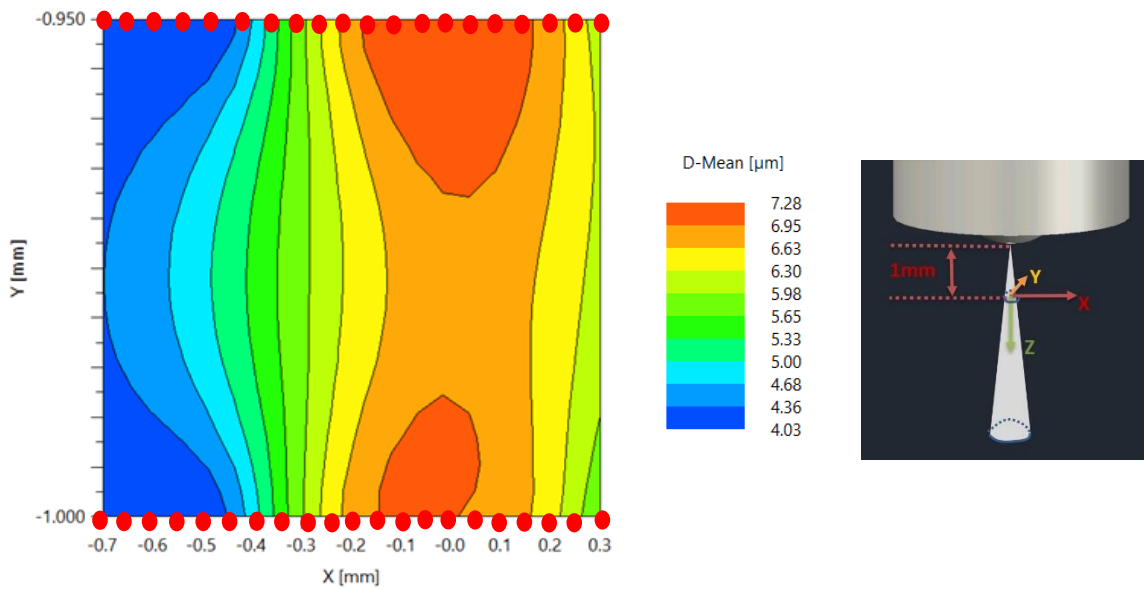
Figure 4-39 shows the contour plot of the diameter of the droplets measured for jet 1 at the distance of 1mm along the x axis of the jet.

Table 4-7 The data for the droplet statistics in very fine mesh configuration at the distance of 1mm along x axis.

	X [mm]	Y [mm]	Z [mm]	Counts	Spherical Validation [%]	D10 [µm]	D20 [µm]	D21 [µm]	D30 [µm]	D31 [µm]	D32 [µm]	D43 [µm]	Concentration [#/cm³]	U Flux [cm³/cm²/s]
1	-0.70	-1.00	1.00	100000	82.86	4.3	4.9	5.5	5.7	6.6	7.8	13.6	31519	0.0039
2	-0.70	-0.95	1.00	100000	83.87	4.2	4.8	5.4	5.6	6.4	7.4	12.4	26328	0.0038
3	-0.65	-0.95	1.00	100000	82.32	4.2	4.8	5.4	5.5	6.3	7.4	12.1	23777	0.0037
4	-0.65	-1.00	1.00	100000	82.33	4.2	4.8	5.5	5.7	6.6	7.8	13.6	35078	0.0039
27	-0.05	-0.95	1.00	58368	46.51	7.0	8.8	11.0	10.9	13.6	16.8	24.0	24052	0.0077
28	-0.05	-1.00	1.00	68776	48.96	6.8	8.5	10.6	10.6	13.2	16.4	23.6	19237	0.0087
29	0.00	-1.00	1.00	71922	50.80	6.7	8.3	10.3	10.3	12.8	15.9	23.1	18453	0.0078
30	0.00	-0.95	1.00	59242	48.49	7.0	8.7	10.9	10.8	13.5	16.6	23.7	15810	0.0078
39	0.25	-0.95	1.00	78797	58.74	6.3	7.7	9.5	9.6	11.9	14.8	22.3	19673	0.0063
40	0.25	-1.00	1.00	97010	63.25	5.8	7.1	8.6	8.8	10.8	13.5	20.9	24799	0.0054
41	0.30	-1.00	1.00	100000	66.86	5.5	6.7	8.1	8.2	10.1	12.5	19.6	28610	0.0049
42	0.30	-0.95	1.00	93336	64.00	5.9	7.2	8.8	9.0	11.0	13.8	21.2	27427	0.0055

4.14 Creating temporal graphs

The PDA measurement can yield valuable information on velocity and size distribution of the jet spray. This is evident from the cyclic ensemble data collection shown in figure 4-41. An

algorithm was used to calculate the mean of velocity graphs Vz (red color) and also the RMS values (green color) as shown in the figure 4-40.

It can be seen from figure 4-41 that the counts per window is above 6000 samples per windowing frame when the windowing frame was around 0.1ms. This shows quiet high number of samples which has been acquired in the measurement at the distance of 1 mm downward the nozzle exit over the whole range of the diameter of the jet spray. The counts per window rate will increase as the distance z increases and it reaches to 8000 counts per window. This shows that there is reasonable level of reliability on the results being presented. It would be more meaningful to use and interpret the graphs using the mean and RMS values onwards.

Since the number of data collection for each point for the very fine grid measurement was 100000 samples, it was possible to calculate the average mean and RMS values using very short time windows from start to finish. The duration of the windowing frame was initially chosen from smallest possible values up to 50 μs. This was a 2-fold decrease in the windowing frame with same number of samples compared to previous work done in the group which was 0.1ms. It was decided initially to use this duration (50 μs) for calculating the mean and RMS values on the graphs and investigating short time scale phenomena and mapping temporal graphs at different heights with each other. After careful investigation, it was observed that a 0.1ms will also be sufficient to resolve short time scale phenomenos as shown in figure 4-41 (yellow lines).
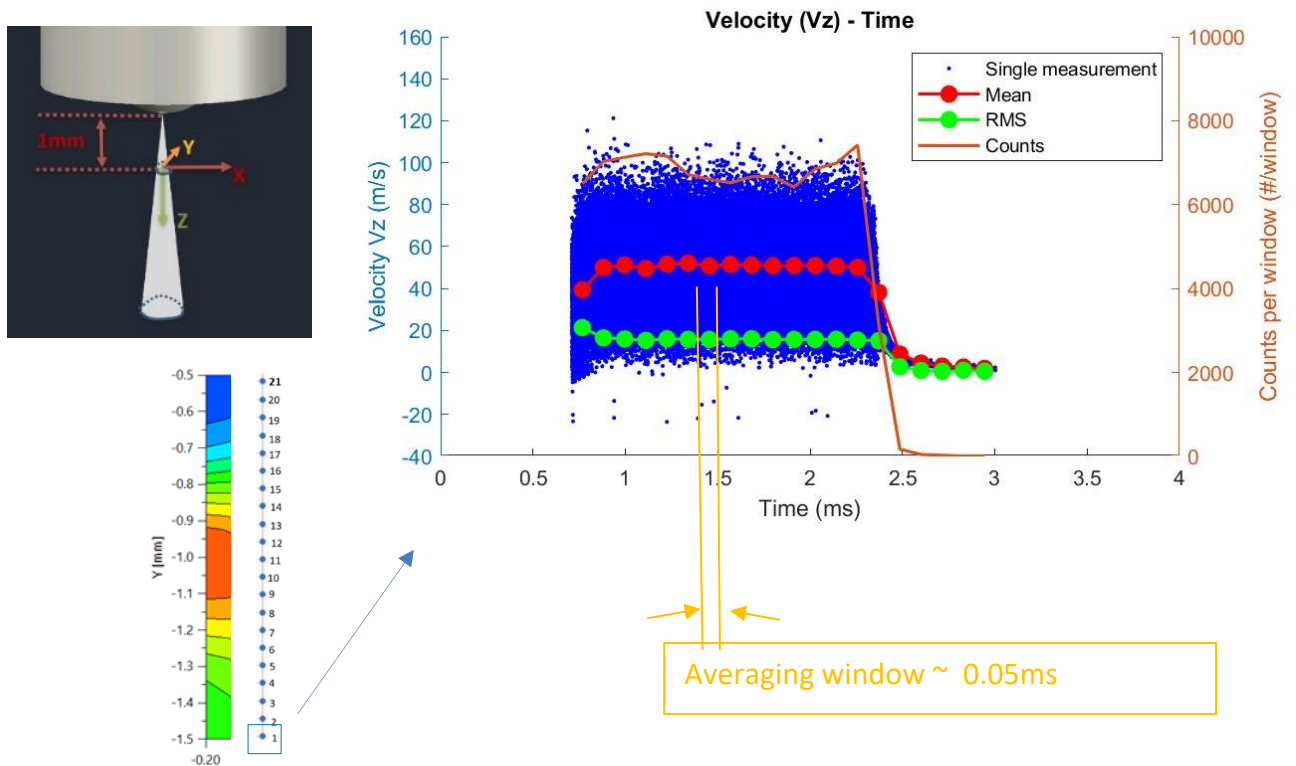
Figure 4-40 Examples of instantaneous variation of droplets velocity and definitions of temporal ensemble average over a time window of 0.05ms.

It is also useful to note that during the injection, there are normally 3 different phase which are referred to needle opening phase, main injection event and needle closing events which are shown in figure 4-41.
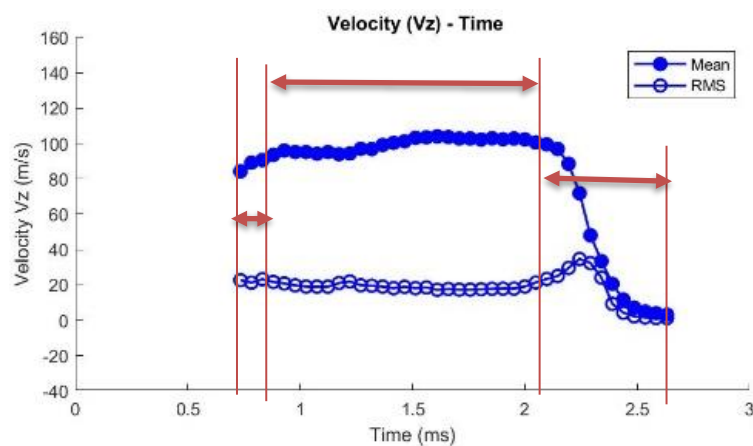
Figure 4-41 Different phase of the injection events referred to as 1. needle opening event, 2. Main injection event, 3. Needle closing event

4.15 Error Analysis and statistical method for PDA system

There are several sources of uncertainty in laser-Doppler anemometry which will cause a wider probability density function of Doppler frequency than compared to the velocity. These uncertainties are:

- Mean velocity gradient broadening,
- Small scale turbulence broadening (length scale),
- Finite transit time broadening (time scale),
- Brownian motion (random trajectory) ,
- Line width of laser
- Electronics characteristics and noise.

There are also sources of systematic error such as:

- The velocity biasing error
- The orientation of the laser beams relative to the geometry
- Positional error introduced by the milling table
- Visual procedure error when locating the measuring volume at a given reference point.

The total Doppler variance σ_T^2 equals the sum of the velocity variance and broadening effects and, assuming total independence and randomness of its constitutive terms, is given by:

$$\sigma^2_T = \sigma^2_{velocity} + \sigma^2_{broadening} \qquad\qquad since\ \sigma^2(x+y) = \sigma^2 x + \sigma^2 y$$

And

$$\sigma^2_{broadening} = \sigma^2_{mean\ gradient} + \sigma^2_{turbulence} + \sigma^2_{Finite\ transit\ time} + \sigma^2_{Brownian} + \sigma^2_{Laser} + \sigma^2_{instrument} + \sigma^2_{others}$$

Mean velocity gradients lead to a broadening of probability density function across the measuring volume and to a mean velocity bias which, according to Durst et. al. (1981), can be corrected, respectively, via

$$\sigma^2 mean\ velocity\ gradient = \left(\frac{l_m}{4}\right)^2 \left(\frac{dU}{dr}\right)^2 + \cdots ..$$ **Equation 9**

$$U\ true - U\ measured = \left(\frac{l_m}{4}\right)^2 + \frac{d^2 U}{dr^2} .....$$ **Equation 10**

where the higher order terms of the expansions are negligible. As it is evident, these broadenings are important in the region where the velocity gradient is strongest like near the wall regions. In the current investigation, these effects were negligible as the measurements inside the spray were mainly at the locations where the velocity gradient in the probing volume was minimum.

Turbulence intensifies the finite transit time broadening in frequency domain instruments. A second turbulent effect results from the small-scale turbulent fluctuations in velocity within the probing volume and can be accounted by:

$$\sigma^2 turbulence = \frac{2}{15}\left(\frac{l_m}{4}\right)^2 \left(\frac{4\pi \sin\varphi}{\lambda}\right)^2 \frac{\varepsilon}{\nu}$$ **Equation 11**

where ε is the energy dissipation rate per mass, for a small angle ϕ, ν is the kinematic eddy viscosity, lm is the Prandtl's mixing length and assuming local and a scattering volume size of the order of the Kolmogorov length scale (smallest length scale in the system).

Finite transit time broadening occurs when more than one particle is within the measuring volume but is limited in frequency counting system. Using a slit of 100μm in the receiving optics will limit the scattering volume to be focused at the centre of the probing uniform. Beside this, utilizing an appropriate validation circuitry with 2 planar detectors for transverse measurement in the current system will ensure that only one particle within the scattering volume will be validated.

Broadening introduced by the deviation of the laser light from monochromatic is negligible in this experiment since the laser light is indeed monochromatic with wavelength of 514nm and 488nm.

Broadening by the Brownian motion is important for very slow laminar flows and since the nature of the flow here in this experiment is turbulent this broadening is also negligible.

In addition to above, velocity bias effects can be significant in turbulent flow measurement when ensemble averaging is used to calculate the mean velocities. Particles of higher velocity will cross the measuring volume more than those of low velocity, and therefore the calculated velocity becomes biased toward higher value. This was shown by McLaughlin and Tiederman (1973). A one directional correction shows negligible error for turbulence intensities up to 15% but an error of 10% for a turbulence intensity of around 40%. Therefore, bias corrections have to take into account the duration of the burst, the particle arrival rate and its relation to turbulence time scale (Durst et al (1981)) but these calculation are out of scope of this work.

It should be mentioned however that ensemble averaging is an accurate estimate of time averaging whenever the time scale of the particle arrival rate is less than the turbulent integral time scale if sampling technique and velocity are uncorrelated or if the sampling time scale is much greater than the turbulent integral scale. Under other conditions an appropriate sampling technique will be necessary to remove the correlation between velocity time consuming an alternative is the use of a time weighting approach such as that one proposed by Dimotakis (1976)

$$\overline{U} = \frac{\sum_{K=1}^{N_S} \left(U_K \Delta t_K \right)}{\sum_{K=1}^{n} \left(\Delta t_K \right)}$$

Equation 12

Where Δt_K is the duration of the Doppler signal when its amplitude varies from maximum to half maximum.

Another source of bias, but in the opposite direction, is introduced by the existence of a correlation between Doppler frequency (velocity) measured by the photomultiplier and the particles residence time inside the measuring volume. That is to say that the fast moving droplets with small residence time produce low Doppler signal amplitudes, while the slow moving droplets with large residence time produce large signal amplitudes, and therefore biasing velocities

towards lower values, as shown by Durão and Whitelaw (1979). Both effects are opposite and become negligible when taken together for a wide range of flows and relationships between particle, sampling and turbulent time scales, as illustrated in Durão et al (1980). Vafidis (1985) used the above equation and reported a mean velocity bias of +2% and a 5% broadening of the rms velocities in regions of high turbulence when comparing with non-corrected data.

In this study the turbulence intensity for measurement of the near-nozzle to far-field region of the spray was lower than 20%. Therefore, for the measurement of spray droplet velocities, the uncertainties of both velocity biasing effects are small and negligible.

The gradual definition of cut-off frequencies in band pass filters means that its misuse is another source of bias because signal that might lie outside bandwidth or very close to the edges will not be considered. In the present systems, passive band pass filters were used with sharp cut-off edges and therefore this biasing effect was negligible. At the same time, the signals pdf distributions were monitored all the time to ensure all the Doppler frequencies are detected.

The relative statistical error of a sample of finite size on both mean and rms velocities can be estimated by Gaussian velocity probability function by

$$Error_{mean} = Z_C \frac{u'}{\sqrt{N_S}}$$ **Equation 13**

$$Error_{rms} = Z_C \frac{1}{\sqrt{2N_S}}$$ **Equation 14**

Where N_S and u' are the sample size and turbulence intensity with Z_C=1.98 for 95% confidence level, Yanta and Smith [95]. In the present measurements the number of samples per measuring point were of order 3000 to 6000 (for example see distance of 10mm) giving a maximum statistical error of 0.73% in the ensembled mean and 2.5% in the rms of the velocity fluctuations for a 20% turbulence intensity.

There are axial and radial positional errors due to the method used to locate the control volume inside measuring region. This relies on visual observation of the beam crossing at a reference

point, which can lead to an uncertainty of about 1/8 th of the measuring volume length, i.e. 50μm; here the method of positioning the reference point was improved this error by 400% compared to Andrea Marchi experiment where the positional errors were 200μm. The tip of the injector (lowest part of the injector nose) was used as the reference point for all measurements at each distance. The movement of traverse was monitored in all three directions with digital gauges with a resolution of ±50μm.

4.15.1 PDA, size accuracy

Droplet diameter measurements were collected continuously over many injection cycles. The ensemble-averages were then calculated using a Matlab code over a time window of 0.1 ms which was found to be sufficient to resolve temporal changes of the fluctuations in the droplet diameters. The total number of samples in each position of the measurements varied from 50,000 to 100,000, and the number of validated samples in the 0.1 ms time interval varied from 3000 to 6000 samples with maximum statistical uncertainties of around 2% in the ensembled mean and 5.6% in the rms values.

Wigley (1993) and Hardalupas et al (1994) have explained in details the uncertainties and limitation associated with the PDA measurements. An important source of uncertainty in the near-injector region was the attenuation of the laser beams and the scattered light due to high concentrations of droplets. The phase-Doppler results have presumption that droplets are spherical and, since sprays are known to include ligaments in the near field, this is a potential source of uncertainty very close to the injector. The verification system of the counter should have rejected non-spherical droplets and only accepted droplets with sphericity of up to 90%. This was confirmed by phase diagrams which shows the rate of rejection of the non-valid measurements. In order to minimize the beam and scattered light attenuation, an injector stand holder was designed and assembled to set up the injector orientation accurately; this arrangement made great improvement in data collection in the core spray near the exit nozzle as demonstrated in the results section.

In the present study a four Photomultipliers (PM) system (Dual PDA Dantec dynamics) was used to maintain a high measurement resolution and to remove measurements ambiguity. This was a significant improvement compared to all previous measurements done in the group since all the previous measurements were using 3 PM and was not utilizing coincidence validation. With this system, the same droplet size was measured twice with two different pairs of PMs positioned at two different locations. One PM pair (1 and 2) was positioned with relatively large separation from each other in the vertical direction to provide very high sensitivity (resolution) and smaller size range, while the other pair (3 and 4) had a shorter separation with larger size range and lower resolution. With this arrangement, two independent size measurements, the 2π-jump uncertainty (an inherent problem with PDA system) is fully removed and the ambiguity of the droplets sphericity will be minimised. The later depended on the validation level which can be set by the user; in this experiment a tolerance of about 5 to 10% was used between the two set of size measurements and implies the level of ambiguity in droplets sphericity.

There are other minor sources of uncertainties like oscillations in phase-diameter curve, low signal-to-noise ratio due to low intensity or extinction which can introduce biasing towards larger droplet size, Gaussian intensity profile in the measurement volume and phase changes which can be due to droplet surface distortions and multiple scattering effects. All these effects can be minimise by proper set up of the transmitting and receiving optics as described in PDA setup in this chapter.

Chapter 5: In-nozzle Flow Measurement in Enlarged Model Injectors

5.1   Introduction

Although the importance of cavitation inside multi-hole injectors has been addressed in many previous investigations where the cavitation formation and its development, fuel spray characteristics and atomisation have been reported, the effect of cavitation (both geometrical and vortex structures) on the emerging jet spray and its stability, liquid breakup and atomisation is not yet fully understood. A part of the current research work was then focused to address some of the above issues by conducting an experimental study on the initiation and development of different type of cavitation inside two 3-D transparent enlarged models (7- and 15-times) of symmetric 6-hole conventional SIDI injectors. The aims are to quantify the effects of the cavitation on the near nozzle jet spray in terms of jet cone angle and its stability and to visualize the near-nozzle spray as it emerges from the nozzle into the stepped-hole section of the injector or into the ambient atmosphere. Special attention has been paid to design the optical model injectors to allow simultaneous imaging of the in-nozzle flow and the exiting spray jet to be able to establish the influence of in-nozzle cavitation on the emerging jet spray. Thus, High speed camera has been used to visualize the in-nozzle flow and emerging spray simultaneously with images of high clarity and resolution. In the first section of the chapter, the results of visualization of in-nozzle flow and near-nozzle spray in 15-times enlarged model injector is presented and discussed first. In this regard, the 15 times enlarged model has a stepped-section through which the near-nozzle exit spray could be visualized too. It was found in the 15 times transparent model that for some cases, the stepped section has limitations for visualizing the near-nozzle emerging spray. Therefore, in the second part of the chapter, the results of visualization of the in-nozzle flow and near-nozzle spray will be discussed and explained in the 7-times enlarged model which does not have a stepped section but has the advantage of a unique design which provides for the first time, good quality image for simultaneous in-nozzle flow and near-nozzle jet spray. Finally, the link between

the in-nozzle flow on the near-nozzle spray in the stepped hole will be anticipated and established. It is expected that the stepped-nozzle would improve the performance of the breakup/atomisation processes due to the fuel flow going through sudden expansion within the confined stepped that promotes the turbulence and interaction with surrounding air. This plus the burst of the cavitation bubbles would help earlier breakup of the fuel and lead to rapid atomisation in the stepped section of the nozzle.

5.2   Results for 15 times enlarged model

In this section, in-nozzle flow including the geometrical and vortex cavitation structures together with the emerging liquid spray jet are visualised using a high-speed camera in a 15 times 3-D enlarged transparent model as described in methodology chapter. The results obtained from the enlarged model test rig are presented and discussed in the following order; first the cavitation development at different needle lifts and cavitation number, CN, is investigated. This will be followed by the identification of geometrical cavitation and the string cavitation in the nozzle and how these types of cavitation can cause erosion and material wear. In the next step, the effect of geometric and vortical cavitation on the emerging spray and cone angle will be presented followed by some analysis on the emerging jet spray.

5.2.1   Cavitation Development

Figure 5-1 shows cavitation development as a function of CN for the lowest measured lift (quarter lift, left column) and at full lift (right column). Here the injection pressure was kept the same for both needle lifts which has caused a smaller Reynolds number at the lower lift due to flow losses through much smaller flow passages between the needle and injector body. All results are given in figure 5-1. The results at CN = 1.04 and at the quarter lift show no sign of cavitation at this lift which is in agreement with all previous results obtained in similar geometry. As CN is increased the geometric cavitation and string cavitation are developing inside the nozzle so that at CN=4.15, the geometric cavitation and string cavitation are covering up to half of the length of the nozzle and at CN= 5.22 they are fully developed covering the whole length of the nozzle hole with the formation of the well-known horse shoe film cavitation. The results at full lift (right column) and CN=1.04 show no obvious geometric cavitation apart from occasional pockets of vapour which

was absent at the quarter of lift, and therefore this cavitation number was taken as the onset of the cavitation. In addition, a persistence narrow vortex was observed at full lift which was fully developed along the nozzle and originated from the sac volume. This suggests that increasing needle lift will increase the flow momentum and its turbulence within the sac, which allow the vortices to gain more speed (strength) and forcing it to loss pressure at its core to cavitate.. Increasing the cavitation number from 1.04 to 2.09 will dramatically change the cavitaton regimes inside the nozzle so that at CN=2.09, the geometric cavitation is almost fully developed covering up to the exit of the nozzle as well as a strong string cavitation along the axis of the nozzle. At higher cavitation numbers, CN=3.12 and higher, the flow becomes fully developed and a line of separation is clearly visible on the flow inside the nozzle hole which indicates the envelope of the horse shoe film cavitation. It is also clear that the extension of both geometrical and vortex cavitations to the exit of the nozzle has affected the jet spray shape and trajectory.
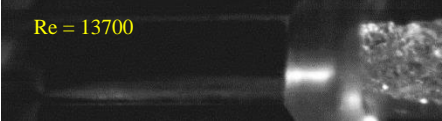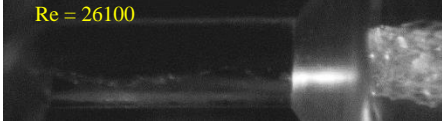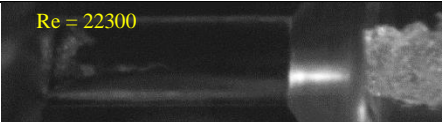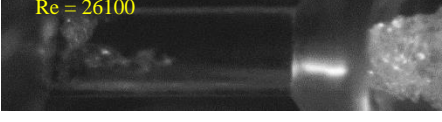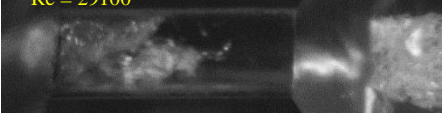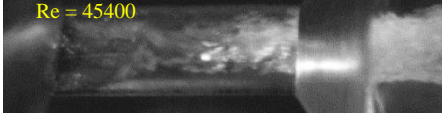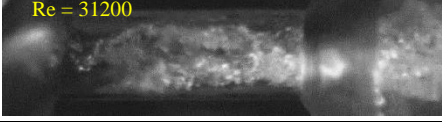
L/D=2.7		Needle Lift	
		¼ lift	Full lift
Injection Pressure (bar) And CN Number	P=1 CN=1.04	Re = 13700	Re = 26100
	P=2 CN=2.09	Re = 22300	Re = 35700
	P=3 CN=3.12	Re = 26100	Re = 40700
	P=4 CN= 4.15	Re = 29100	Re = 45400
	P=5 CN=5.22	Re = 31200	Re = 50300

Figure 5-1. Cavitation development at quarter lift (left column) and full lift (right column) at different CNs.

The results are in agreement with previous studies in similar geometry and that the comparison between the quarter and full lifts shows a clear delay in the onset of the cavitation and its

development with the quarter of the lift (lowest measured) at all measured CN numbers which may be due to considerable loss of flow (axial and radial) momentum. This could be due to much narrower flow passage that increased friction loss and hence suppression of turbulence inside the sac volume and nozzle hole, which in turn will affect the pressure gradient and therefore the formation and development of cavitation. The more turbulent the flow is, the Reynolds number will be higher and this means the cavitation number will also be higher based on our definition. This means the flow is more likely to form cavitation. Another useful observation is on the emerging spray with CN so that the jet spray becomes brighter as the CN increases. This suggests that cavitation enhances liquid jet break up/atomization and thus improving the intensity of the scattered light. This is expected as at higher CN more bubbles collapse inside the nozzle and also as they exit from the nozzle which will help and accelerate the liquid breakup outside and consequently better atomization however cavitation can sometimes lead to instability which can cause poor atomisation. It should also be mentioned that cavitation can sometimes cause instability in the spray structure and might create poorer atomization.

5.2.2 Geometrical cavitation

The following image sequences, presented in figure 5-2, characterise the behavior of geometrical cavitation bubbles of the upper left side of the nozzle when they interact and trap within the recirculation zone. The recirculation zone can clearly be seen to have a suction effect (which is caused by the recirculation zones and the pressure drop at the top left corner of the nozzle).Here the highlighted bubble (dashed circle) is trapped within the low pressure zone and moves in the opposite to the direction of the mean fluid flow due to the presence of the adverse pressure gradient near the wall forcing the flow moves towards the nozzle entrance.. The velocity vector remains horizontal, which suggests that the highest vapour fraction is at the top edge of the nozzle entry. The backward movement of the bubble without tangential motion indicates the maximum recirculation at the top of the nozzle.
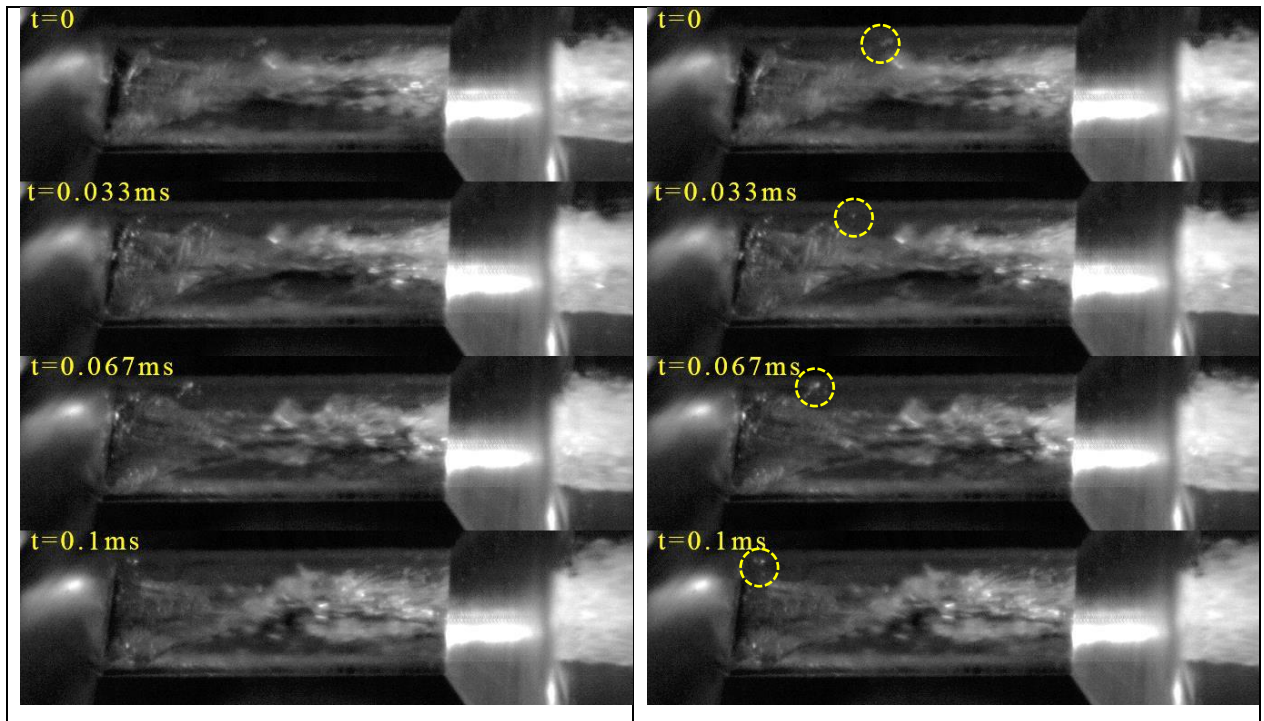
Figure 5-2. Image sequences of in-nozzle flow cavitation and spray at full lift, P5 (V1), Re=50200, CN=5.22.
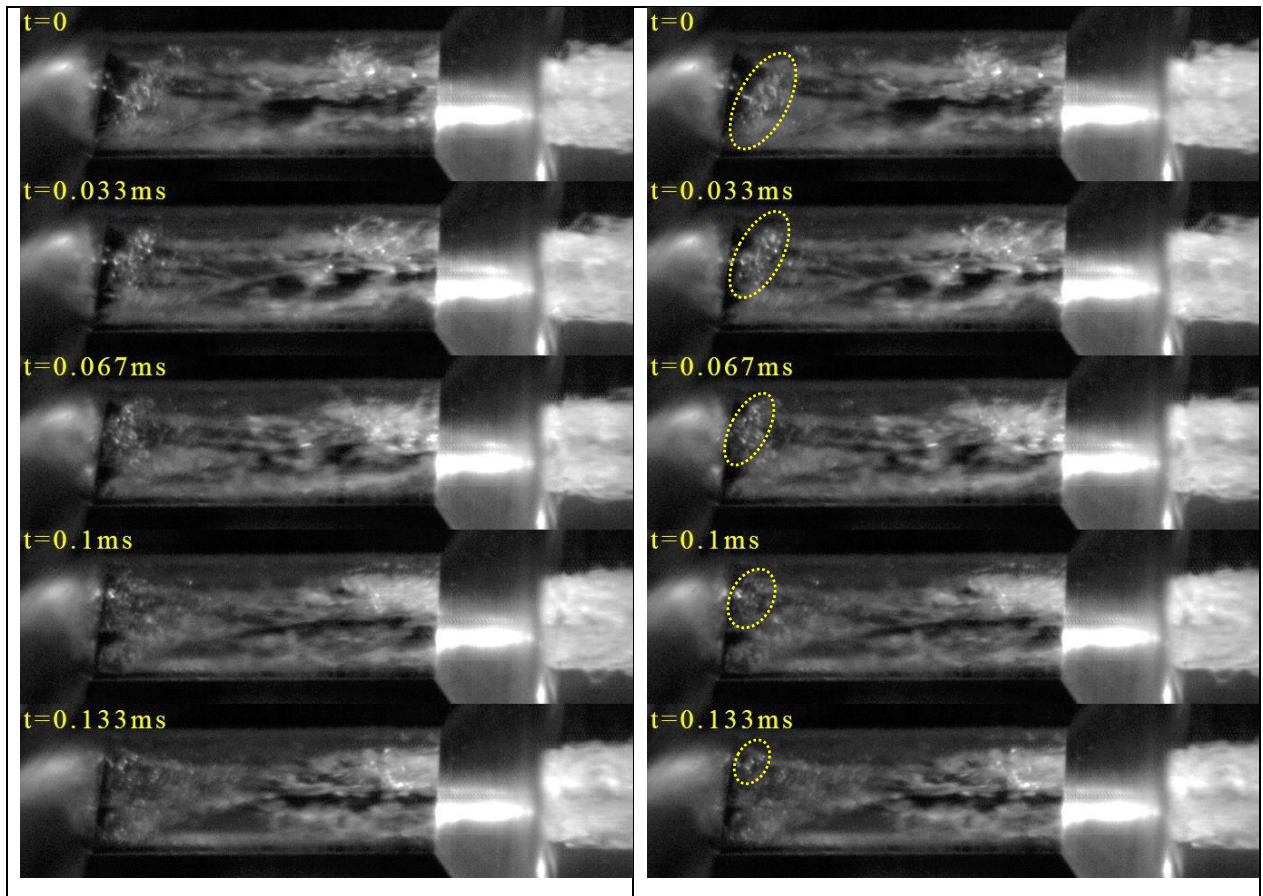
Figure 5-3. Image sequences of in-nozzle flow cavitation and spray at full lift, P4 (V2), Re=45300, CN=4.15,

Similarly in Figure 5-3, the sequence of images show that the highlighted bubbles generated near the nozzle entrance on the envelope of the horse shoe film cavitation are convected towards the low pressure zone near to upper part of the nozzle wall. These are moving upwards and towards the recirculation zone having almost no horizontal component of velocity vector. This may imply suction generated by the low pressure zone, although exclusion of the string vortex cavity causing a circumferential motion on the bubbles may not be discarded.
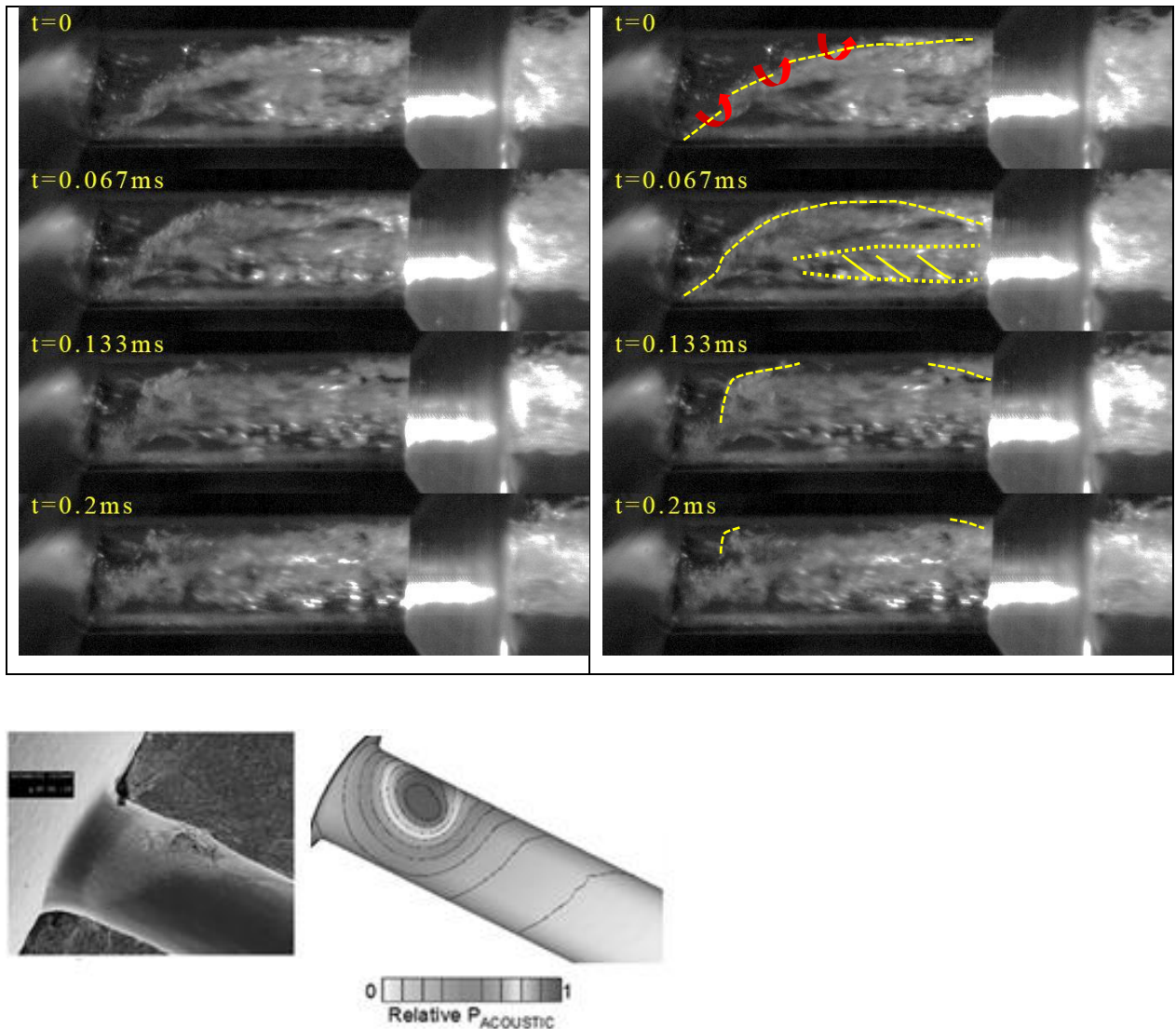
Figure 5-4. Left: Impact of the vortex cavitation on geometric at Full Lift, P4, bar CN = 4.15, and Re=45300; possible erosion. Right: SEM of cavitation erosion inside the nozzle hole and the relative acoustic pressure [26]

Another interesting observation was the interaction between the geometrical and vortex cavitation and an example is presented in Figure 5-4, which clearly shows the displacement and rolling of the leading edge of the geometric cavitation on the top surface near the hole entry at full lift, P=4 bar, bar CN = 4.15, and Re=45300. It shows that at t=0ms the edge of the envelope of the horseshoe film cavitation is rolling up forming a string along its edge. This can well be due to the interaction between the horseshoe film cavitation along the upper part of the nozzle hole and the strong vortex cavitation along the core of the nozzle hole. At t=0.067ms the newly formed

string along the edge of the horseshoe cavitation becomes stronger and shifted up towards the upper wall surface zone in the recirculation region. At t=0.133ms, the string is shifted further up towards the top of the nozzle. Also at t=0.067s and 0.133s, the presence of a large corkscrew vortex cavitation is clearly evident which appears at the lower part of the nozzle hole with large tangential velocity component and carries a considerable momentum thus affecting flow around it, turning the horseshoe cavitation clockwise and dispersing any other smaller bubbles tangentially towards the top of the nozzle as well as along it. The tangential shift of the geometrical cavitation around the nozzle hole axis caused by this vortex is apparent from the images over 0.2ms time lapse over which the whole structure of the horseshoe film cavitation has been changed. Such events occur periodically, perhaps due to the main vortex having a period of its own depending on its strength and size which varies from time to time and affects the in-nozzle flow accordingly and create more flow instability. In addition, it is expected that during such intermittent periods (when the horseshoe cavitation undergoes such drastic changes including shifting up towards the upper wall surface, deformation and break down) the newly formed smaller strings and bubbles will burst as they get close to the upper wall causing localised erosion on the upper nozzle surface as shown by [26]. This has been further investigated on another possibility of bubble burst and the results are shown in Figure 5-5.

Figure 5-5 shows the displacement and possible impact of bubble pockets on the top surface of the nozzle at full lift, P = 4 bar, CN = 4.12, and Re=45400. Here, in both cases at different instances, bubbles generated in the near inlet nozzle region are tracked in 4 consecutive images over 0.1ms time. These pockets of bubbles are moving upwards towards the upper wall surface zone having almost no horizontal component of the velocity vector. The observed movement suggests that the bubble pockets propagate vertically upwards in the near entry region of the nozzle. It is obvious that the flow inside the nozzle has components in all three directions since the flow is 3 dimensional with all axial, radial, and tangential components of velocity around a vortex. Since the flow imaging has been obtained using a single camera, the observed flow is only in two dimensions. Thus, it can be concluded that the bubble motion observed is the combination of axial and tangential component of the velocity vector. A simple velocity calculation was made from images of Figures 5-5 using Photron Fastcam software, when a distinct bubble pocket was

tracked crossing the centre line of the nozzle. The vertical (or tangential) velocity of the bubble pocket was found to be almost 20m/s whereas the mean axial velocity calculated from the flow rate measurement was 17.14 m/s. This may imply that the main vortex having a relatively strong tangential velocity would affect the bubbles movement when they are entering the nozzle inlet forcing them to move upwards towards the upper surface and their possible burst as they get close to the wall. This again may suggest that the vortex rotation would bring more bubbles available to the vicinity of the maximum erosion which has been observed by SEM in another nozzle hole as it is shown in figure 5-4.

t = 0.000ms

t = 0.033ms

t = 0.066ms

t = 0.100ms
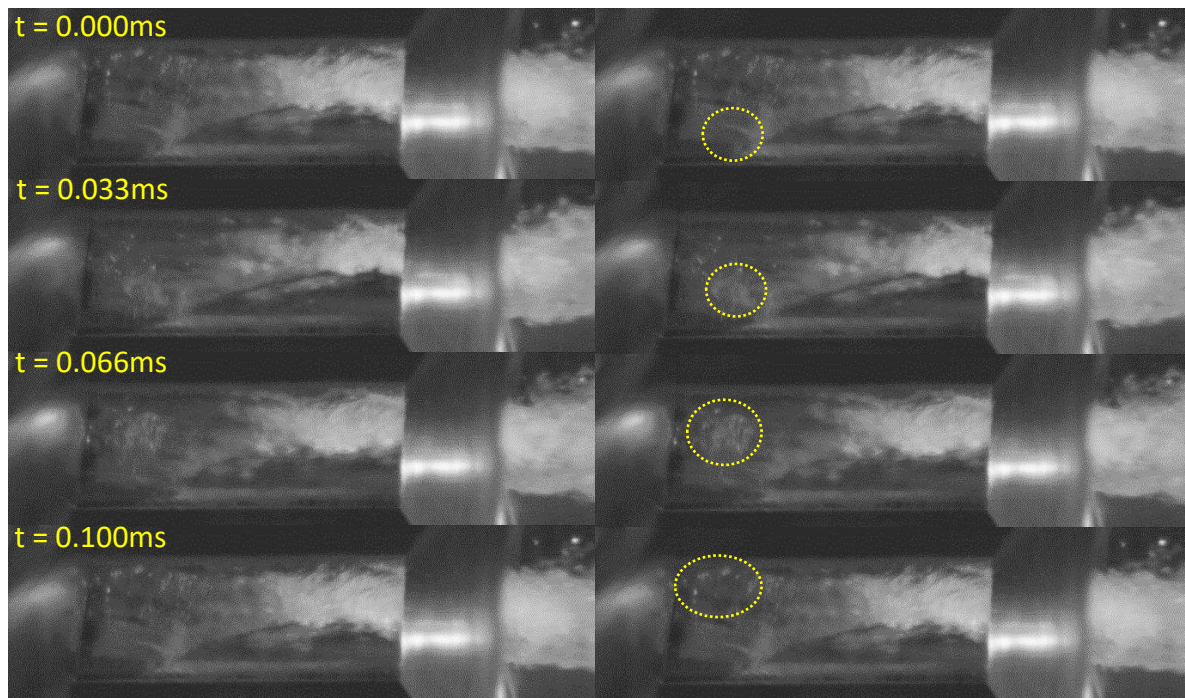
Figure 5-5. Left: Cavitation film break up and possible impact of bubble pockets to the top surface at full Lift, P = 4 bar, CN = 4.12, and Re=45400; Right: Cavitation break up at the nozzle entrance and possible migration of the bubble pockets towards the top corner of the nozzle hole.

The velocity of the bubbles are very significant and of similar order of the flow itself. When the bubble burst through micro-burst process with velocities much higher (by order of magnitude) when they get near the surface where the pressure in recovered their possible impact would result on further erosion. In a real-size nozzle, periodic burst of the bubble pockets entering the nozzle on the top surface can contribute to erosion in that region due to high velocity impact (over 100m/s). It should be mentioned that flow inside a nozzle is very sensitive to the design of

the sac volume and that SEM of the real-size nozzle will provide a better comparison regarding the maximum erosion region.

Figure 5-6 shows an instant that two counter (highlighted) rotating vortex cavitation coexist at the same time inside the nozzle hole originated from the top and bottom side of the nozzle at the inlet and get closer together as they convected downstream so that they almost merged together nearer to the exit. It is difficult to locate the origin of these vortices at the inlet but by comparing this with SEM image of cavitation erosion at the nozzle entrance [26] , shown on the right of Figure 5-6, it can be speculate that one of these vortex is likely to be developed at 3 o'clock position and the other at 9 o'clock position around nozzle entry within the sac volume. Although the SEM image is from another nozzle with slightly different sac volume design, it could be seen that the two counter rotating vortices might be responsible for this type of erosion.
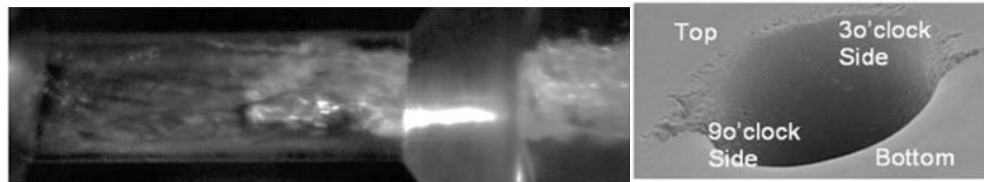
Figure 5-6. Left: Two counter rotating strings developed inside the nozzle hole at Full Lift, P = 4 bar, CN = 4.15, and Re=45300, Right: SEM image of cavitation erosion at the nozzle entrance [26]

5.2.3 Effect of cavitation on the emerging spray angles

Investigations have suggested that string cavitation can alter the spray cone angle and can induce instability in the spray pattern [4]. Effects of string formation on the spray cone angle were further analysed to acquire any link between such vortex structure development and the change in the near-nozzle spray pattern.

Figure 5-7 shows the position of the strings inside the nozzle hole affecting the spray axis angle and cone angle at full lift for low CN (left). The column shows the directionality of a vortex at low CN number and its link to spray axis and cone angle. At CN=1.05, in the first image (t=0) the string is aligned almost horizontally along the centreline of the nozzle. It was observed, for all similar cases, that the resulting cone angle has an axis parallel to that of the nozzle or string. In the second image (t=0.333ms) the string is tilted downwards so that the downstream part of the string is close to the bottom of nozzle exit. The result shows that the spray cone axis has also tilted downwards below the original nozzle axis. In the third image, (t=7ms), the downstream part of

the string pointing towards the top of nozzle exit and it shows that the spray cone axis has tilted above the original axis. Therefore, this behaviour might suggest that the spray cone angle being affected by the directionality of induced string cavitation.
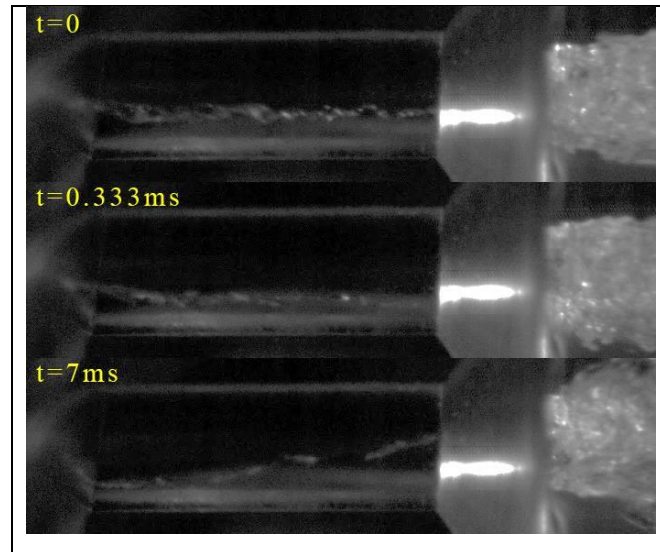
Figure 5-7. Directionality of the vortex cavitation and its effect on spray at Full Lift for: CN=1.05, P=1 bar and Re=26100;

It is interesting to note that more liquid breakup can be seen on the lower edge of the emerging spray in the second image and on the upper edge of the emerging spray in the third images which are corresponded to the locations of the exiting strings. Vortex axis carries radial momentum with lowest pressure observed at the centre of such vortex producing string cavitation. Therefore, wherever string cavitation is seen the vortex effects become visible. Tilt of vortex away from spray cone axis results in spray cone axis angle being altered in the same direction.

5.2.4 Reverse Vortex Structure

At injection to atmosphere at low cavitation numbers, with no geometrical cavitation, a transient reverse vortex structure was found to be initiated outside the nozzle near its exit in tenth of a millisecond and moved into nozzle towards its inlet and developed/ and maintained its structure inside the nozzle for several milliseconds. This vortex structure was randomly appeared in the nozzle due to its transient nature. The reverse vortex advances and grows, in the absence of the geometric cavitation. This phenomenon is an air entrainment into the nozzle from exit

rather than cavitation. The mechanism is related to the presence of a vortical structure of the liquid flow inside the nozzle [2, 4]; this usually happens when the liquid flow entering into nozzle from sac volume has different velocities (momentums) around the nozzle inlet. The reverse air entrainment occurs when the pressure in the core of vortex drops below atmospheric pressure and allows the air to be sucked into the nozzle from the exit.

Figure 5-8 describes the development of reverse vortex structure at different time sequence and quarter needle lift, 0.85bar injection pressure and CN=0.88. This structure develops in cavitation numbers below 1, which signifies onset of cavitation generally. In the second image at t=0.33ms air starts to penetrate into the nozzle hole from the exit and move towards the inlet with time so that at a time t=2.33ms it passes the inlet and penetrates into the sac volume. It is interesting to note that, in this case, in fact there are two string structures coiled together as they move into the nozzle, which can clearly be observed in the images at t=1.0ms onwards. The two strings rotate in the same direction. There appears to be a phase difference of π radians between the two helically wound strings particularly at t= 1.66 and 2.33ms. This reverse vortex structure was even present at CN up to 1.77 at quarter needle lift without geometrical cavitation being observed. For cavitation numbers greater than 1.84 at quarter needle lift, no reverse vortex structure was detected. This is perhaps due to the fact that increasing the upstream pressure will result in a more uniform flow into the nozzle and weaken the strength of the liquid vortex, which in turn will increase of the pressure in the core of the vortex to above atmospheric and thus it would be much more difficult for the air to penetrate into the nozzle inside the vortical structure. That is why this phenomenon is much less frequent at full lift for the low CN and almost none at higher CN numbers.

Increasing the needle lift for the same low cavitation number seems to decrease the duration of the air entrainment and penetration inside the nozzle. This could be well due to the fact that increasing the needle lift will increase Reynolds number, which means higher momentum, better mixing and more turbulence in the flow within the sac volume. This suggests that the flow into the nozzle has a more uniform velocity around the nozzle inlet and therefore reducing the possibility of formation of the liquid vortex inside the nozzle and weakening its strength (or intensity). As a result this can allow a pressure recovery of the liquid vortex especially at its core

163

where the pressure is high enough to resist against the air being sucked into the nozzle from outside. Consequently the air wouldn't penetrate more easily into the nozzle hole and hence the duration of the penetration of such a structure will be decreased.

Effect of pressure on development of reverse vortex was examined by maintaining the needle lift at quarter lift and varying the pressure from 0.6 bar to 1.77 bar corresponding to CN numbers of 0.62 to 1.83, respectively. Although only individual cases were taken, without averaging, no correlation can be found between the injection pressure and the duration of penetration of such vortex development at lower cavitation numbers. Further observation showed that duration of such events can vary even in the very similar operating conditions.

Figure shows the development of air entrainment (reverse Vortex) Structure inside the nozzle at 1/4 lift, CN=1.04, Re=13700. It is suggested that the driving force that causes the air to have inverse flow is the pressure garadient between the ambient pressure outside the nozzle and the low pressure zone along the axis of the vortical structure inside the nozzle.
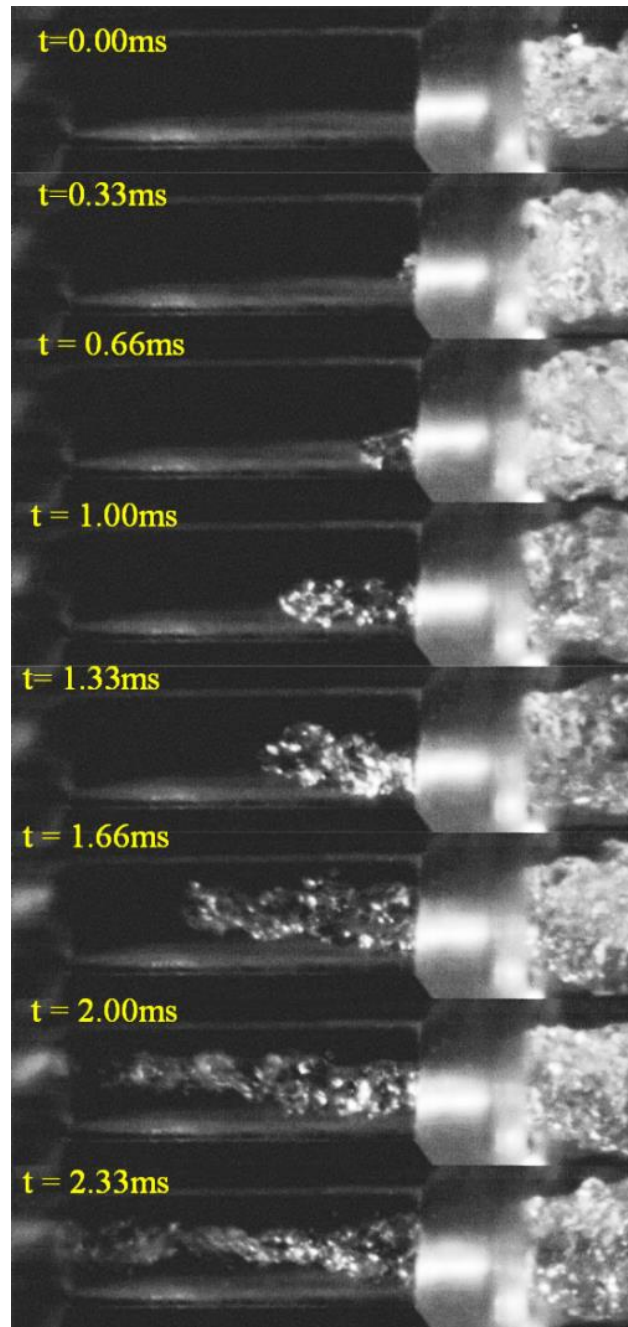
Figure 5-8. Development of air entrainment (reverse Vortex) Structure inside the nozzle at 1/4 lift, CN=1.04, Re=13700

Figures 5-9 and 5-10 shows the time sequence of two air entrainment structures developing inside the nozzle at the same condition of quarter lift and CN=1.04 and Re=13700, but at two different times t_1 and t_2. The left column shows air entrainment structure at t_1, in which one string can be identified. However, the second column, t_2, shows two helically wound strings, particularly at

t=1.3ms which suggests that there can be different modes of operations for these strings. The two strings rotate in the same direction.
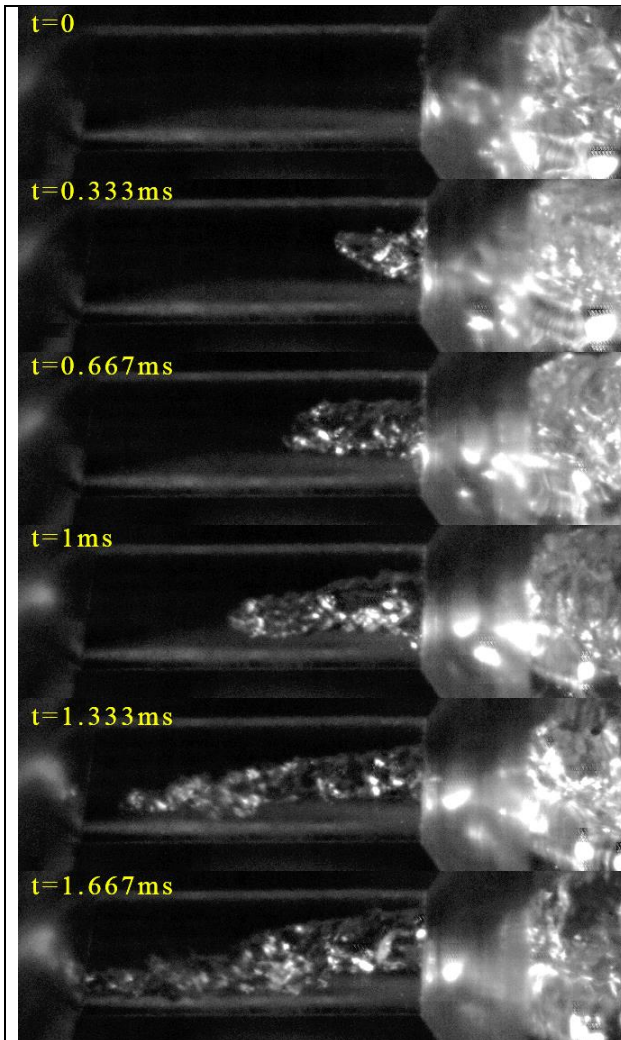
Figure 5-9. Images of air entrainment sequences at quarter lift, P1 (V1), Re=13700, CN=1.04, t_1=Frame: 5490-5540.
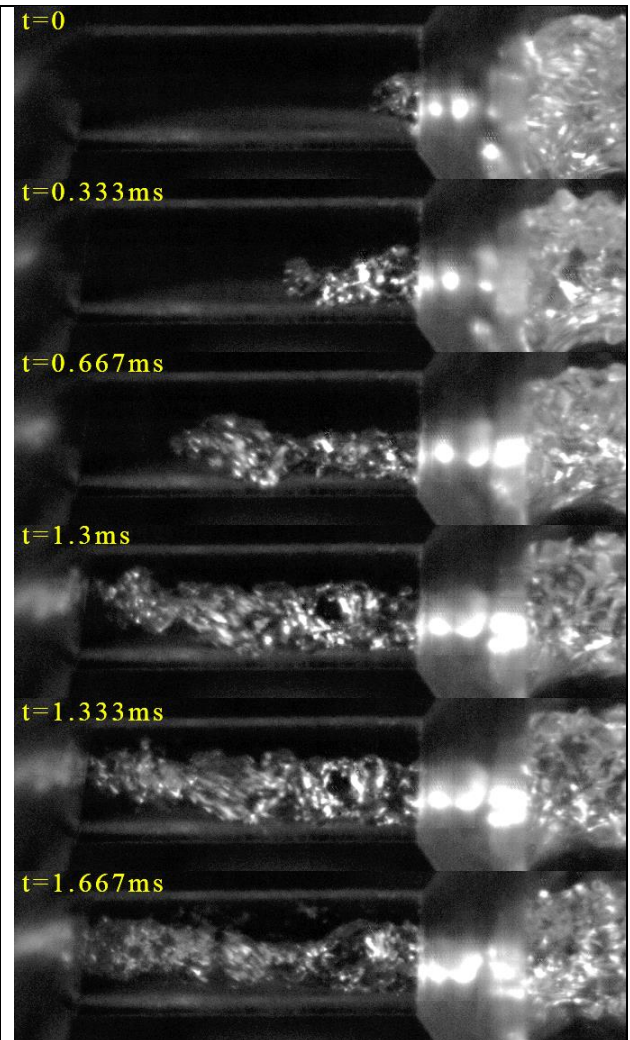
Figure 5-10. Images of air entrainment sequences at quarter lift, P1 (V1), Re=13700, CN=1.04, t_2=Frame: 890-930
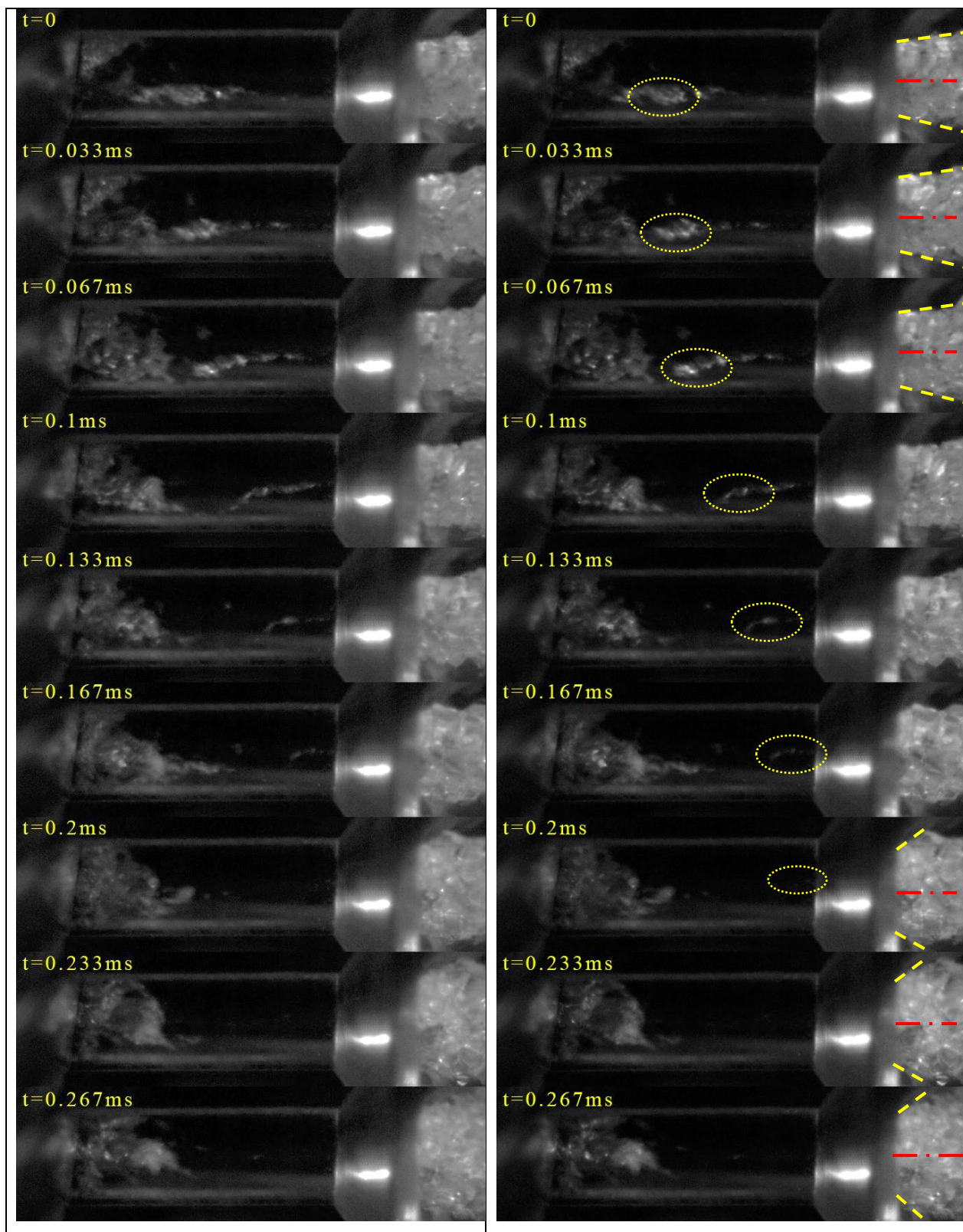
Figure 5-11. Image sequences of in-nozzle string cavitation and its impact on emerging spray at quarter lift, P3 (V1), Re=26100, CN=3.12, Frame 682-690

In Figure 5-11, a string is observed being generated at the nozzle entry, travelling towards the exit and entering the spray. The string is larger at the entry, shrinking towards the nozzle exit as expected due to pressure recovery in the region further downstream, causing the collapse some of the cavitating structure. However, the spray cone angle has been affected significantly when comparing frame t=0, when no cavitation can be observed at the exit, to frames t=0.2-0.267ms, when the string has entered the exit and the spray cone angle is significantly increased outwards. By measuring the cone angle an increase from approximately 20˚ to 60˚ is observed in the very near-nozzle area of the jet, caused by the string cavitation.
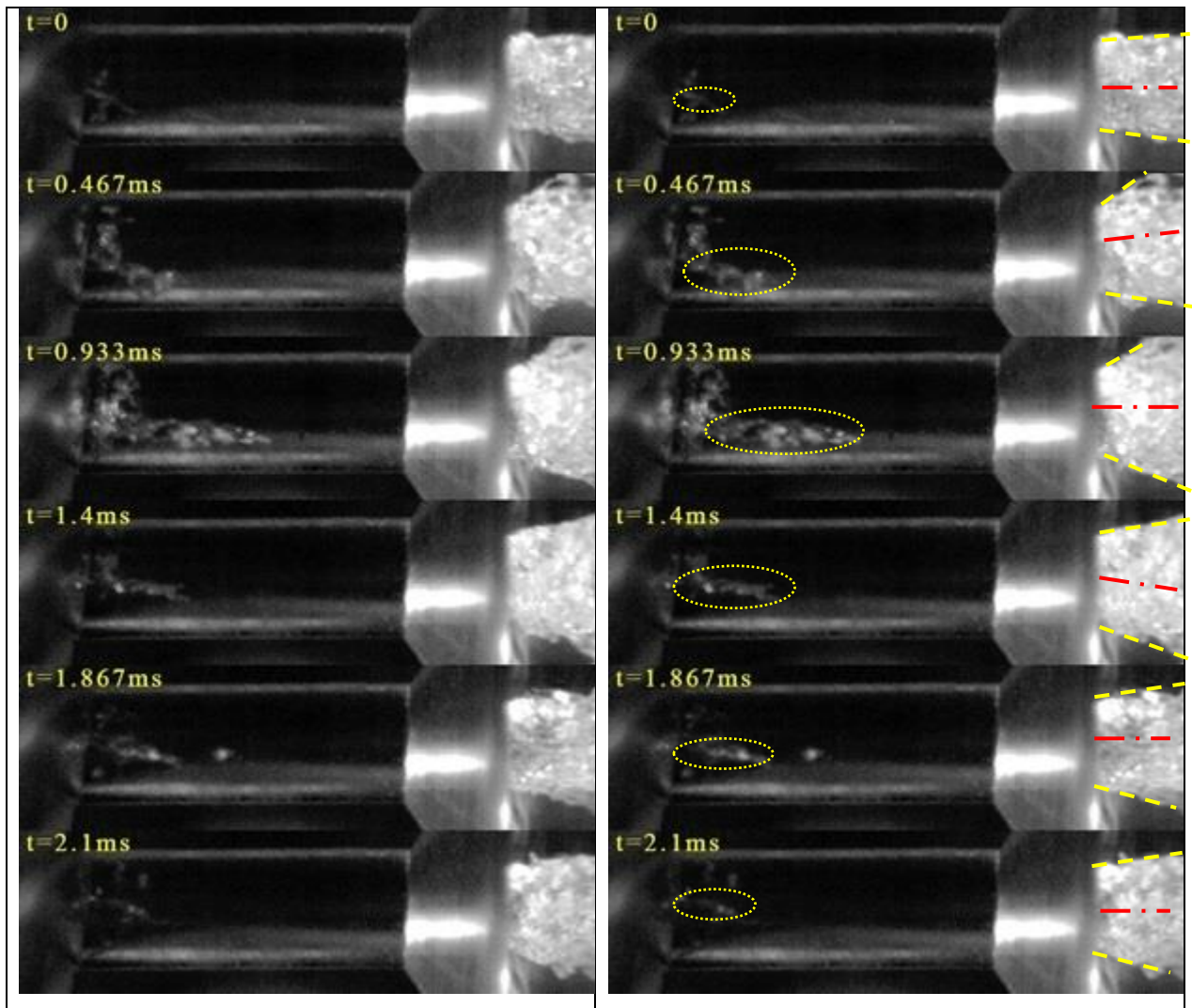
Figure 5-12. Image sequences of in-nozzle string cavitation and its impact on emerging spray at quarter lift, P2 (V2), Re=23300, CN=2.09, Frame: 2064-2128

In Figure 5-12, effect of string cavitation on emerging spray via the cone angle is observed. String begins to develop at t=0 with a spray cone angle of around 15⁰. The propagation of the string

towards the nozzle exit causes the spray cone angle to increase so that amaximum spray cone angle is observed at t=0.933ms of around 60º where the string is more developed and extended up to middle of the nozzle. In addition, the results show that the spray cone angle is correlated with the status of the string cavitation, for example, the spray angle at t=2.1ms is very similar to that of t=0 where the state of string cavity structures and its development are also similar. Thus, it is very evident that the string cavitation would clearly affect the emerging spray pattern and stability. Furthermore, the periodic fluctuations of the cone angle about the spray axis have clearly been observed causing an intermittent wave-like instability on spray pattern.
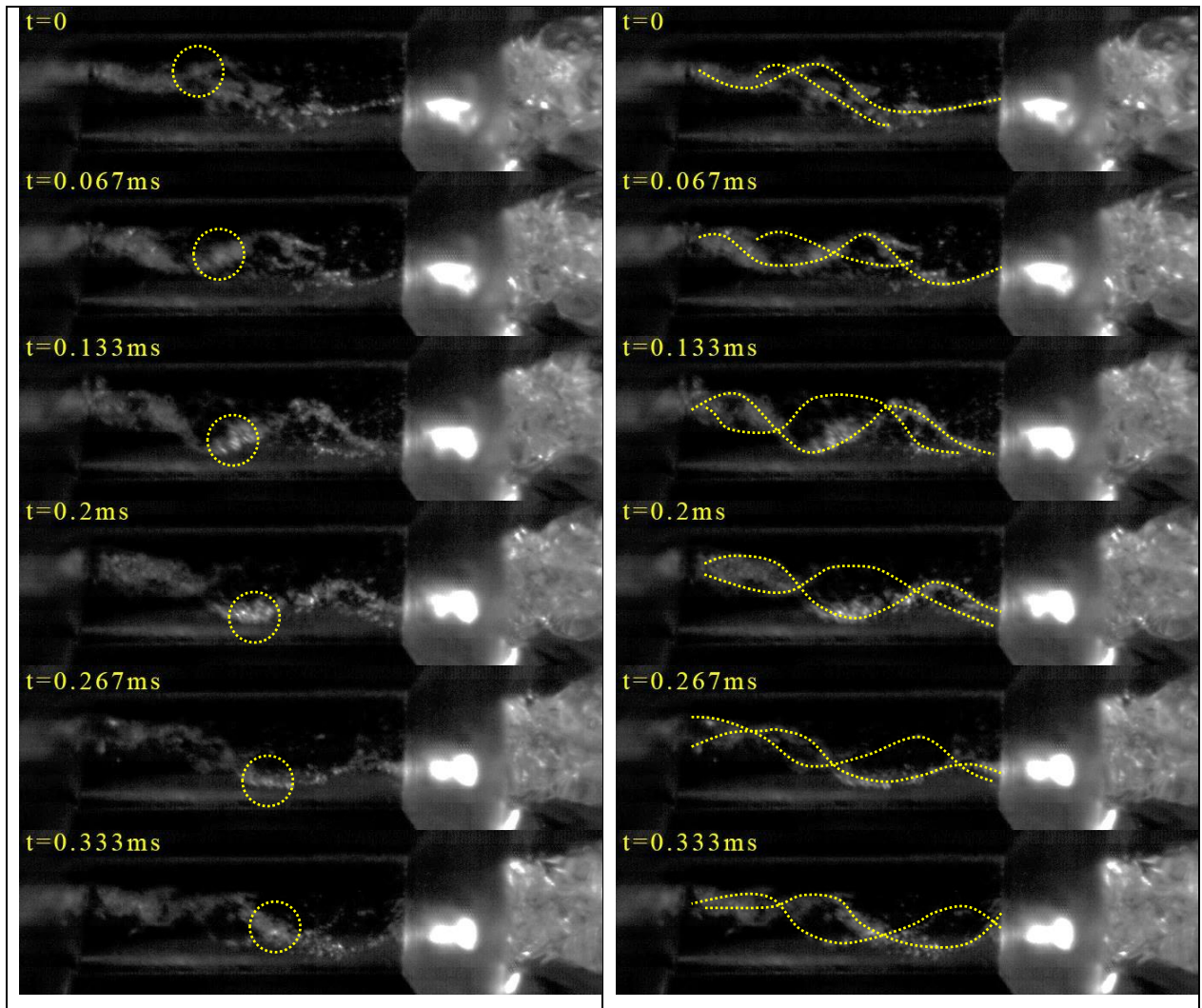
Figure 5-13. Image sequences of in-nozzle string cavitation and its impact on emerging spray at quarter lift, P1.77, Re=19500, CN=1.84, Frame: 14117-14127

Further image analyses made in Figure 5-13 where it shows the sequence of two string structures that are intracting at quarter lift and a CN of 1.84.. The phase difference between the two interacting strings remains approximately π radians. A cloud of bubbles is tracked in figure 5-13 (left column), from t=0 to t=0.333ms. Observed movement suggests that these cloud propagates both horizontally and vertically along the nozzle. It is observed in previous images that the string is 3 dimensional (3D) and has components in all three directions since the flow inside the nozzle is 3D with both radial and axial components of velocity around the vortex. Due to the use of a single camera, the flow is observed only in 2D. Thus, it can be concluded that the vertical motion observed is the vertical component of the radial velocity vector. Measurements were taken for Figures 5-13, using Photron Fastcam software, where in the distinct bubble structure, positioned

on a string, was tracked crossing the centre line of the nozzle, where vertical velocity is assumed equal to the radial velocity vector. Similarly axial velocity was also tracked and calculated. This was done for a number of cases and thus, estimated average velocities are as follow in Table 5-1.

Table 5-1. Axial and Radial Velocity Measumerent at quarter lift, P1.77, Re=19500, CN=1.84, Frame: 14117-14127

	Axial Velocity Calculation		Radial Velocity Calculation	
	ΔX (pixels/frame)	V_x (m/s)	ΔY (pixels/frame)	V_y (m/s)
Prior to centre line	16	7.2	11	4.9
At the centre line	12	5.4	14	6.3
Past the centre line	14	6.3	12	5.4
Mean		6.3		5.5

It can be observed from table 5-1 that the mean axial velocity measured in Fastcam software is 6.3m/s compared to 7.44m/s of that has been measured by flowmeter. The difference between these two values could be partially due to the light distortion between the nozzle and the Perspex. It can also be because of the fluctuations in the discharge coefficient caused by cavitations in each nozzle. However, it suggests that the mean radial velocity calculated in Fastcam software can be validated to have the same error. It can be seen from the table 5-1 that the mean radial velocity is 5.5m/s which shows a very significant radial component compared to that of 6.3m/s of axial velocity. It can be clearly seen from figure 5-13 that the spray cone angle is affected by the radial velocity component of the in-nozzle flow.
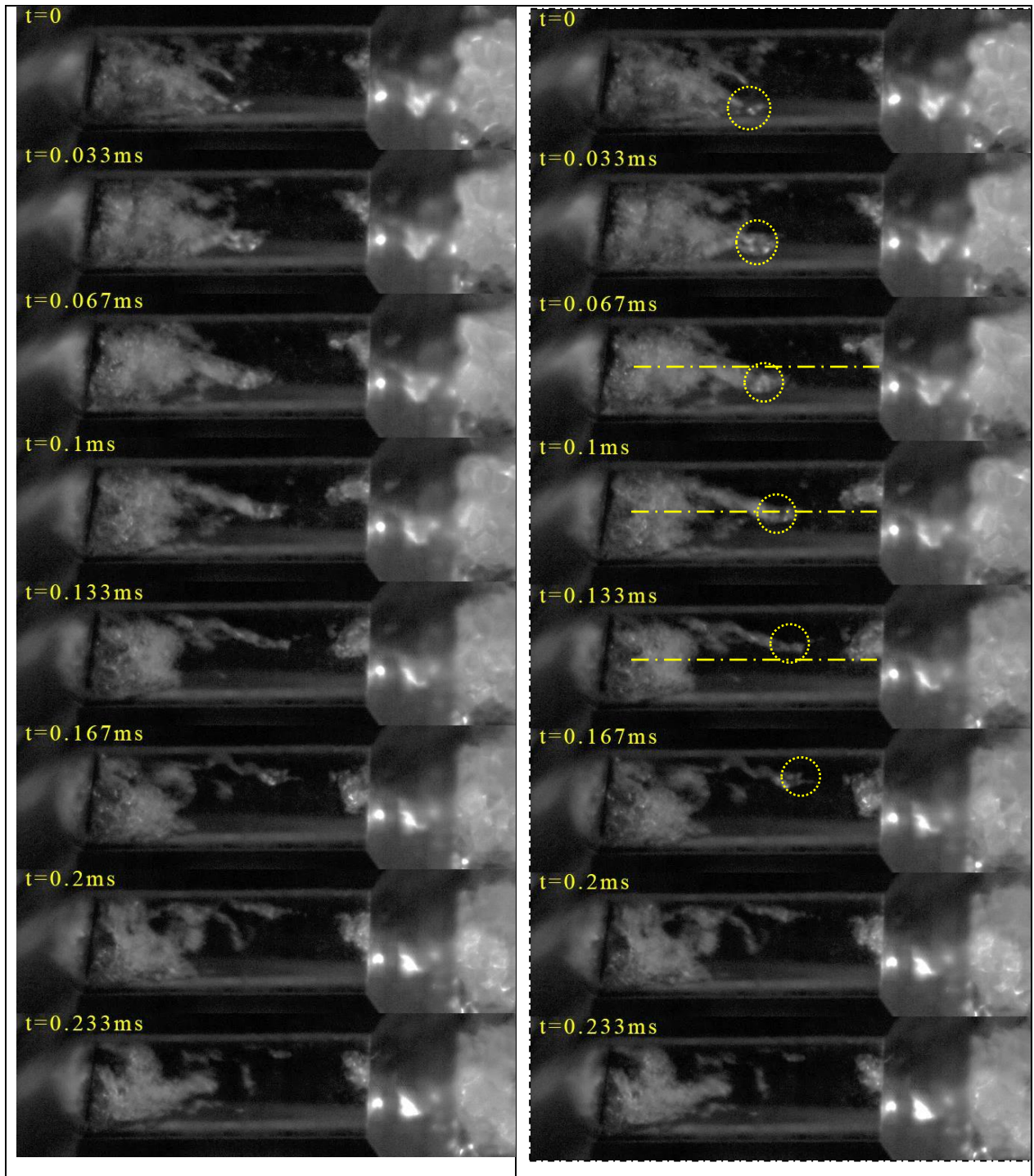
Figure 5-14. quarter lift, P5 (V1), Re=31100, CN=5.28, Frame: 1063-1070

Figure 5-14 shows a sequence of the flow at quarter lift and CN=5.28. A bubble, along a narrow string structure, becomes visible at the bottom part of the nozzle, below the centre line at t=0. Theses distinct bubble structures, positioned on a string, were tracked crossing the centre line of the nozzle, at t=0.133ms in the same manner as in figure 5-14. It can be seen that the bubbles will

fade in the last two sequences. This has been done for a number of similar cases and the measured average values are presented in table 5-2.

Table 5-2 Axial and Radial Velocity Measurement at quarter lift, P5 (V1), Re=31100, CN=5.28, Frame: 1063-1070

	Axial Velocity Calculation		Radial Velocity Calculation	
	ΔX (pixels/frame)	V_x (m/s)	ΔY (pixels/frame)	V_y (m/s)
Prior to centre line	22	9.9	19	8.55
Past the centre line	20	9	17	7.65
Mean		9.45		8.1

It can be observed from table 5-2 that the mean axial velocity measured in Fastcam software is 9.45m/s compared to 11.47m/s of that has been measured by flowmeter. The difference between these two values suggests higher fluctuations in the discharge coefficient caused by cavitations at the pressure of 5bar and CN=5.28. However, it suggests that the mean radial velocity calculations in Fastcam software can be still validated to have the same error as axial velocities. It can be seen from the table 5-2 that the mean radial velocity is 8.1m/s which shows again a very significant radial component compared to that of 9.45m/s of axial velocity. It can be clearly seen from figure 5-14 that the spray cone angle is severely affected by the radial velocity component of the in-nozzle flow.
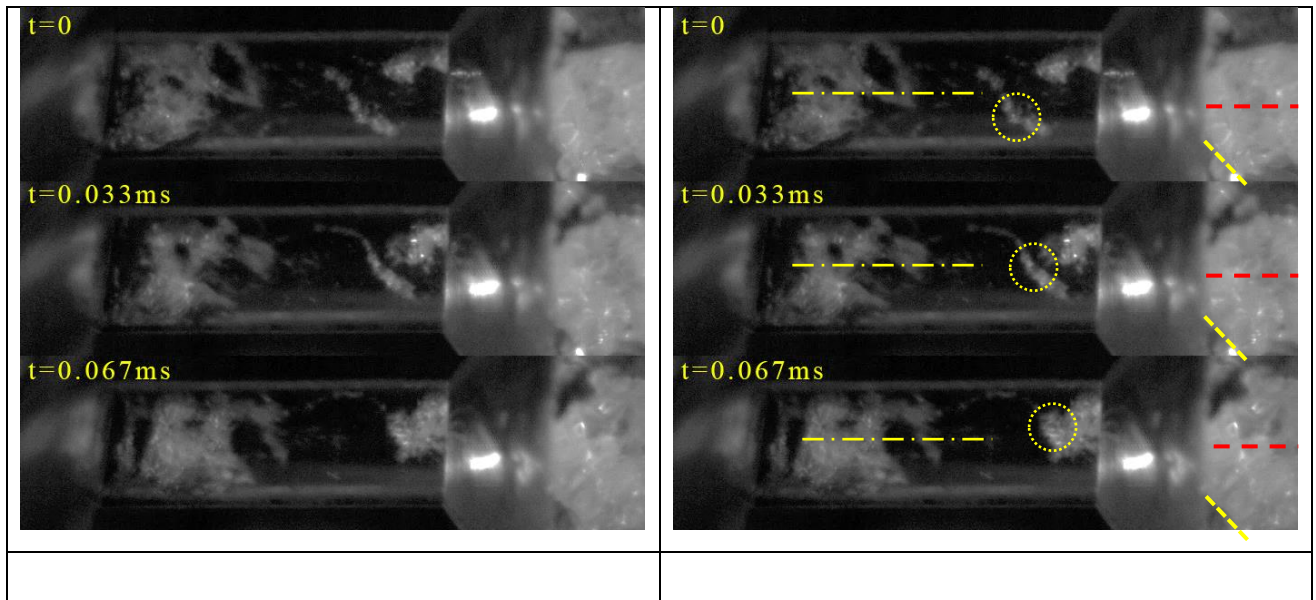
Figure 5-15. Quarter lift, P5 (V1), Re=31100, CN=5.28, Frame: 1230-1232

Table 5-3 Axial and Radial Velocity Measurement at quarter lift, P5 (V1), Re=31100, CN=5.28, Frame: 1230-1232

	Axial Velocity Calculation		Radial Velocity Calculation	
	ΔX (pixels/frame)	V_x (m/s)	ΔY (pixels/frame)	V_y (m/s)
Prior to centre line	24	10.8	17	7.65
Past the centre line	22	9.9	19	8.55

Figure 5-15 shows 3 frames of the sequence of the flow at quarter lift, injection pressure of 5bar and CN=5.28, where a bubble structure is tracked in the near of the nozzle exit area in the same condition as in figure 5-14. Similar bubbles have been tracked for a number of cases and Table 5-3 shows the mean axial and radial velocity components of the bubbles being tracked. It is clear from the table 5-3 that both the mean axial and radial velocities are very close to each other having the values of 9.9m/s and 8.5m/s, respectively. Having a closer look at the upper angle of the spray, it can be seen that the splashes on the surface of the exit hole cause significant light distortion which prevents visualising the upper angle edge. However the lower angle of the spray

could be clearly seen at t= 0.067ms having the value of about 45 degree where there seems to be no splashes on the exit hole surface thus having much less light distortion. This confirms that the magnitudes of both axial and radial velocities are very close to each other and that the spray can have a cone angle of about 90 degree.

The near-nozzle jet spray was analysed in MATLAB for the average value of 2000 images for each experimental condition. It should be emphasized that the flow under consideration is a continuous flow and considering the nature of in-nozzle two phase flow which may introduce ambiguity in the overall average results.

It should be mentioned that for the case of 1/4 lift and for the injection pressure of 1bar, The intensity of the bright area within the spray was not enough to capture the exact spray edges. Hence the Matlab code was not able to detect the edge of the spray. In addition, for higher pressures of 3, 4 and 5 bar at 1/4 lift, there were significant amount of splashes which prevents the software to calculate the angles. For the rest of the cases, 2000 images were analysed for each experimental condition. The maximum deviation of the spray edge angles was 7 degrees, which gives a maximum angle intensity of 7/8.83=0.79, which means that the statistical error in mean cone angle for 2000 images would be 2 x 0.79/$\sqrt{2000}$ = 0.018 or 1.8% with 95% confidence level and the corresponding standard deviation would be 2 x 1/$\sqrt{2 \times 2000}$ = 0.032 or 3.2% according to Yanta estimation [95]. Figures 5-16 to 5-19 shows the scatter plot of the upper angle, lower angle, axis angle and the cone angle variation in each cases. Figure 5-16 shows that the upper angle of the spray measured with respect to the horizontal line. The upper angles are assumed negative and the lower angles are positive.
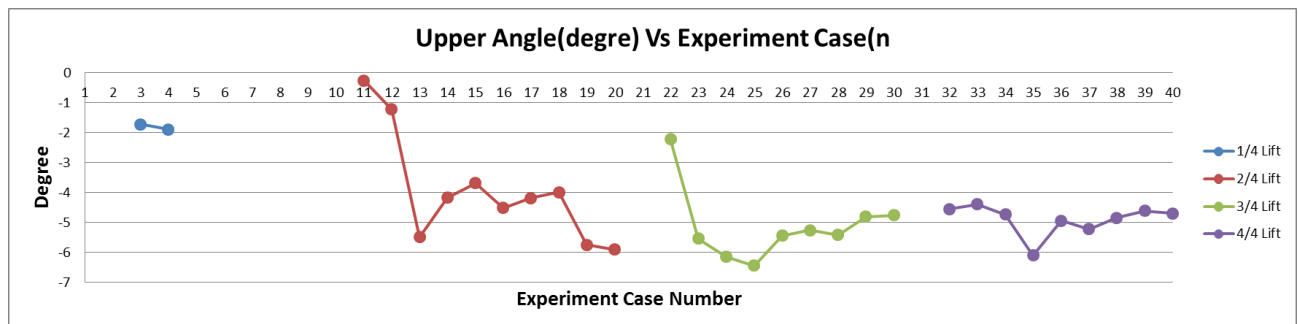
Figure 5-16 Upper Angle measured in Matlab software (in negative values)

It can be observed from figure 5-16 that the upper angles are varying between 0 to 7 degrees for all the cases. However the main domain is between 3 to 7 degrees corresponding to 85% of the cases. It is also evident that for the very low injection pressure at needle lift of 1/4, half and 3/4 (Case 3, 4, 11, 12 and 22), the upper angle is almost horizontal.
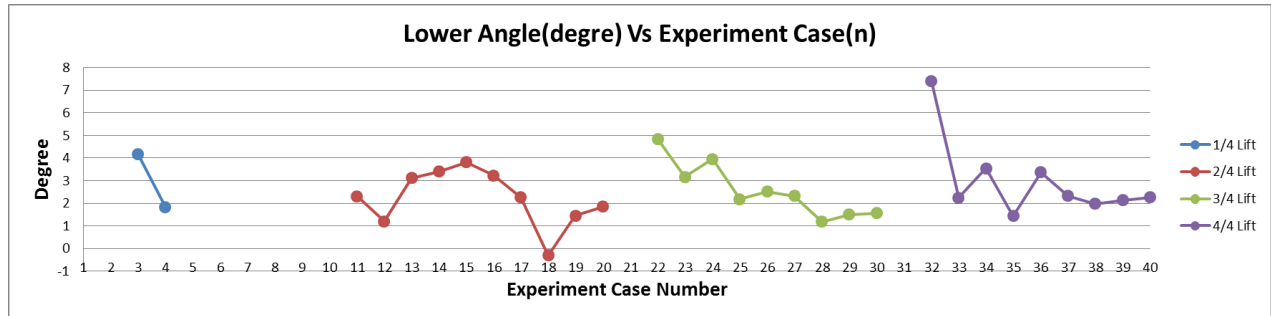
Figure 5-17 Lower Angles measured in Matlab software (in positive values)

Figure 5-17 shows the lower angle of the spray in positive values. Once again it is obvious from the figure that the lower angle varies within the range of -1 to 8 . However 90% of the cases are within the range of 1 to 4 degrees. The negative value of the lower angle (Case 18, 2/4 needle lift, CN = 2.08) suggests that it has been contracted towards the axis rather than being expanded from the axis of the spray. It can also be seen that for needle lifts of 3/4 and full, the lower angle tends to be reduced and obtains more stability as the injection pressure and the CN number increases.
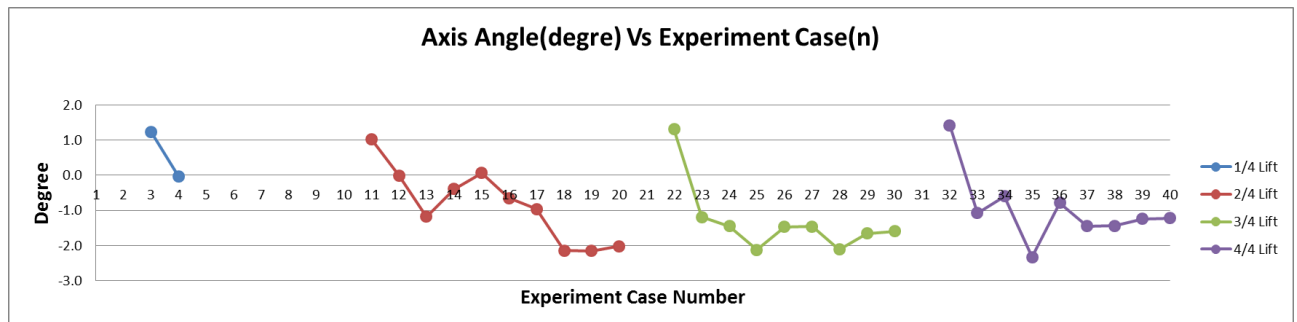
Figure 5-18 Axis Angles measured in Matlab software

Figure 5-18 shows the changes in the axis of the spray in all the measured cases. It can be seen that for low injection pressure of 1bar, the plot has peaks with positive values. It can also be observed that the spray axis changes from positive values at low injection pressures to negative values at high injection pressures. The effect of the pressure on the stability of the spray is also observed.
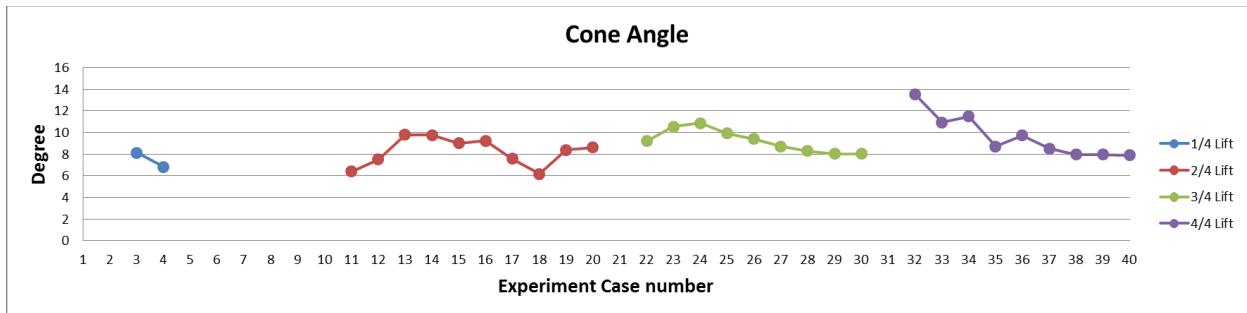
Figure 5-19 Cone Angles measured in Matlab Softwarees

Figure 5-19 shows the spray cone angles for all the measured cases. It can be claimed from the chart that as the pressure increases at the needle lifts of 3/4 and 4/4, the Cone angle decreases and tend to have an assymptode of about 8 degree.
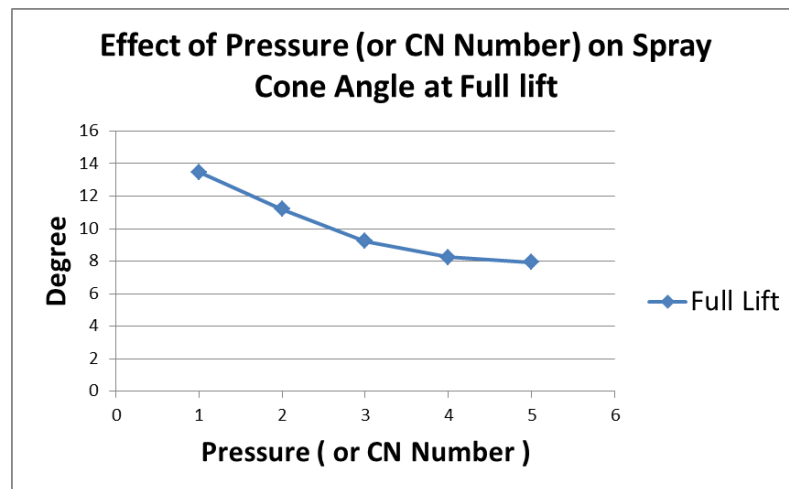
Figure 5-20 Effect of Pressure on Spray Cone angle at Full Lift.

Figure 5-20 shows variations of the overall cone angles as a function injection pressure (or CN) and shows a steady decrease in cone angle with pressure up to P=4bar and then it became almost uniform from 4 to 5bar. This may be expected as the pressure increases the flow momentum and turbulence will increase too which makes the emerging jet stronger and less susceptible to small in-nozzle flow variation.

177
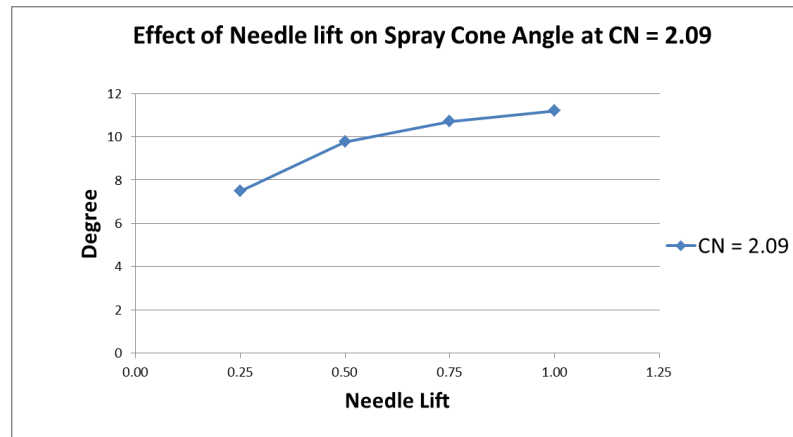
Figure 5-21 Effect of Needle Lift (right) on Spray Cone angle at CN = 2.09.

Figure 5-21 shows variations of the cone angle as a function of needle lift at a given pressure and shows that the angle increases with lift. As mentioned earlier on the flow losses occur when the needle lift is reduced which causes lower flow momentum and suppressing the turbulence. This suggests that there would be a higher level of diffusion at the higher lift causing larger cone angles. In addition, as it has been shown above, the in-nozzle cavitation at the lowest lift was suppressed (delayed) and less intense compare to those at the full lift which implies less influence on the emerging jet and therefore smaller cone angles at the lower lifts.

5.3 Results for 7 times enlarged model

Sample images of the results for 7 times enlarged model are shown in Fig. 5-22. A sequence of images of the in-nozzle flow and the emerging spray at quarter lift and full lift at cavitation numbers of CN = 1, 1.5, 1.75, 2, and 2.5. Cavitation was not present at CN range between 0.75 to 1.0. Increasing cavitation above 1 induces cavitation in the nozzle and resulted to full film cavitation at CN=2 at full lift. It can be claimed that as the cavitation number rises from 1.0 to 2, the upper near-nozzle spray angle increases due to cavitation as can be seen from the images shown in Fig. 5-22.
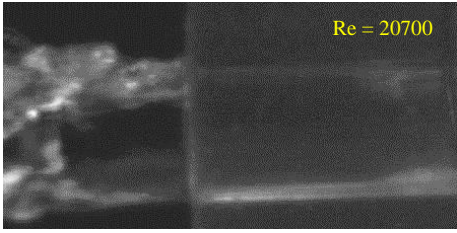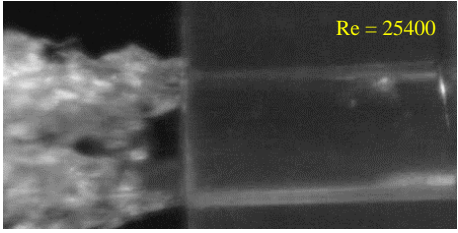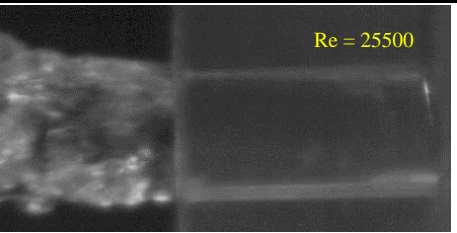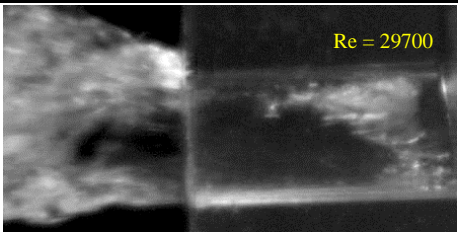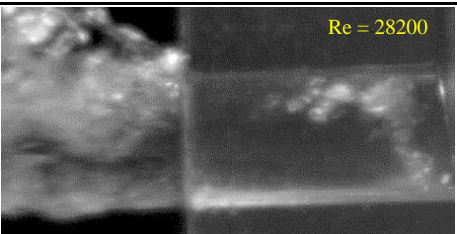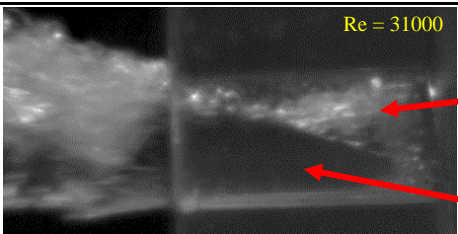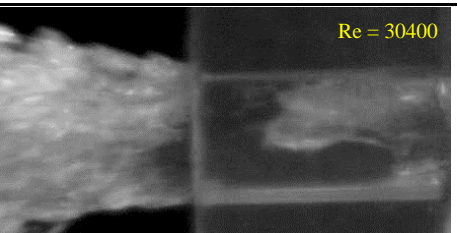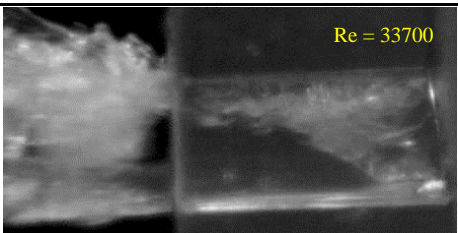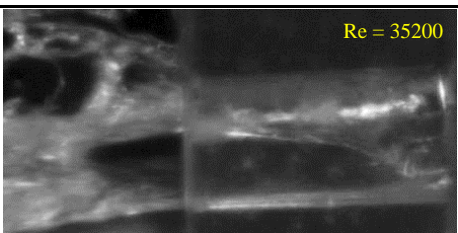
		Quarter lift	Full lift
	Needle Lift		
Cavitation Number	CN=1	Re = 20700	Re = 25400
	CN=1.5	Re = 25500	Re = 29700
	CN=1.7	Re = 28200	Re = 31000
	CN =2	Re = 30400	Re = 33700
	CN =2.5	Re = 32900	Re = 35200

Caviation bubbles

liquid

Figure 5-22 Cavitation development at quarter lift (left column) and full lift (right column) at different CNs for 7 times enlarged model.

As cavitation number gradually increases from 1.5 to 2.0, the geometric cavitation becomes more intense and stretches down the nozzle towards the exit. Another observation is that the structure of the geometric cavitation on top of the nozzle undergoes a transition with increase in CN from a cluster of bubbly cloud vapour at CN=1.5 into a smoothly horseshoe film cavitation as evident from images at CN=2 respectively; At full lift, as CN increases further from 2 to 2.5, the film cavitation is stretched out and will reach the nozzle exit. Consequently, a pocket of air will be sucked into the upper part of the nozzle and hydraulic flip will occur. This will have huge impact on the structure and the angle of the upper and lower edge of the near exit spray. It can be seen from Fig. 5-22 that the majority of the visible volume of the fluid (VOF=1) is located at the lower half of the nozzle.

Figure 5-23 shows a sequence of cavitation shedding at CN = 2 captured at 200000 frames per second at CN=2. The whole sequence covers a time duration of 150 μsec. there is a 25 μsec between each image. It was observed that these cavitation structures are expanding and contracting with a frequency of shedding of 8-12 KHz.
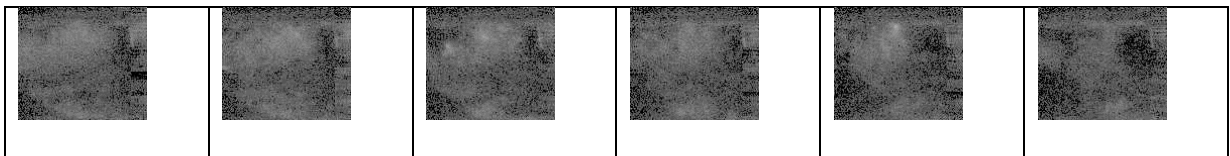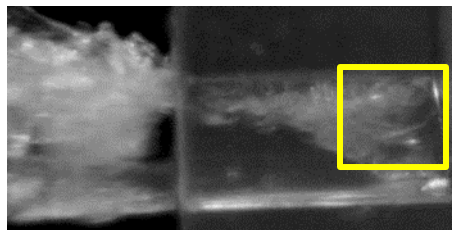
Figure 5-23 Cavitation shedding at the inlet of the nozzle at 200,000 frame per second, the frequency for shedding was observed to be 8 to 12 KHz

5.3.1 CFD simulations

Fig 5-24 shows the contour plots of the instantaneous VOF at t = 25 μs ASOI for fuel pressure of 20MPa using the lagrangian VOF model for a similar SIDI fuel injector [96]. Although the pressure condition in this work [96] is much higher than the pressure conditions in the current study, similarities are observed in the structure and VOF distribution of the real-size injector and the 7 times enlarged model which emphasizes the importance of using enlarged model. It is argued here that the "bubbles" shown in the VOF plot in Figure 5-24 (in the sac volume and nozzle entrance) is not due to cavitation, but due to the slow scavenging of the air in this region (at the start of simulation) by the liquid flow. However, further work needs to be done to understand how these complex flows interact with the surrounding air and how primary breakup is induced.
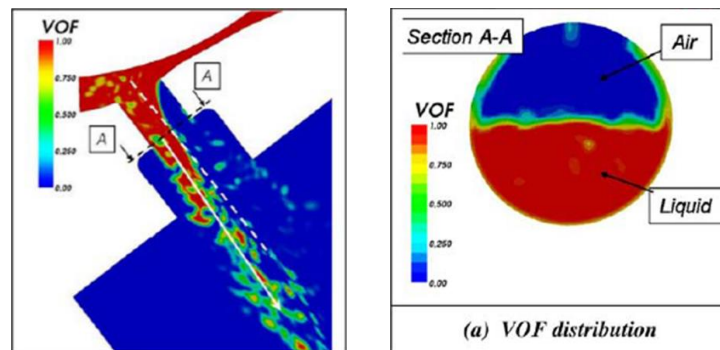
Figure 5-24 Contour plots of the instantaneous VOF fields of in-nozzle flow and the very near-nozzle spray in gasoline stepped multi-hole injector at t = 25 μs ASOI (fuel pressure = 20MPa) [96]

Figure 5-25 shows CFD simulation of a similar SIDI nozzle configuration using the cavitation modelling at 0.1 ms ASOI at pressure of 200 bar using Ansys. It is clear from the figure 5-25 that there are 2 distinct cavitation regimes, one is the string cavitation and the other is geometric cavitation.
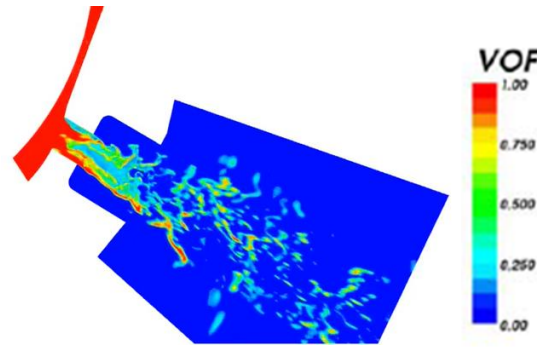
Figure 5-25 Contour plots of instantaneous VOF field of in-nozzle flow and near-nozzle spray at on the mid-plane of gasoline stepped multi-hole injector

Figure 5-26 shows a similar SIDI nozzle configuration and the 3D simulation for the ligaments' breakup [97]. Here an Eulerian-Eulerian method was used where all phases share a single velocity field. Mass transfer between fuel and fuel vapour is considered with the use of the Rayleigh-Plesset cavitation model. Turbulence is considered with the RANS approach, where flow variables are decomposed into mean and fluctuation terms. Stochastic impact of turbulence is considered through the two additional transport equations of the k-ω-SST turbulence model. These are used to close the system of partial differential RANS equations for mass and momentum conservation. [97]
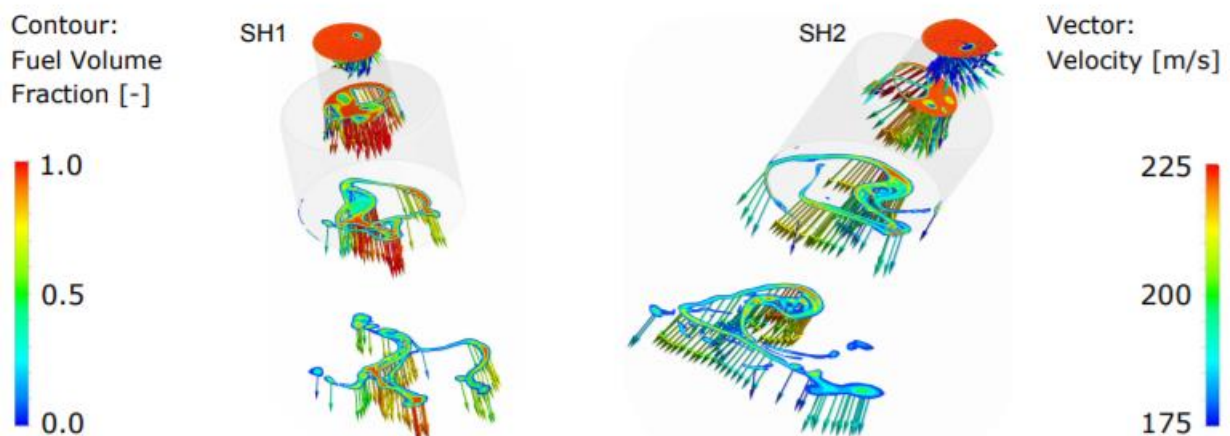
Figure 5-26 Contour plot of VOF field and velocity vector of in-nozzle floe and near-nozzle spray in stepped-multihole injector [97]

It could be seen in figure 5-26 that the VOF of the flow is higher on the outer part of the nozzles. This is due to the angle of the axis of the nozzle with respect to the injector axis. It is also clear that void areas are visible where possible geometric and string cavitation are taking place. [97]
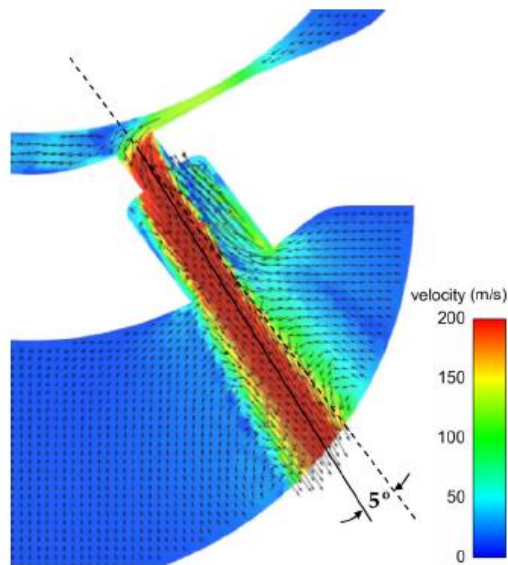
Figure 5-27 Contour plot of VOF field and velocity vector of in-nozzle flow and near-nozzle spray in stepped-multihole injector at 200 bar injection pressure [97]

5.3.2   Breakup regimes

Fig 5-28 shows a sequence of 6 consecutive images of the in-nozzle flow and the emerging spray at CN = 2.0 during 100μs. The sequence depicts the near-nozzle structure of the spray with the extension of the smooth curved line that is stretched out of the nozzle. At t = 0, a pocket of bubbles was observed at the lower part of the nozzle inlet. This moves down and reaches the nozzle exit at t=100μs. This shows that the average velocity of this pocket is around 20m/s. However the upper part of the spray has much lower velocity (around 7m/s; tracked by the bold yellow circles) compared to the bottom part of the nozzle where the bulk of the liquid exists.
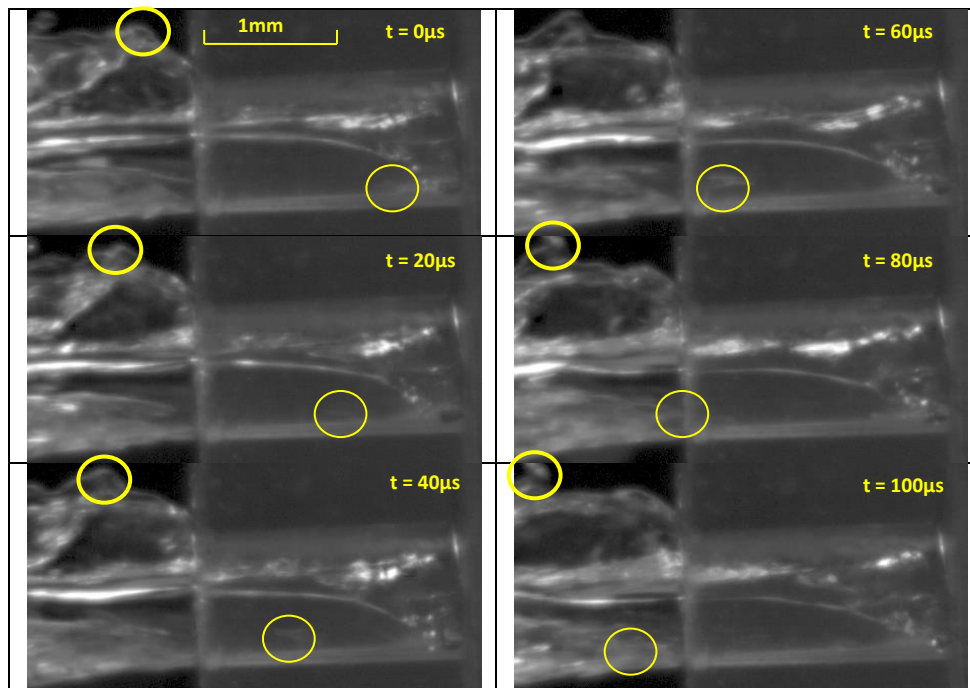
Figure 5-28 a) Comparison of the velocity field at the upper part where a stochastic ligament experience breakup and the lower part of the very near-nozzle spray where the main jet exists (CN=2)

Figure 5-29 suggests three different mechanisms seen responsible for breakup of different parts of the near-nozzle spray in the 7-times enlarged model. a) The stochastic ligament breakup at the upper part of the spray b) The stochastic sheet (shell) breakup at the upper part of the spray. c) Main jet breakup at the lower part of the spray. In all these breakup regimes cavitation and turbulence and aerodynamic drag forces play an important role. Note the inverse T shape of the jet spray at the exit.
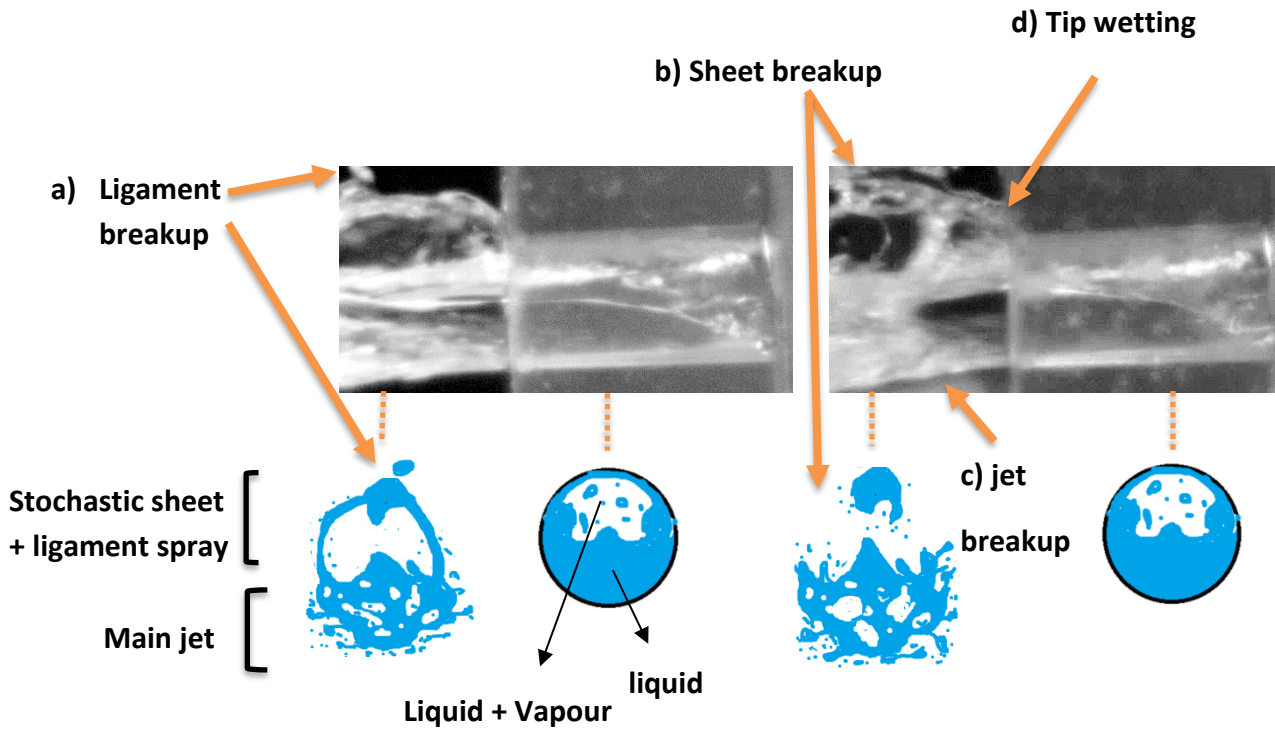
Figure 5-29 Possibility of three different mechanisms seen responsible for breakup of different parts of the near-nozzle spray. a) The stochastic ligament breakup at the upper part of the spray b) The stochastic sheet (shell) breakup at the upper part of the spray. c) Main jet breakup at the lower part of the spray d) tip wetting at the upper part of the nozzle tip where cavitation/hydraulic flip occurs

Figure 5-30 shows a schematic for the stochastic ligament spray region created at the sides of

the spray.
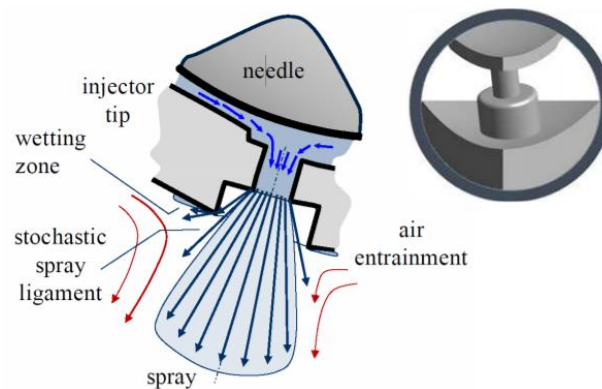
Figure 5-30 a) The stochastic ligament spray and the main spray of the near-nozzle jet proposed in this study also proposed in [98]

5.3.3 Nozzle tip wetting

Figure 5-31 shows the breakup of the stochastic ligament spray (frame rates up to 100,000fps)

being formed at the upper side of the nozzle exit which could ultimately contribute to the nozzle

tip wetting in the areas where cavitation/hydraulic flip occurs.
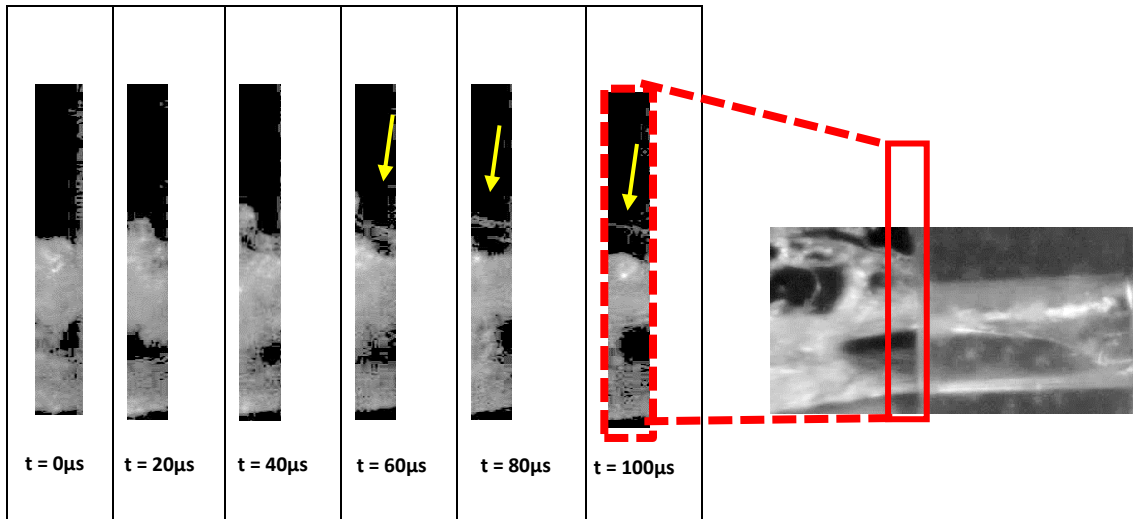
Figure 5-31 the yellow arrow shows the breakup of the stochastic ligament spray being formed at the upper side of the nozzle exit which could ultimately contribute to the nozzle tip wetting in the areas where cavitation/hydraulic flip occurs

$t = 1.5\,\mathrm{ms}$ $t = 2.5\,\mathrm{ms}$ 50/0.70 bar, 90°C

(b)   (b)
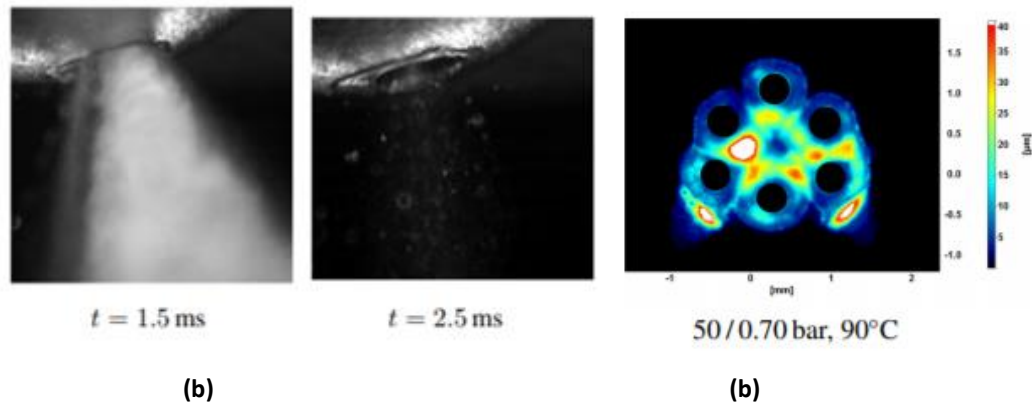
Figure 5-32 (a) High-speed visible light images of spray and tip wetting of a two-hole injector, field of view 1.5 × 1.5 mm2 . Injection of n-heptane at 200 bar; the solenoid is energized for 1.5 ms and the injection ends at around 1.8 ms. (b) Fuel distribution and the wetted areas on injector tip, 4 ms AESOI, the white colored areas shown are saturated film formation, it is clear that the maximum film formation is inside the inner circle of the nozzles [23]

5.3.4 Directionality of string cavitation

Figure 5-33 shows a sequence of the position of the strings inside the nozzle hole affecting the geometric cavitation region and consequently resulting in a change in spray axis angle and cone angle at quarter lift for CN=2 during time resolution of 200μs. The figure shows the directionality of the vortex and its link to spray axis and cone angle. In the first image (t=0) at the bottom of the column the string is inclined downward along the centreline of the nozzle. It was observed that the resulting cone angle has an axis inclined downward to that of the nozzle or string. In the second image (t=100μs) the string is tilted slightly upward from its original position so that it merges with the geometric cavitation region.

(a)   (b)

Figure 5-33 Left (a) Directionality of the vortex cavitation and its effect on spray at Full Lift, Right (b) The corresponding cross-sectional image of the string geometric locus, (Gavaises et al 2008)

The result shows that the spray cone axis has also tilted upward above the original nozzle axis. In the third image, (t=200μs), the string is completely merged with the geometric cavitation region

and will create shedding with the frequencies of 8-12 KHz mainly visible at the top of nozzle exit

and it shows that the spray cone axis has tilted above the original axis. Therefore, this behaviour

confirms the spray cone angle being affected by the directionality of induced string cavitation.

For this model further analysis was done on spray cone angle using Matlab programme just as 15

times enlarged model. The definitions used for spray cone angles for 7 times enlarged model are

shown in Figure 5-34 which shows an individual jet spray with the overall cone angle, top and

bottom half angle, nozzle axis and jet spray axis; the latter may move above or below the nozzle

axis depending on in-nozzle geometrical and vortex cavitation. The nozzle axis has been used as

the reference 0 degree angle for the presentation of the results. The cone spray angles were

measured at different CN numbers for different needle lifts.
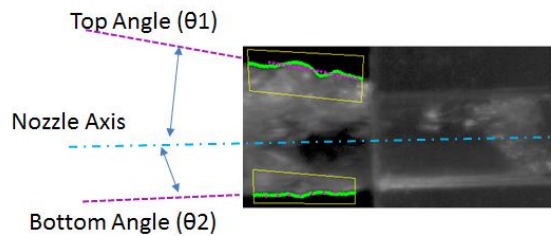
Figure 5-34 Top angle and bottom angle for 15 times enlarged model as measured by Matlab Software; nozzle axis angle is used = 0

Figure 5-35 and 5-36 shows variations of the upper and lower angle (respectively) of the 7 times

enlarged model as a function of CN numbers for quarter and full lift. The results show that the

absolute value of the angle increases with increase in CN numbers. It could be claimed that as

cavitation number increases for both lifts, the cavitation collapse of bubbles will increase the

turbulence of the flow which will result in greater radial velocities and will lead to this increase in

the upper angles for both lifts. However as mentioned earlier for the 15 time enlarged model,

losses occur when the needle lift is reduced from full to quarter half which causes lower flow

momentum and suppressing the turbulence. This suggests that there would be a higher level of diffusion at the higher lift causing larger cone angles. In addition, as it has been discusses for 15 times enlarged model, the in-nozzle cavitation at the lowest lift was suppressed (delayed) and less intense compared to those at the full lift which implies less influence on the emerging jet and therefore smaller cone angles at the lower lifts. It can be seen that for CN of 2.5 the upper angle was not clearly present due to the hydraulic flip.
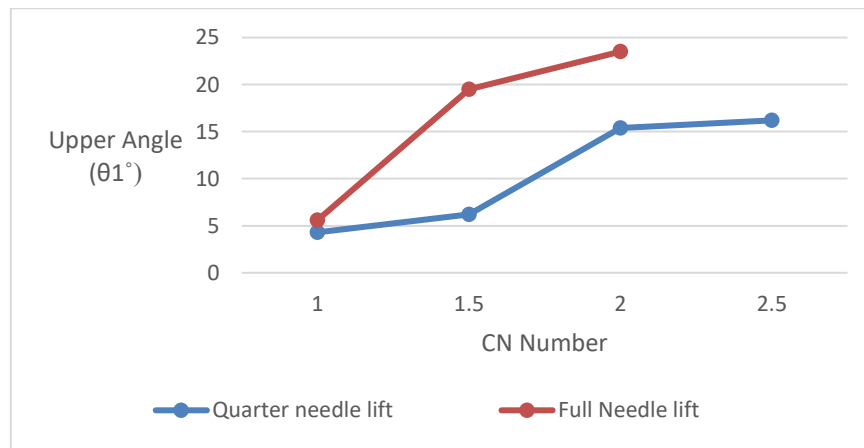
Figure 5-35 Effect of CN Number on Upper Angle
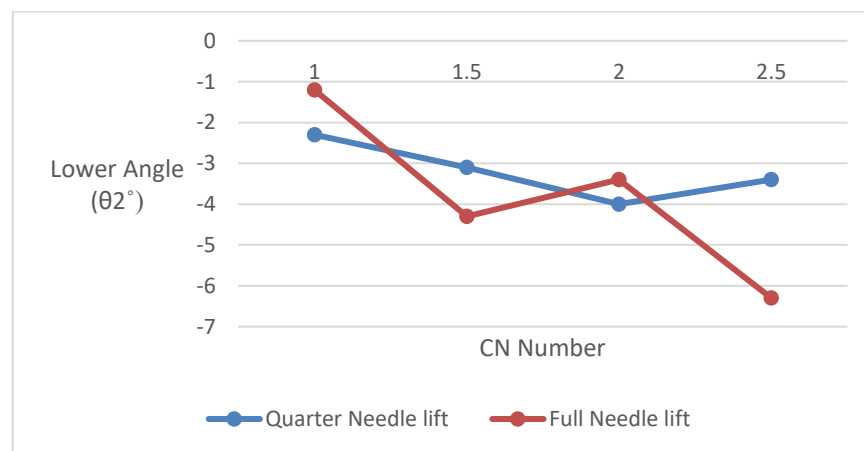
Figure 5-36 Effect of CN Number on Lower Angle

5.4   Summary

In this chapter, high-speed visualisation (Mie Scattering) technique was used to visualise the in-nozzle flow and cavitation development inside a 15-times transparent enlarged model of a conventional multi-hole injector (6-holes symmetric). The near-nozzle exit jet spray was also visualised simultaneously and quantitatively measured along with the in-nozzle flow cavitation to further understand the effect of cavitation on the near-nozzle jet spray instability. Geometric and string cavitation was observed in the nozzle and their site of occurrence was visualized. It was seen that both geometric and string cavitation can influence the stability of the near-nozzle exit spray. A reverse backwards vortex were also observed inside the nozzle at low cavitation numbers which affected the spray structure and cone angles. Two counter rotating strings were observed at high cavitation numbers which caused a highly turbulent in-nozzle flow. The directionality of the string cavitation and the spray angle was also visualized. Here is the summary of the main findings from the 15-times enlarged model.

- The interaction between the geometrical and vortex cavitation shows the displacement and rolling of the leading edge of the geometric cavitation on the top surface near the hole entry at full lift and high cavitation and Reynolds number.

- The displacement and possible impact of bubble pockets on the top surface of the nozzle at full lift and high cavitation and Reynolds number were also visualised and analysed. The bubbles burst through micro-burst process with velocities much higher (by order of

magnitude) when they get near the surface where the pressure in recovered and their possible impact would result on further erosion.

- Two counter (highlighted) rotating vortex cavitation coexist at the same time inside the nozzle hole originated from the top and bottom side of the nozzle at the inlet and get closer together as they convected downstream so that they almost merged together nearer to the exit.

- Directionality of the vortex cavitation and its effect on spray at Full Lift were visualized which shows that the position of the string inside the nozzle might affect the spray angles.

- At injection to atmosphere at low cavitation numbers, with no geometrical cavitation, a random transient reverse vortex structure was found to be initiated outside the nozzle near its exit in tenth of a millisecond and moved into nozzle towards its inlet and developed/ and maintained its structure inside the nozzle for several milliseconds. It was found that increasing the needle lift for the same low cavitation number seems to decrease the duration of the air entrainment and penetration inside the nozzle.

- It was observed that string cavitation can influence the size of the cone angle. It was seen that as the string cavitation is reached towards the end of the nozzle, the cone angle increases significantly.

- The variations of the overall cone angles as a function injection pressure (or CN) was analysed which shows a steady decrease in cone angle with pressure up to P=4bar.

- The variations of the cone angle as a function of needle lift at a given pressure shows that the angle might increases with increasing the needle lift.

In the second phase of the experimental investigation, a new original 7-times enlarged model of the same injector was designed and manufactured utilising a CAD software that allowed an enhanced simultaneous visualisation of the in-nozzle flow and near-nozzle jet spray. In this phase, the transparent model was uniquely designed in SOLIDWORKS that allowed both in-nozzle flow region and the near-nozzle exit spray region to remain optically sharp enough in the same depth-of-the-field region of the camera (DoF of less than 1mm) . The main contribution of the author was to enhance the visualization technique that allowed simultaneous visualization of the link between in-nozzle flow pattern and the near-nozzle jet spray. The main finding in this phase are:

- The structure of the geometric cavitation on top of the nozzle undergoes a transition with increase in CN from a cluster of bubbly cloud vapour into a smoothly horseshoe film cavitation;

- Cavitation shedding at CN = 2 was captured at 200,000 fps.

- It was seen that a pocket of air will be sucked into the upper part of the nozzle at CN higher than 2 and hydraulic flip occurs. This will have huge impact on the structure and the angle of the upper and lower edge of the near exit spray and will ultimately result in the formation of a stochastic ligament spray at the top side of the nozzle.

- The possibility of three mechanisms are likely to be responsible for the breakup of the near-nozzle spray at high CN numbers in enlarged model. The first mechanism is the stochastic ligament breakup at the upper part of the spray at the 12 o clock position. These ligaments are likely to be the resultant of the interaction of the highly turbulent flow inside the nozzle and the upper surface of the nozzle close to the nozzle exit. The second mechanism is likely to be the stochastic sheet (shell) breakup which is likely to be formed

circumferentially on both sides of the nozzle wall located at first and fourth quadrant at the cross section of the nozzle exit. The last mechanism responsible for the breakup is the main jet breakup at the lower part of the spray. In all these breakup regimes cavitation and turbulence and aerodynamic drag forces play an important role.

- It was observed that the stochastic ligament spray can contribute to tip nozzle wetting at the upper part of the nozzle.

- It was observed that the string cavitation inside the nozzle hole affects the geometric cavitation region and consequently resulting in a change in spray axis angle and cone angle.

- The results show that the absolute value of the angle increases with increase in CN numbers.

- It was revealed that the hydraulic flip happens earlier than expected and at lower cavitation numbers compared to 15 times enlarged model.

Chapter 6: Spray Visualisation in Real-size High-pressure Experimental Test Rig

6.1   Introduction

In this chapter, fuel spray characteristic from the stepped multi-hole nozzle have been investigated by visualising the spray using a high speed camera at different operating conditions. Table 6-1 provides the running conditions of the fuel jet spray investigated under different injection pressures and durations. The injection pressures were chosen in a manner to represent the working pressure range of the injector (40-180 bar) with 100 bar set as the upper limit due to limitations of the fuel injection system at the time. Pressures lower than 40 bar were also investigated to obtain the full set results.

Table 6-1 Operating conditions for the experiment for visualisation of the real size spray

Duration / Pressure	0.6	0.65	0.7	0.8	0.9	1	1.5	2	2.5
20								x	
30								x	
40								x	
50								x	
60								x	
80								x	
100	x	x	x	x	x	x	x	x	x

It should also be noted that some previous spray results [88] and [89] from two different injectors has been presented for comparison. Some details of the current injector and the other two types of injector are shown in table 4-3 in methodology chapter. Injector 1 and 2 are from previous works and injector 3 is the one used in the current study.

6.2   Volumetric and mass rate flow analysis

Figure 6-1 and 6-2 shows the syringe which was used for volumetric efficiency measurement. The fuel was injected into an isolated syringe and up to 2000 injections at different duration and pressure were measured. The total mass was then calculated on a 0.1 milligram precision scale (10^{-4} gram). The volume was then isolated and calculated by multiplying the total mass by the specific volume of the fuel. Afterwards, the mass rate per injection and the volume per injection for the current injector at 3 different pressures was measured by dividing the values by 2000.

It is clear that as the pressure increases the flowrate increases too. It is also clear that during 1ms and 2ms the flow rates increases linearly with time.
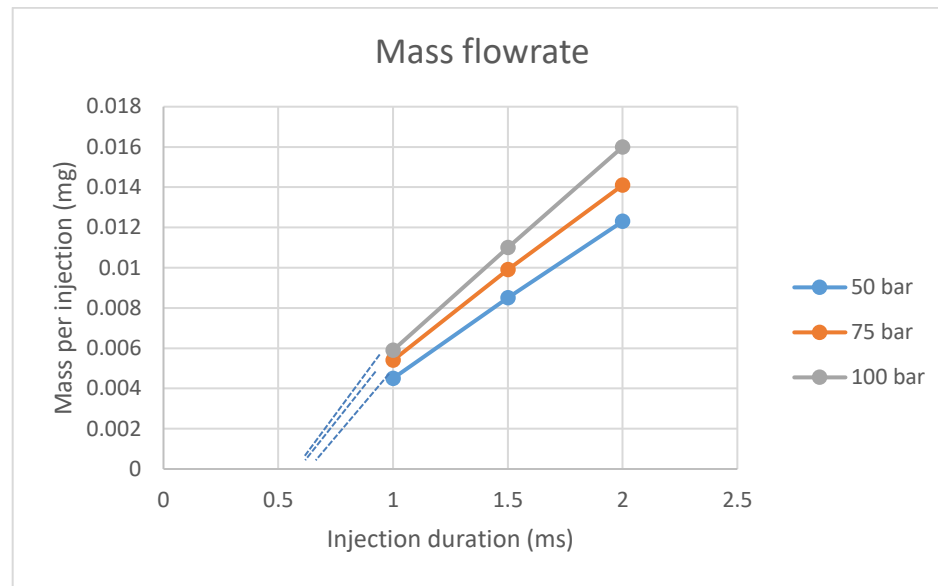
Figure 6-1 Mass flow rate per injection for the current injector at 3 different pressures
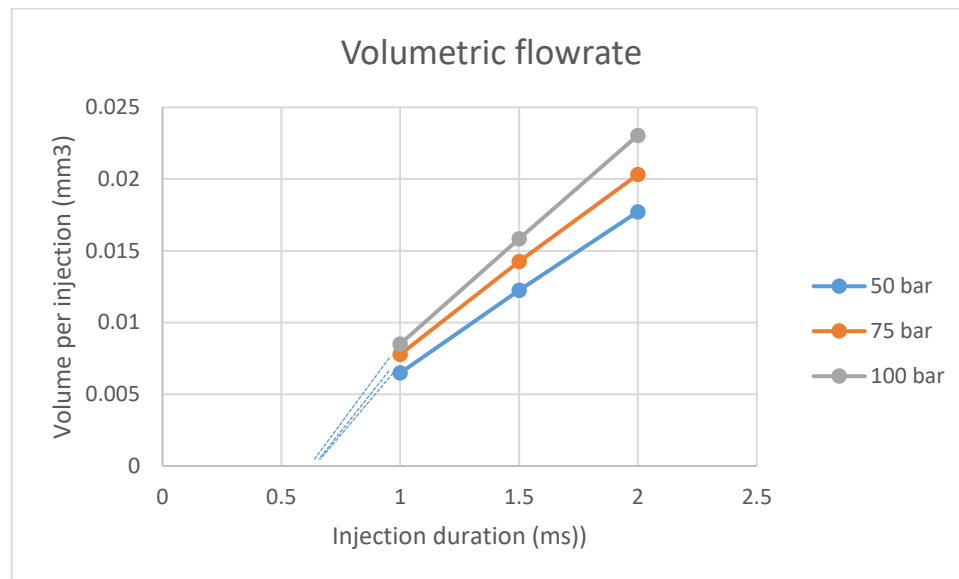
Figure 6-2 Volumetric flow rate per injection for the current injector at 3 different pressures

6.3   Settings for Mie scattering and shadowgraphy

Due to compact multi-hole nozzles arrangement and also because of the asymmetric

spray pattern, it was impossible to separate all the spray jets individually for imaging.

Thus, during the spray visualisation, it was decided to analyse spray cone angle for two

sprays overlapped on each other. Tables 6-3 below shows the camera setting with

different magnification ratios used to visualise the overall spray and the near-nozzle

spray.

Table 6-2 shows the camera setting with different magnification ratios used to visualise the overall spray and the near-nozzle spray

Mie Scattering			
Class	Overall Spray Angle 0	Overall Spray Angle 90	Near-nozzle 3 holes
Pixel/mm ratio	8.5	8.4	84
Magnification (ratio of object size to CMOS image size)	0.3	0.3	3
Image size (pixels)	384x672	384x672	384x320
Shutter speed/framerate	1/309000 sec 20000 fps (50 µs)	1/309000 sec 20000fps (50 µs)	1/309000 40000fps (25µs)

Table 6-3 Shadowgraph setup of camera

Shadowgraph		
Class	Near-nozzle 3 holes	Near-nozzle 1 hole
Pixel/mm ratio	84	84
Magnification	3	3
Image size	384x320	128x320

Shutter speed/framerate	1/2700000	1/2700000 sec
	40000fps (25µs)	80000fps (12.5 µs)

6.4   Initial development of the spray

In figure 6-3 the plane of view of the injector spray is presented from 5 different rotational angles.

(a)   (b)   (c)   (d)   (e)
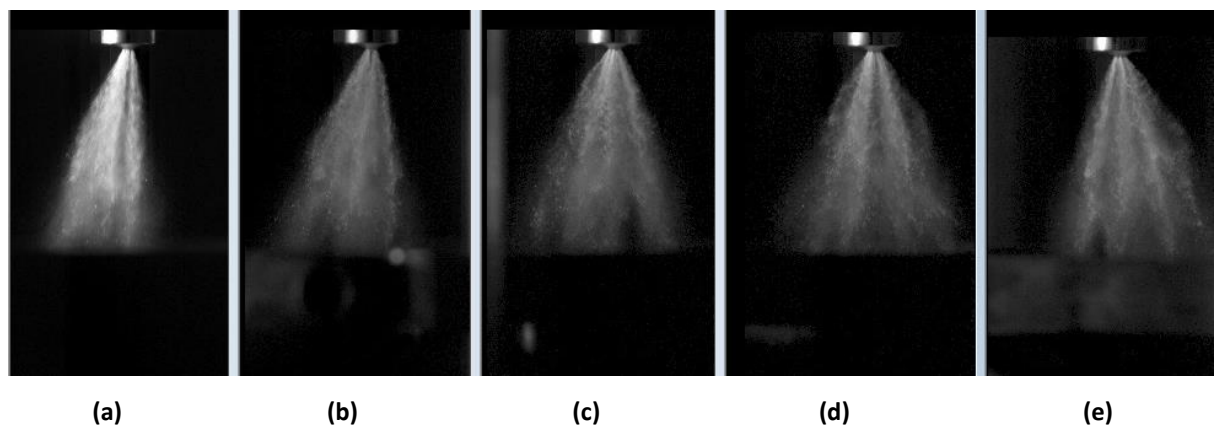
Figure 6-3 Spray visualization at 100 bar injection shown from different angles (a) 0 degree (b) 20 degree (c) 45 degree (d) 90 degree (e) 180 degree

Out of these views, only 0 degree and 90 degree configurations has been investigated further.

From the time of the start of needle lift, till it is fully lifted, there is a transient phase present where the spray structures, macroscopic and microscopic, are continually changing due to the transient movement of the needle which causes rapid changes in pressure in the sac volume and in the nozzle itself which will ultimately influence the transient development of the spray in this phase as the first parts of the spray is exiting the nozzle. It is known that the AESOI (After Electronic Startof Injection) time is the time when the electronic trigger takes place. It is also known that the ASOI (After Start of

Injection) time is defined as the time when the spray is visible for the first time from the nozzle which is 0.65 ±0.05 ms AESOI. By observing the injector needle pulse graph, the transient phase exists between 0.65 ms AESOI and 0.7 ms AESOI approximately which is equal to 0 ms to 0.05 ms ASOI. The ASOI is defined as the time when the spray is visible for the first time from the injector. Development of the spray after the transient phase and creation of the fully developed spray is seen by the distinct characteristics of the spray at varying pressure, as shown in Figure 6-4.
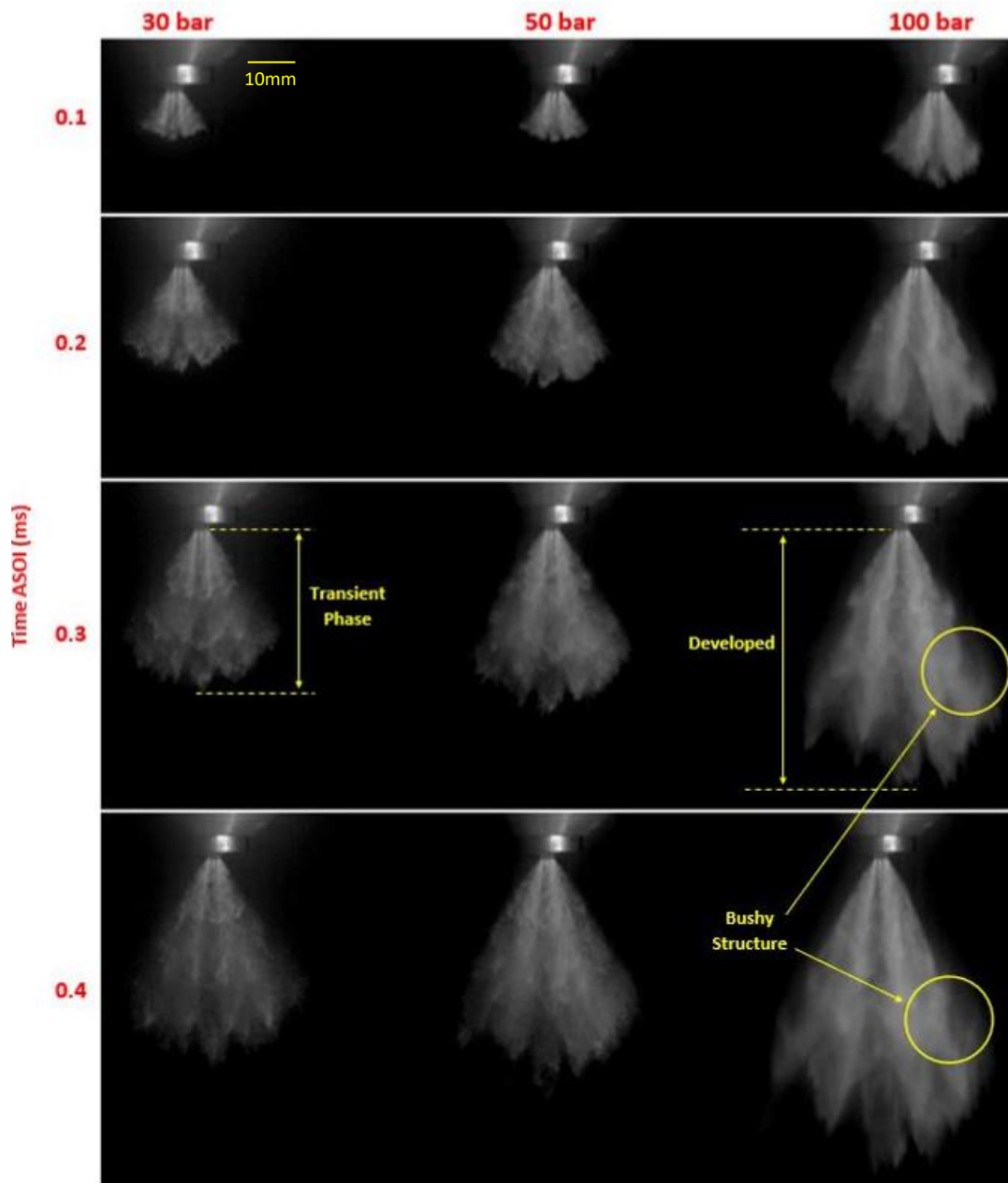
Figure 6-4 Images showing spray development of injector 3 and the existence of transient phase at different pressures and times ASOI.

6.5   Overall spray pattern

In the next phase, the overall spray pattern was visualised as a function of time ASOI. After the overall spray pattern is shown, the structure of the spray is compared with Bosch multi-hole conventional injector (#1) with straight nozzles. This is important in order to understand the effect of stepped hole on the spray structure and how the fuel and air is mixed in the combustion chamber before the spray is fully evaporated. It was decided to study the spray characteristics only under atmospheric condition in order to gain a better insight into how to conduct the PDA measurement with enough spray visualisation backup. Therefore the effect of back pressure was not the focus of our study. In this manner, the spray tip penetration and cone angles were also calculated, and the results are presented in this chapter. The near-nozzle exit spray is also visualised in order to gain better understanding of the structure and the shape of the jet spray and the phenomena dominating the breakup of the jet.

Fig 6-5 shows the sequence for the overall spray structure of the stepped-nozzle Bosch injector. The injector is operating at 100 bar rail pressure and 2ms driver pulse duration. There are 7 holes in this injector and only 5 of the jets are visible from the view shown in figure 6-5. The sequence begins at 0.1ms ASOI and continues in 0.1ms time steps. It could be seen from figure 6-5 that the core of the jet is wider compared to conventional injectors in figure 6-6 with enhanced atomisation and has a more irregular pattern in the fully developed mode. There seems to be more instability in the spray and the two middle jets are sometimes flapping from one side to another side creating a snake shape

pattern. This is more evident towards the end of the injection event as could be seen from figure h to i. It can also be seen that the spray tip vicinity is also more atomised compared to the conventional injector.

Another feature which is evident from the structure of the spray in figure 6-5 is the A shape of the spray and the interaction between the adjacent jets. This shows that there is a high amount of air entrainment from the surrounding air which causes the two adjacent jets to interact with each other and create an A shape.

It was observed that there is high interaction between each jet and the adjacent jet and therefore a distinct boundary between each jet is not recognisable as the spray develops further downstream in comparison with conventional multi-hole in figure 6-6 where there is a clear boundary between each jet and less interaction is visible between each individual jets.
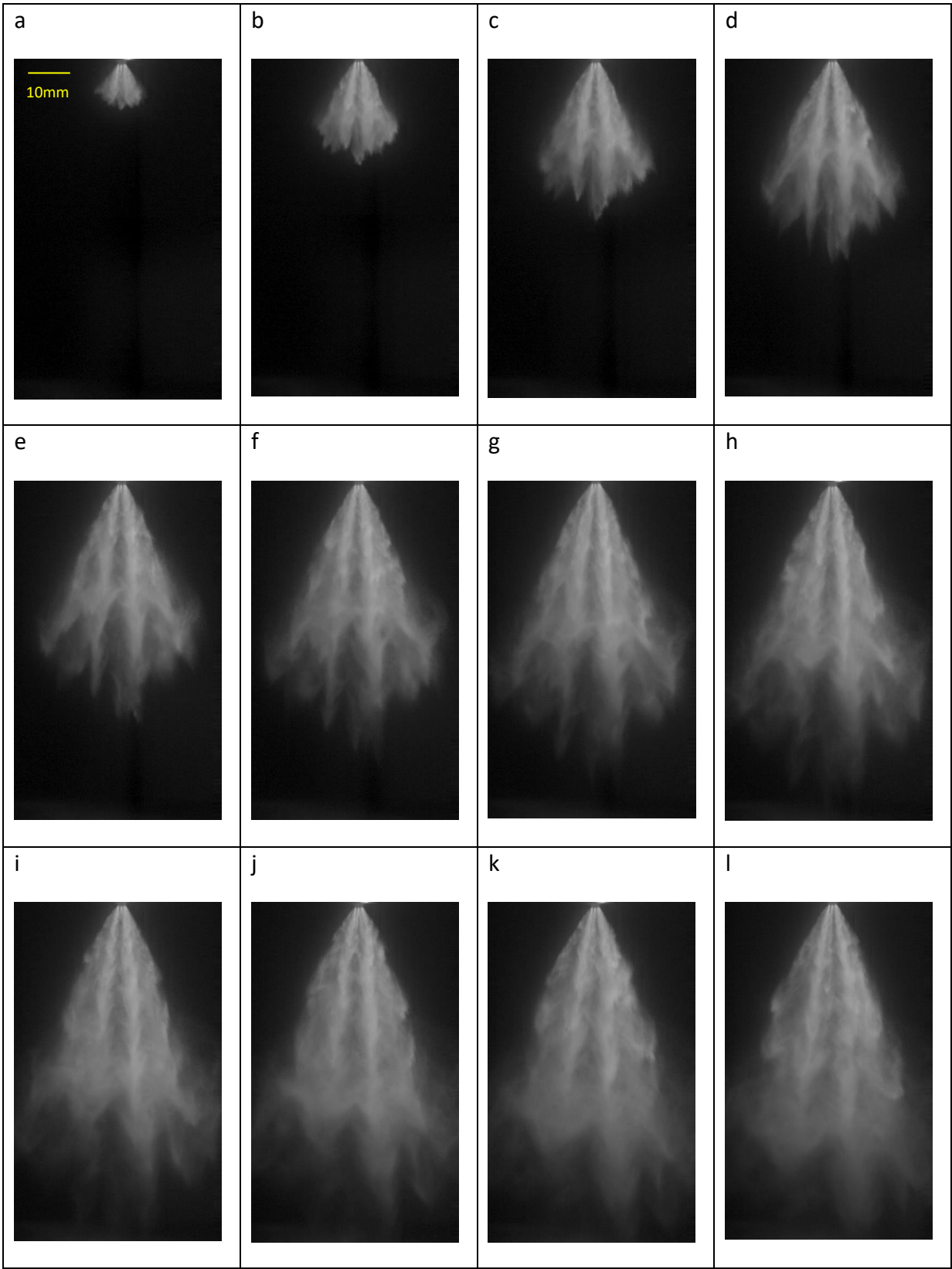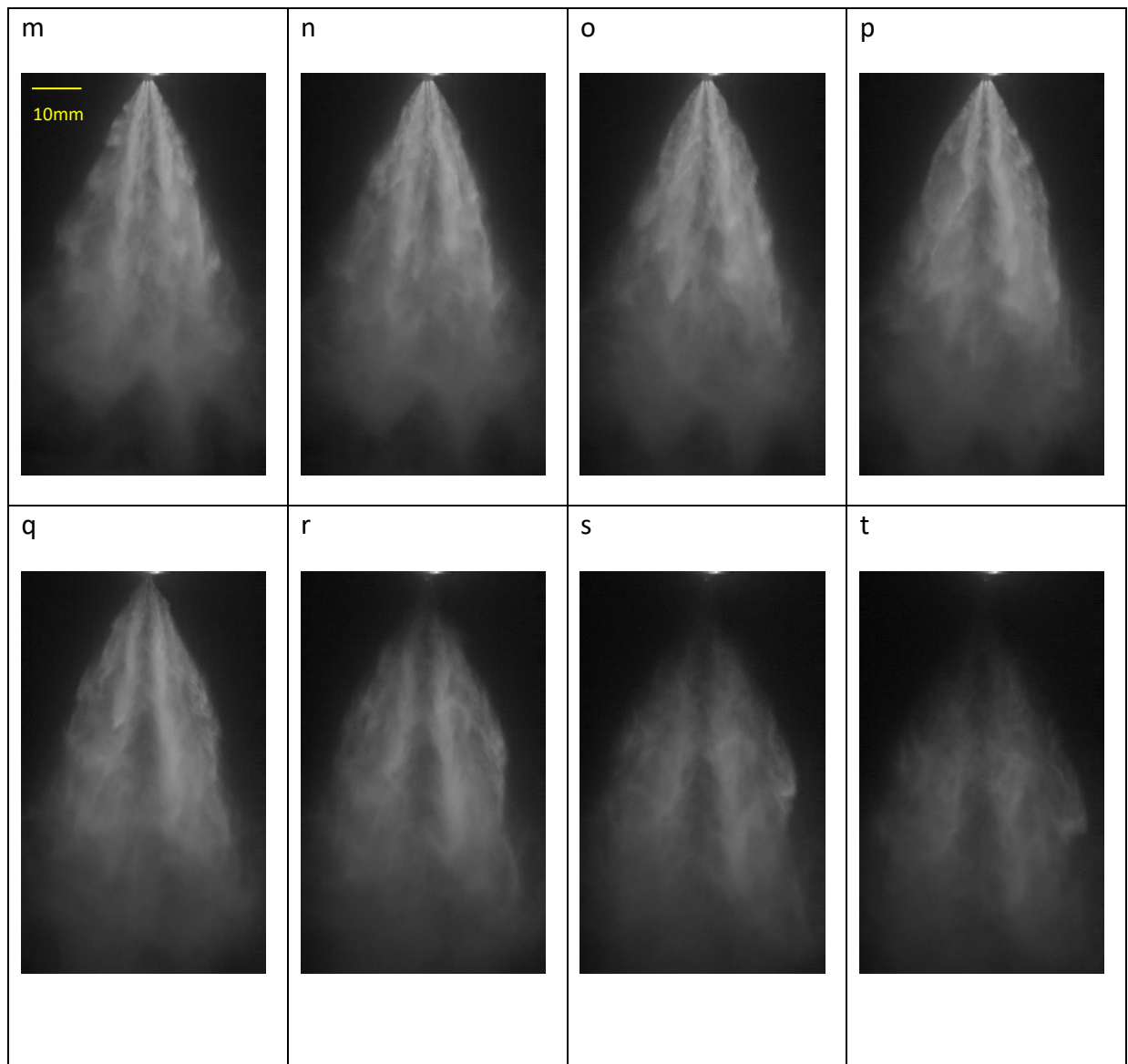
Figure 6-5 The overall spray structure of the stepped-nozzle Bosch injector. The injector is operating at 100 bar rail pressure and 2ms driver pulse duration. The sequence begins at 0.1ms ASOI and continues in 0.1ms time steps.

An example of the overall spray structure of the conventional Bosch injector is shown

in figure 6-6. The injector is operating at 120 bar rail pressure and 2ms driver pulse

injection duration. The sequence begins at 0.125ms ASOI and continues in a time step

of 0.125ms [88]. Here the centre of the jet is clearly very bright indicating the presence

of the core of the jet spray, and the tip of the spray is sharp and narrow. This is perhaps

due to lack the presence of a step in the conventional injector which is subject to lesser

amount of early-air entrainment and therefore exhibit a sharper and brighter patterns

alongside the axis of the jet.
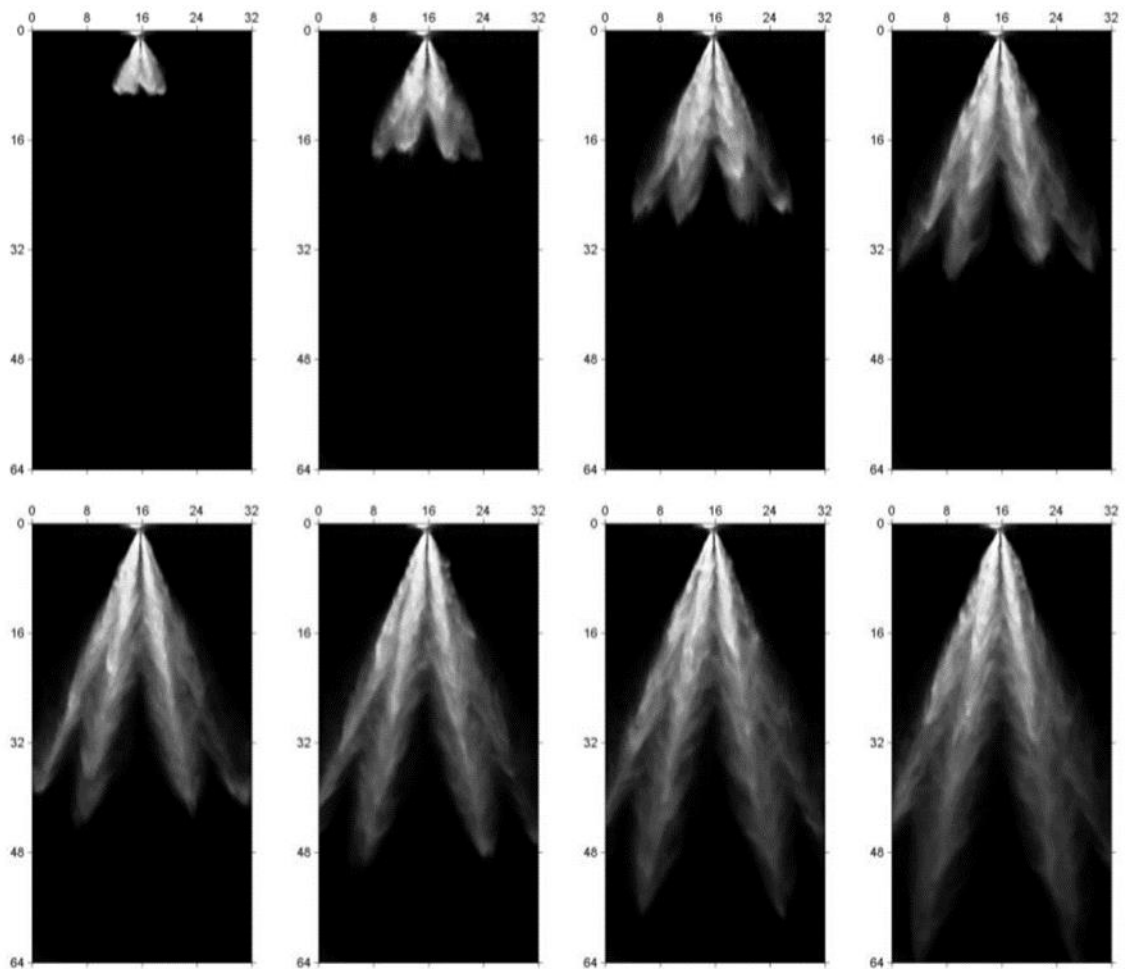
Figure 6-6 An example of the overall spray structure of the conventional Bosch injector(#1). The injector is operating at 120 bar rail pressure and 2ms driver pulse duration. The sequence begins at 0.125ms ASOI and continues in 0.125ms time steps [88]

The overall jet penetration of the stepped-nozzle injector was compared with that of the

conventional injector. It was found that the overall tip penetration of the current injector

(stepped-hole nozzle) was almost 50mm at 0.75ms ASOI (1.5ms AESOI) according to the

graph in figure 6-14 which is similar to that of the conventional injector at the same ASOI

of 0.75ms according to figure 6-6. Due to the fact that the size of the stepped-hole nozzle

was not precisely provided, it is not possible to directly compare the penetration

together however disregarding the design of the injector, it could be concluded that both

injector exhibits more or less same performance with relation to tip penetration length.

6.5.1 Effect of injection duration on spray pattern

The effect of injection duration on the spray characteristics was also investigated. There

are two reasons for this. The primary goal is to find out the time required as the minimum

injection duration to produce a stable injection. This is particularly important for multiple

injection strategies as well as the minimum load capacity of the engine in stratified mode

[88]; The second reason is to determine whether any changes in injection duration during

the stable range resulted in any changes to the spray structure.

It should also be mentioned that two different side viewing angles were examined for

the spray pattern with respect the central axis of the injector. One angle was 90 degree

and the other angle was 0 degree. In the 90-degree configuration the spray pattern has

a symmetric shape similar to 6 hole conventional injector but with an extra hole located

in the middle of the spray pattern. The cone angles in this configuration has been

measured and reported to be around 73±2 degrees at pressure of 100 bar. Also, that the

extra jet is vertical which is evident in the figures 6-9 compared to conventional injector

in figure 6-6. In addition, the spray was visualised from 0-degree angle. In this configuration, the spray has asymmetric shape and the tip penetration was calculated for this configuration. Due to the compact configuration of the injector holes it was not possible to isolate one spray and therefore a pair of sprays were isolated. The only option was to isolate a pair of sprays with the optics arranged such that the rear spray remained out of focus and entirely obscured by the visualised spray in the foreground.

Figure 6-7 shows the overall spray structure of the stepped-nozzle injector for the duration of 1 ms. The injector is operating at 100 bar rail pressure and is sprayed into the ambient pressure. The sequence begins at 0.1ms ASOI and continues in 0.1ms time steps. It could be observed that at the start of the spray, there are some irregularities in the structure of the spray ie the core of the two brighter jets are sometimes wobbling and snaking into right or left side. This shows that even at lower injection duration there are instabilities in the structure of the spray.
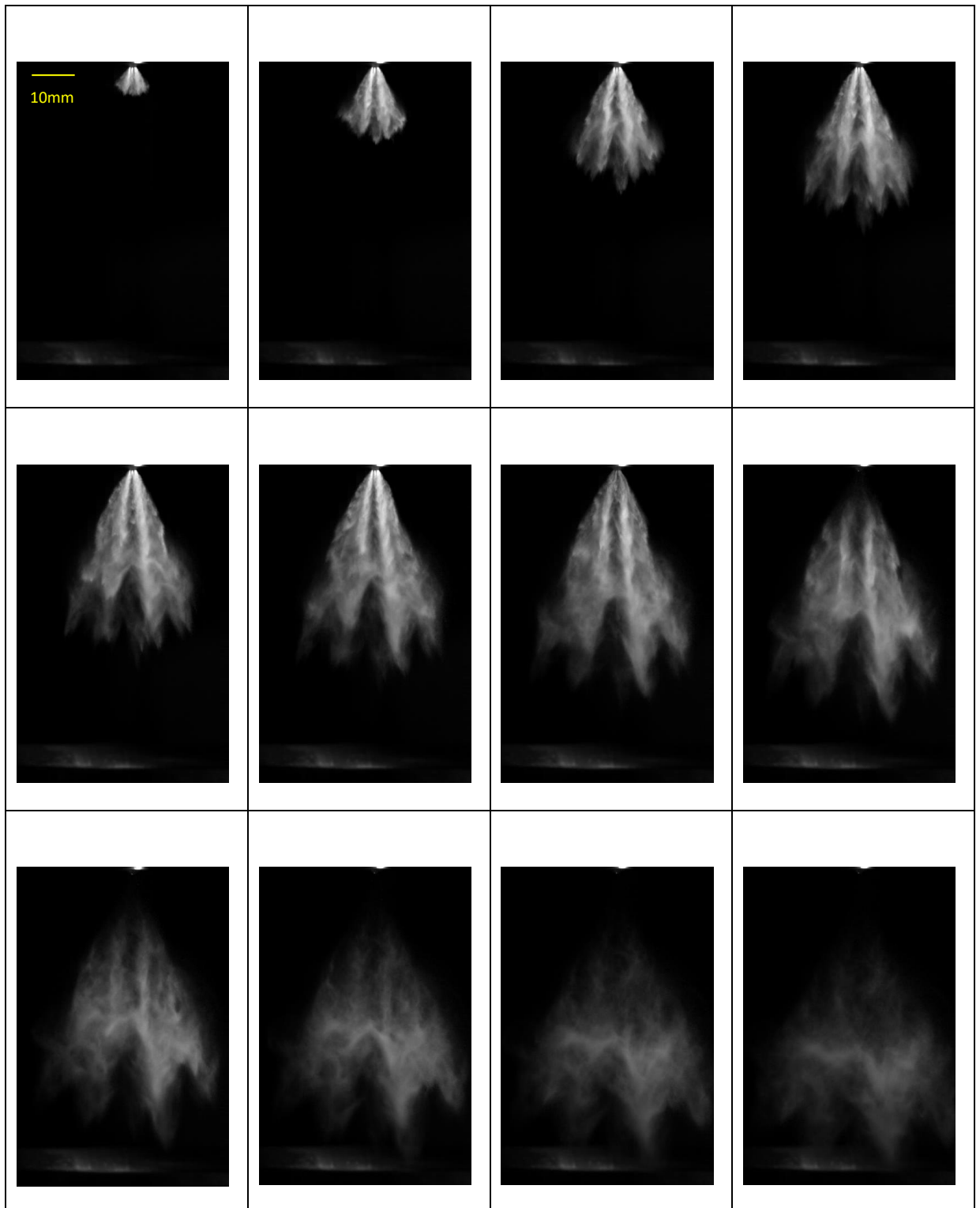
Figure 6-7 Sequence images of the overall spray structure of the stepped-nozzle Bosch injector (#3) at 100 bar rail pressure and 1ms driver pulse duration; the sequence begins at 0.1ms ASOI and continues in 0.1ms time steps.
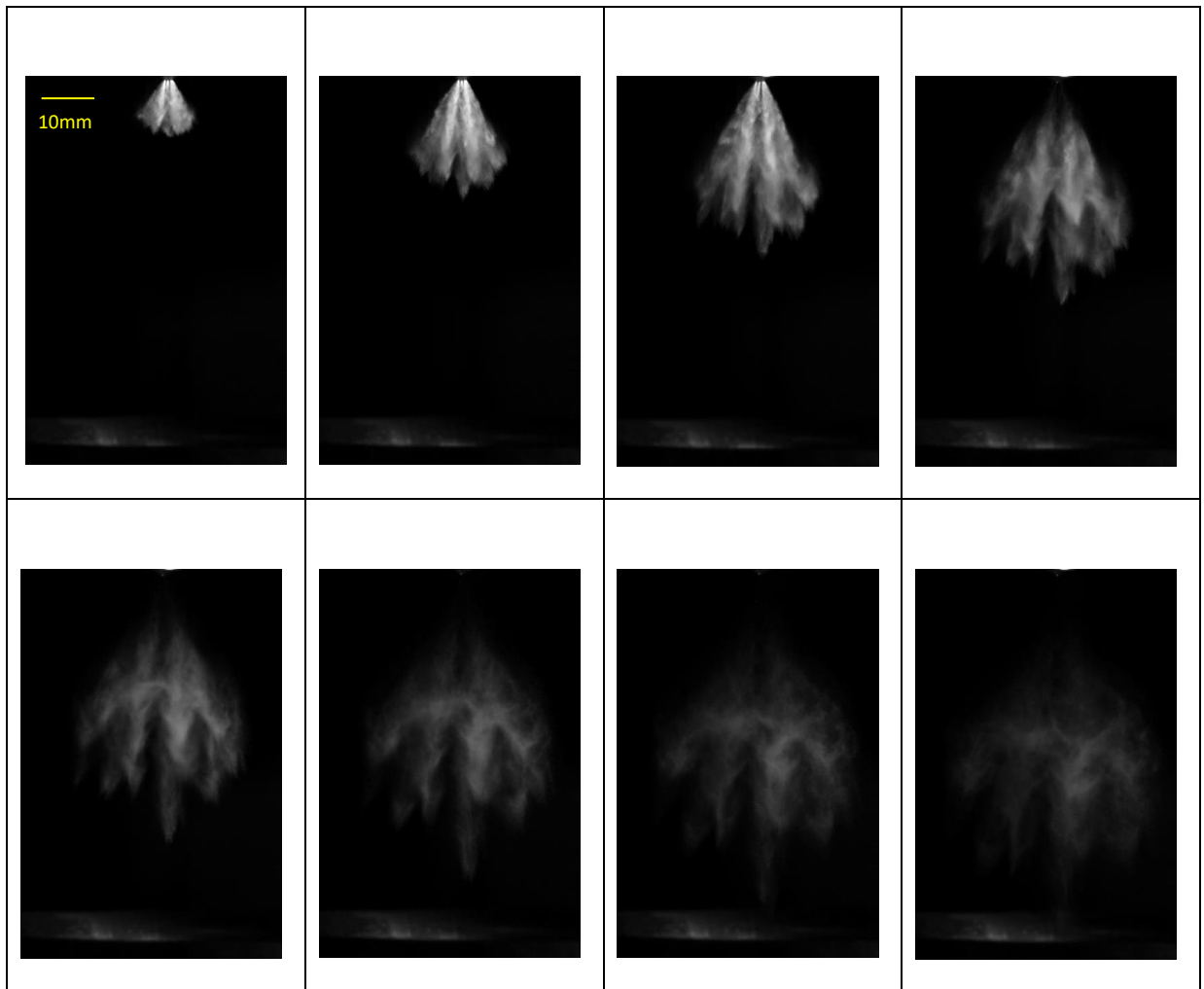
Figure 6-8 The overall spray structure of the stepped-nozzle Bosch injector. The injector is operating at 100 bar rail pressure and 0.7ms driver pulse duration. The sequence begins at 0.1ms ASOI and continues in 0.1ms time steps.

Figure 6-8 shows the overall spray structure of the stepped-nozzle Bosch injector. The injector is operating at 100 bar rail pressure and 0.7ms driver pulse duration. The sequence begins at 0.1ms ASOI and continues in 0.1ms time steps. It could be seen that the spray exhibit a more irregular shape while being injected at shorter duration.

6.5.2 Effects of Varied Injection pressure on spray pattern

Figures 6-9, 6-10, 6-11 and 6-12 shows the spray visualisation of the current injector under investigation (injector #3) at 0.25ms, 0.5, 0.75 and 1 ms ASOI and 2ms driver pulse duration for varying rail pressures. The images are at 120 bar, 60 bar, 40 bar and 20 bar rail pressure, respectively. It is obvious that the pressure increases the tip penetration at similar ASOI time. Figure 6-13 shows the spray visualisation of Magneti Marelli injector (injector #2) at 0.25ms ASOI and 2ms driver pulse duration for varying rail pressures. The images are at 120 bar, 60 bar, 40 bar and 20 bar rail pressure, respectively. Comparing the images of 6-9 and 6-13, it could be seen that at the same conditions, the resultant spray from injector 3 (stepped hole Bosch) is more denser and has high interaction between adjacent jets while the structure of the jets in injector two (Magneti Marelli) is spaced more widely with clear boundary between each jet. It could be seen from figure 6-14 that the penetration of the current injector at 100 bar at 0.25 ASOI (0.9 AESOI) is around 22mm. This is also visually shown in figure 6-9. It could be seen from figure 6-13 that the penetration of injector 2 at the pressure of 120 bar at 0.25 ms ASOI is around 23mm. this shows that injector 2 and 3 exhibits similar performance with respect to tip penetration however it should be mentioned that a direct comparison could not be made between the two injectors here since the internal design of the two injectors are different than each other and also the exact size and angle of the holes of each nozzles are different. It has been shown in [88] that the internal design of Magneti Marelli has a guide for the needle movement which is different than that of the current injector and

can influence the internal flow inside the hole and ultimately the tip penetration of the

spray.
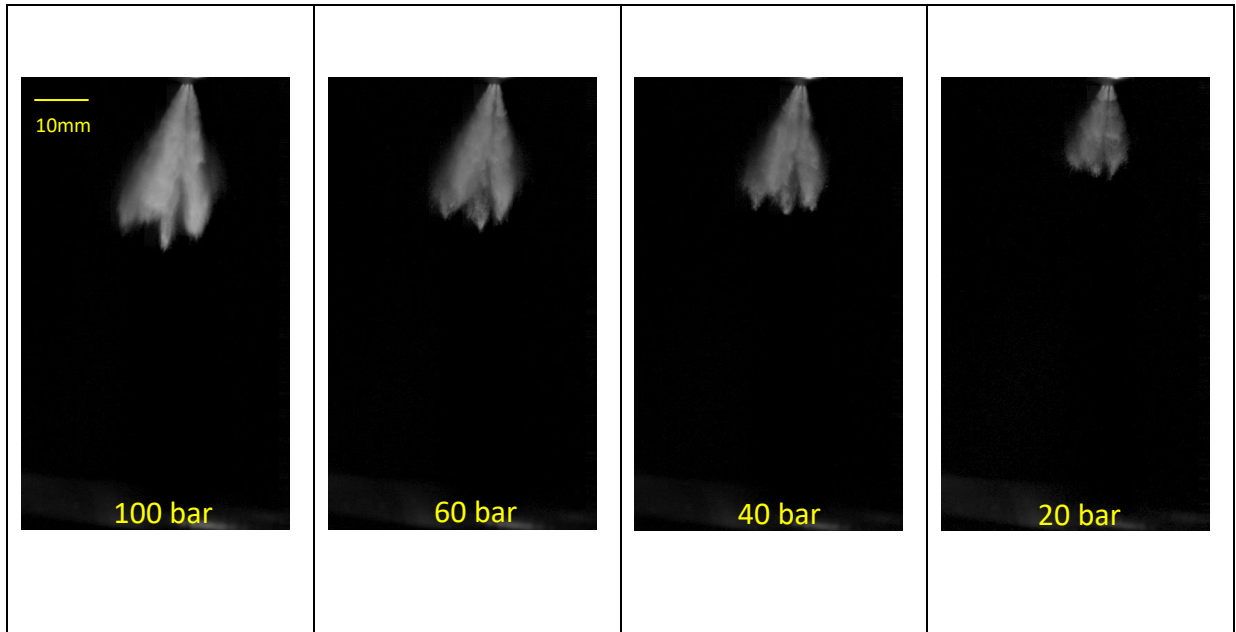
Figure 6-9 The spray visualisation of the injector under investigation at 0.25ms ASOI and 2ms driver pulse duration for varying rail pressures. The images are at 100 bar, 60 bar, 40 bar and 20 bar rail pressure, respectively.
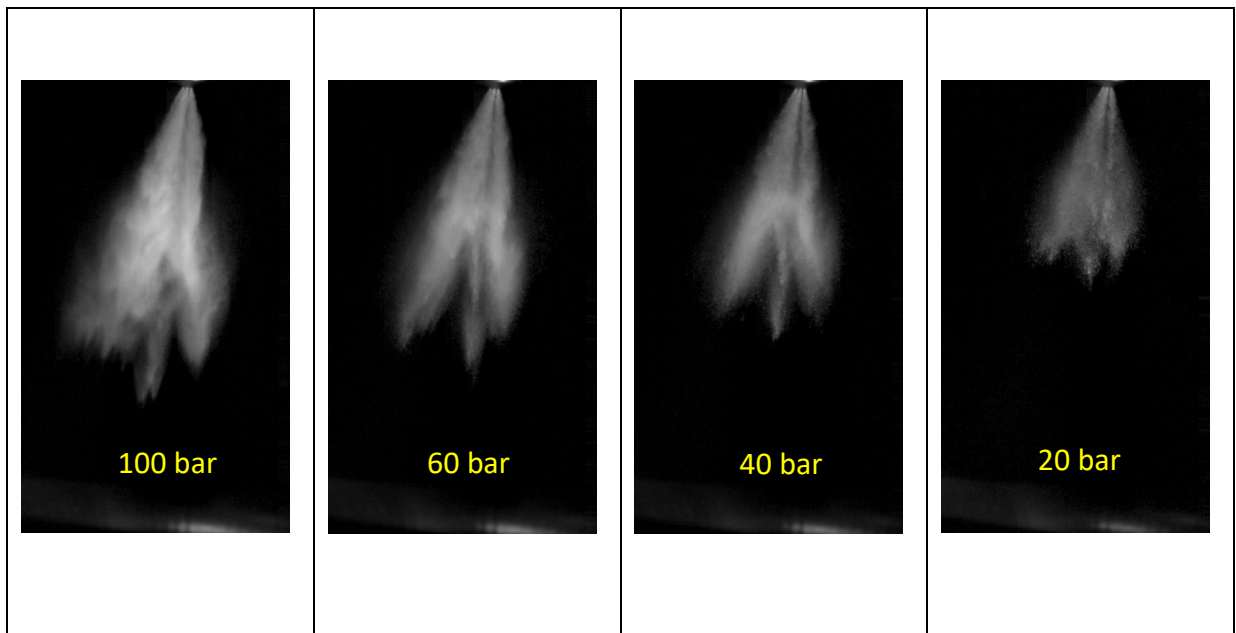
Figure 6-10 The spray visualisation of the injector under investigation at 0.5ms ASOI and 2ms driver pulse duration for varying rail pressures. The images are at 100 bar, 60 bar, 40 bar and 20 bar rail pressure, respectively.
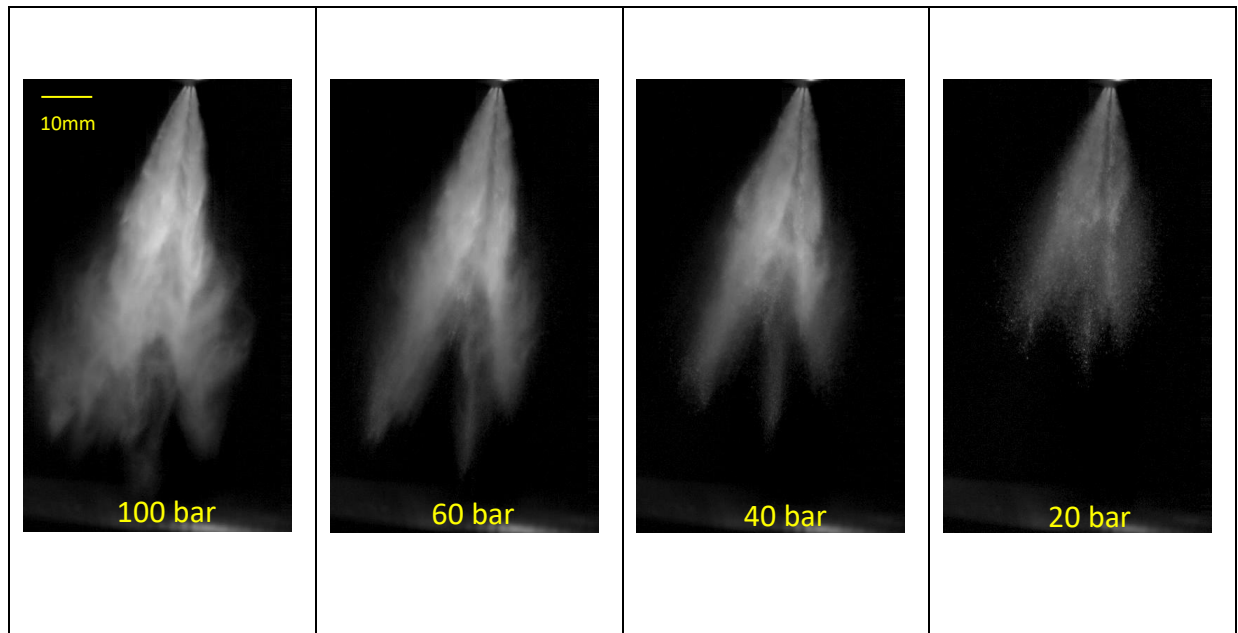
Figure 6-11 The spray visualisation of the injector under investigation at 0.75ms ASOI and 2ms driver pulse duration for varying rail pressures. The images are at 100 bar, 60 bar, 40 bar and 20 bar rail pressure, respectively.
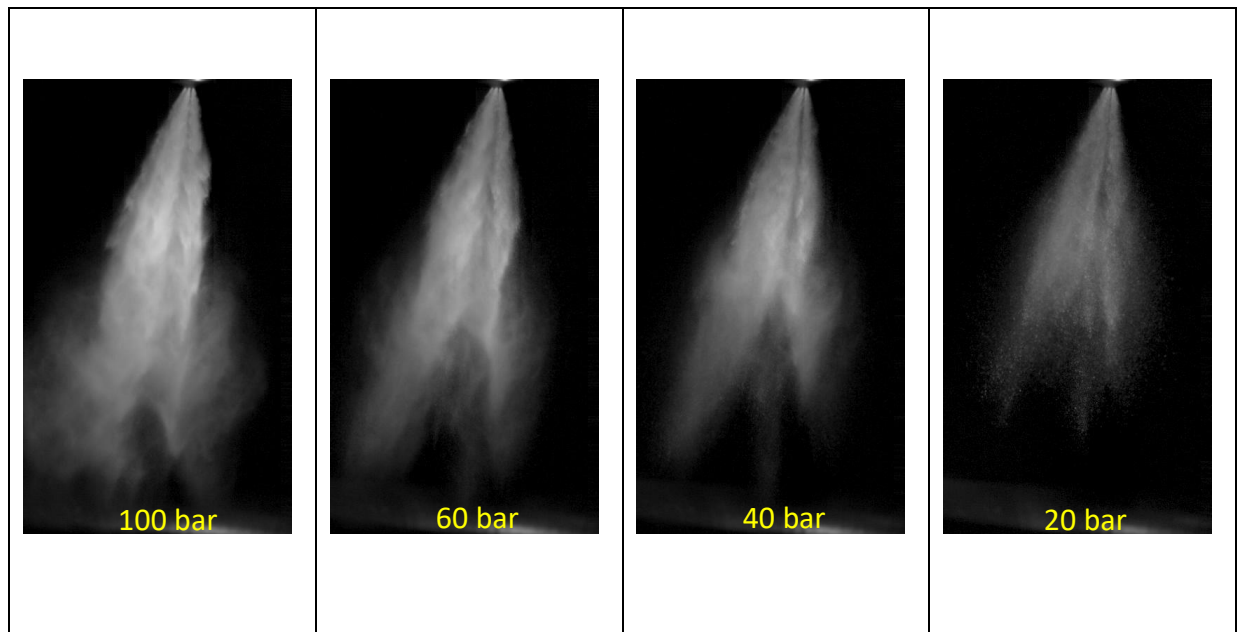
Figure 6-12 The spray visualisation of the injector under investigation at 1ms ASOI and 2ms driver pulse duration for varying rail pressures. The images are at 100 bar, 60 bar, 40 bar and 20 bar rail pressure, respectively.
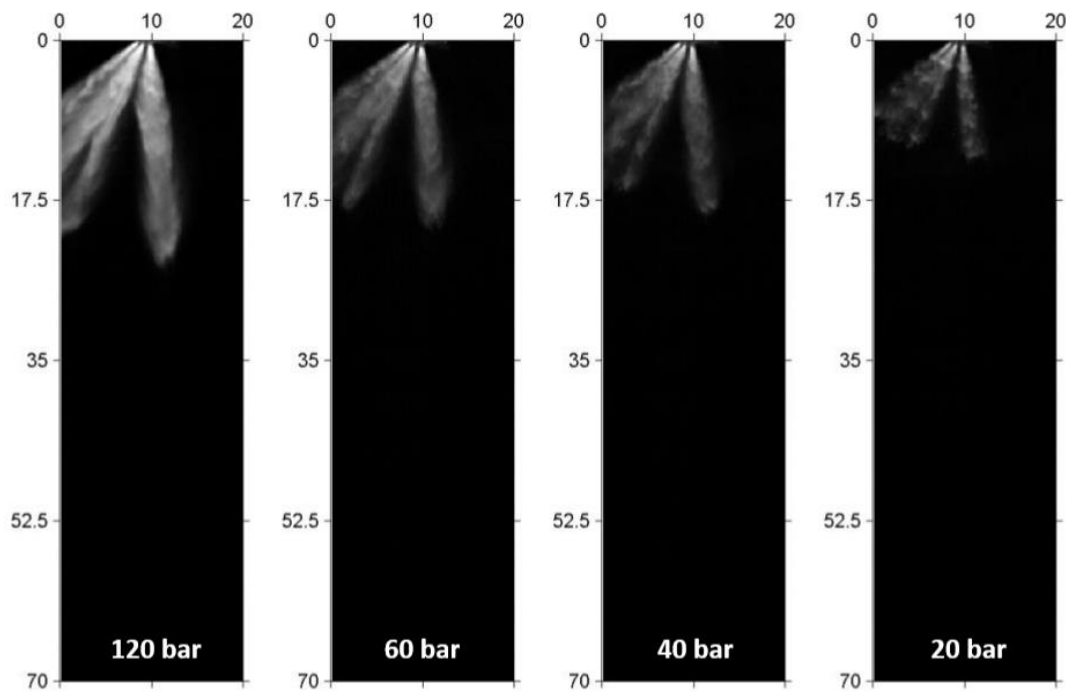
Figure 6-13 The spray visualisation as a reference point for comparison from one nozzle of Magneti Murelli injector (injector 2) at 0.25ms ASOI and 2ms driver pulse duration for varying rail pressures. The images are at 120 bar, 60 bar, 40 bar and 20 bar rail pressure, respectively.

6.6 Spray tip penetration and cone angle

Understanding the changes in the overall cone angle and the spray penetration at varying

injection pressure in multi-hole injectors, is of great importance. There are a few reasons

behind this. One reason is that during the late compression injection event (stratified

mixture) when the spray will travel towards the piston with a speed comparable with the

piston speed and possibility any spray impingement on the piston cylinder, which could

result in unburned hydrocarbon production and incomplete combustion. Another reason

is again to prevent impingement of the spray plume on the wall of the cylinder for the

homogeneous mixture during the intake injection. Spray penetration should be studied

in order to understand the boundary of the physical spray and the maximum spatial limit

each individual jet can reach in order to fully adapt and utilise the spray pattern inside

the combustion chamber. Hence, the effect of varying injection pressure will be first investigated in the next section. The injection pressure of 50 and 100 bar was investigated.

6.7   Effects of Varied Injection pressure on maximum spray tip penetration

The effect of injection pressure on the spray penetration has been examined in this section. It is important to characterise the tip penetration as a function of time in order to obtain a good set of experimental result that could be used as a reference for verification of theoretical models.

In figure 6-14 the spray penetration for two different pressure of 50 bar and 100 bar is shown. It can be seen that the spray penetration has higher values when the pressure is 100 bar compared to the curve of 50 bar. These figures have been obtained from average of 50 injections in Matlab Software. It could be seen in the figure that the slope of both curves are steeper from 0.8ms AESOI (0.15ms ASOI) until 1.2 ms AESOI (0.55ms ASOI) . From 1.2ms AESOI onwards there is a slight decrease in the slope of both curves. This happens at the distance of 30mm away from nozzle for the pressure of 50 bar and at the distance of around 40mm away from nozzle with 100 bar pressure. This slight decrease could be due to the the aerodynamic drag of the ambient air which can reduce the speed of the fully atomised droplets significantly. The calculations for the standard deviation for the spray tip penetration was done for 50 images for each local ASOI times and are shown in figure 6-14.

The equation for calculation of the standard deviation is:

$$S = \sqrt{\sum \frac{(x-\bar{x})^2}{n-1}}$$ **Equation 15**

As an example, for 1ms ASOI the standard deviation was calculated from the penetration values of 50 images to be 2.1mm at 100 bar injection pressure.
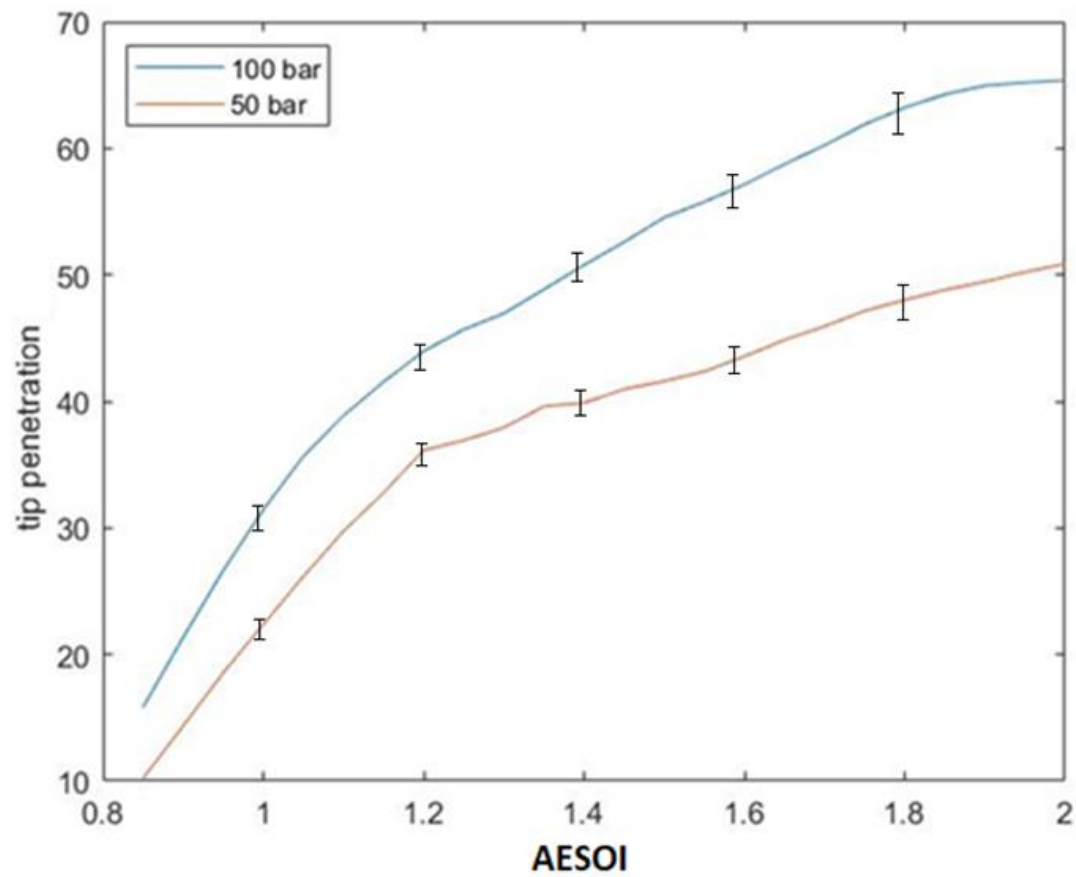
Figure 6-14 Comparison of the jet tip penetration(mm) at injection pressures of 50 bar and 100 bar.

In another effort the spray tip penetration for the three regions shown in figure 6-15 was obtained and compared with each other. The combined results are presented in Figure 6-16.
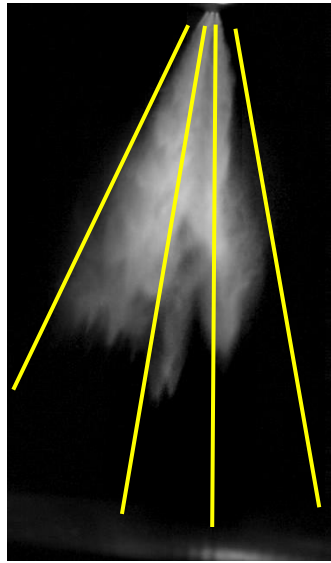
Figure 6-15 Schematics of the spray tip penetration in the case of multiple axial tip penetration in 3 different regions

It is clear from Figure 6-16 that the penetration in the centre region is the maximum in any time ASOI. However, it could also be seen that the right region has a slightly higher penetration than the left region. This is ofcourse expected due to the the difference between the angles of each jet plus the difference in the discharge coefficient for each hole under turbulent conditions and also perhaps existence of a flapping central jet which affects the adjacent jets around itself.
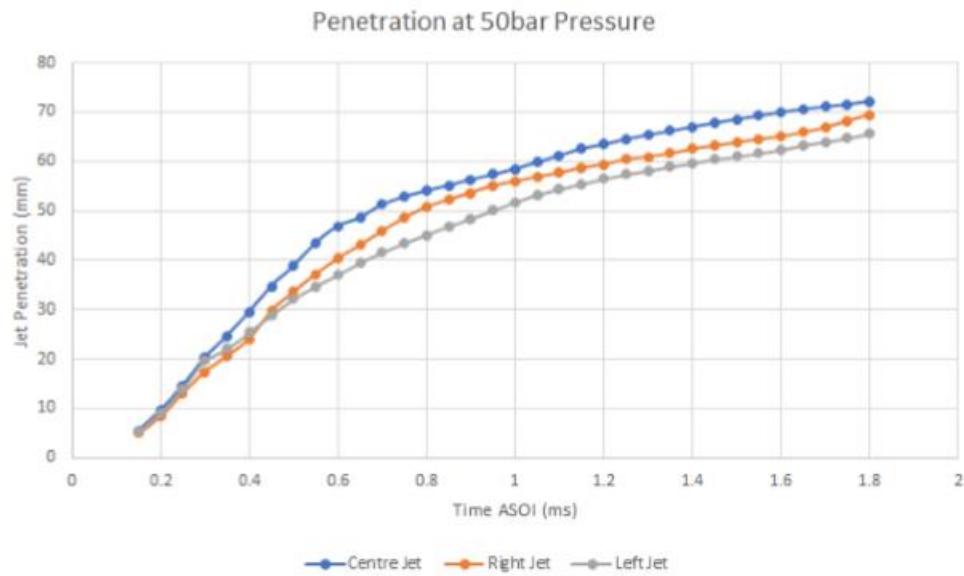
Figure 6-16 The spray axial tip penetration for 3 different regions at 50 bar pressure. It is clear from the images that the center region has higher tip penetration compared to the right and left regions.
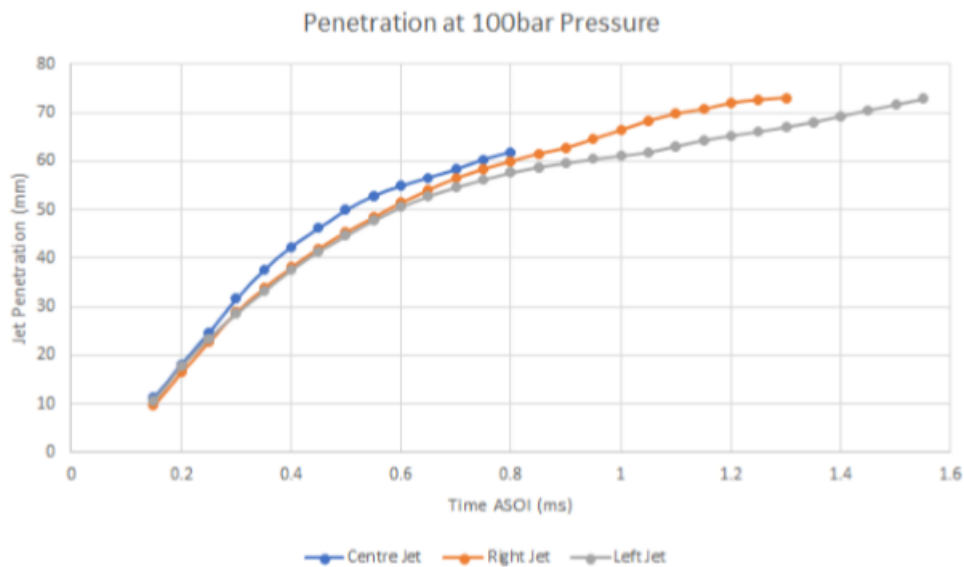
Figure 6-17 The spray axial tip penetration for 3 different regions at 100 bar pressure. It is clear from the images that the center region has higher tip penetration compared to the right and left region.

6.8   Effects of Varied Injection Pressure on Spray Cone Angle

It is also important to investigate the effect of injection pressure on the spray cone angle. This is particularly of importance because the spray needs to be injected in the combustion chamber in a side-mounted position and the overall cone angle determines the range over which the fuel is translated and mixed with air inside the combustion chamber. This is important for fuel mixture preparation in the combustion chamber and reaching a stoichiometric combustion in homogeneous mode. It is also important for stratified combustion mode when a short duration spray is injected closed to the vicinity of the spark plug. Any instability in the cone spray angle can perhaps cause misfires or unburned hydrocarbons which is not ideal for a complete clean combustion.

Figure 6-18 shows cone angle for the spray at pressure of 50 and 100 bar at different ASOI times. It could be seen that the average spray cone angle for 50 bar was found to be 63.2 degrees. This was 72.1 degrees at 100 bar. There was an increase of around 9 degrees from 50 bar to 100 bar. For mean calculation for each graph, 50 images were analysed for each ASOI time. The standard deviation was also obtained from equation 16 for each case. The maximum standard deviation for the sample mean was found to be 0.12 degrees.
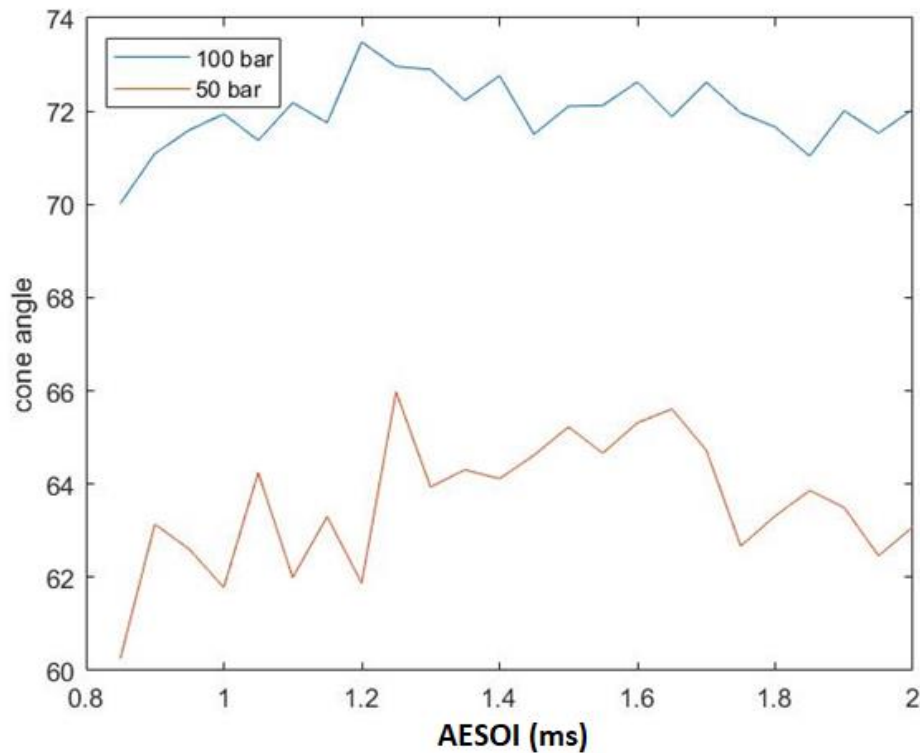
Figure 6-18 Spray mean cone angle measurement

6.9 Mie scattering of near nozzle at different angles

In this section, the near-nozzle Mie scattering visualisation of 3 jets of the spray at different angles of 0, 20, 90, and -90 configuration will be shown. At the beginning, the nozzle design was studied under the microscope with high magnification ratio. The injector was rotated at different angles and the spatial change in the location of the nozzle hole configuration was studied. This was important to obtain a better 2D understanding of the position of each of the jet spray at the near-nozzle area. Figure 6-

19 shows a magnified photo of the tip of the injector and the hole that was under investigation.
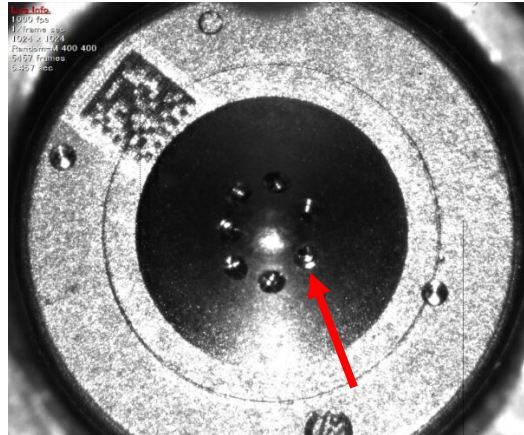
Figure 6-19 shows a magnified photo of the tip of the injector and the hole that was under investigation.

Using this information, one can better isolate the jets when for visualisation, shadowgraph and PDA measurement. This is important for the next section where in the shadowgraph configuration the jet cone angle will be analysed. In addition to this, the shape and size of the core jet can approximately be measured using both Mie scattering and shadowgraph technique. this data will be used in PDA measurement in the next chapter.

In general, the individual spray jet angle can be calculated by isolating one of the sprays. As this was not possible in the experiment due to the very narrow spacing configuration of the nozzle holes, two of the spray jets were isolated and overlapped on each other and the jet angle was calculated for them. This is clear from the figure 6-20 a) below which shows the 0 degree configuration.
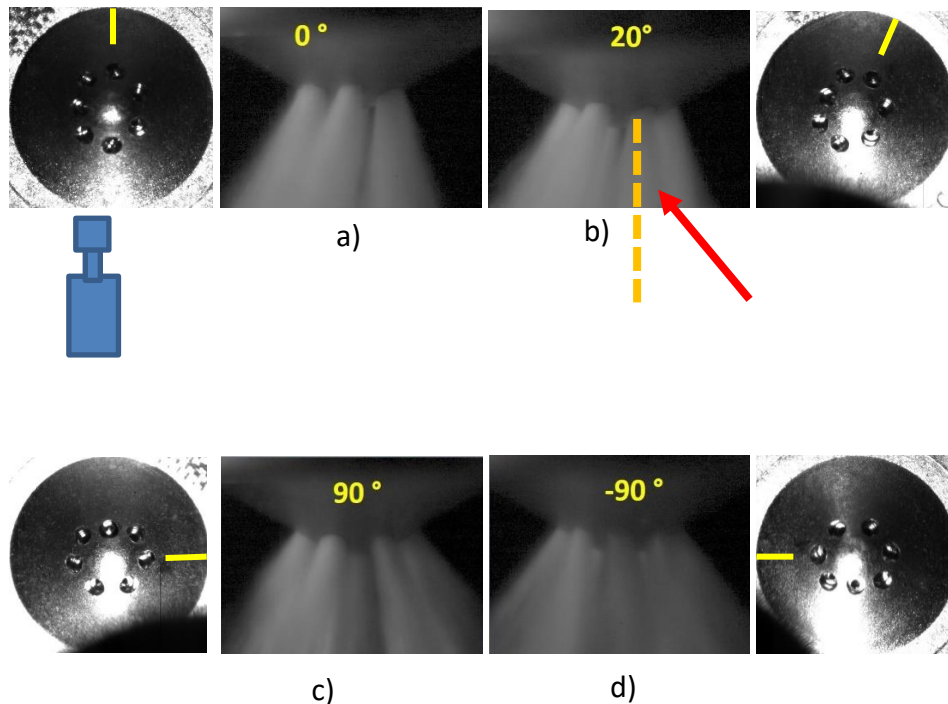
Figure 6-20 shows the tip of the injector was photographed under high magnification condition in order to obtain the best angle for spray visualisation, shadowgraph and PDA measurement.

6.10 Shadowgraphy of near-nozzle jet spray (0 angle)

Figure 6-21 shows examples of high speed Mie scattering technique and near-nozzle shadowgraphy used to visualize the spray structures in order to obtain qualitative characteristics of the spray and more importantly to prepare the test rig for PDA measurement. In addition to this, the shape and size of the core jet can be measured optically and this data will be used in PDA measurement in the next chapter.
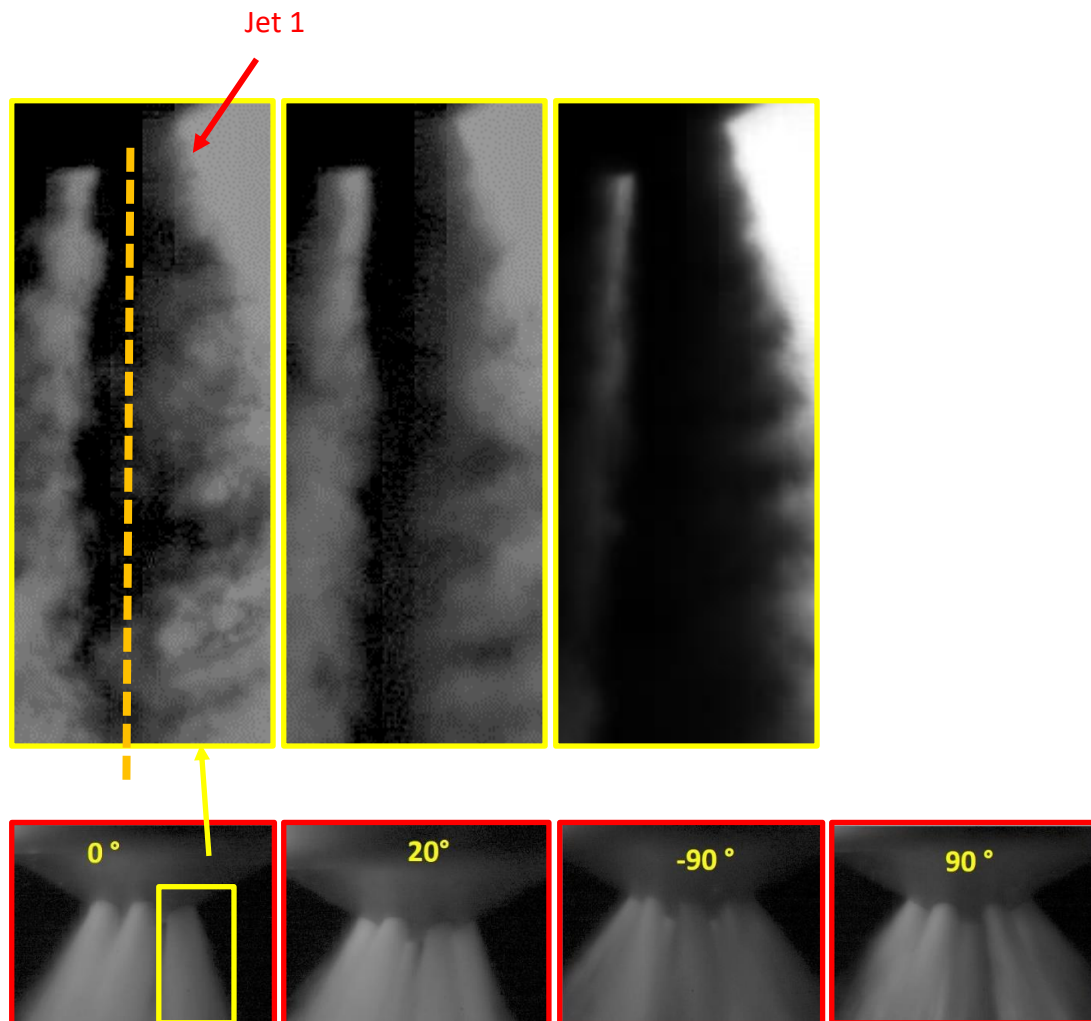
Figure 6-21 Examples of high speed Mie scattering technique and near-nozzle shadowgraphy used to visualize the spray structures

In this section, the near-nozzle shadowgraphy visualisation of the spray at 0 angle configuration is briefly presented. This study is important to understand the location of each jet at the very-near nozzle vicinity of the tip of the injector. At the beginning of the injection, a shadowgraph of 3-hole nozzle configuration has been studied as in figure 6-

22. For the first step, the near-nozzle shadowgraph setup was configured in a manner that the tip of the injector would be visible.
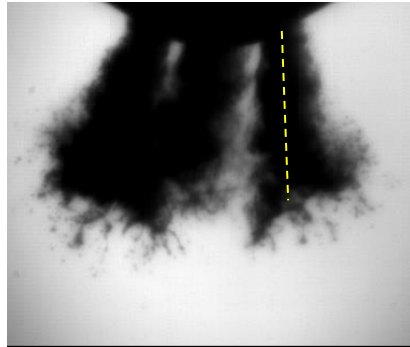
Figure 6-22 Shadowgraphy of 3 jet near the nozzle

It can be seen from figure 6-22 that the tip of the spray is fairly atomised with small droplets sharply visible in the image. It is also evident that jet 1 is almost vertical from this view. Later on when conducting PDA measurement, axial component of the jet 1 is calculated using PDA system. Also one can find information about the standard deviation of the changes in the edge of the near-nozzle jet spray. It could be seen from figure 6-23 that there is high fluctuations in the brightness of the images at the edge of the spray.
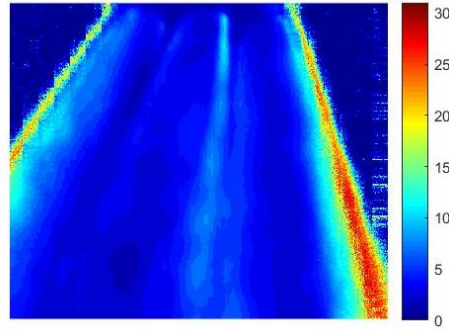
Figure 6-23 Brightness fluctuation of the stochastic ligament spray region

(a)   (b)   (c)
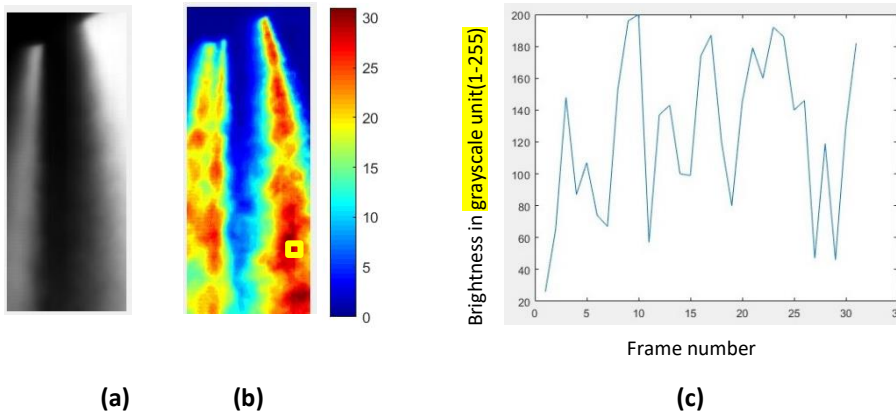
Figure 6-24 (a) Average of 100 images of shadowgraph of the near-nozzle jet spray at 50 bar (b) Falsecolormap of the standard deviation of the Brightness fluctuations at the edge of the jet 1 which shows that the maximum standard deviation is around 30. (c) Temporal variation of the fluctuations of the brightness from 20 to 200 at a point highlighted in yellow square in figure 6-24 (b). Here 0 is assumed to be pure black and 256 is pure white. The Matlab code is given in the appendix.

Figure 6-23 shows average of 100 images of shadowgraph of the near-nozzle jet spray at

50 bar. It can be seen that both edge of the spray are visible and therefore a Matlab

analysis was performed in order to obtain the level of fluctuations in the brightness of

the pixels which is shown in figure 6-24 (b). Falsecolormap of the standard deviation of

the brightness fluctuations at the edge of the jet 1 shows that the maximum standard

deviation is around 30. Figure 6-24 (c) presents the temporal variation of the fluctuations

of the brightness of the highlighted yellow point in figure 6-24 (b). It is clear from figure

6-24 (c) that the brightness values vary from 20 to 200. Here 0 is assumed to be pure black and 256 is pure white. This is expected as the edge of the spray has lower velocity and is less denser and therefore the fluctuations of the brightness is higher compared to the core of the spray.

6.11 Impingement at different heights

In this section, the impingement of the spray on the transparent surface will be visualised using a novel method that utilize simultaneous visualization of the impingement phenomena from side view and bottom view using one camera in order to find the approximate x,y coordinates of the centre of the jet 1 plume at the early stage of impingement after the impact on the transparent surface. In order to do this, two transparent glass was grided and was configured 90 degree with respect to each other according to figure 6-25.
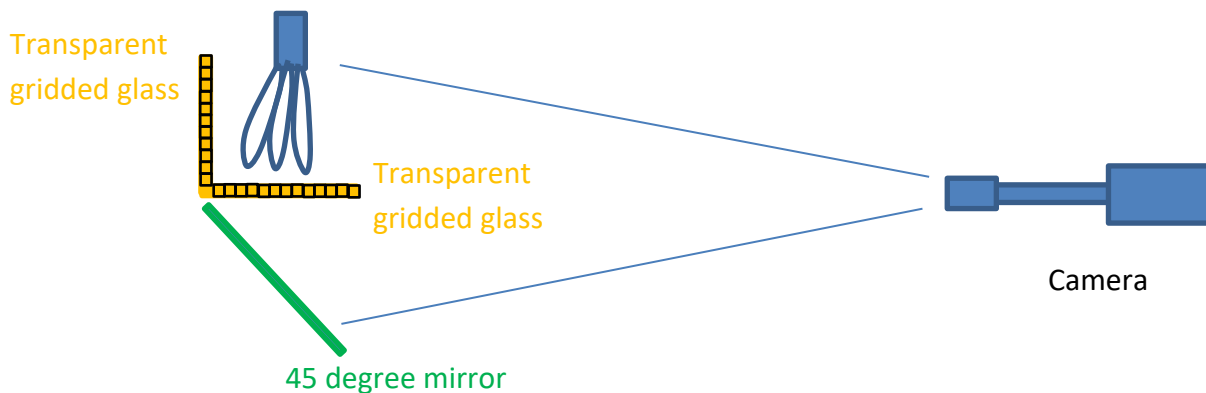
Figure 6-25 Configuration of two transparent gridded glass which allowed simultaneous visualisation of the spray impingement from two different views

The results of the early stage of the spray impingement are shown in figure 4-26.

(a)   (b)   (c)
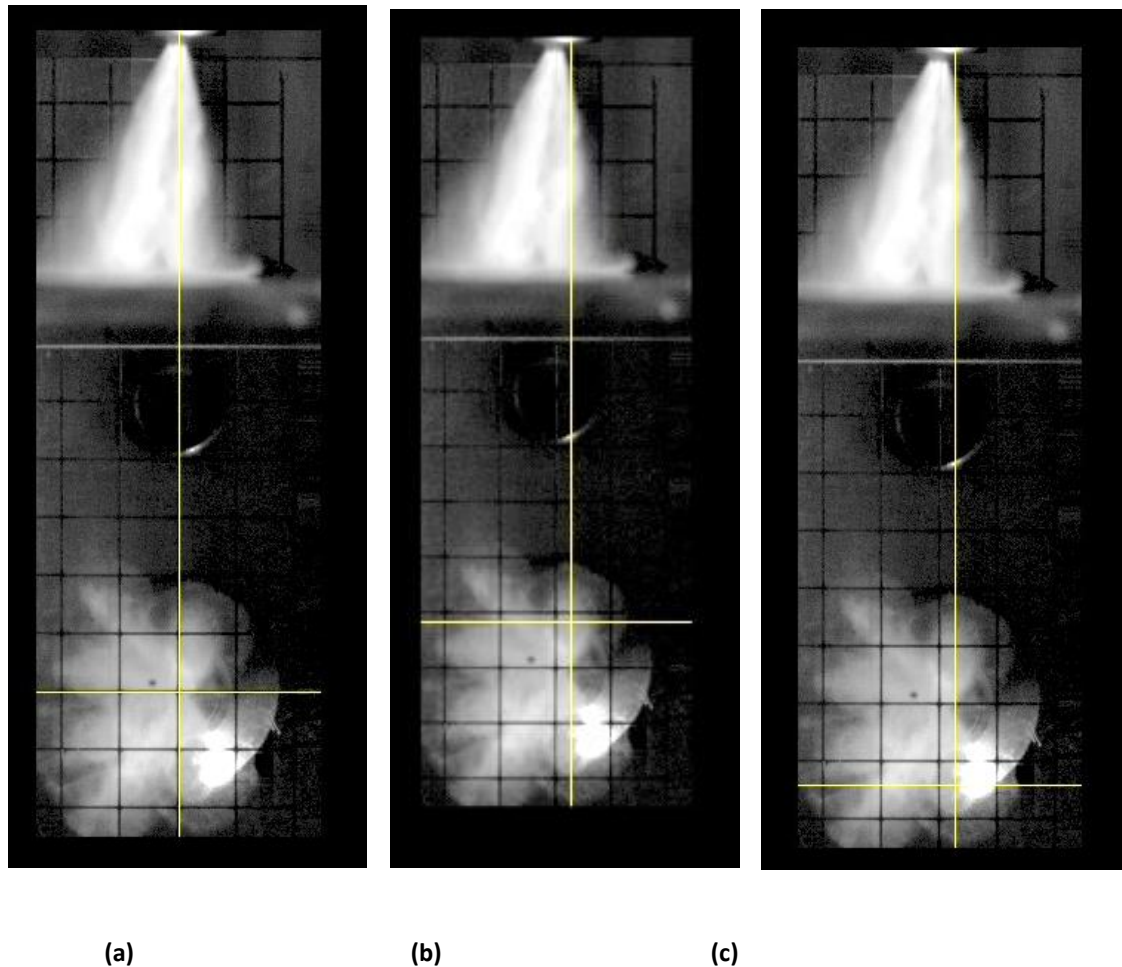
Figure 6-26 Impingement of the spray from side view and bottom view: (a)The mirror was perfectly aligned in such a way that the grids in both view are aligned with each other. The yellow line in (a) extends and aligned with bottom view which shows the centre of the injector (b) impingement of the upper right jet is shown (c) impingement of the lower right jet is shown which is jet 1 under investigation. The tilting angle is around 5 degrees.

In order to obtain the centre of impingement further qualitative analysis was conducted.

Figures 6-27 to 6-29 shows the impingement of the tip of jet 1 on the transparent plate

which was fitted in order to obtain qualitative information about the location of the core

of jet 1 when it impinges on the plate at different ASOI times and at different distances.

It is clear from figure 6-27 that the angle of the centroid of jet 1 at the early stage of

impingement at the height of 20mm is measured to be approximately 250 degree with respect to horizontal line. Therefore, the rotation angle of 360 – 250 = 110 degree is necessary in order to isolate jet 1 in a manner that can provide maximum exposure for receiving optics for the PDA measurement. This angle has been measured in other heights of 30mm and 40 mm and the results are approximately 250 degrees which is similar to 20mm height.
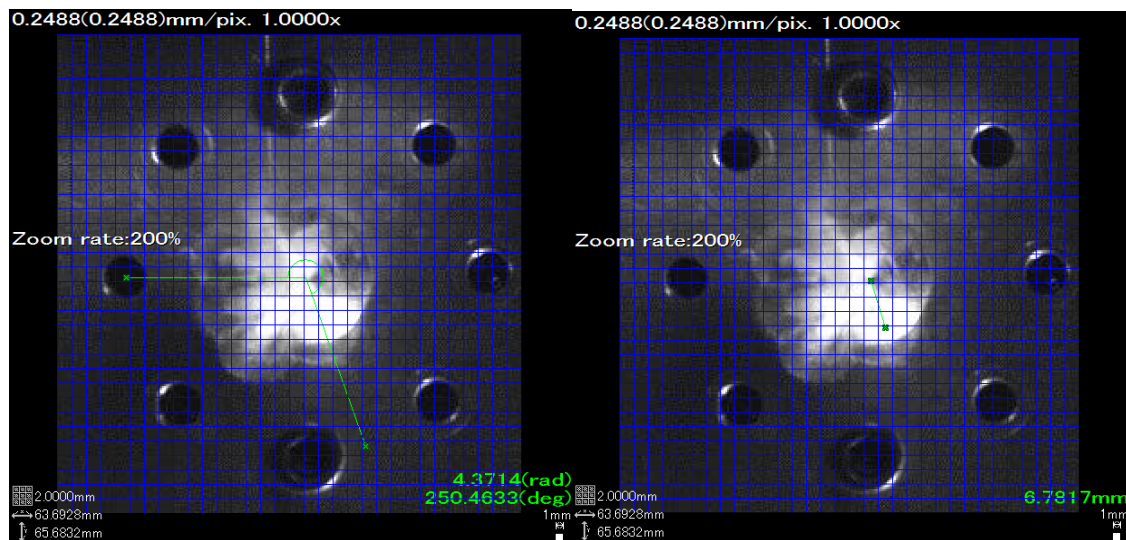
Figure 6-27 Angle of the optical centroid of the isolated jet impingement on the flat surface at 20mm distance away from the tip at 0.35ms ASOI
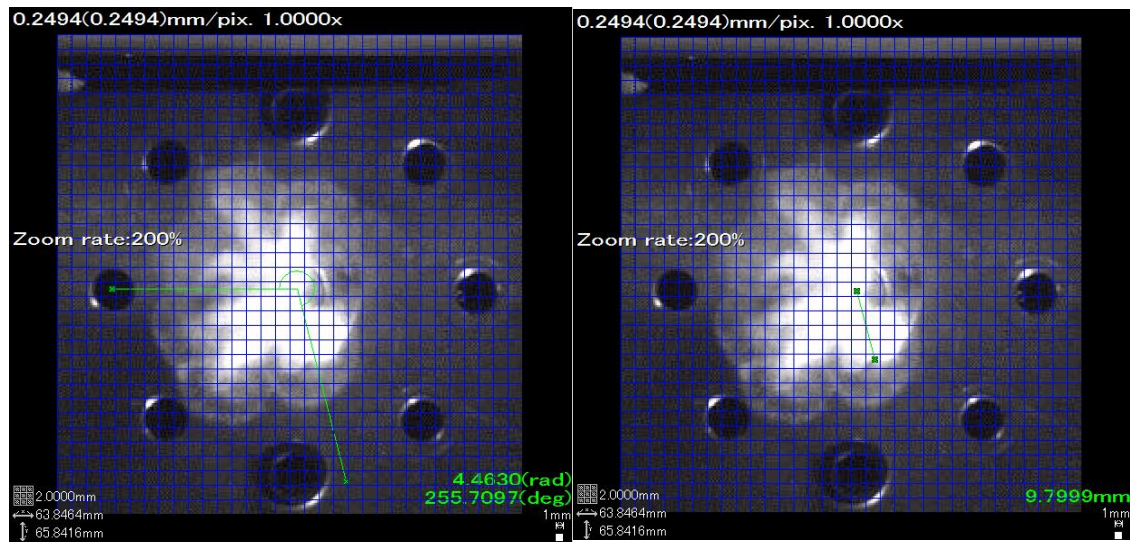
Figure 6-28 Angle of the optical centroid of the isolated jet impingement on the flat surface at 30mm distance away from the tip at 0.5ms ASOI
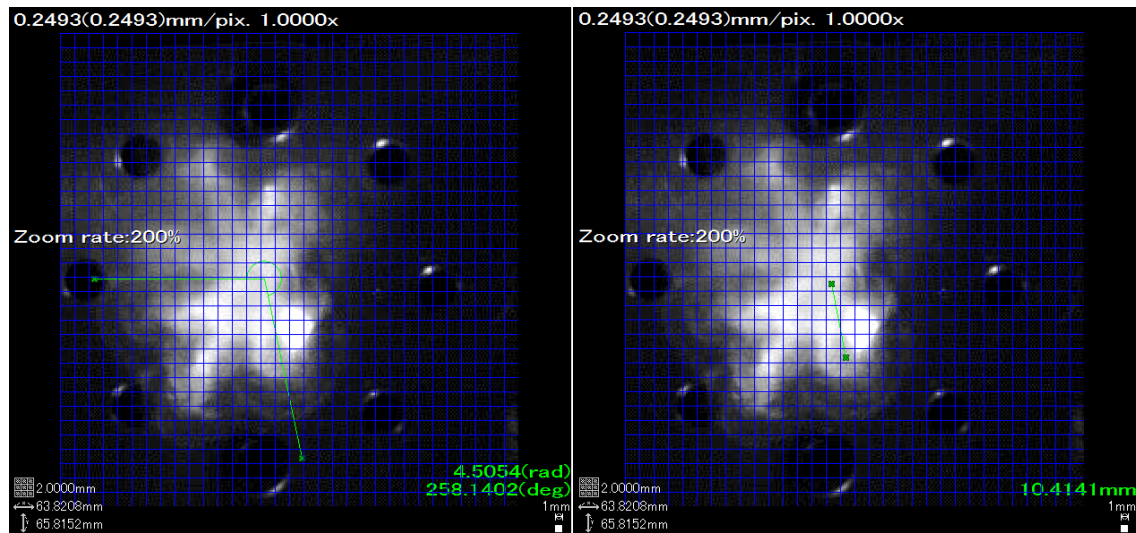
Figure 6-29 Angle of the optical centroid of the isolated jet impingement on the flat surface at 40mm distance away from the tip at 0.8ms ASOI

6.12 Summary

In this chapter, a real-size injector test rig was designed and manufactured using SOLIDWORKS which enabled the stepped injector to rotate along the axis of the needle 360⁰ freely and allowed high-speed visualization of the spray plumes from different angles. It also enabled the measurement of the spray cone angle from different angles. It further allowed the investigation of the full spray structure, near-nozzle and very near-nozzle exit spray behaviors by means of visualization and helped to setup the PDA system for in the next part of the experiment. The new findings of the spray visualisation are:

- The core of the jet is wider compared to conventional injectors has a more irregular pattern in the fully developed mode

- Two middle jets are flapping from one side to another side creating a snake shape pattern.

- The structure of the spray in the fully developed mode exhibits an A shape which is believed to be due to the compact and dense nature of arrangement of hole which allow higher interactions between the adjacent jets and high air entrainment in-between each individual jets.

- It was observed that there is high interaction between each jet and the adjacent jet and therefore a distinct boundary between each jet is not recognisable as the spray develops further downstream in comparison with conventional multi-hole

where there is a clear boundary between each jet and less interaction is visible between each individual jets.

- The overall jet penetration of the stepped hole Bosch injector (injector #3) was compared with conventional straight-hole Bosch injector (injector #1). It was seen that at ASOI of 0.75ms (AESOI 1.5ms), the tip penetration for the stepped hole nozzle was around 50mm which was similar to the tip penetration for the conventional multi-hole at the same ASOI. Due to the fact that the exact size and angles of the stepped-hole nozzle was not provided, it is not possible to directly compare the penetration together but discarding the internal design, it could be claimed that both injectors are operating within same range in terms of tip penetration.

- The overall jet penetration of the stepped hole Bosch injector (injector #3) was also compared with Magneti Marrelli stepped hole injector (injector #2). It could be seen that the of the penetration of the stepped hole Bosch injector at 100 bar at 0.25 ASOI (0.9 AESOI) is around 22mm which is similar to the penetration of stepped hole Magneti Marrelli injector at the pressure of 120 bar at 0.25 ms ASOI which is also around 23mm. It should be mentioned that a direct comparison could not be made here again since the internal design of the two injectors are different than each other and also the exact size and angle of the holes of each nozzles are potentially different. However disregarding these facts, it could be

seen that both injectors are operating more or less at the same range in terms of tip penetration.

- It could be seen that as the pressure increases from 50 bar to 100 bar the spray cone angle increase from around 64 degree to 72 degrees. It can be seen that the range of variation of the spray angle for all cases is around 2-3 degrees.

Chapter 7: PDA measurement of the spray in Real-size High-pressure Experimental Test Rig

7.1   Introduction

In this chapter the results of the PDA measurement of the spray will be presented and discussed. The coarse grid measurement results will be discussed first, followed by the fine grid measurement to provide the overall behavior of the spray in terms of droplets axial velocity and size distribution in x-y plane at different axial (z) locations. Temporal and spatial distributions of droplets axial velocity and diameter will be presented next for different y-locations and at different z-locations to quantify and characterize the performance of the injector. The weber number at the maximum velocity points (core of the spray) at each z location will be discussed and compared with previous works. Temporal profiles present the variation in droplet velocities and diameters throughout the injection process, over a time window of 0.1 ms, at a given measuring point that is located along x or y axis of the jet. Spatial velocity profiles/contour plots present all measuring points located at a cross-section of the jet at certain time after the electronic start of injection (AESOI) that is representative of the entire injection process.

7.2   Coarse grid results

In a polar cylindrical coordinate system, a droplet can have two velocity components. One is axial component, which is parallel to the z axis, denoted as V_z, which corresponds to LDA1 signal. Another is the radial component which, denoted as V_r, can vary in any direction in the (x,y) or (r,θ) planes. As mentioned before in methodology chapter, in this study a 2-D component (orthogonal) PDA system was used and it was aligned with spray axis in such a way to measure the V_z component directly, and the other component V_r (LDV4 signal) would be a combination of x,y or r,θ components. ; LDA4 signal calculates the velocity which is perpendicular to the blue beams. Since the tilting angle is around 5 degrees, the magnitude of the axial component V_z (LDA1) on average could be around 9 times bigger than that of the radial component, V_r (LDA4), and only the axial velocity measurements has been reported.

The first round of the measurement involved setting up the traverse for coarse grid measurement of an area of 2mm x 4mm (this area is called region 1) at the distance of 1mm below the nozzle exit with grid length of 0.4mm in both X and Y directions. The adopted co-ordinate system is shown in figure 7-1(a) with its origin (0, 0, 0) on the injector axis as shown in figures 7-1(a) and (b). The selected region 1 is shown in figure 7-1 (b), which covers the three adjacent spray jets 1, 2 and 3. Figure 7-1(c) shows the contour plot of axial velocity at z=1mm. It was necessary to obtain this contour velocity plot to find the approximate location of the high velocity core jets and the geometry and shape of the cross section of jets. The plot also provides information of jet spray

interactions and also identifies the relative positions of jet 2 and 3 as shown in figure 7-1(c).

As it can be seen from figure 7-1(c), the traverse started to measure from the point at the bottom left corner (x=-2mm, y=-2mm) on a 11 x 6 grid (11 points along x and 6 points along y direction) and finished the measurement at the point of (2, 0) at the top right corner. In this configuration, the PDA system was able to measure up to 66 points, and at each point 10000 sample data were collected.

From figure 7-1(c) the core of the three jets can be clearly identified with maximum velocity regions of up to 90m/s as shown in red color. The region which is in dark blue color corresponds to lowest velocities i.e. 0-10 m/s which means there is no physical droplet/jet spray within this region. The pale blue contour corresponds to velocities of up to 30 m/s which could be considered as the edge of the spray where the interaction between aerodynamic drag forces of the ambient stagnant air and the moving spray droplets are taking place and can be contributed to air entrainment. The green contour plots are densely spaced which shows the highest velocity gradient region of the spray increasing from 30m/s to 70m/s over a short distance and ultimately reaching 90 m/s at the core of the sprays. The approximate coordinate of the core of jet 1 is assumed to be a point inside the red/amber region with highest velocities ie (-0.4 ± 0.2, -0.9 ± 0.2). The error of ± 0.2 is due to the grid size which will be reduced to ±0.025 when using a finer grid in the next section. Another observation is that the center of jet 2 and 3 are in symmetric positions in accordance to their physical position as shown in the figure 7-

1(b). The coordinates of the center of jet 2 is approximately located at the point (1.5, -0.4) while the center of jet 3 is located at the point of (-1.5, -0.4). This shows that these two jets are aligned horizontally with respect to the x axis and this can possibly provide maximum visibility for the probing volume while scanning jet 1 at the very near-nozzle distance of 1mm.

By further observing figure 7-1(c), it can also be seen that jet 1 and 2 has higher velocities compared to jet 3. Considering the coarse grid that was used for this measurement, this could be partially due to the fact that the measuring point may have not been exactly located at the core of the jets, and partially due to the longer scattering optical path for jet 3 (see figure 7-1(b)) causing more attenuation in scattered light coming from jet 3 as it has to pass through the dense jet spray 1 before reaching the photodetector, and thus weaker signal and less validated data from it compared to jets 1 and 2. Another interesting observation is the interaction region between jets 1&2 and 1&3 where the results show uniform velocity distribution with average droplet velocities of 60 m/s.
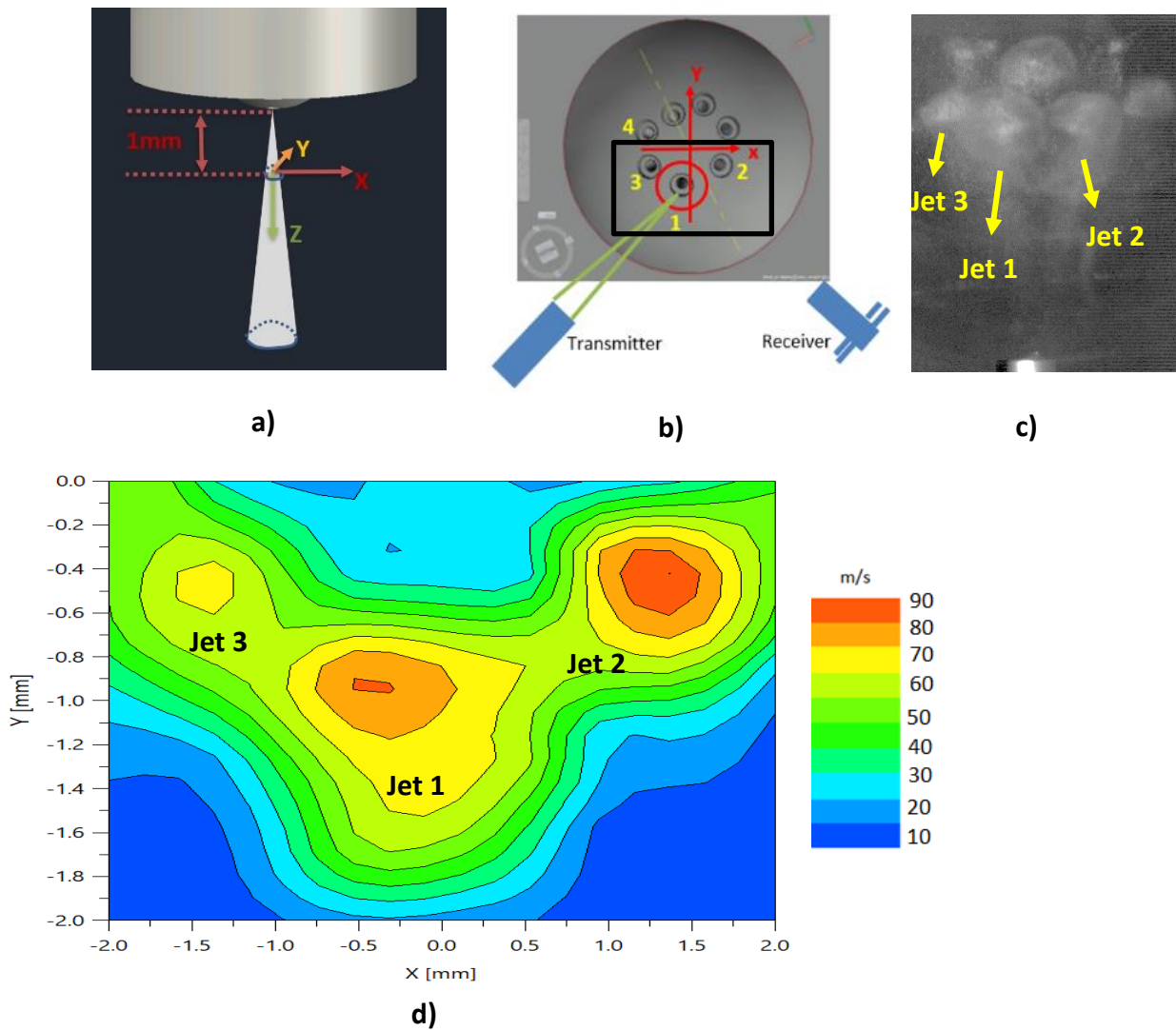
Figure 7-1 Coarse grid measurement set up. (a) Coordinate system at z=1mm; (b) multi step nozzle holes layout; (c) Impingement on a 45 degree plate showing tilting anle of 5 degrees from side view d) Contour plot measurement of axial velocity distributions, averaged over the entire injection period, for the three spray jets at z=1mm, 100 bar injection pressure and 2ms injection duration.

It should be mentioned that the velocity information which is shown in the contour plot of figure 7-1-(c) is the time-averaged velocity of all the data that has been obtained over the complete cycle of injections of 2ms from start to finish which includes the opening and the end of injection velocities. This indicates that the maximum temporal velocity that a droplet will obtain during the main injection event ie at 1.5ms after electronic start

of injection (AESOI) could be higher than the time-averaged values shown in the contour plot. As mentioned in methodology chapter, a novel in-house Matlab code was developed to create the 2-D temporal contour plot of velocities/droplets diameter of the jet as a function of time at each z location in order to compare the instantaneous changes in these values as the jet develops and completes one injection cycle. This is discussed in section 7.3.3.

7.2.1 Coarse grid time-averaged contour plot of velocities

The coarse grid measurement were done for all distances of z= 1mm, 2.5mm, 5mm, 10mm, 15mm, 20mm, and 35mm in the x,y plane. The selection of measurement planes was based on the primary and secondary droplet break-up lengths, which are believed to be less than 2.5mm and 10mm for straight nozzle respectively based on previous works [46]. However it is believed that these lengths are shorter with the step nozzle which can be realized by comparing the spray images near the nozzle exit and more accurately by comparing diameters obtained from PDA from near the nozzle.

This was to obtain contour plots of velocities at different z locations and to plot the temporal and spatial features of the centre of the jet and the relative size and shape of the jet diameter along x and y axis in all z locations. The location of peak axial velocity of jet 1, i.e. maximum V_z, at each z location will be considered as the core center of the jet 1 for the corresponding z plane. The estimated center of the jet 1 is used as a reference point for creation of fine grid contour plots of velocities for each z in order to find a more

accurate position of the centre and to create time-averaged/temporal and spatial 2-D contour plot/graphs of velocities.

Figure 7-2 shows the 2-D contour plot of mean axial velocities for coarse grid measurement in x-y plane at different z locations from z=1mm to z=35 mm for an injection pressure of 100 bar and an injection duration of 2ms; the presented velocities are time averaged over the entire injection period. Careful measurements were taken to find the boundaries of the jet 1 and to identify the diameter of the spray jet 1 along the y-direction within the measuring grid. It can be seen from figure 7-2 that in all contour plots, the pale blue area of the jet is included in the grid length and the blue curve is almost tangent to the lowest limit of the grid with velocities of around 10-20m/s. Contour velocity distributions at different z-locations in figure 7-2 are similar to that described above in figure 7-1(a) for z=1mm, but the magnitude and the location of the core centre are different at each z-location. It is evident from figure 7-2 that the velocities decrease constantly with increase in z so that at the centre of jet 1 the velocity decreased from around 90 m/s at the distance of 1 mm to around 40 m/s at the distance of 35 mm away from tip of the nozzle.

a) z=1mm   b) z=2.5mm

c) z=5mm   d) z=10mm

e) z=20mm   f) z=35mm
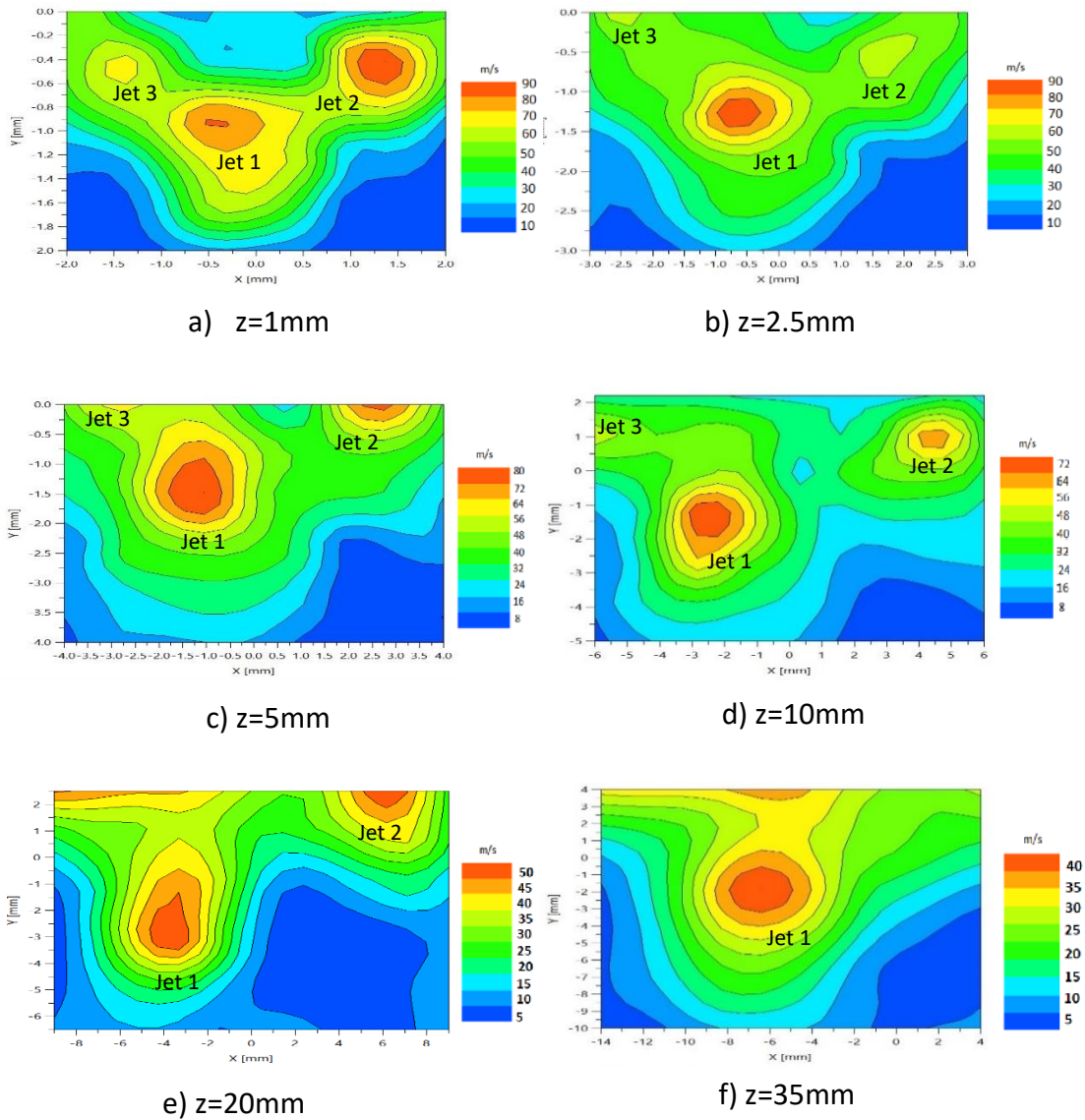
Figure 7-2 Coarse grid contour plot measurement of axial velocity distributions, averaged over the entire injection period, for the three spray jets at different z locations, 100 bar injection pressure and 2ms injection duration. (a) z=1mm; (b) z=2.5mm; (c) z=5mm; (d) z=10mm; (e) z=20mm; (f) z=35mm.

By further looking at the results presented in figure 7-2, it could be found that the

centre of jet 1 with highest velocity peaks are located at following coordinates (±

0.1mm error) corresponding to each z location:

Table 7-1 (x,y) Coordinate of the centre of jet 1 at different z locations using the coarse grid method

Z location	(x,y) Coordinate of the centre of jet spray
1	(-0.4,-1)
2.5	(-0.5,-1.2)
5	(-1.2,-1.3)
10	(-2.5,-2)
20	(-4.5,-2.5)
35	(-6.5,2.3)

Although the internal geometries of this injector (particularly the trajectory of the nozzles), the results clearly show a shift of the jet core centre away from injector axis and is expected to be aligned by the nozzle axis.

7.3   Fine grid results

The approximate x-y coordinates of the maximum velocity contour plots extracted from the coarse grid measurement have been used as a reference for defining a finer grid measurement with grid length of 0.1mm and a higher resolution of 11 x 11 (totally 121 points) over a smaller region in x and y direction for each z location. This was to ensure that only jet 1 is isolated and investigated while maintaining a higher accuracy. It was also necessary to focus on only one jet due to the limitations in the amount of fuel available. The velocity/droplet diameter contour plots of jet 1 are therefore obtained

with higher accuracy which will yield more insight into the spatial and temporal behavior of the jet 1 at different z locations.

7.3.1   Fine grid time-averaged contour plots of velocities

Figure 7-3(a to f) shows the time-averaged contour plots of velocities of jet 1 in the fine grid mode measured over the entire cycle of injection at different z locations for 100 bar injection pressure and 2ms injection duration. The contour plots have been obtained by BSA software and the data from the measurements has been postprocessed further in Matlab to create temporal contour plots of velocities which will yield novel understanding of the jet structure at different z locations.

It can be observed from figure 7-3(a) that the maximum time-averaged velocity of the center of the jet at the distance of z=1mm is around 90m/s. It is also evident that this maximum velocity is almost the same for z=2.5 mm (figure 7-3(b)) from nozzle exit while there is a slight change in the velocity contour plots. It could be seen from figure 7-3(c to f) that this time-averaged velocity at the centre of the jet 1 decreases to around 80, 72, 50 and 40m/s at the locations of z=5, 10, 20 and 35mm respectively. This continuous decrease is due to the loss of momentum of the droplets partially due to the secondary breakup nearer to the injector, and more importantly due to aerodynamic drag forces which is exerted on the surface of these droplets causing droplets deceleration and the transfer of momentum from the fuel droplets to the air molecules. It is obvious that as the distance z increases, the sharp edge of the contour lines becomes smoother. This is

believed to be partially due to the aerodynamic drag forces in front of the spray that resists against the high velocity regions of the spray as the spray develops further downstream the nozzle and partially due to the air entrainment from the side of the jet which could have similar effect.

a) z=1mm   b) z=2.5mm

c) z=5mm   d) z=10mm

e) z=20mm   f) z=35mm
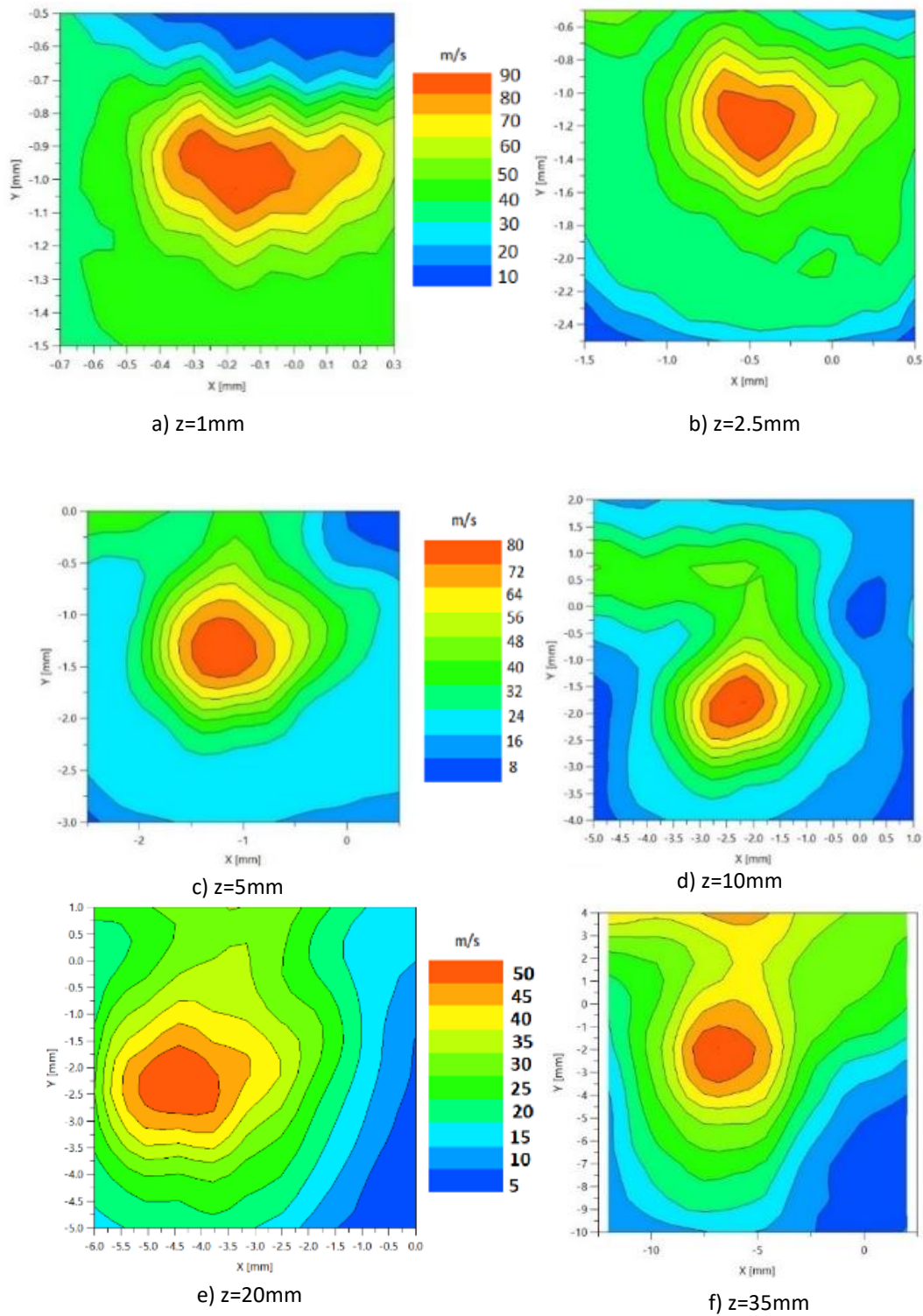
Figure 7-3 Fine grid contour plot measurement of axial velocity distributions, averaged over the entire injection period, for the spray jet 1 at different z locations, 100 bar injection pressure and 2ms injection duration. (a) z=1mm; (b) z=2.5mm; (c) z=5mm; (d) z=10mm; (e) z=20mm; (f) z=35mm.

By looking further into figure 7-3 a to f, it could be seen that the approximate location of the x-y coordinates of the maximum velocity regions (Vz) which are shown in red color are as follows:

Table 7-2 (x,y) Coordinate of the centre of jet 1 at different z locations using the fine grid method

Z location	(x,y) Coordinate of the centre of jet spray
1	(-0.2,-1)
2.5	(-0.5,-1.2)
5	(-1.2,-1.3)
10	(-2.2,-1.7)
20	(-4.5,-2.2)
35	(-6.8,-2.5)

These x-y coordinates will be used as a reference for another round of measurement in which the grid is using the highest resolution possible offered by the traverse system (0.05 mm) according to methodology which is explained in chapter 4 and the results are presented as temporal graphs for each point and spatial graphs along y-axis later in this chapter.

7.3.2 Fine grid time-averaged contour plot of droplet diameters

Figure 7-4(a to f) shows the time-averaged 2-D contour plot of the droplet diameters over the entire period of injection in x-y plane in the fine grid measurement mode at each z locations from z=1mm to z=35 mm at 100 bar injection pressure and 2ms injection

duration. Comparing the overall contour plots of mean diameters in figure 7-4 in each z location with velocity contour plots in figure 7-3 in the same z location, it is evident that the peak value of the mean dimeter is located in the vicinity of the core jet where maximum velocity also occurs. This was expected as the larger droplets with higher mass possess higher momentum and thus larger velocity. This is a typical characteristic of the jet flow where the x-y location of the maximum velocity and droplet size coincides with each other.

a) Z=1mm

b) Z=2.5mm

c) Z=5mm

d) Z=10mm

e) Z=20mm

f) Z=35mm
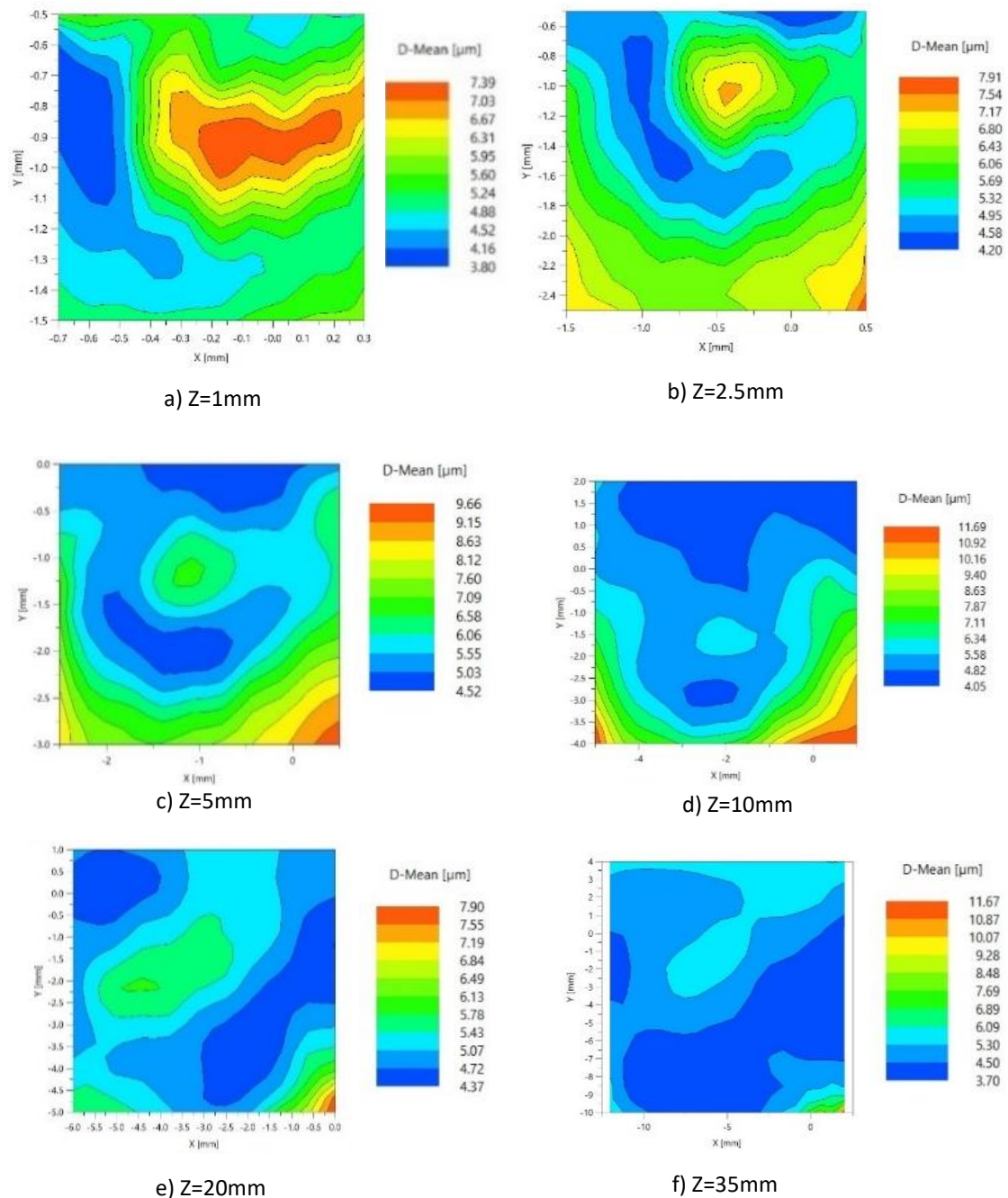
Figure 7-4 Fine grid contour plot measurement of droplet diameter distributions, averaged over the entire injection period of jet 1 at different z locations, 100 bar injection pressure and 2ms injection duration. (a) z=1mm; (b) z=2.5mm; (c) z=5mm; (d) z=10mm; (e) z=20mm; (f) z=35mm.

Further looking at the figures 7-3 and 7-4 , it seems that there is a slight difference between the location of the peak of velocities and droplet diameters. This could be partly

due to the complex nature of the flow inside the nozzle, especially when it is expanded in the stepped-nozzle, which may cause the emerging jet to be more turbulent and unstable with some intermittent flapping and ultimately results in slight amount of shift in the x-y location of the maximum values of velocities compared to that of droplet diameters.

Looking further into figure 7-4(a to f), it could be found that the time-averaged maximum droplet diameter (D10) at the center of the jet decreases steadily from 7.5 µm at 1mm to 5.5µm at 10mm and to 5.2µm at 35mm as shown in figure 7-5 below. It could be also seen that D32 at the centre of the jet also decreases steadily from around 18.5 µm at Z= 1mm to around 11 µm at Z = 35mm.
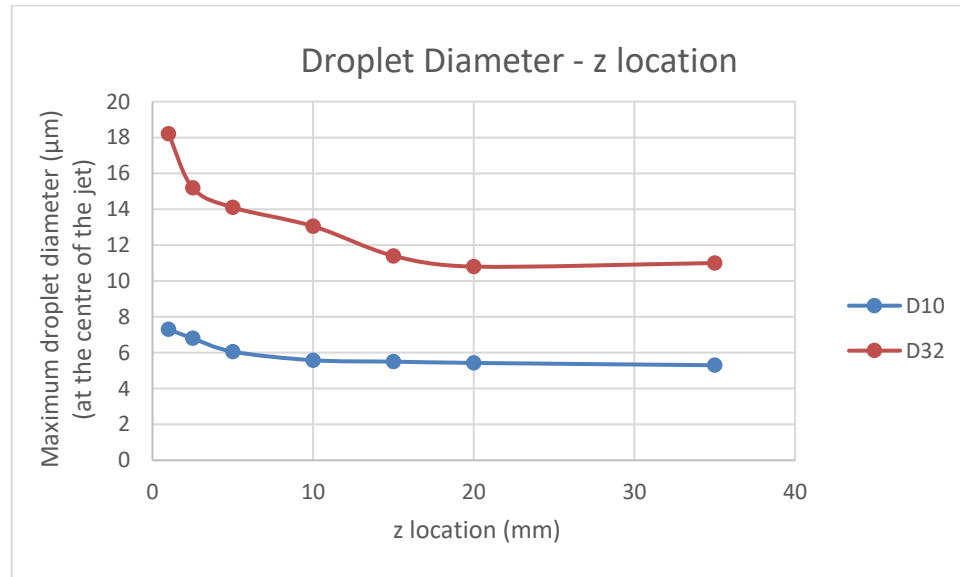
Figure 7-5 Time-averaged maximum droplet diameters (D10 and D32) variation at the center of the jet

It should be mentioned again that the values presented in figures 7-3 and 7-4 are the time averaged values over the entire injection period and it is essential to obtain

temporal contour plots of the velocities/diameters using a novel in-house Matlab code. The results of temporal contour plots/graphs of velocities and droplet diameters are presented in the next following sections. Nevertheless a comparison of the results between the mean droplet diameters of the current stepped multi-hole injector (7.5 μm at 100 bar and z=1mm) with a conventional straight multi-hole injector [46] (~15 μm at 120 bar and z=2.5mm) and an outward opening pintle-type injector [54] (~13 μm at 200 and z=5mm) shows a good advantage of the current injector relative to the other two injectors and suggest it has a better atomization capability; note that all three cases considered here have used the same PDA system. The improved atomization performance can be due to the stepped part of the current injector where the fuel undergoes through a sudden expansion process whereby the flow becomes 3-D and highly turbulent and becomes susceptible to earlier breakup and rapid atomisation; this will be discussed more later in this chapter.

7.3.3   Fine grid temporal contour plot of droplet velocities

It would be difficult to estimate the exact location of the primary/secondary breakup by only looking at the time-averaged velocity/diameter contour plots presented in figure 7-3 and 7-4 since they only present the average values of these quantities over the entire injection period. Therefore, it is necessary to obtain the temporal droplet velocity/diameter contour plots at different AESOI time in order to investigate any instantaneous change in shape/structure of spray and therefore reach a better understanding of the primary/secondary breakup regions. As mentioned in the

methodology chapter, a novel Matlab code was written in order to batch process the data obtained from BSA software for all the measured points in the x-y grid and the temporal contour plot of the velocity/diameter for 3 different AESOI time during the main injection event. The Matlab code is given in the appendix which has the capability to calculate the temporal contour plots (of parameters such as velocity, droplet diameter, SMD, Weber number etc.) at any AESOI with any windowing time based on the user selection. In this study 3 AESOI time were chosen. These include 1ms, 1.5ms and 2ms AESOI which are considered to be at the start, in the middle and at the end of the main injection cycle. In all these AESOI times, the needle is fully open. The temporal velocities/droplet diameters are calculated over a time window of 0.05ms as explained in methodology which is a good improvement compared to previous work of Marchi [54] without any compromise on the number of samples collected within this time window.

Figure 7-6 a-l shows the fine grid temporal 2D contour plots of velocities at different AESOI time at different locations near the nozzle exit. Each row has 3 contour plots which presents the temporal jet velocities at 1ms, 1.5ms and 2ms AESOI from left to right at a sprecific z location. As an example, the first row shows the temporal velocity contour plots at z=1mm for the start of injection (left plot - 1ms AESOI), at the middle of injection (centre plot- 1.5 ms AESOI), and at the end of injection (right plot – 2 ms AESOI). All the three plots are related to the main injection event as described in the methodology.

It is evident in figure 7-6a that the core of the jet (yellow contours) reaches temporal velocities of up to 120m/s as evident from the colorbar. As expected, these temporal

maximum velocities are higher than the time-averaged maximum values seen in figure 7-3a. This is a new finding in our understing of the temporal behaviour of the spray at different AESOI.

In addition, it has been reported in the previous works in multihole injectors [46] [88] that when the jet is fully developed during the main injection event i.e. from 1ms to 2ms, the average velocity values of the jet will remain constant. However, no information was provided in the literature review on the details of the temporal contour velocity plots and how they change their shape and values over time from start to the end of the main injection. It is clear from figures 7-6 a to c that the y length of the main body of the jet (yellow region) decreases in size from 0.6mm in figure 7-5a to 0.4 mm in figure 7-5c. This can be due to the trapped fuel left over inside the nozzle from previous injection, which comes out in the next injection with an expanded tip spray (as was shown in spray image of 6-21, and also in accordance with other previous works) and then recover to fully develop size later. It is also clear from comparing figure 7-6a with figure 7-6c that the average velocity of the yellow region at 2ms is slightly smaller as evident from the colorbar. This clearly shows the transient behaviour of the jet (micro-jets) during the main injection event. It also suggests that the discharge coeficient of the nozzle might change and perhaps slightly reduce during the main injection event.

Another observation from figures 7-6 a to c is that there are a few local peaks which are shown by red circles as 1, 2, 3, and 4. This suggests that the main core of the jet might be comprised of actual 4 smaller jets which will be referred to 'micro-jets' or 'sub-jets'

from now on in this work which are tightly close to each other like a T shape at the beginning of the main injection event. This has been proposed in figure 5-28 in the 7 times enlarged model where the very near nozzle jet is comprised of stochastic ligament spray with lower ratios of VOF. It suggests that the lower parts of the jet is actually where the VOF ratio is much lower.

Furthermore, it is clear from figure 7-6a to c that the y coordinates of these local peaks (1,2,3,4) are changing as AESOI time changes from 1ms to 1.5ms and to 2ms. By comparing figure 7-6 a and b in more details, it could be found that the y coordinates of the top local peaks 1, 2 and 4 moves downward by 0.1 mm from -0.8mm in figure 7-6a to -0.9mm in figure 7-6 b while the y coordinate of the bottom local peak 3 moves upward by 0.1mm from -1.2mm in figure 7-6a to -1.1mm in figure 7-6b. This will result the microjets to get closer to each other in the y direction and also results in the overall jet (yellow region) to be contracted in shape along y direction as shown in figure 7-6 a and b. This trend continues from figure 7-6 b to figure 7-6 c where the top peaks 1, 2, and 4 of the microjets are further moving downward while the bottom peak 3 is moving upward. This ultimately results in peak 2 and 3 to be merged into a single peak. It also reults in the overall jet (yellow region) to be further contracted in shape along y direction. This may be due to the injection-to-injection instability caused within the stepped part of the nozzle and appears in figure 7-6 (a and b) as the measurements have been obtained over many cycles of injection. This provides us with new insights into the

understanding of the underlying dynamics of the jet spray in the stepped -hole and the very near nozzle region.

Another observation from figure 7-6 a to c is that the velocity of the centre of each individual micro-jets (1,2,3,4) may not change over time from 1ms to 1.5 ms. This will result in the color of the centre of the microjets to reamin almost same in bright yellow (120m/s) at 1ms, 1.5ms. However it seems that when jet 2 and 3 merges together at 2ms, the velocities seems to reduce slightly and the color changes to dark yellow (110m/s).

In addition to this, it is clear from figures 7-6 a to c that the temporal velocity of a fixed point in the centre of the contour plots at z=1mm ie (-0.2,-1) will slightly increase during the main injection event as the centre of microjet '2' moves down and approches the centre point of the contour plot (-0.2,-1) from 1ms to to 2ms. This behaviour is later demonstrated in the temporal velocity graphs of the center of the jet at z=1mm ie (-0.2,-0.9) and (-0.2, -1.05) in figures 7-8 d and e where the tempoal velocity graphs are increasing at these fixed points in space during the main injection event from values around 90m/s at 1ms to values around 110m/s at 2ms AESOI. It could be claimed that the temporal velocities at these fixed points in the centre of the jet are increasing due to the dislocation of microjet '2' moving downward by 0.1mm from 1ms to 2ms. This phenomenon has not been reported in previous works which involves experimental technique including Mie scattering, shadowgraphy, X-ray phase contrast imaging, SLIPI, or other techniques.
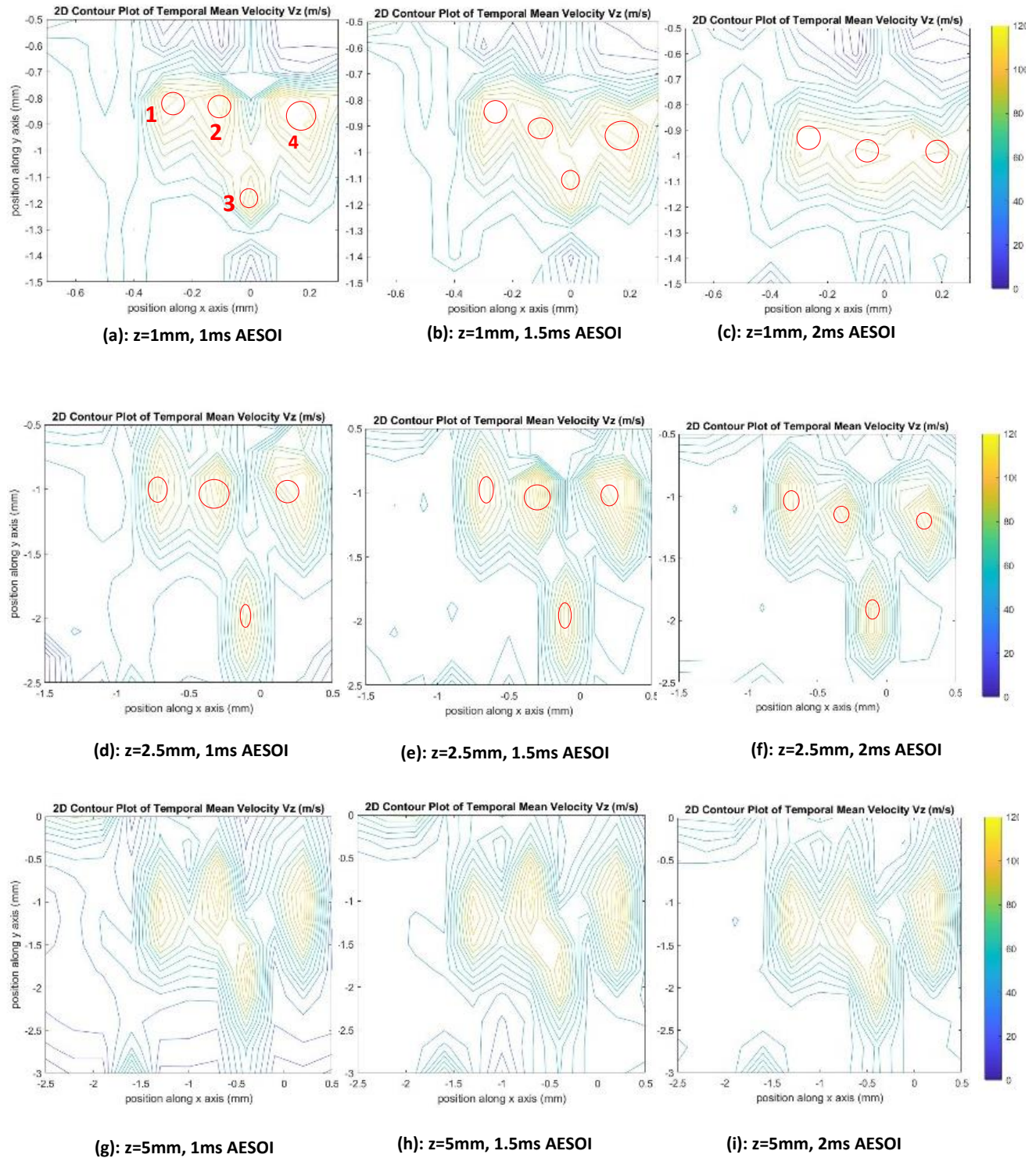
Figure 7-6 Fine grid temporal 2-D contour plot measurement of axial velocity distributions, averaged over 0.05ms, for the spray jet 1 at 3 different AESOI times (1ms, 1.5ms and 2ms) at z location of of 1, 2.5 and 5 mm, 100 bar injection pressure and 2ms injection duration.

Figures 7-6 d to f (middle row) shows the 2-D temporal contour plots of velocities at z=2.5mm for 3 different AESOI times of 1ms, 1.5ms, 2ms. It is evident from the figure that the contour plot of velocities at z=2.5mm have similar shape and structures to those observed at z=1mm (figure 7-6 (a to c)). More specifically, it can be seen from figure 7-6 d that at 1ms AESOI, the overall jet (yellow region) is comprised of 4 distincts smaller jets refered to as 'micro-jets' with T-shaped structure similar to what has been observed at z=1mm at 1ms AESOI. The y coordinates of the three upper micro-jets (1,2 and 4) of the contour plots shown in red circle in figure 7-6d stretches and moves downward, similar to that at z=1mm, by around 0.3mm from -1mm at 1ms AESOI to -0.7mm at 2ms AESOI during the main injection event while the lower peak (3) moves upward slightly by 0.2mm from -2.2mm at 1ms AESOI to -2mm at 2ms AESOI. These figures confirms that the jet is being contracted during the main injection event and the effect is still visible at z=2.5mm. This will once again confirm that the discharge coeeficient of the nozzle might actually slightly reduce during the main injection event.

In addition to this, it is clear from figures 7-6 d to f that the temporal velocity of a fixed point in the centre of the contour plots at z=2.5mm ie (-0.5,-1.5) will slightly increase during the main injection event as the centre of microjet '2' moves down and approches the centre point of the contour plot ie (-0.2,-1) from 1ms to to 2ms. This behaviour is similar to what has been observed at z=1mm. It could be claimed that the temporal velocities at these fixed points in the centre of the jet are increasing due to the dislocation of microjet '2' moving downward by 0.1mm from 1ms to 2ms. This fact can

be verified in the next section by observing the temporal velocity graphs at the centre of the jet at z=2.5mm in figure 1-1 in Appendices which actually confirms that the velocities are increasing from around 100m/s to 110 m/s from 1ms to 2ms during the main injection event. It was seen in this section that the temporal contour plots exhibit very useful information on the instantaneous values of velocities at each point in the x-y plane at a specific z location. In addition, the results show a possibility of spray instability which can be attributed to the injection-to-injection instability. Similarlys, the temporal contour plots of droplet diameters have been obtained in the next section and will be discussed in order to enhance our understanding of the near-nozzle spray structures.

7.3.4 Fine grid temporal contour plots of droplet diameters

Figure 7-7 (a to c) shows the fine grid temporal contour plot of droplet diameters at 3 different AESOI time of 1ms, 1.5ms, 2ms at z=1mm away from the nozzle exit. Similar to the velocity contour plots at z=1mm, it can be seen that there are 4 distincts diameter peaks in the same locations where the velocity peaks are located in figure 7-6a and this again confirms the presence of the so-called 'sub-jets' or 'micro-jets' at these locations. It can be seen that the cross section of the jet exhibit a T-shape which may probably due to the presence of air entrainment penetration in those parts of the jet where velocities are much smaller.

(a): z=1mm, 1ms AESOI   (b): z=1mm, 1.5ms AESOI   (c): z=1mm, 2ms AESOI
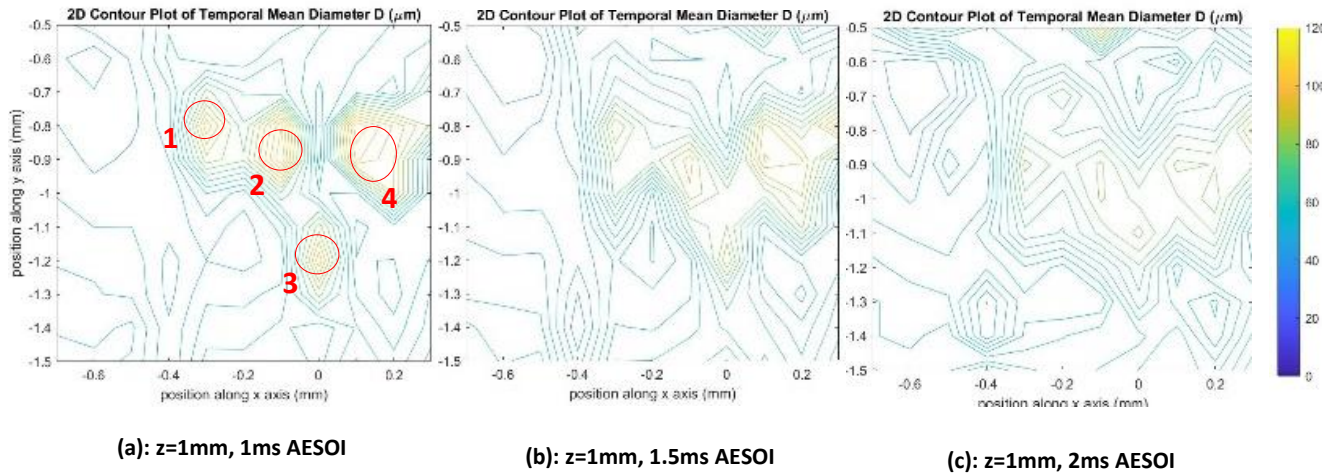
Figure 7-7 Fine grid temporal 2-D contour plot measurement of droplet diameter distributions, averaged over 0.05ms, for the spray jet 1 at 3 different AESOI times (1ms, 1.5ms and 2ms) at z=1mm, 100 bar injection pressure and 2ms injection duration.

It can be seen from figure 7-7 a to c that the maximum droplet diameter values drop from around 10 μm at 1ms to 8μm at 1.5ms and finally decreases to around 6.5 μm at 2ms AESOI. This can be confirmed from the temporal droplet diameter graphs at the centre of the jet in section 7.4.2 in figure 7-9 e where the droplet diameter values decrease constantly from around 10 μm to 6.5 μm during the main injection event. The underlying reason behind this could be due to the fact that as the spray velocities increases, the turbulence and the cavitation also increases inside the injector and this will lead to higher atomisation level and ultimately smaller droplet sizes.

7.4   Temporal velocity and droplet diameter graphs

The next step in the experiment was to use the PDA system to quantify the spray characteristics by obtaining the temporal variation of droplet velocity and diameter of the jet spray along its y diameter. The path along which the measurements have been made, was chosen to pass through the highest velocity regions of the jet or the so called

'sub-jets' or 'micro-jets' which were seen in the previous section using minimum grid value of 0.05 mm according to the method explained in methodology chapter in section 4.9 and 4.15. The results were obtained along the y-direction of the jet for z locations of 1, 2, 5, 10, 20, and 35 mm and are presented in the next sections. Due to the similarity in analysis, some of the graphs are attached in the appendix.

7.4.1 Temporal velocity at z = 1mm

The temporal velocity/diameter graphs of 21 points along y axis of the jet has been obtained at z = 1mm and x=-0.2mm for the duration of 2 ms and injection pressure of 100 bar using an original Matlab software code. The x location of this round of measurement was selected according to the method explained in section 4.9 in methodology in order to measure maximum velocity region of the jet. However, only 8 points are presented here in the figure 7-8 a to h. Each point is located at a distance of 0.15mm away from the next point along y and hence the graphs are presented in a uniform order from a to h along the arbitrary diameter of the jet. The temporal variation of velocity profiles illustrated describe fully the injection process from start to finish.

According to Mitroglu [46], in a conventional multi-hole injector, the temporal velocities are sharply increasing from values close to zero to maximum velocity during the needle opening period. They will maintain their maximum value during the main injection event and will drop sharply again to values close to zero during the needle closing event [46]. This sharp change in the temporal velocity graphs is believed to be the result of the presence of slow-moving large droplets that passes through the measuring volume of

the PDA system at the beginning and at the end of the injection event. These large droplets are formed from the stagnant liquid fuel which is trapped in the sac-volume before the injection needle opens and while the needle closes. It is clear that for conventional injectors, these droplets have lower velocities both at the beginning and at the end of the injection event and therefore a critical weber number will possibly not be reach during these phases. This means that the possibility of secondary atomisation is minimum. However, figure 7-6 a shows that there is a slight difference in the temporal graph of the non-stepped multi-hole injector and the stepped-nozzle injector. Here in the stepped-nozzle injector, the temporal graph does not feature a clear sharp increase at the beginning of the injection at z=1mm. Instead, the initial velocities are starting from much higher values and will remain at their maximum values before being decreased sharply to near-to-zero values following the needle closing event. It could be claimed that the presence of the stepped section of the nozzle can confine and direct the trajectory of bigger droplets/ligaments along the axis of the nozzle. These slow-moving large droplets/ligaments are then collided with high velocity jet which is produced at the beginning of the main injection event and will be pushed and perhaps further disintegrated into smaller droplets/ligaments. This will ultimately result in enhanced primary breakup and secondary atomistaion of these slow-moving large droplets/structures. This is evident from the smaller droplet diameters detected by the PDA system compared to those of conventional non-stepped nozzles [46].

Another observation from figure 7-8 a is that at y=-1.5mm, the temporal velocities are stable at 50m/s with RMS values of around 20m/s for the whole duration of the main injection event ie from 1ms to 2ms. As evident in figure 7-8 b at y= -1.35mm, the temporal graphs exhibit similar shape with constant velocities of 50m/s with RMS values of 20m/s similar to y=-1.5mm. This suggest that these two points have similar temporal behaviour and that there is a uniform low velocity region with minimum thickness of around 150μm where the spray velocities are not changing during the main injection event from 1ms to 2ms. This is believed to be the outer part of the spray which is under the influence of stochastic ligament breakup. These stochastic ligaments are usually formed in the regions where the ratio of the volume of fluid (VOF) is small compared to the core of the liquid jet in the nozzle as a result of interaction of the outer part of the jet with the cylindrical surface of the counterbore stepped section [8].

As the observation continues along y axis, it could be found in the next graph at y= -1.2 in figure 7-8 c that the velocities are increased from around 50m/s to 70m/s compared to the previous velocity graph at y=-1.35mm. It is also clear from figure 7-8 c that the temporal graph at y=-1.2mm exhibit an increasing trend itself. Here the temporal velocities are increasing from around 70m/s at 1ms AESOI to 80m/s at 2ms AESOI. This contradicts with the previous claim that the jet velocities are fully developed (maintain a constant velocity) during the main injection event. In fact, this increase even though only around 10m/s, shows that there is a continuous transient phase during the main injection event. The transient nature of the far-field spray at z=15mm has been reported

recently in the work of Duke et al. where the angle of the far-field spray decreases towards the injector axis during the main injection event. However no study has been done on the transient nature of the near-nozzle spray and for the first time this has been done in this work according to the knowledge of the author.

The transient nature of the near-nozzle spray evolution during the main injection event is also evident at y=-1.05mm and y= -0.9mm in figures 7-8 d and e respectively, where the increasing trend in the velocity graphs are clearly visible. In figure 7-8 d where y=-1.05mm, the temporal velocities are increasing from around 90m/s at 1ms AESOI to around 100m/s at 2ms AESOI during the main injection event which is an increase of 10m/s. Finally, in figure 7-8 e, at y=-0.9mm, the temporal velocities are increasing from around 100m/s to 110m/s during the main injection event from 1ms to 2ms. This increasing trend has not been reported in any previous works before.

a) y=-1.5mm

b) y=-1.35mm

c) y=-1.2mm

d) y=-1.05mm

e) y=-0.9mm

f) y=-0.75mm

g) y=-0.6mm

h) y=-0.5mm
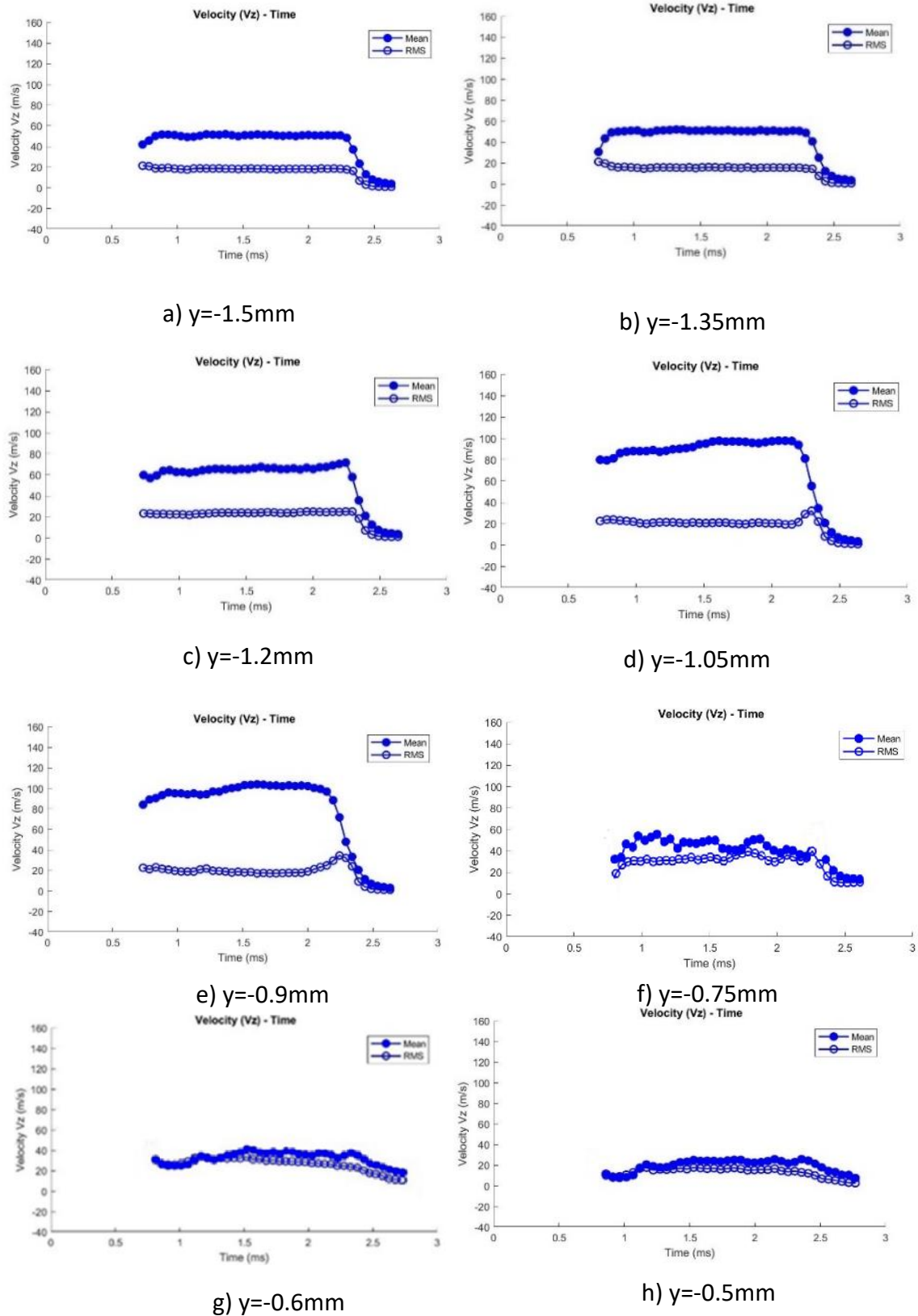
Figure 7-8 Temporal variation of average axial velocity over a time window of 0.05ms at z = 1mm, x=-0.2mm and at different y locations for 100 bar injection pressure and 2ms injection duration.

Moving on to the next point in figure 7-8e where y=-0.9mm to figure 7-8f where y=-0.75mm, a sudden drop of velocity from 120m/s to 65m/s is clearly visible. It could be concluded that y=-0.9mm is where the maximum velocity of the jet takes place and this point could be used as a reference point for maximum velocity in the x-y plane at z=1mm. It could be seen that the temporal jet velocities continue to decrease from 65m/s at y= -0.6mm in figures 7-8g to 60m/s at y=-0.5mm. This suggest that the measurement path has passed the high velocity core of the jet at this point. Here velocities of around 30m/s are observed with RMS values of around 20m/s. Finally, it could be seen from the final graph in figure 7-8 h at y=-0.5mm that the velocities at this point are not further decreased and maintain rather constant value of around 30m/s. Here, the shape and structure of the graph suggest similar behaviour to the previous point at y=-0.6mm where the velocities are also around 30m/s. This suggest that the high velocity region is finished and the stochastic ligament spray region is reached.

The temporal analysis of velocities for z=1mm has been extensively investigated in this section however the results of other locations of z are attached in the appendices. Since the analysis of the temporal behaviour of other locations would be similar to the example explained above, therefore further explanation of other z locations is above the scope of this work.

7.4.2 Temporal droplet mean diameter at z = 1mm

After analysis of the temporal velocity graphs of the jet along y axis at z=1mm and x=-0.2mm (section 7.4.1), it would be useful to examine the temporal droplet mean

diameter graphs of the jet along the same path at z = 1mm for the duration of 2ms and injection pressure of 100 bar using the Matlab software code. The x location of this round of measurement was selected according to the method explained in section 4.9 in methodology which was used to measure maximum velocity region of the jet similar to previous section. 8 points are presented here in the figure 7-9a to h similar to the temporal velocity graphs (figure 7-8a to h). Each point is located at a distance of 0.15mm away from the next point along y axis and hence the graphs are presented in a uniform order from a to h along the arbitrary diameter of the jet.

It has been observed in the work of Marchi [54] that at the start of injection and at the end of injection, the droplet mean diameter is much bigger compared to the main injection event. Here in the stepped-nozzle injector, the temporal graph of droplet mean diameter does not feature this kind of behaviour. Instead, the size of the droplet diameters at the start of injection exhibit very small values which is similar to those of the main injection event (5-10μm). It is only at the end of injection after the needle closing event that the size of the droplets starts to get increased and becomes larger (10-15 μm) as shown in figure 7-13 a to e. As previously observed from the temporal velocity graphs, it could be speculated that the presence of the stepped section of the nozzle can confine and direct the trajectory of larger droplets/ligaments along the axis of the nozzle. These slow-moving large ligaments/droplets are then followed by a powerful higher velocity jets and will be pushed and perhaps further disintegrated into smaller droplets/ligaments at the beginning of the injection. This will consequently enhance the

primary breakup and the secondary atomistaion at the very near-nozzle area of the jet. Therefore, much smaller droplet diameters will be formed and detected by the PDA system.

It is evident from figures 7-9 (a to e) that from start of injection up to around 2.3ms AESOI the mean diameter values are remained below 10µm. It is only after 2.3ms that the mean diameter values will increase sharply from values below 10 µm to maximum values around 15 µm. This is obviously the result of the needle closing event. It should be mentioned that although the resulting droplet diameters produced during this phase are larger than to those of the main injection event, however these values are still lower than the mean droplet diameters reported in a non-stepped conventional injector at similar conditions at z locations further away from the nozzle exit [46]. This proves the higher performance of the stepped-nozzle injector compared to that of non-stepped nozzles.

Looking further into the graphs of figure 7-9 individually, a more detailed information could be extracted from each graph at each y location. As an example, it could be seen from figure 7-9 a that at y=-1.5mm, the temporal droplet mean diameter values are around 6 µm with RMS values of around 2µm. Moving to the next graph in figure 7-9 b at y=-1.35, the temporal droplet mean diameter are exhibiting similar values to that of the previous point at y=-1.5mm. This trend is almost the same up until graph 7-9 d at y= -1.05mm where there is a slight increase in the mean droplet diameters to values around 7µm. It is at point y= -0.9 where maximum droplet diameters of around 10µm is observed

during the main injection event. The droplet mean diameters drops to smaller values of around 7 µm with some minor fluctuations. It then continues to drop at y=-0.6mm when it reached 5µm. It is then remain at 5µm for the point of y =-0.5.

An interesting observation in the temporal mean diameter graphs in figure 7-9 a to h is that the increasing tail of the graph which is the result of the needle closing event is getting smaller in size as y increases from -1.5mm to -0.5mm. This clearly suggests that the larger droplets, that are formed at the end of injection as a result of needle closing event, are more produced at the outer side of the jet at y=-1.5mm (which is closer to the PDA instrument and is further away from the injector axis) than the inner side of the jet at y-0.5mm (which is closer to the injector axis). It is interesting to realise that the side where y=-1.5 is the location where the jet is more stable in terms of droplet diameter values during the main injection event. This phenomenon has not been reported in any previous work and has been observed for the first time according to the knowledge of the author. It could be claimed that the large droplets are more likely to be formed from the outer side of the jet rather than the inner side of the jet. One justification which could perhaps explain the reason behind this phenomenon could be obtained by referring back to the observations gained from the 7-times enlarged model. It was seen in figure 5-28 in the enlarged model that the main part of the jet with high VOF ratio is located actually at the bottom side of the spray according to figure 5-28. This was due to the hydraulic flip at the top side of the spray. It could be

a) y=-1.5mm

b) y=-1.35mm

c) y=-1.2mm

d) y=-1.05mm

e) y=-0.9mm

f) y=-0.75mm

g) y=-0.6mm

h) y=-0.5mm
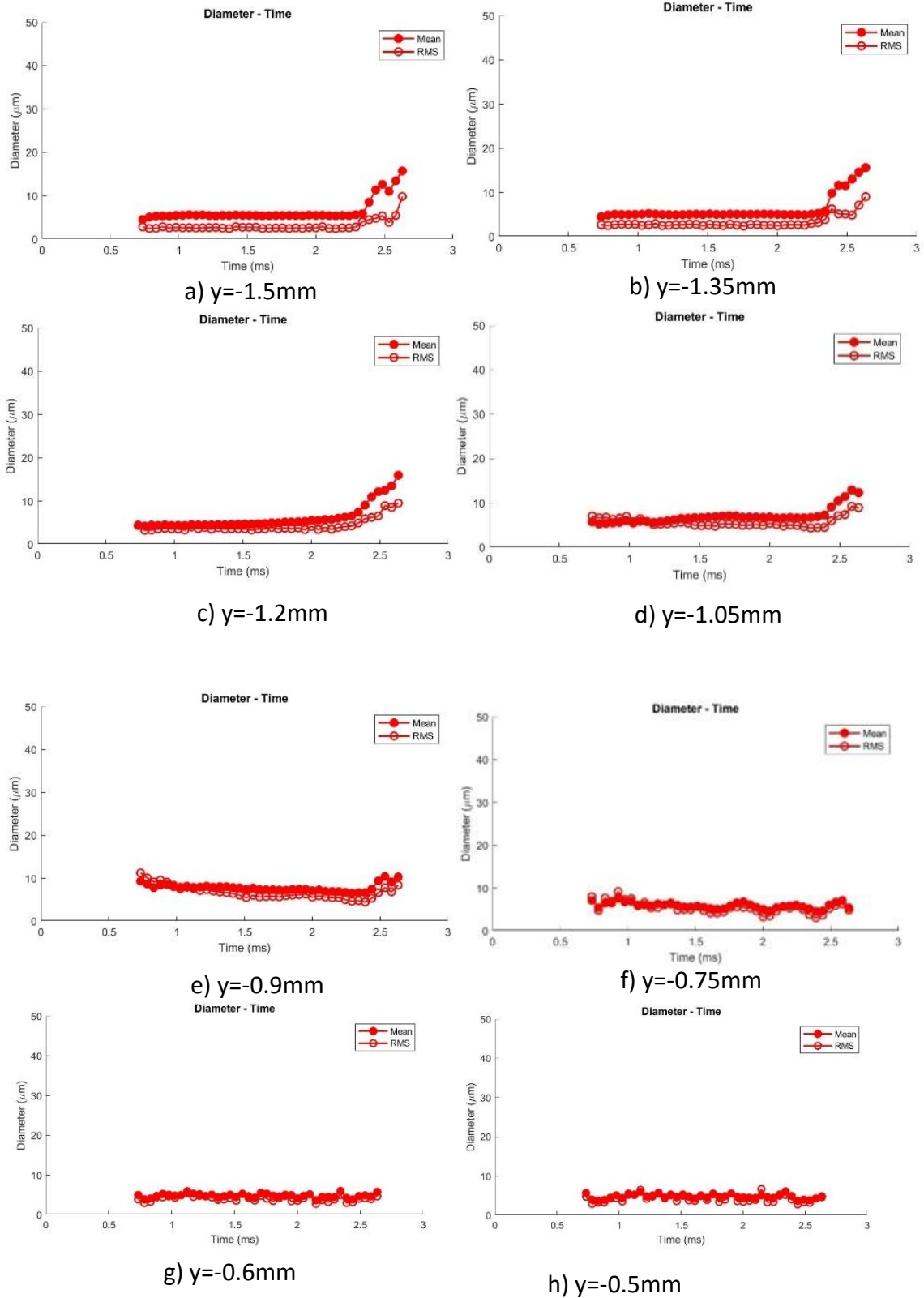
Figure 7-9 Temporal variation of average mean diameter over a time window of 0.05ms at z = 1mm, x=-0.2mm and at different y locations for 100 bar injection pressure and 2ms injection duration.

claimed that the hydraulic flip might happen at the inner side of the nozzle which is closer to the injector axis and therefore the main jet is formed at the outer edge of the spray. It is only by the enlarged model visualisation that this behaviour could be explained in the real-size model. Therefore, utilising the enlarged models has been proved useful in enhancing the current understanding of the underlying behaviour of the needle closing event observed in the temporal mean diameter graphs in the real-size stepped nozzle injector under investigation.

7.5   Velocity and mean droplet diameter distributions

In this section spatial velocity and mean droplet diameter distribution of the jet spray is presented at different z locations. For this reason, both average and instantaneous distributions are presented which can yield important information and can shed light into new findings with regards to the characteristics of the spray in terms of velocity and droplet diameter

7.5.1   Average axial velocity and mean droplet diameter distribution

The spatial velocity and diameter profiles averaged over the duration of main injection event (1ms to 2ms as shown in figure 7-10) have been obtained for all z locations using the Matlab code. These results are presented in figure 7-11 a to e. In each figure in 7-11 a to e, the droplet velocity (Vz) and diameter profiles along y axis are compared in the same z location. In addition, the maximum velocity and droplet diameters could be compared between different z locations.
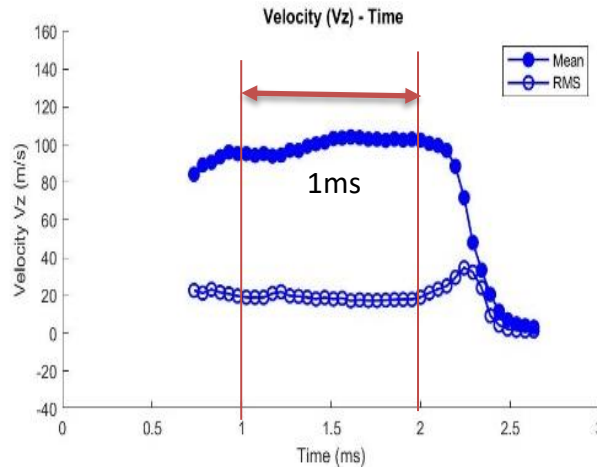
Figure 7-10 Spatial velocity averaged over a time window of 1ms from 1ms to 2ms AESOI

The results shown in figure 7-11 a to e show a jet-like profile with peak velocity values at

the centre of the jet for all the z locations. However there is a very slight shift of 0.05mm

between the peak of velocity and the peak of diameter values in some cases. It is also

evident from figure 7-11 a, b and c that the spray exhibit higher stochastic behavior at

the left edge where velocity remains around 50m/s and RMS values are smaller. This

region is believed to be caused by flapping of the spray and has been only reported

recently by Thevenin et al in [98]. The flapping is believed to be caused partially by the

instabilities ie the turbulence and cavitation inside the smaller nozzle and also partially

by the early air entrainment that the counterbore provides for the jet and partially due

to the impact of the ligaments coming out of the smaller nozzle with the inner surface of

the counter bore. Here the stochastic ligaments are being contained and bounced back

by the inner surface of the counter bore of the stepped section of the nozzle.

In another observation, it could be seen from figure 7-11 a that at z=1mm the maximum

velocity achieved is around 120m/s at point y=-0.95. It can also be seen that the

stochastic ligament spray might exist on the right side of the spray where the RMS values

268

of velocities starts to decrease. It could be claimed that the stochastics spray region on both sides of the spray has velocities of less than 60m/s.

It could be seen from figure 7-11 b and c that the maximum velocity drops to 115m/s and 110m/s while the stochastic ligament spray region velocity are less than 60m/s and continues to drop. The sudden drop of 10m/s of the uniform velocity region of the left side of the spray (stochastic ligament spray) from z=2.5 to z=5mm shows that there is high amount of air entrainment and aerodynamic drag forces which ultimately cause the jet to lose momentum and perhaps disintegrates into smaller ligament/droplets. It could therefore be claimed that the stepped-nozzle can enhance the atomization of the spray by exposing the outer part of the spray to high amount of early air-entrainment through the process of stochastic ligament spray formation and flapping.

It could be seen from figure 7-11 d that at z=10mm, the maximum velocity drops to 100m/s. It is then in figure 7-11 e that the maximum velocity drops significantly to 80m/s and the left side of the spray is continuously losing momentum. It is clear that at this point the velocity of the stochastic ligament spray region is not a constant line with zero gradient and instead it has a positive gradient. This is due to the intense air entrainment which gradually change the profile from a zero gradient to a positive gradient region with much more efficient air entrainment.

It could also be seen that the maximum diameter changes from 8µm at z=1mm to around 5 µm at z=20mm. It should once again be mentioned that the values shown in

figure 7-11 are average values and later on in section 7.5.2, the instantaneous values

will be further investigated.

a) Z=1mm

b) Z=2.5mm

c) Z=5mm

d) Z=10mm
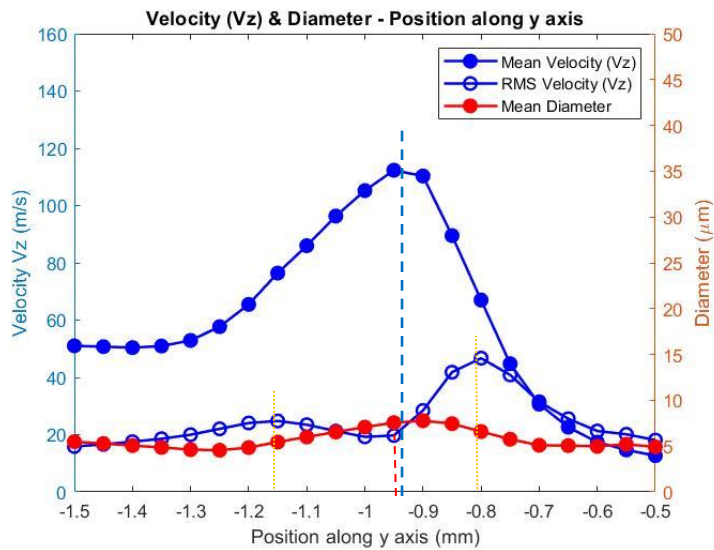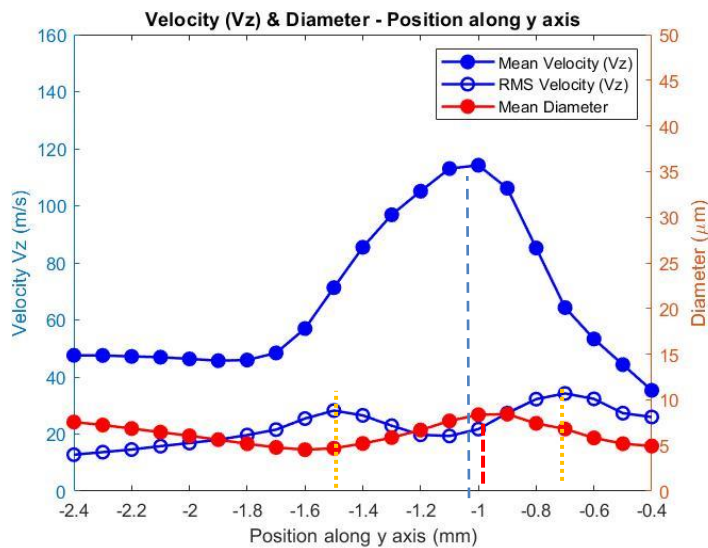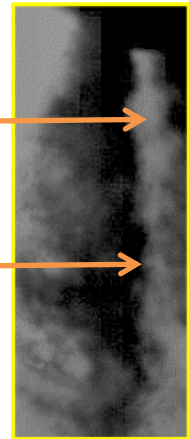
e) Z=20mm
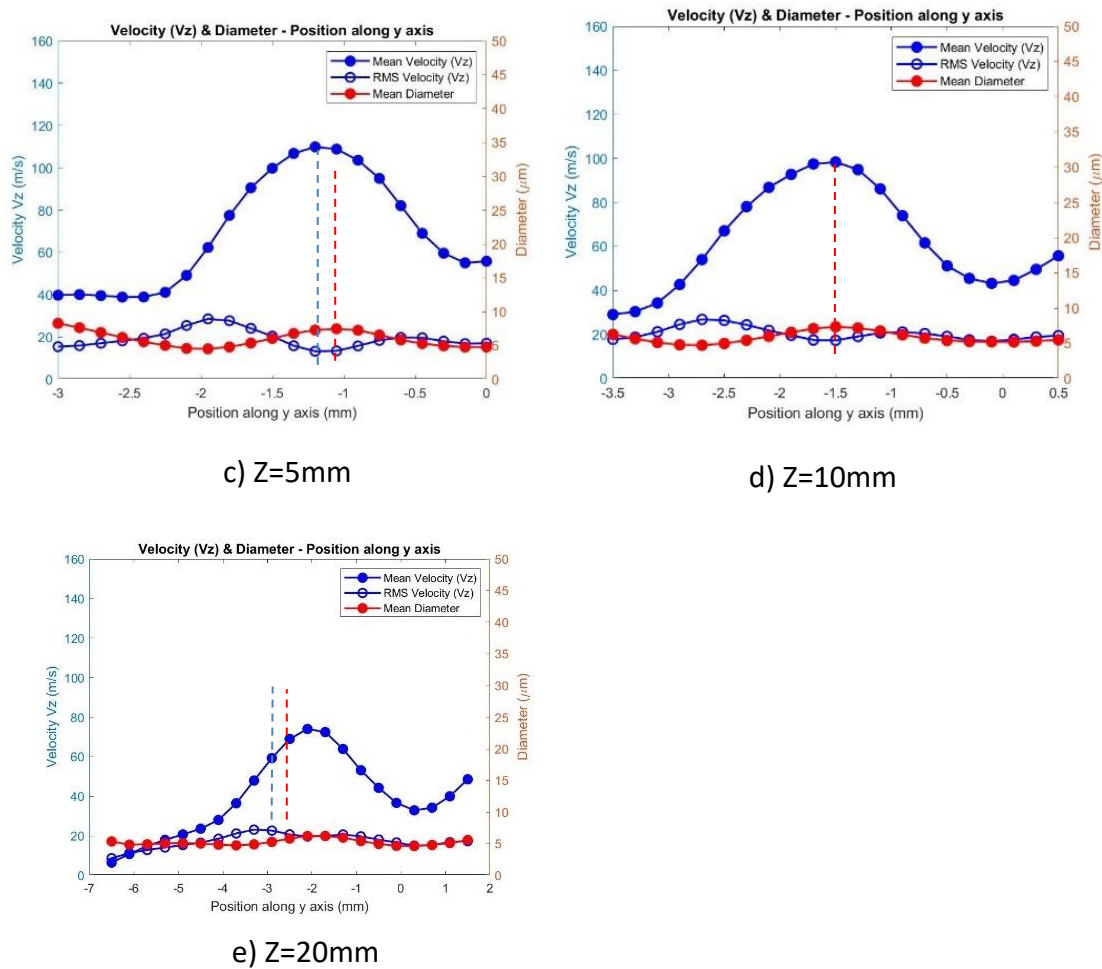
Figure 7-11 Spatial axial velocity and mean diameter graphs averaged from 1ms to 2ms at different z locations

It would be useful to compare the average velocity distribution of the near-nozzle jet spray at z=1mm with the in-nozzle velocity distribution of a transparent model of Bosch HDEV 5 injector which has been obtained by using micro-PIV and ultra high speed imaging technique at the same pressure of 100 bar identical to our study. Figure 7-12 shows the average 2D velocity and pressure distribution (contour plots) in a nozzle of transparent model of HDEV5 Bosch stepped injector [7]. The velocity and pressure

distribution inside the sac volume and the nozzle are shown by color contours. It could

be seen from figure 7-12a that the maximum velocity reaches up to 120 m/s near the

exit of the nozzle. It could also be seen from figure 7-12 b that the maximum pressure of

around 100 bar occurs inside the sac volume where the flow is stagnant. It is clear that

the right edge of the nozzle has a sharper edge than the left side. Therefore cavitation is

more likely to occur at the upper right side of the nozzle due to the sudden drop in the

local pressure as a result of sudden change of direction of the flow. This is evident from

the zero-pressure region in figure 7-12 b at the upper right side of the nozzle which is

shown in dark blue color. It is also evident from figure 7-12a that the core of the flow

inside the nozzle exists mainly on the left side as has been seen in the 7 times enlarged

model in chapter 5. This means the maximum velocity distribution of the flow inside the

nozzle is much more on the left side than the right side at the exit of the nozzle.

(a)   (b)
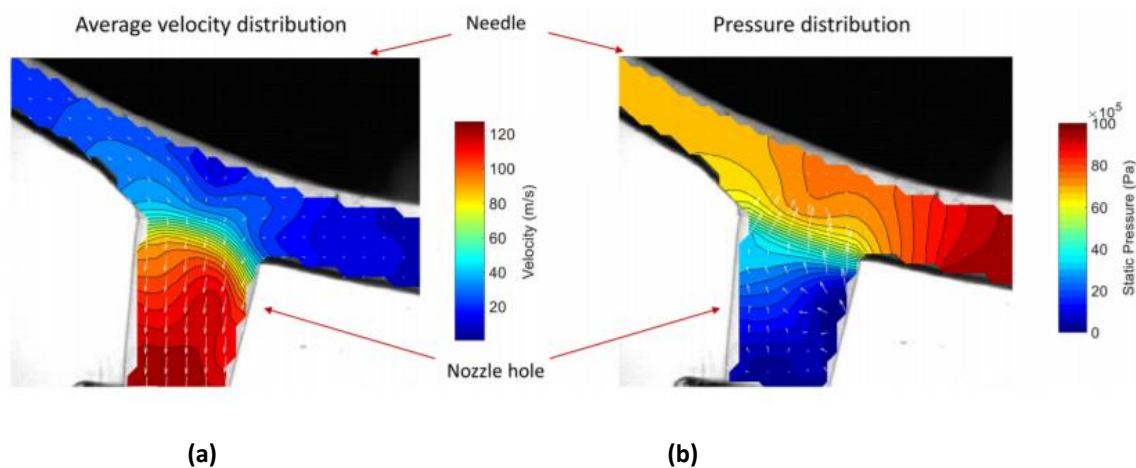
Figure 7-12 Average 2D velocity and pressure distribution (contour plots) in a nozzle of transparent model of HDEV5 Bosch stepped injector (identical to the injector used in our study) [7]

Figure 7-13 a shows the 5 lines which crossed through the axis of the nozzle at equal distance which are located from nozzle inlet to the nozzle exit. The velocity graphs along these lines are obtained and presented in figure 7-13b. It could be seen from figure 7-13b that along line 1, the velocity graphs are around 100m/s starting from the left side and up to three quarters of the diameter of the nozzle. It is evident that the velocities on line 1 suddenly drops on the far right side of the diagram, and this is due to the presence of low pressure zones which can cause cavitation which blocks the flow. It could be seen from figure 7-13 b that as the number of the line increases, the velocities increase too. It is evident that at the exit of the nozzle, the average velocity is around 120m/s. This is exactly in agreement with the PDA measure of the near-nozzle spray at locations of z=1mm which was obtained in this study.

(a)   (b)
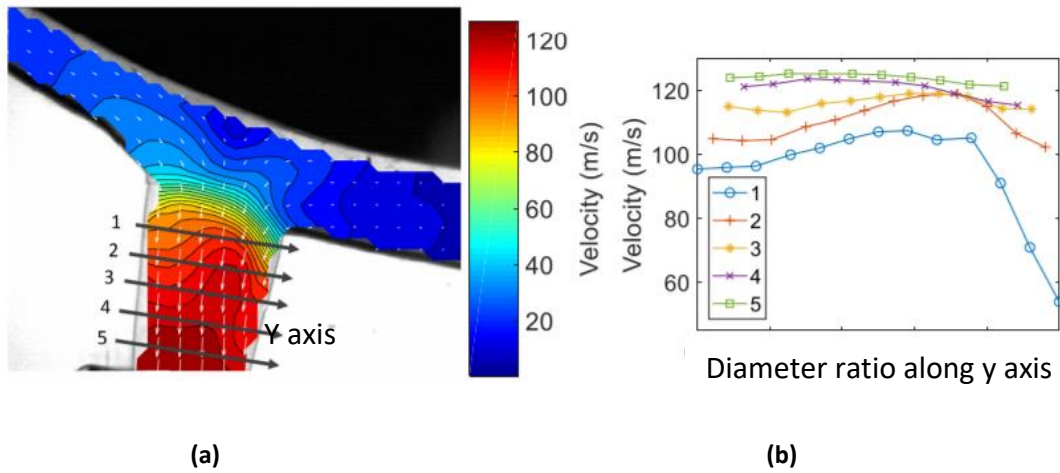
Figure 7-13 (a) Average 2D velocity and distribution (contour plot) in a nozzle of transparent model of HDEV5 Bosch stepped injector (identical to the injector used in our study) (b) Average velocity distribution along y axis of the nozzle similar to the current study [7]

7.5.2 Instantaneous axial velocity and mean droplet diameter distribution

In this section the instantaneous spatial velocity and diameter graphs of the jet spray at 3 different times at the start, middle and end of the main injection event will be presented and compared at each z location shown in figure 7-15 a to o. Each row shows the instantaneous profiles at 3 different time of 1ms (left), 1.5ms (middle) and 2ms (right) at a specific z location. The sampling window chosen for these 3 times was 0.1ms shown in figure 7-14.
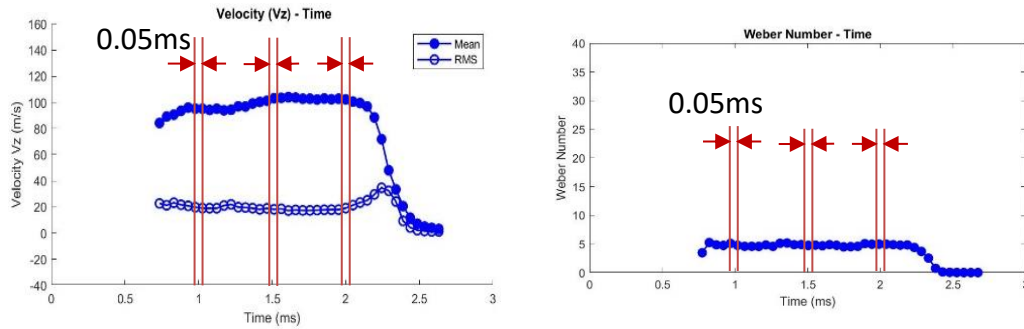
Figure 7-14 Instantaneous spatial velocity and droplet diameter were presented at 1ms , 1.5ms and 2ms averaged over a time window of 0.05ms

This will allow small changes in the profile to be detected and will yield a better understanding of the changes in the spatial velocity and diameter profiles as a function of time in each z location. It will also exhibit quantitative characteristics of the jet spray dynamics as it develops during the main injection event.

Figure 7-15 a to c (first row) shows the spatial velocity and diameter graphs of the jet spray along y direction at 1ms (left), 1.5ms (middle) and 2ms(right) AESOI at z=1mm. It is evident from figure 7-15a that at the start of the main injection event, maximum

velocity of the jet reached 120m/s at 1ms AESOI at y=-0.85mm while the maximum droplet diameter reached 10μm. It could be observed from figure 7-15b that after 0.5ms at 1.5ms AESOI, the velocities still remains at around 120m/s however the position of the peak of the velocity profile moves slightly to the left to point y=-0.9mm. It could be seen from the diameter profile in figure 7-15b that maximum droplet diameter is reduced to 8μm. It is then evident from figure 7-15c that at the end of injection event at 2ms, the maximum velocity of the jet reduces slightly to around 110m/s while the location of the peak of the velocity moves further to the left to point y=-1mm. It could also be seen that the maximum dimeter at the end of injection is reduced further to around 7 μm. The continuous shift of the maximum velocity region of the jet (although only 0.15mm) and the reduction of the droplet diameter from 10 μm to 7 μm from start to the end of the main injection event at point z=1mm indicates that the jet flow has a transient nature even during the main injection event which could be due to the increasing turbulence and instabilities inside the nozzle as a result of cavitation and turbulence increase inside the in-nozzle flow as see in chapter 5 and also due to the continuous air-entrainment at the near-nozzle jet. This in fact implies that the in-nozzle flow has a transient nature by itself during the main injection event and this behaviour can influence the characteristics of the spray particularly the maximum droplet diameter in the near-nozzle region of the spray which reduces from 10μm to 7 μm in one injection cycle.

Another observation from figures 7-15a to c is that the thickness of the high velocity region of the jet is reduced from 1ms to 2ms shown by yellow horizontal arrow. It could be clearly seen from figure 7-15a that the thickness of the jet which contains velocities higher than 80m/s (region between the two maximum RMS values) is equal to the length of the yellow arrow which is around 0.4mm. It is clear from figure 7-15b and c that this thickness reduces to 0.3mm and 0.2mm respectively. This clearly shows the contraction and the transient nature of the jet during the main injection event as has been demonstrated before in the section 7.3.3 in figure 7-6 (a) to (c) by using contour plot of velocities at similar instantaneous times during the main injection event. This behaviour was not seen in previous works and for the first time, it is reported in this work.

Figure 7-15 d to f (second row) shows the spatial velocity and diameter graphs of the jet spray along y direction at 1ms (left), 1.5ms (middle) and 2ms(right) AESOI at z=2.5mm. It is evident from figures 7-15d to f that similar behaviour and trend is seen here for z=2.5mm compared to z=1mm. Firstly, it is evident from figure 7-15d that the maximum velocity of the jet is around 120m/s at 1ms AESOI at y=-0.9mm while the maximum droplet diameter reached 9µm. It could be observed from figure 7-12e that after 0.5ms at 1.5ms AESOI, the velocities still remains at around 120m/s however the position of the peak of the velocity profile moves slightly to the left to point y=-1mm. It could also be observed from the diameter profile in figure 7-15e that maximum droplet diameter is reduced to 7.5µm. This is in line with the results obtained at z=1mm. It is then evident from figure 7-15f that the maximum velocity of the jet reduces slightly to around 110m/s

while the location of the peak of the velocity moves further to the left to the point y=-1.1mm. It could also be seen from figure 7-15f that the maximum dimeter at the end of injection is reduced further to around 6.5 μm. All these trends for z=2.5mm are in line with the results observed for z=1mm here. The continuous reduction of the droplet diameter from 9 μm to 7 μm from start to the end of the main injection event for z=2.5mm , similar to z=1mm, confirms the transient nature of the droplet diameter which can influence the dynamics of the spray in terms of velocity distribution and droplet diameter. It can also be sees that the change in the location of the peak velocity is 0.2mm which is greater than 0.15mm for z=1mm. This shows that the angle of the near-nozzle jet spray will perhaps slightly change as reported in Duke et al recently. [8]

Another observation with regards to the velocity profile of the jet at z=2.5mm is that the thickness of the high velocity region of the jet is reduced from 1ms to 2ms shown by yellow horizontal arrow similar to z=1mm. It could be clearly seen from figure 7-15d that the thickness of the jet which contains velocities higher than 80m/s (The region between the two maximum RMS values) is equal to the length of the yellow arrow which is around 0.8mm. It is clear from figure 7-15e and f that this thickness reduces to 0.7mm and 0.6mm respectively. This behaviour has been demonstrated before in figure 7-6 d to f where the jet is being contracted which shows the transient nature of the jet spray. Similar trends are seen for z=5, 10 and 20mm.

(a): z=1mm, 1ms AESOI

(b): z=1mm, 1.5ms AESOI

(c): z=1mm, 2ms AESOI

(d): z=2.5mm, 1ms AESOI   **(e): z=2.5mm, 1.5ms AESOI**   **(f): z=2.5mm, 2ms AESOI**

(g): z=5mm, 1ms AESOI   **(h): z=5mm, 1.5ms AESOI**   **(i): z=5mm, 2ms AESOI**

(j): z=10mm, 1ms AESOI   **(k): z=10mm, 1.5ms AESOI**   **(l): z=10mm, 2ms AESOI**
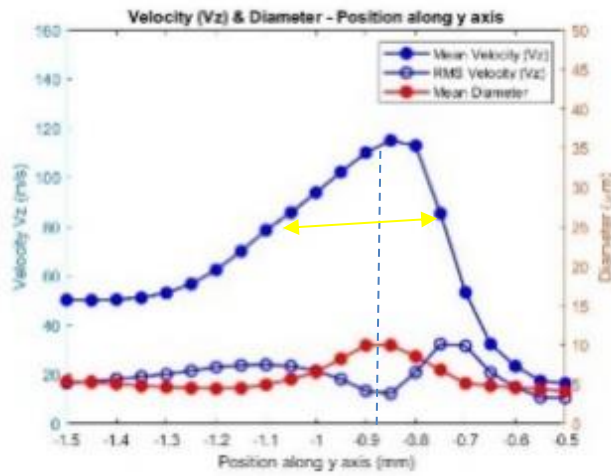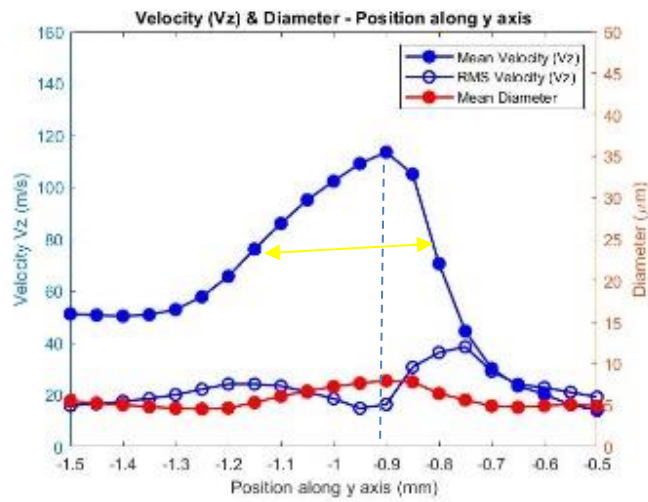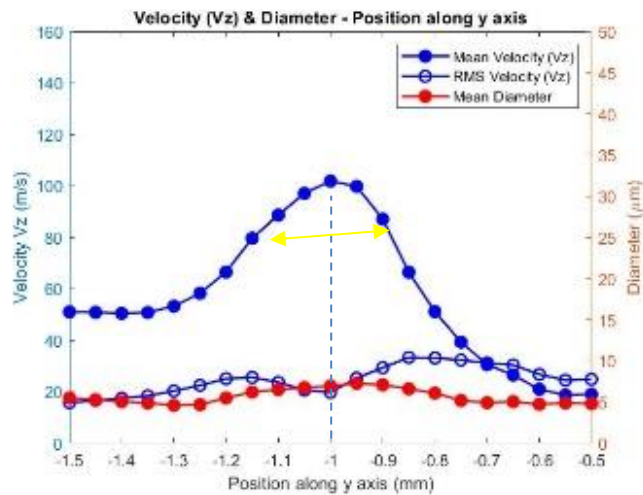
(m): z=20mm, 1ms AESOI   **(n): z=20mm, 1.5ms AESOI**   **(o): z=2mm, 2ms AESOI**
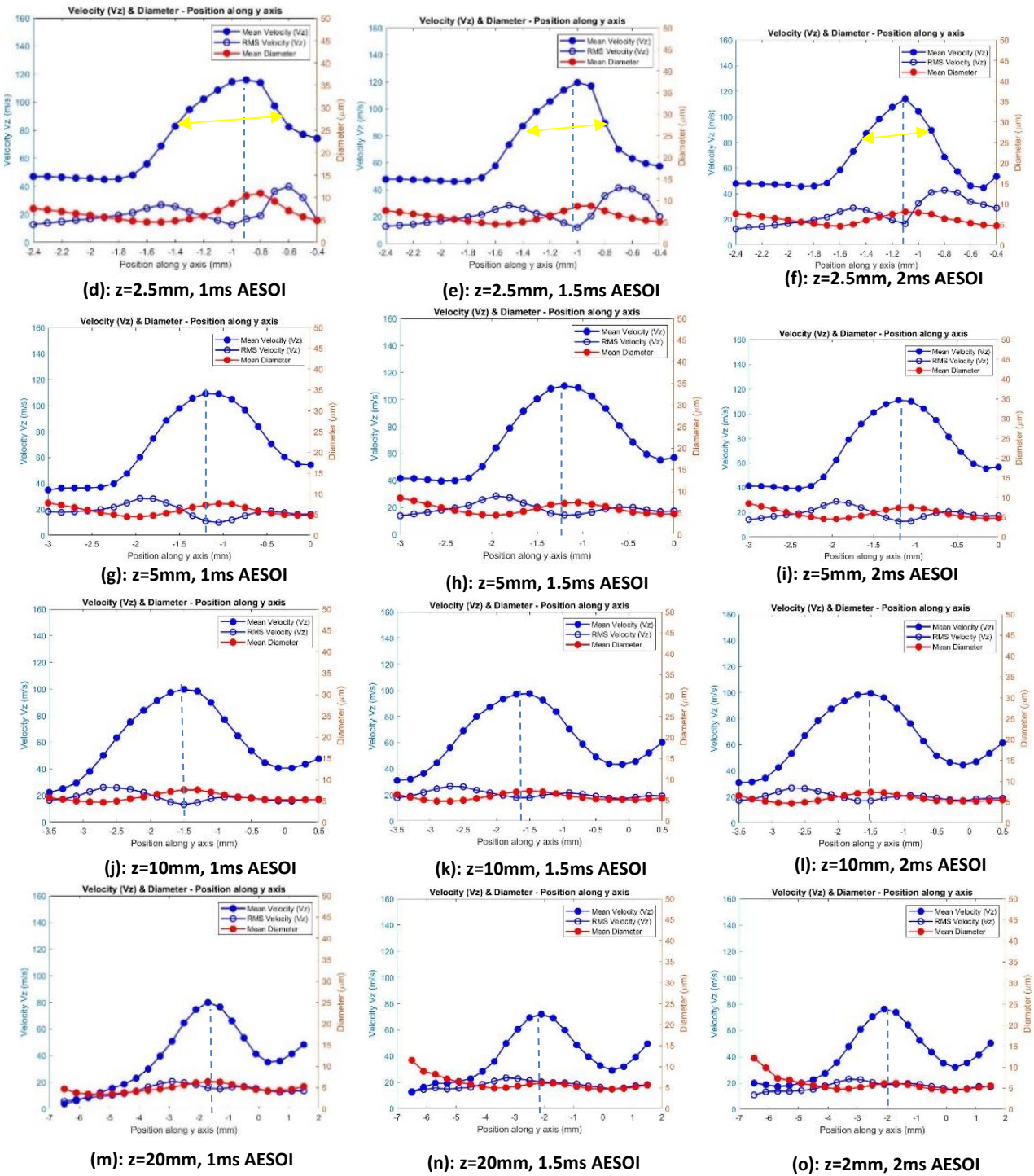
Figure 7-15 Spatial velocity and diameter graphs at 1ms (left), 1.5ms(middle), 2ms(right) ASOI injection for different z locations at 100 bar injection pressure and 2ms injection duration

contraction and instability of the jet during the main injection event as has been demonstrated before in the section 7.3.3 by using contour plot of velocities at similar instantaneous times during the main injection event.

7.5.3   Comparison of temporal droplet diameter (D10) and SMD (D32) graphs

Figure 7-16 shows temporal mean diameter (D10) (blue colour) and SMD (D32) (red colour) for two y locations on the same z plane. As an example in the first row, figure 7-16 (a) shows the SMD and diameter graphs at z=1mm, y=-1.5mm which is located on the edge of the spray while figure 7-16 (b) shows the SMD and diameter graphs at z=1mm, y=-1.05mm which is located at the centre of the jet. From observing the overall trends of the SMD graphs at the edge of the spray (red color) in figures 7-16 (a) (c) (e) and (g) at z= 1, 2.5, 5, and 10mm respectively, it could be seen that the SMD graphs at the edge of the spray remains almost constant around 10 μm (or less) for the duration of the main injection event (ie 1ms to 2ms) followed by a sharp increase during the closing event of the needle. It is also clear from figures 7-16 (a) (c) (e) and (g) (z= 1, 2.5, 5, and 10mm respectively) that the SMD graphs at the edge of the spray during the main injection event (ie from 1ms to 2ms) has almost similar values compared to diameter graphs (blue) with only slight difference. On the other hand, it is clear from figures 7-16 (b) (d) (f) and (h), that the SMD values at the centre of the jet at any z location are between 2-3 times higher than the average droplet diameters. This is perhaps due to the higher velocity and droplet size at the core of the spray compared to the edge of the spray that can increase the SMD values up to threefold. It is also interesting to note from figure 7-16 (b) that at the z locations closer to the nozzle exit (ie z=1) and in the centre of the spray, SMD values are starting from around 30μm at the start of the injection event (ie 1ms) and are reducing to 20 μm towards the end of injection (ie 2ms) and this shows that there is a decreasing trend in the temporal SMD graphs at the centre of the jet very close to the nozzle exit.

(a): z=1mm, y=-1.5mm

(b): z=1mm, y=-1.05mm

(c): z=2.5mm, y=-2.4mm

(d): z=2.5mm, y=-1.2mm

(e): z=5mm, y=-3mm

(f): z=5mm, y=-1.3

(g): z=10mm, y=-3.5mm

(h): z=10mm, y=-1.4mm
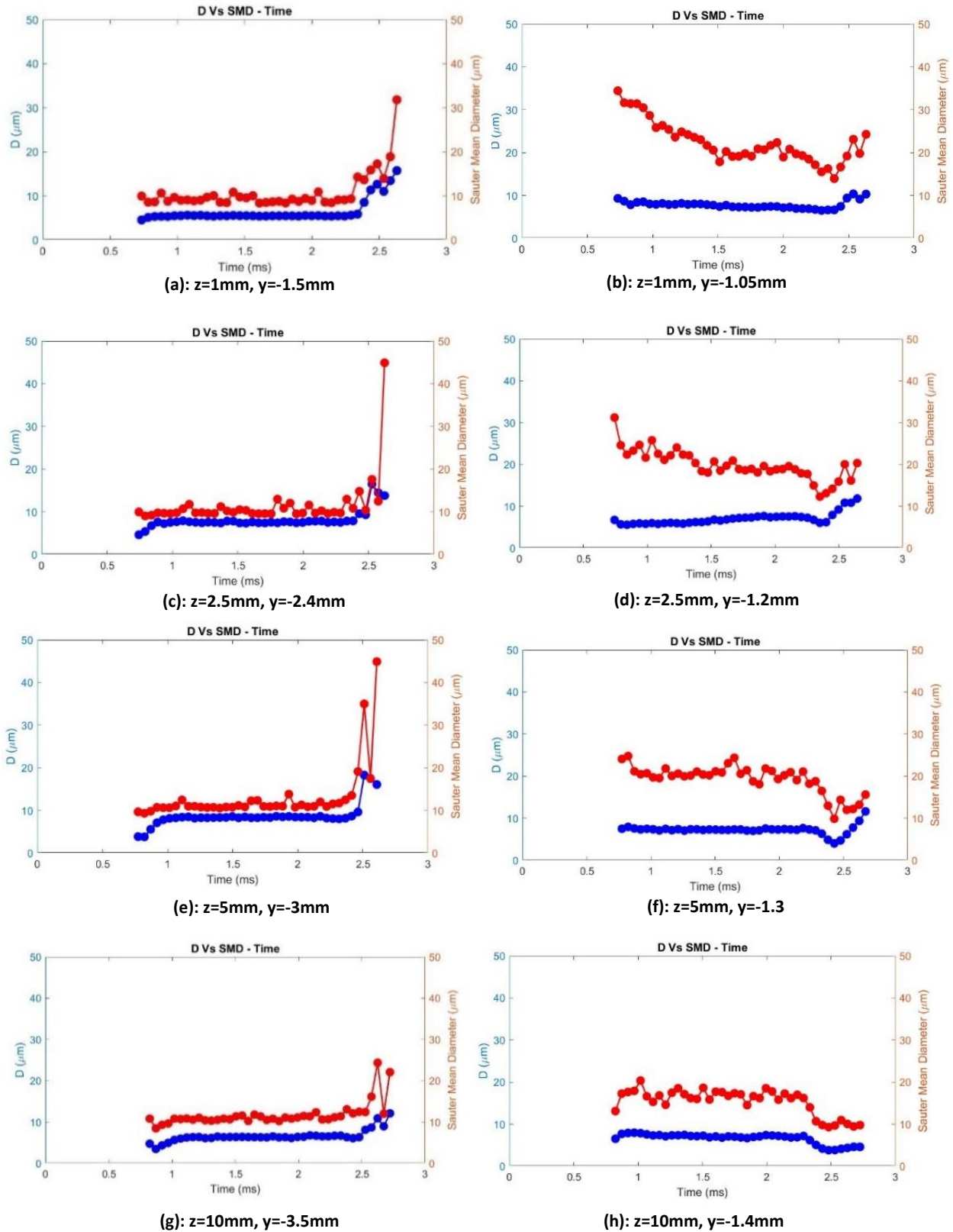
Figure 7-16 Temporal mean diameter (D10) and SMD (D32) for two y locations (edge on the left and centre of the jet on the right) at different z locations for 100 bar injection pressure and 2ms injection duration

This could be due to the increasing trend in the number of samples passing through the probing volume during the main injection event.

7.5.4 Instantaneous mean droplet diameter (D10) and SMD (D32) distribution

Figure 7-17 (a) to (o) shows the instantaneous mean droplet diameter and SMD distribution along y axis for 3 AESOI time of 1ms, 1.5ms, and 2ms for different z locations. Each row shows the graphs related to same z location. It could be seen from all the cases that there is a jet shape for all the graphs with a peak at the centre of the graph. It could also be seen that the peak of the SMD is more or less located at the same position as the peak of the diameter graphs.

It is apparent from figure 7-17 a to c that, at z=1mm, the instantaneous SMD distribution at 1ms AESOI has higher peak compared to 1.5ms and 2ms respectively. This was also shown in the previous section where there is a decreasing trend in the temporal SMD graph in figure 7-16 b. This trend is also evident at z=2.5mm in figures 7-17 d to f where the peak of the instantaneous SMD graph reduces from 30μm at 1ms AESOI to around 20μm AESOI.

It could be seen from figure 7-17 (g) to (o) that for the z locations of 5mm and above, the SMD distribution does not change significantly from the start to the end of the main injection event.

(a): z=1mm, AESOI=1ms

(b): z=1mm, AESOI=1.5ms

(c): z=1mm, AESOI=2ms

(d): z=2.5mm, AESOI=1ms **(e): z=2.5mm, AESOI=1.5ms** **(f): z=2.5mm, AESOI=2ms**

(g): z=5mm, AESOI=1ms **(h): z=5mm, AESOI=1.5ms** **(i): z=5mm, AESOI=2ms**

(j): z=10mm, AESOI=1ms **(k): z=10mm, AESOI=1.5ms** **(l): z=10mm, AESOI=2ms**
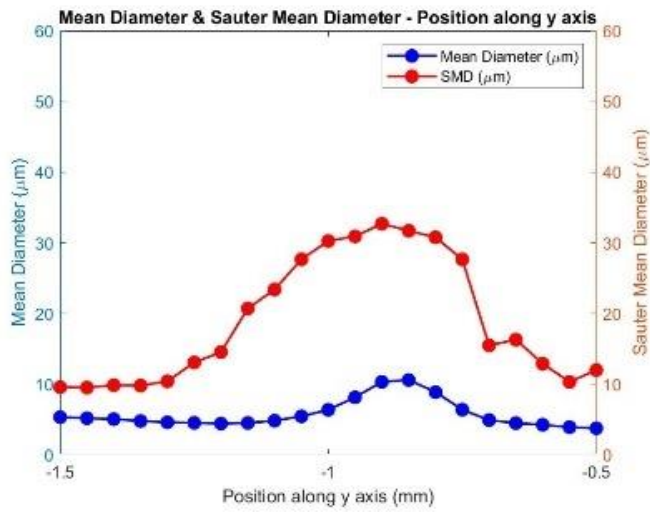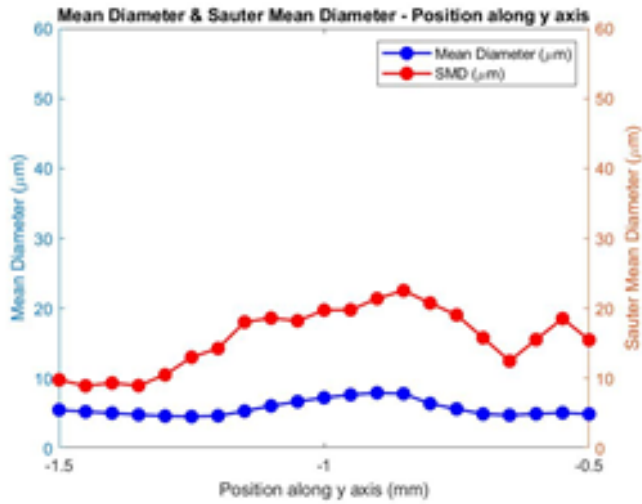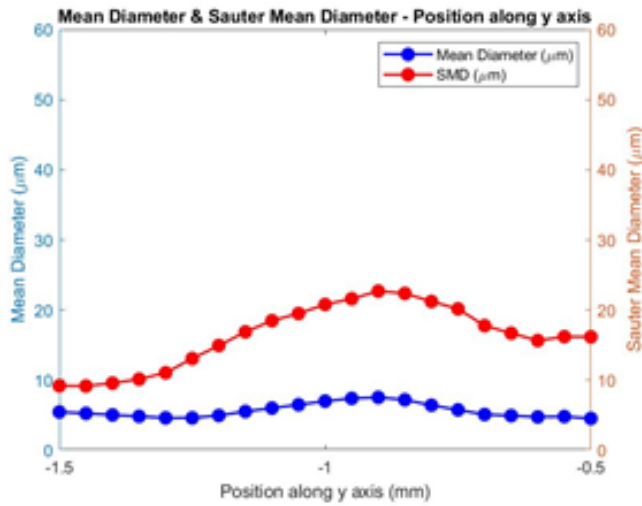
(m): z=20mm, AESOI=1ms **(n): z=20mm, AESOI=1.5ms** **(o): z=20mm, AESOI=2ms**
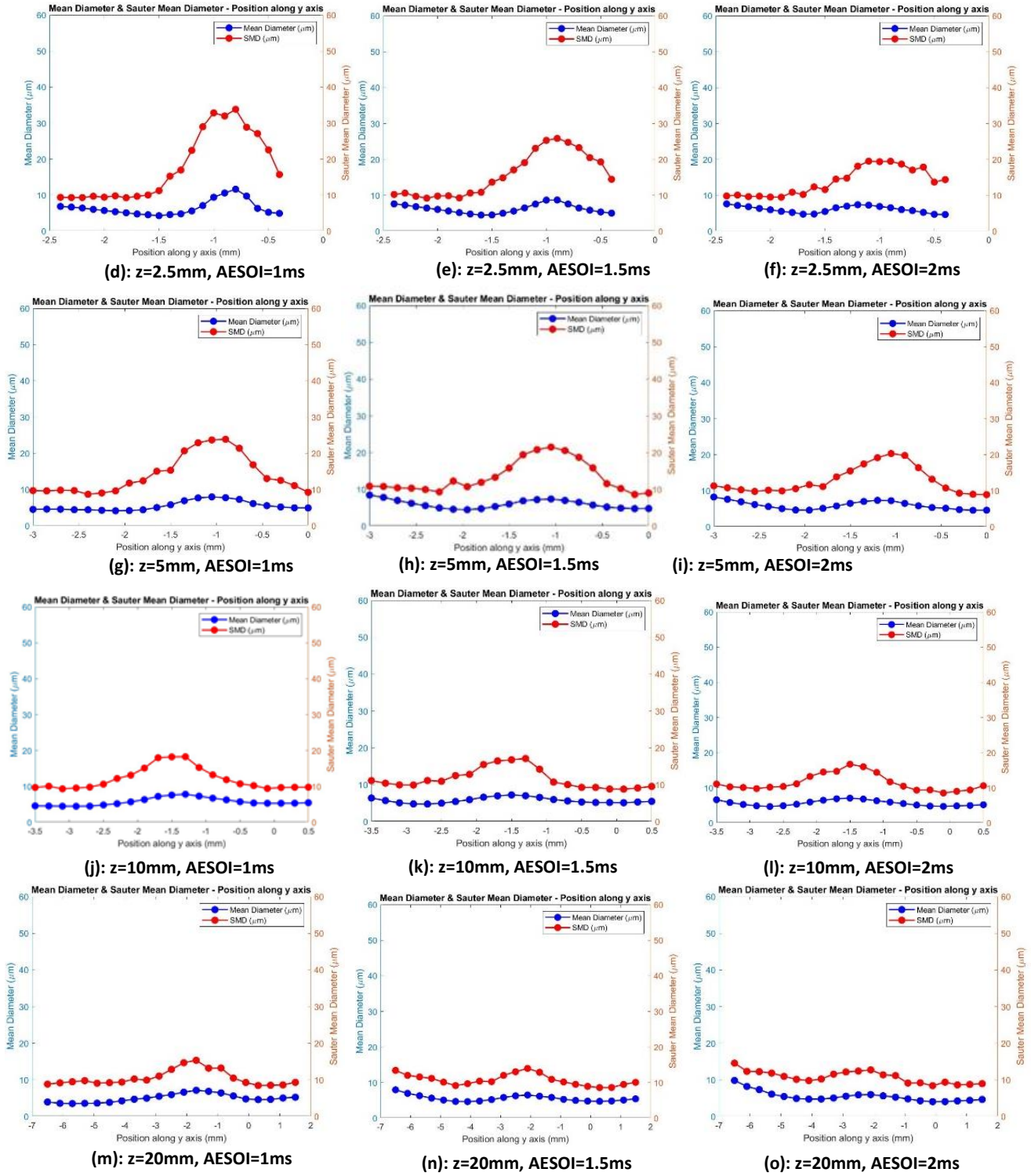
Figure 7-17 Spatial mean diameter (D10) and SMD (D32) along y axis at 1ms (left), 1.5ms (middle), and 2ms (right) ASOI injection for different z locations at 100 bar injection pressure and 2ms injection duration

7.5.5 **Temporal Weber Number graphs**

Figure 7-18 (a) to (h) shows the temporal weber number analysis for different y and z locations at 100 bar injection pressure and 2ms injection duration. Each row in the figure is related to the same z with different y location. As an example, figure 7-18 (a) shows the temporal weber number at the edge of the jet where z=1mm and y=1.5mm while figure 7-18 (b) shows temporal weber at the centre of the jet where z=1mm and y= -1.05mm. It could be seen that the weber number for the centre of the jet is higher than that of the edge of the jet. At the edge of the jet the weber numbers are very low close to zero which means that the spray is fully atomised and there is no more atomisation. This behaviour is same for all z locations. It is also evident that the Weber numbers at the centre of the jet are rather constant and less than 10 for all the z locations. It demonstrated that the critical weber number of 12.5 has been reached earlier and this means that the secondary atomisation is happening either inside the stepped-hole or at z locations smaller than 1mm from the nozzle tip.

(a): z=1mm, y=-1.5mm

(b): z=1mm, y=-1.05mm

(c): z=2.5mm, y=-2.4mm

(d): z=2.5mm, y=-1.2mm

(e): z=5mm, y=-3mm

(f): z=5mm, y=-1.3

(g): z=10mm, y=-3.5mm

(h): z=10mm, y=-1.4mm
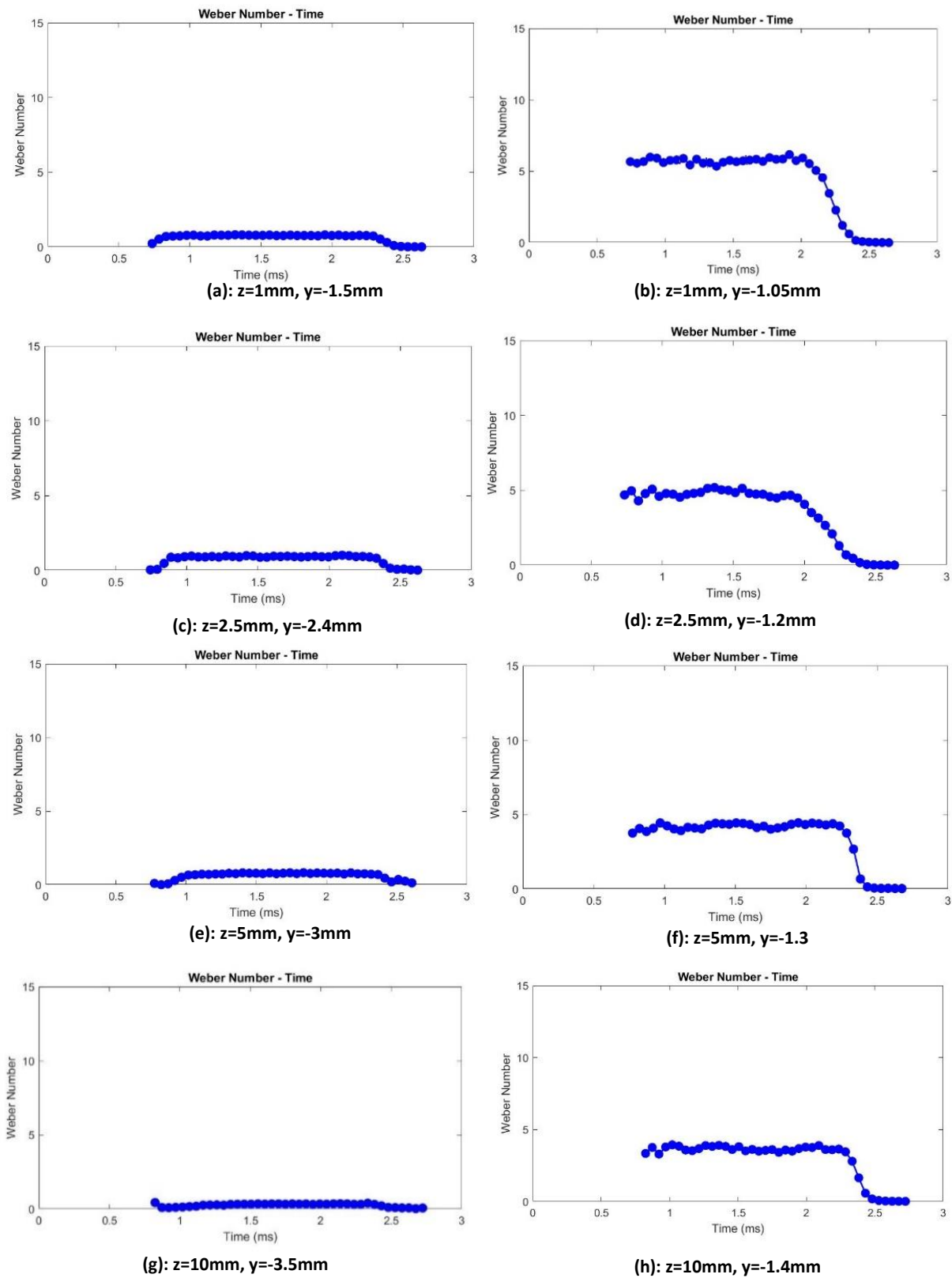
Figure 7-18 Temporal Weber Number Analysis for two different y locations (edge on the left and centre of jet on the right) at different z locations for 100 bar injection pressure and 2ms injection duration

7.5.6   Instantaneous spatial Weber Number distribution

Figures 7-19 (a) to (o) shows the instantaneous spatial Weber Number distribution

along y axis at different z locations for 3 different times of 1ms, 1.5ms and 2ms AESOI

for the pressure of 100 bar and the injection duration of 2ms. It is clear that the weber

(a): z=1mm, AESOI=1ms
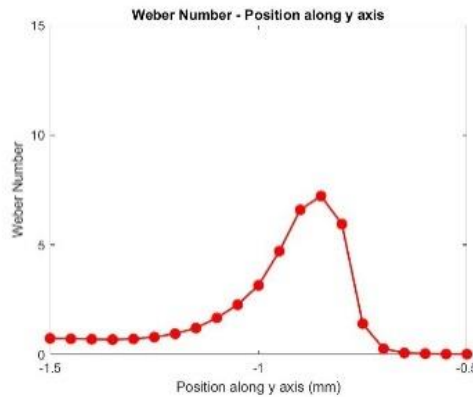
(b): z=1mm, AESOI=1.5ms
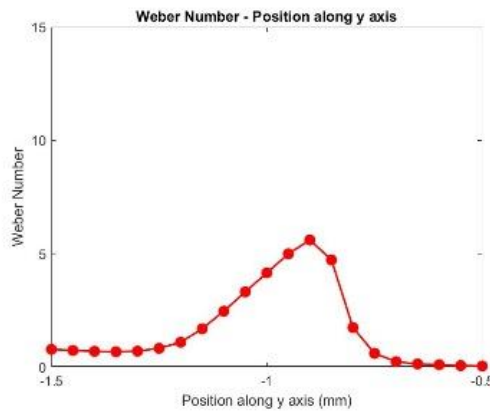
(c): z=1mm, AESOI=2ms
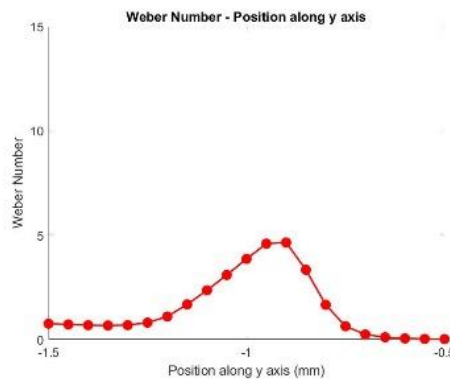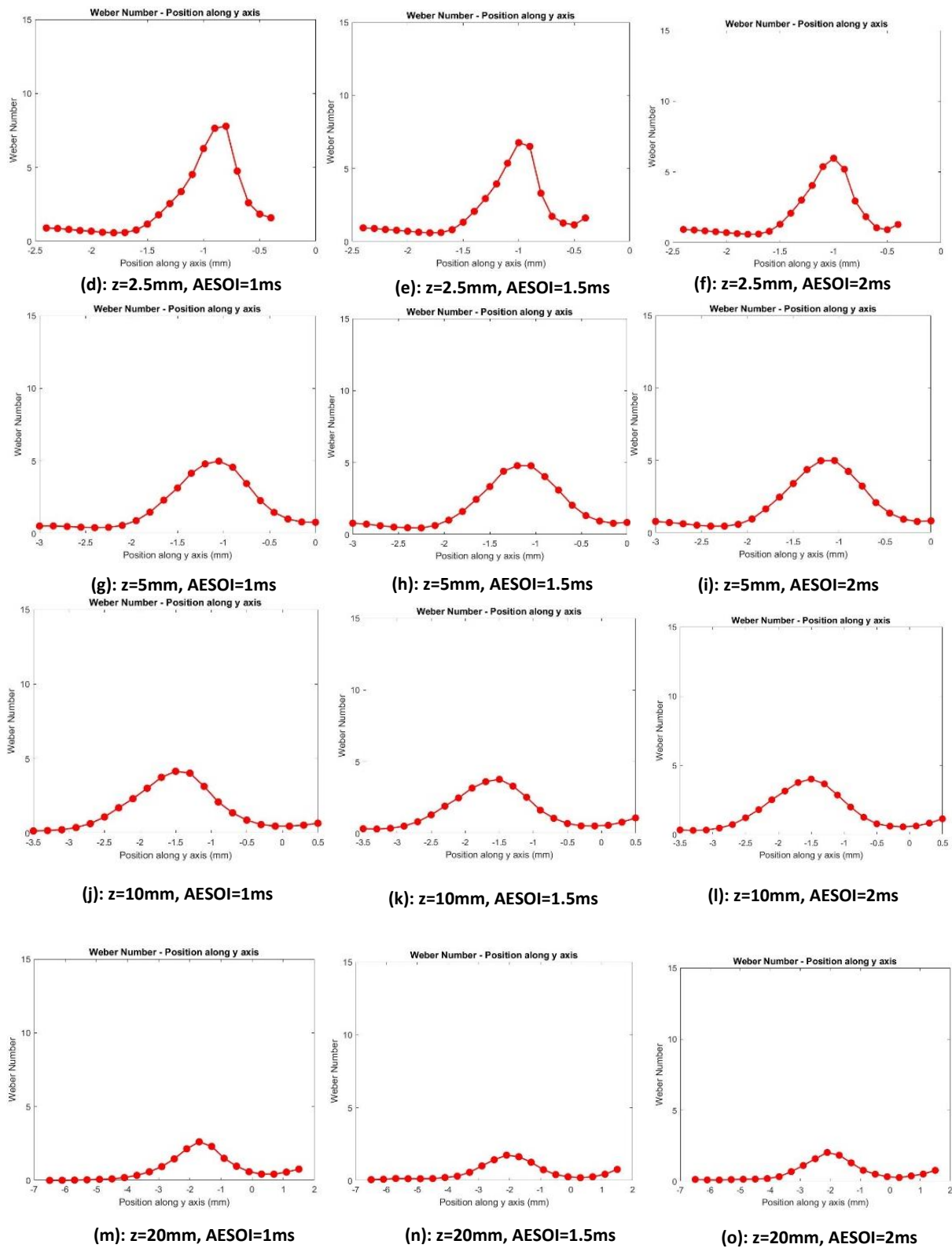
Figure 7-19 Spatial Weber Number Analysis along y axis at 1ms (left), 1.5ms (middle), and 2ms (right) ASOI injection for different z locations for 100 bar injection pressure and 2ms injection duration

number distribution has a jet shape. It is evident from figure 7-19 (a) to (c), the peak of the weber number distribution drops from values around 8 at 1ms AESOI to 5 at 1.5ms AESOI and continues to decrease to around 2 at 2ms AESOI. This decreasing trend is also evident for z=2.5mm in figures 7-19 d to f while the weber numbers have almost same values as z=1mm. However for z location of z=5mm and above (ie figure 7-19 (g) to (o), the peak of the Weber number distribution is less than 5 and does not change significantly during the main injection event from 1ms AESOI to 2ms AESOI.

7.5.7 Comparison of the performance of the injector with respect to the previous works

Figure 7-20 (a) shows the peak values of Weber number at the centre of the jet at different z locations averaged over 1ms during the main injection event. It is clear that the Weber numbers are less than critical weber number and are smaller than 12.5. Comparing the Weber numbers with the work of Andrea Marchi, it could be seen that the performance of the stepped injector is better than that of the pintle type injector.

stepped-nozzle multihole injector

Piezo injector

(a)   (b)
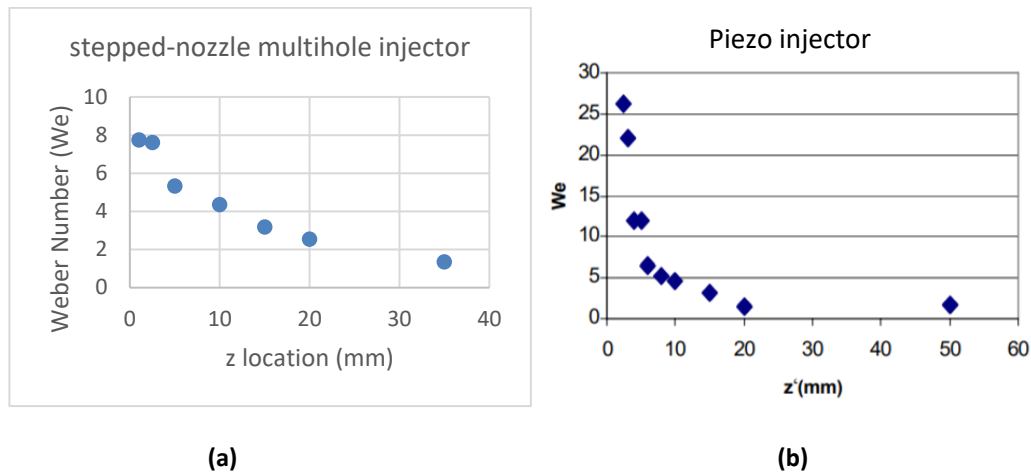
Figure 7-20 Weber number as a function of z for the current stepped-nozzle injector and the previous work of A. Marchi [44]

7.6   Summary

In this chapter, a Fiberflow Dantec PDA measurement system was setup to measure spray characteristics including droplet diameters and velocities at different axial location from the very near-nozzle distance from the injector (z=1mm) up to a distance of z=35mm from the injector, to investigate early breakup. Due to the very closed-spaced compact arrangement of the nozzle holes located at the injector tip region, high attention was given to the setup and location of the probe position at the edge of the injector tip. In order to do this, the zero point of the traverse reference system was carefully chosen using a novel technique which ensured that it was exactly located on the symmetric axis of the injector tip. In addition, one of the nozzle jet sprays was carefully isolated and the mounting was rotated and aligned in a specific direction that allowed the spray droplets to have maximum exposure to the PDA detector system while travelling through the probe region. This alignment was configured to ensure that the

vertical projection of the droplet velocities are maximum while travelling through the probe region. The main finding of this phase of the measurements are as follow:

- The new injector set up arrangement and optical set up ensured the minimum attenuation of the transmitting beams and collecting scattered light that allowed full measurements of droplets velocity and diameters across the spray at the vicinity of injector at z=1mm, which is a major achievement compared to previous works.

- It was found that the droplets can reach velocities of up to 120m/s at 100 bar. This was in very good agreement with the in-nozzle flow velocity of a stepped hole injector which was obtained by micro-PIV at the same injection pressure. This proved accuracy of the measurements to be very good at a distance of 1mm away from nozzle exit.

- A comparison of the results between the mean droplet diameters of the current stepped multi-hole injector (7.5 μm at 100 bar and z=1mm) with a conventional straight multi-hole injector [46] (~15 μm at 120 bar and z=2.5mm) and an outward opening pintle-type injector [54] (~13 μm at 200 and z=5mm) shows a good advantage of the current injector relative to the other two injectors and suggest it has a better atomization capability; note that all three cases considered here have used the same PDA system. The improved atomization performance can be due to the stepped part of the current injector which could affect the internal flow turbulence where the fuel undergoes through a sudden expansion

process whereby the flow becomes 3-D and highly turbulent and becomes susceptible to earlier breakup and rapid atomization.

- It was observed from the temporal velocity contour plots that the core of the velocity of the centre of the jet reaches 120m/s at 100 bar injection pressure. As expected, these temporal maximum velocities are higher than the time-averaged values at the centre of the jet.

- It was seen that at z=1mm, due to the closed spacing compact arrangement of the holes, the space between the adjacent jets 1&2 and 1&3 is associated with average droplet velocities of up to 60 m/s which shows high interaction of adjacent jets with each other and therefore the formation of a more uniform spray with less visible boundary between adjacent jets.

- Approximate x-y coordinates of the centre of the jet where maximum velocity (Vz) happens at each z location were obtained

- It was obtained from the temporal contour plot of velocities that the y length of the main body of the jet decreases slightly over the main injection duration period and this suggests that although it is believed that the jet is in steady state during the main injection event, it is actually changing its shape and becomes slightly contracted during the main injection event.

- It was observed from the temporal contour plot of velocities that the main core of the jet is comprised of 4 smaller jets which are referred to 'micro-jets' or 'sub-jets' which are tightly close to each other like a T shape and this is in agreement with what was proposed in the 7-times enlarged model of the injector.

- It was observed that the y coordinates of the local peaks in the jet are changing as AESOI time changes from 1ms to 1.5ms and to 2ms.

- It could be claimed that the temporal velocities at a fixed point of measurement at the centre of the jet could be either increased or decreased during the main injection event due to the dislocation of microjets which are located close to the point of measurement.

- The presence of the local peaks were observed in the temporal droplet diameter contour plot in the same x,y location as they were observed in the temporal velocity contour plots.

- It was observed from the temporal diameter contour plots that at z=1mm, the maximum droplet diameter values decrease from around 9 μm at 1ms to 7.5μm at 1.5ms and finally decreases to around 6.5 μm at 2ms AESOI.

- A uniform low velocity region with minimum thickness of around 150μm was seen at the edge of the jet at z=1mm. This is the outer part of the jet which is under the influence of stochastic ligament breakup. These stochastic ligaments are usually formed in the regions where the ratio of the volume of fluid (VOF) is small compared to the core of the liquid jet in the nozzle as a result of interaction of the outer part of the jet with the cylindrical surface of the counterbore stepped section.

- It was observed that the velocities obtained from the temporal velocity graphs are in good agreement with the velocities obtained from temporal velocity contour plots

- It was observed from the temporal velocity graphs that the spray velocity at the inner side of the jet edge (which is closer to the injector axis) has higher fluctuations compared to the temporal velocity graphs for the points which are located at the outer edge of the jet (further away from injector axis) . This is perhaps related to the existence of the low VOF region at the inner side of the jet where cavitation and hydraulic flip can possibly occurs and creates fluctuations in the temporal velocity graph of the spray. This can ultimately cause tip wetting on the inner side of the jet more than the outer side.

- It was observed from the temporal graphs of droplet diameter that the larger droplets, that are formed at the end of injection at the tail of the graphs as a result of needle closing event, are more pronounced at the outer side of the jet where the core of the main jet exists (which is closer to the PDA instrument and is further away from the injector axis) than the inner side of the jet (which is closer to the injector axis).

- It could be claimed from comparing the spatial axial velocity graphs at different z locations that the stepped-nozzle can enhance the atomization of the spray by exposing the outer part of the spray to high amount of early air-entrainment which ultimately results in reduction of velocity at the edges of the spray

- Comparison of the spatial velocity graphs at z=1mm obtained by PDA measurement with the spatial velocity graphs obtained by micro-PIV technique shows very good agreement and precision of the PDA results.

- The SMD values at the edge of the spray at any z location is small (less than 10 μm) and are slightly higher than the average droplet diameter values (5-6 μm)

- The SMD values at the centre of the jet at any z location are higher (20-30 μm) and are between 3-4 times higher than the average droplet diameters (6-9 μm)

- It was observed from instantaneous spatial SMD and droplet diameter graphs at z=1mm and z=2.5mm that the maximum SMD at the centre of the jet during the main injection event drops from around 30 μm to 20 μm.

- It could be seen that the weber number for the centre of the jet is higher than that of the edge of the jet

- It was observed that the Weber numbers at the centre of the jet are less than 10 for all the z locations. This shows that there is likely no secondary atomisation happening from the point z=1mm onwards. It demonstrated that the critical weber number of 12.5 has been reached earlier before the point of z=1mm and this means that the secondary atomisation is happening either inside the stepped-hole or at z locations smaller than 1mm from the nozzle tip.

- Comparing the Weber numbers with the work of Andrea Marchi on the piezo injector, it could be seen that the performance of the stepped multihole injector is better than that of the pintle type injectors

Chapter 8:   Conclusion and recommendation for further work

8.1   Conclusion

The current research work aimed to address some of the issues associated with cavitation inside the multi-hole nozzle and its link to the spray stability and atomisation. In addition, spray characteristics and performance of a new design of a multi-hole injector was quantified by measuring droplets velocity and diameter across the spray and compared with other types of injectors. The results and main contributions are presented in four phases as follow:

Geometric and string cavitation was observed in the nozzle and their site of occurrence was visualized. It was seen that both geometric and string cavitation can influence the stability of the near-nozzle exit spray. This has been reported before in previous works. The vertical (or tangential) velocity of the bubble pocket was found to be almost 20m/s whereas the mean axial velocity calculated from the flow rate measurement was 17.14 m/s. A reverse backwards vortex were observed for the first time inside the nozzle at low cavitation numbers which affected the spray structure and cone angles. Two counter rotating strings were visulised for the first time at high cavitation numbers which caused a highly turbulent in-nozzle flow. The directionality of the string cavitation and the spray angle was also visualized for the first time. It was visualized for the first time that the interaction between the geometrical and vortex cavitation shows the displacement and

rolling of the leading edge of the geometric cavitation on the top surface near the hole

entry at full lift and high cavitation and Reynolds number. The displacement and possible

impact of bubble pockets on the top surface of the nozzle at full lift and high cavitation

and Reynolds number were also visualised and analysed. The bubbles burst through

micro-burst process with velocities much higher (by order of magnitude) when they get

near the surface where the pressure in recovered and their possible impact would result

on further erosion. It was shown that two counter (highlighted) rotating vortex cavitation

coexist at the same time inside the nozzle hole originated from the top and bottom side

of the nozzle at the inlet and get closer together as they convected downstream so that

they almost merged together nearer to the exit. Directionality of the vortex cavitation

and its effect on spray at Full Lift were also visualized as this has been reported in

previous works.   At injection to atmosphere at low cavitation numbers, with no

geometrical cavitation, a random transient reverse vortex structure was found to be

initiated outside the nozzle near its exit in tenth of a millisecond and moved into nozzle

towards its inlet and developed/ and maintained its structure inside the nozzle for

several milliseconds. It was found that increasing the needle lift for the same low

cavitation number seems to decrease the duration of the air entrainment and

penetration inside the nozzle. It was observed that string cavitation can influence the

size of the cone angle. It was seen that as the string cavitation is reached towards the

end of the nozzle, the cone angle increases significantly. The variations of the overall

cone angles as a function of injection pressure (or CN) was analysed which shows a

steady decrease in cone angle with pressure up to P=4bar. The variations of the cone

angle as a function of needle lift at a given pressure shows that the angle might increases with increasing the needle lift.

In the second phase of the experimental investigation, a new original 7-times enlarged model of the same injector was designed and manufactured utilising a CAD software that allowed an enhanced simultaneous visualisation of the in-nozzle flow and near-nozzle jet spray. In this phase, the transparent model was uniquely designed in SOLIDWORKS that allowed for the first time both in-nozzle flow region and the near-nozzle exit spray region to remain optically sharp enough in the same depth-of-the-field region of the camera (DoF of less than 1mm) . The main contribution of the author was to enhance the visualization technique that allowed simultaneous visualization of the link between in-nozzle flow pattern and the near-nozzle jet spray. The main new findings in this phase are:

The structure of the geometric cavitation on top of the nozzle undergoes a transition with increase in CN from a cluster of bubbly cloud vapour into a smoothly horseshoe film cavitation; Cavitation shedding at CN = 2 was captured at 200,000 fps. It was seen that a pocket of air will be sucked into the upper part of the nozzle at CN higher than 2 and hydraulic flip occurs. This will have huge impact on the structure and the angle of the upper and lower edge of the near exit spray and will ultimately result in the formation of a stochastic ligament spray at the top side of the nozzle. Three mechanisms were seen to be responsible for the breakup of the near-nozzle spray at high CN numbers. The first mechanism is the stochastic ligament breakup at the upper part of the spray at the 12 o

clock position. These ligaments could be the resultant of the interaction of the highly turbulent flow inside the nozzle as they emerge outside the nozzle. The second mechanism could be the stochastic sheet (shell) breakup which is believed to be formed circumferentially on both sides of the nozzle wall located at first and fourth quadrant at the cross section of the nozzle exit. The last mechanism responsible for the breakup is possibly the main jet breakup at the lower part of the spray. In all these breakup regimes cavitation and turbulence and aerodynamic drag forces play an important role. It was observed that the stochastic ligament spray may contribute to tip nozzle wetting at the upper part of the nozzle. It was also observed that the string cavitation inside the nozzle hole affects the geometric cavitation region and consequently resulting in a change in spray axis angle and cone angle The results show that the absolute value of the angle increases with increase in CN numbers. It was revealed that the hydraulic flip happens earlier than expected and at lower cavitation numbers compared to 15 times enlarged model.

In the third phase of the experiment, a real-size injector test rig was designed and manufactured using SOLIDWORKS which enabled the stepped injector to rotate along the axis of the needle 360° freely and allowed high-speed visualization of the spray plume from different angles. It also enabled the measurement of the spray cone angle from different angles. It further allowed the investigation of the full spray structure, near-nozzle and very near-nozzle exit spray behaviours by means of visualization and helped to setup the PDA system for in the next part of the experiment. The main finding

of the spray visualisations are: The core of the jet is wider compared to conventional injectors and has a more irregular pattern in the fully developed mode. Two middle jets are flapping from one side to another side creating a snake shape pattern. The structure of the spray in the fully developed mode exhibits an A shape which is believed to be due to the compact and dense nature of arrangement of hole which allow higher interactions between the adjacent jets and high air entrainment in-between each individual jets. It was observed that there is high interaction between each jet and the adjacent jet and therefore a distinct boundary between each jet is not recognisable as the spray develops further downstream in comparison with conventional multi-hole where there is a clear boundary between each jet and less interaction is visible between each individual jets. The overall jet penetration of the stepped hole Bosch injector (injector #3) was compared with conventional straight-hole Bosch injector (injector #1). It was seen that at ASOI of 0.75ms (AESOI 1.5ms), the tip penetration for the stepped hole nozzle was around 50mm which was similar to the tip penetration for the conventional multi-hole at the same ASOI. Due to the fact that the exact size size and angles of the stepped-hole nozzle was not provided, it is not possible to directly compare the penetration together but discarding the internal design, it could be claimed that both injectors are operating within same range in terms of tip penetration. The overall jet penetration of the stepped hole Bosch injector (injector #3) was also compared with magneti marrelli stepped hole injector (injector #2). It could be seen that the of the penetration of the stepped hole Bosch injector at 100 bar at 0.25 ASOI (0.9 AESOI) is around 22mm which is similar to the penetration ofstepped hole magneti marrelli injector at the pressure of 120 bar at 0.25

ms ASOI which is also around 23mm. It should be mentioned that a direct comparison could not be made here again since the internal design of the two injectors are different than each other and also the exact size and angle of the holes of each nozzles are potentially different. However disregarding these facts, it could be seen that both injectors are operating more or less at the same range in terms of tip penetration. It could be seen that as the pressure increases from 50 bar to 100 bar the spray cone angle increase from around 64 degree to 72 degrees.It can be seen that the range of variation of the spray angle for all cases is around 2-3 degrees. It was observed that the edge of the spray is less denser and therefore the fluctuations of the brightness in the shadowgraphs are higher at the edge of the spray compared to the core of the spray. The rotation angle of 360 – 250 = 110 degree is necessary in order to isolate jet 1 in a manner that can provide maximum exposure for receiving optics for the PDA measurement.

In the fourth phase of the experiment, a Fiberflow Dantec PDA measurement system was setup to measure spray characteristics including droplet diameters and velocities at different axial location from the very near-nozzle distance from the injector z=1mm up to a distance of z=35mm from the injector, to investigate early breakup. Due to the very closed-spaced compact arrangement of the nozzle holes located at the injector tip region, high attention was given to the setup and location of the probe position at the edge of the injector tip. In order to do this, the zero point of the traverse reference system was carefully chosen using a novel technique which ensured that it was exactly

located on the symmetric axis of the injector tip. In addition, one of the nozzle jet sprays

was carefully isolated and the mounting was rotated and aligned in a specific direction

that allowed the spray droplets to have maximum exposure to the PDA detector system

while travelling through the probe region. This alignment was configured to ensure that

the vertical projection of the droplet velocities are maximum while travelling through

the probe region. The main finding of this phase of the measurements are as follow: The

new injector set up arrangement and optical set up ensured the minimum attenuation

of the transmitting beams and collecting scattered light that allowed full measurements

of droplets velocity and diameters across the spray at the vicinity of injector at z=1mm.

It was found that the droplets can reach velocities of up to 120m/s at 100 bar. This was

in very good agreement with the in-nozzle flow velocity of a stepped hole injector which

was obtained by micro-PIV at the same injection pressure. A comparison of the results

between the mean droplet diameters of the current stepped multi-hole injector (7.5 μm

at 100 bar and z=1mm) with a conventional straight multi-hole injector [46] (~15 μm at

120 bar and z=2.5mm) and an outward opening pintle-type injector [54] (~13 μm at 200

and z=5mm) shows a good advantage of the current injector relative to the other two

injectors and suggest it has a better atomization capability; note that all three cases

considered here have used the same PDA system. The improved atomization

performance can be due to the stepped part of the current injector where the fuel

undergoes through a sudden expansion process whereby the flow becomes 3-D and

highly turbulent and becomes susceptible to earlier breakup and rapid atomization. It

was observed from the temporal velocity contour plots that the core of the velocity of

the centre of the jet reaches 120m/s at 100 bar injection pressure. As expected, these

temporal maximum velocities are higher than the time-averaged values at the centre of

the jet. It was seen that at z=1mm, due to the closed spacing compact arrangement of

the holes, the space between the adjacent jets 1&2 and 1&3 is associated with average

droplet velocities of up to 60 m/s which shows high interaction of adjacent jets with each

other and therefore the formation of a more uniform spray with less visible boundary

between adjacent jets. Approximate x-y coordinates of the centre of the jet where

maximum velocity (Vz) happens at each z location were obtained. It was obtained from

the temporal contour plot of velocities that the y length of the main body of the jet

decreases slightly over the main injection duration period and this suggests that although

it is believed that the jet is in steady state during the main injection event, it is actually

changing its shape and becomes slightly contracted during the main injection event. It

was observed from the temporal contour plot of velocities that the main core of the jet

is comprised of 4 smaller jets which are referred to 'micro-jets' or 'sub-jets' which are

tightly close to each other like a T shape and this is in agreement with what was proposed

in the 7-times enlarged model of the injector. It was observed that the y coordinates of

the local peaks in the jet are changing as AESOI time changes from 1ms to 1.5ms and to

2ms. It could be claimed that the temporal velocities at a fixed point of measurement at

the centre of the jet could be either increased or decreased during the main injection

event due to the dislocation of microjets which are located close to the point of

measurement. The presence of the local peaks were observed in the temporal droplet

diameter contour plot in the same x,y location as they were observed in the temporal

velocity contour plots. It was observed from the temporal diameter contour plots that at z=1mm, the maximum droplet diameter values decrease from around 9 μm at 1ms to 7.5μm at 1.5ms and finally decreases to around 6.5 μm at 2ms AESOI. A uniform low velocity region with minimum thickness of around 150μm was seen at the edge of the jet at z=1mm. This is the outer part of the jet which is under the influence of stochastic ligament breakup. These stochastic ligaments are usually formed in the regions where the ratio of the volume of fluid (VOF) is small compared to the core of the liquid jet in the nozzle as a result of interaction of the outer part of the jet with the cylindrical surface of the counterbore stepped section. It was observed that the velocities obtained from the temporal velocity graphs are in good agreement with the velocities obtained from temporal velocity contour plots. It was observed from the temporal velocity graphs that the spray velocity at the inner side of the jet edge (which is closer to the injector axis) has higher fluctuations compared to the temporal velocity graphs for the points which are located at the outer edge of the jet (further away from injector axis) . This is perhaps related to the existence of the low VOF region at the inner side of the jet where cavitation and hydraulic flip can possibly occurs and creates fluctuations in the temporal velocity graph of the spray. This can ultimately cause tip wetting on the inner side of the jet more than the outer side. It was observed from the temporal graphs of droplet diameter that the larger droplets, that are formed at the end of injection at the tail of the graphs as a result of needle closing event, are more pronounced at the outer side of the jet where the core of the main jet exists (which is closer to the PDA instrument and is further away from the injector axis) than the inner side of the jet (which is closer to the injector axis).

It could be claimed from comparing the spatial axial velocity graphs at different z locations that the stepped-nozzle can enhance the atomization of the spray by exposing the outer part of the spray to high amount of early air-entrainment which ultimately results in reduction of velocity at the edges of the spray. Comparison of the spatial velocity graphs at z=1mm obtained by PDA measurement with the spatial velocity graphs obtained by micro-PIV technique shows very good agreement and precision of the PDA results. The SMD values at the edge of the spray at any z location is small (less than 10 μm) and are slightly higher than the average droplet diameter values (5-6 μm). The SMD values at the centre of the jet at any z location are higher (20-30 μm) and are between 3-4 times higher than the average droplet diameters (6-9 μm). It was observed from instantaneous spatial SMD and droplet diameter graphs at z=1mm and z=2.5mm that the maximum SMD at the centre of the jet during the main injection event drops from around 30 μm to 20 μm. It could be seen that the weber number for the centre of the jet is higher than that of the edge of the jet. It was observed that the Weber numbers at the centre of the jet are less than 10 for all the z locations. This shows that there is likely no secondary atomisation happening from the point z=1mm onwards. It demonstrated that the critical weber number of 12.5 has been reached earlier before the point of z=1mm and this means that the secondary atomisation is happening either inside the stepped-hole or at z locations smaller than 1mm from the nozzle tip. Comparing the Weber numbers with the work of Andrea Marchi on the piezo injector, it could be seen that the performance of the stepped multihole injector is better than that of the pintle type injectors

8.2   Recommendation for further work

For the enlarged model, it could be recommended that the micro-PIV technique could

be used in order to find contour velocities of the in-nozzle flow inside enlarged models

of the injector and validate them by the current CFD codes. This could be done similar

to the work of Mamaikin et al [7]. It could be recommended that the internal geometry

of the injector would be obtained by means of X-ray tomography in order to replicate a

3D transparent real-size of the same injector. The dimensions could also be used to

create a realsize model in CAD software which could be used for valication of different

CFD simulation codes. The transparent real-size could be used for micro-PIV

measurement of the internal flow as well as PDA measurement of the very near-nozzle

jet spray. the combined micro-PIV of the in-nozzle flow of the transparent real-size

model along with PDA of the same model at very near-nozzle distance similar to the

current work may yield fascinating results which could then be used as a reference

point for CFD codes related to the mixure formation of the spray inside the

combustion chamber.

In addition, the Matlab code could be used in conjunction with the PDA system to

design a sensor which can create instantaneous live 2-D velocity contour plot of

continuous injections i.e. in airplane engines.

References

[1]   Andriotis, A., Gavaises, M. & Arcoumanis, C., "Vortex flow and cavitation in diesel injector nozzles.," *Journal of Fluid Mechanics, 610, pp. 195-215 2008.*

[2]   Arcoumanis C. , Gavaises M. , Nouri J.M. , "The Role of Cavitation in Automotive Fuel Injection System.," *School of Engineering and Mathematical Sciences City University London, England.*

[3]   Arcoumanis, C., M. Gavaises, J.M. Nouri, E. Abdul-Wahab and R. Horrocks,, "Analysis of the flow in the nozzle of a vertical multi-hole diesel engine injector.," *Transactions Journal of Engines, SAE paper 980811, SAE Transactions, 1998. 107(3)..*

[4]   Gavaises, M., A. Andriotis, D. Papoulias, N. Mitroglou and A. Theodorakakos,, "Characterization of string cavitation in large-scale Diesel nozzles with tapered holes.," *Physics of Fluids, 2009. 21: p. 052-107..*

[5]   Gavaises. M, "Flow in valve covered orifice nozzles with cylindrical and tapered holes and link to cavitation erosion and engine exhaust emissions.," *International Journal of Engine Research 2008 9: 435..*

[6]   Karathanassis I., Koukouvinis P., Efstathios, "High-Speed Visualization of Vortical Cavitation Using Synchroton Radiation," *Journal of Fluid Mechanics,* 2019.

[7]   Mamaikin D. ,Knorsch T. , Rogler P. , Wensing M.,, "Experimental investigation of fow field and string cavitation inside a transparent real-size GDI nozzle," *Experiments in fluids,* 2020.

[8]   Daniel J. Duke, Alan L. Kastengren, Katarzyna E. Matusik, Andrew B. Swantek, Christopher F. Powell, Raul Payrid, Daniel Vaquerizo, Lama Itanie et al, "Internal and Near Nozzle Measurements of Engine Combustion Network "Spray G" Gasoline Direct Injectors," *Experimental Thermal and Fluid Science,* 2017.

[9]   Skogsberg M., A Study on Spray-Guided Stratified Charge Systems for Gasoline DI Engines', Chalmers University of Technology, 2007.

[10]   International Council on Clean Transportation, "Comparing CO2 emmission levels of a modern medium size car model under laboratory and on-raod testing conditions," [Online]. Available: https://theicct.org/sites/default/files/Gas%20_v%20_Diesel_%20CO2_emissions_%20EN_%20Fact%20_Sheet%202019_05_07_0.pdf.

[11]   Kapus, P.E. et al., "Ethanol direct injection on turbocharged SI engines – Potential and challenges," *SAE paper series,* pp. (2007-01-1408), 2007.

[12]   Zhao F., Laia M.-C. , Harringtonb D.L.,, "Automotive spark-ignited direct-injection gasoline engines,," *Progress in Energy and Combustion Science,* vol. 25, 1999.

[13]   Zhao F., Laia M.-C., Harringtonb D.L.,, "Automotive spark-ignited direct-injection gasoline engines,," *Progress in Energy and Combustion Science 25 (1999)..*

[14]   Rober Bosch GmBH, [Online]. Available: https://www.bosch-presse.de/pressportal/de/en/gasoline-injection-systems-42304.html.

[15]   P. T. Marchitto L., "Characterization of air/fuel mixture and combustion processes in a DISI engine through advanced optical and X-ray based diagnostics," 2015.

[16]   "Mercedes brings lean-burn, stratified BlueDirect to CLA-Class for 7% boost in fuel economy; new all-wheel A-Class cars," [Online]. Available: https://www.greencarcongress.com/2014/02/20140207-mb.html.

[17]   Powen Tu PhD Thesis, "Numerical and Experimental Study of Spray Characteristics in the Gasoline Direct Injection Engine," 2016.

[18]   [Online]. Available: https://www.tomorrowstechnician.com/bosch-celebrates-40th-anniversary-of-fuel-injection/.

[19]   Robert Bosch GmBH, , [Online]. Available: https://www.bosch-presse.de/pressportal/de/en/gasoline-injection-systems-42304.html.

[20]   Kazour, J., Befrui, B., Husted, H., Raney, M. et al, "Innovative Sprays and Particulate Reduction with GDi Injectors," *SAE Technical Paper 2014-01-1441, 2014, doi:10.4271/2014-01-1441..*

[21]   Daniel J. Duke, Alan L. Kastengrenc, Katarzyna E.Matusika, Andrew B. Swanteka, Christopher F.Powell, Raul Payri, Daniel Vaquerizod, LamaItanie ,Gilles, Bruneauxe, Ronald O.Grover Jr. f Scott Parrish, "Internal and Near Nozzle Measurements of Engine Combustion Network "Spray G" Gasoline Direct Injectors," *Experimental Thermal and Fluid Science (EXP THERM FLUID SCI) 88,* 2017.

[22]   Mielke, M., Kim, K., Peng, X., Lee, W. Gu, X., Masor, G.,Gee, S., Hamamoto, M., Lu, R., Gaudiosi, D., Shirk, M., "100 μJ, 20 W Femtosecond Fiber Laser for Precision Industrial Micro-Machining,," *Optical Society of America, 2013.*

[23]   Leick P., "Experimental characterization of tip wetting in gasoline DI injectors," *ICLASS 2018, 14th Triennial International Conference on Liquid Atomization and Spray Systems, Chicago, IL, USA, July 22-26, 2018.*

[24]   Brennen, Cavitation and Bubble Dynamics, London: Oxford University Press, 1995.

[25]   Phoevos Koukouvinis, Nicholas Mitroglou, Manolis Gavaises, Massimo Lorenzi , Maurizio Santini, "Quantitative predictions of cavitation presence and e 1 rosion-prone locations in a high pressure cavitation test rig," *Journal of Fluid Mechanics,* vol. 819, no. doi:10.1017/jfm.2017.156, pp. pp. 21-57, 2017.

[26]   Gavaises, M., D. Papoulias, A. Andriotis, E. Giannadakis and A. Theodorakakos., "Link Between Cavitation Development and Erosion Damage in Diesel Injector Nozzles," *SAE 2007-01-0246. 2007.*

[27]   The United States Council for Automotive Research, "Summary report on the transportation combustion engine efficiency colloquium held at USCAR,," March 3 and 4, 2010,. [Online]. Available: https://inspire.ornl.gov/OriginalDocument/6c560576-42e1-4d28-a8f7-3b0e151a463e.

[28]   IJER Editorial: R D Reitz, H Ogawa, R Payri, et al, "The future of IC engines," *International Journal of Engine Research,* p. 23, 2018.

[29]   Association of professors from German, Austrian and Swiss universities, [Online].
         Available: https://www.wkm-ev.de/images/20170708-englisch-Die-Zukunft-des-
         Verbrennungsmotors.pdf.

[30]   Reitz R. D., Atomization and Other Breakup Regimes of a Liquid Jet, Ph.D. thesis,
         Princeton University, Princeton, NJ, 1978..

[31]   Tekawade A. , Mitra P. , Sforzo B. A. , Matusik K. E. , Kastengren A. L. ,Schmidt D. P.
         , Powell C. F. , "A comparison between CFD and 3D X-ray Diagnostics of Internal
         Flow in a Cavitating Diesel Injector Nozzle," *ILASS-Americas 30th Annual
         Conference on Liquid Atomization and Spray Systems, Tempe, AZ, May 2019,* 2019.

[32]   Torelli R. , Sforzo B. A. , Matusik K. E. , Kastengren A. L. , Fezzaa K. , Powell C. P. ,
         Som S. , Pei Y. ,Tzanetakis T. ,Zhang Y. , Traver M. , Cleary D. J. , "Investigation of
         Shot-to-Shot Variability during Short Injections," *ICLASS 2018, 14th Triennial
         International Conference on Liquid Atomization and Spray Systems, Chicago, IL,
         USA, July 22-26, 2018,* 2018.

[33]   Koukouvinis P., Mitroglou N., Gavaises M., Lorenzi M., Santini M., "Quantitative
         predictions of cavitation presence and erosion-prone locations in a high pressure
         cavitation test rig," *Journal of Fluid Mechanics,* vol. 819, no.
         doi:10.1017/jfm.2017.156, pp. pp. 21-57, 2017.

[34]   Nicholas Mitroglou, Michael McLorn, Manolis Gavaises, Celia Soteriou, Mark
         Winterbourne, "Instantaneous and ensemble average cavitation structures in
         Diesel micro-channel flow orifices," *Fuel,* vol. 116, pp. 736-742, 2014.

[35]   Nouri J.M., Mackenzie, S., Gaskell, C. and Dhunput, A.,, "Effect of viscosity,
         temperature and nozzle length-to-diameter ratio on internal flow and cavitation in
         a multi-hole injector.," *In Proc. IMechE Seminar on Fuel Injection. 2012, March 14-
         15, London.*

[36]   P G Aleiferis, J Serras-Pereira, A. Augoye, T. J. Davies, R. F. Cracknell, D.
         Richardson, "Effect of fuel temperature on in-nozzle cavitation and spray
         formation of liquid hydrocarbons and alcohols from a real-size optical injector for
         direct-injection spark-ignition engines.," *International Journal of Heat and Mass
         Transfer, 2010, 89, 3033..*

[37]   Benjamin Balewski, Barbara Heine and Cameron Tropea, , "Experimental investigation for correlation between nozzle flow and spray using LDV PDA High Speed photography and X ray radiography," *Proceedings ILASS-Europe 2008, Sep. 8-10, Como Lake, Italy.*

[38]   Andriotis A and Gavaises M., "Visualization of String Cavitation Formation and Development inside Transparent Diesel Injector Nozzle Replicas," *Proc. 22th Conf. on Liquid Atomization and Spray Systems (ILASS), Como, Italy, 8-10 Sept, 2008.*

[39]   Nouri J.M., Mitroglou, N., Yan Y. and Arcoumanis C.,, "Internal flow and cavitation in a multi-hole injector for gasoline direct injection engines.," *SAE 2007-01-1405 April 2007..*

[40]   Changzhao Jiang, Matthew C. Parker, Jerome Helie, Adrian Spencer, Colin P. Garner, Graham, "Impact of gasoline direct injection fuel injector hole geometry on spray," *Fuel,* 2018.

[41]   Battistoni, M., Magnotti, G., Genzale, C., Arienti, M. et al, "Experimental and Computational Investigation of Subcritical Near-Nozzle Spray Structure and Primary Atomization in the Engine Combustion Network Spray D," *SAE Int. J. Fuels Lubr. 11(4):337-352, 2018, https://doi.org/10.4271/2018-01-0277..*

[42]   Tianyun Li, Seoksu Moon, Kiyotaka Sato , Hideaki Yokohata, "A comprehensive study on the factors affecting near-nozzle spray dynamics of multi-hole GDI injectors," *Fuel,* vol. 190, p. 292–302, 2017.

[43]   Zigan L., Schmitz, I., Wensing, M., Leipertz, A., Reynolds number effects on atomization and cyclic spray fluctuations under gasoline direct injection conditions. Fuel Systems for IC Engines, Woodhead Publishing, 253-263, 2012.

[44]   Andrea Marchi PhD Thesis, , "Internal flow and spray characteristics of an outwards opening pintle-type of gasoline-injector," 2009.

[45]   Nouri, J. M., N. Mitroglou, and C. Arcoumanis., "Spray Structure of double injection from Multi-hole Injectors for Gasoline Direct-Injection Engines.," , 2006,..

[46]   Mitroglou N., "Multihole Injectors for Direct Injection Gasoline Engines," *PhD Thesis, City University London Library, UK, 2006..*

[47]   Sivathanu Y., Lim J., Kulkarni V., "Time-dependent line-of-sight extinction tomography for multi-hole GDI injectors," *International Journal of Spray and Combustion Dynamics,* no. https://doi.org/10.1177/1756827716673522, 2017.

[48]   Befru B. i, Aye A. , Bossi A. ,Markle L. E., and Varble D. L. , "ECN GDi Spray G: Coupled LES Jet Primary Breakup - Lagrangian Spray Simulation and Comparison with Data," *ILASS Americas 28th Annual Conference on Liquid Atomization and Spray Systems, Dearborn, MI, May 2016.*

[49]   Fraidl G., W. Piok, A. Fürhapter, H. Sikinger and A. Pinter,, "The potential of next generation gasoline direct injection technologies.," Associazione Tecnica dell'Automobile, 56:5-17, 2003..

[50]   Wirth, M., D. Zimmermann, R. Friedfeldt, J. Caine, A. Schamel, M. Davies, G. Peirce, A. Storch, K. Ries-Müller, K.P. Gansert, G. Pilgram, R. Ortmann, G. Würfel, J. Gerhardt,, "A Cost Optimised Gasoline Spray Guided Direct Injection System for Improved Fuel efficiency," 2004.

[51]   Mitroglou N., Nouri, J.M., Gavaises M. and Arcoumanis C.,, "Spray Characteristics of a Multi-hole Injector for Direct-injection Gasoline Engines.," Int. Journal of Engine Research 7(3), p.255-270, 2006..

[52]   Marchi A., Nouri J.M., Yan Y., and Arcoumanis C., "Internal Flow and Spray Characteristics of Pintle-Type Outwards Opening Piezo Injectors for Gasoline Direct-Injection Engines," *SAE 2007-01-1406 2007.*

[53]   Nouri J.M., Abo-Serie E., Marchi A, Mitroglou N. and Arcoumanis C.,, "Internal and near nozzle flow characteristics in an enlarged model of an outward opening pintle-type gasoline injector.," *Journal of Physics: Conference Series 85 (1), p.012-035 (2007).*

[54]   Marchi A., "Internal Flow and Spray Characteristics of an Outwards Opening Pintle-type Gasoline-Injector," *PhD Thesis, City University London, UK, 2009.*

[55]   Kim S., Yan Y., Nouri J.M. and Arcoumanis C., "Effects of intake flow on the spray structure of a multi-hole injector in DISI engine," *International Journal of Automotive Technology, 10(3), pp. 277-284, 2009..*

[56]   Mitroglou N., Nouri, J.M., Gavaises M. and Arcoumanis C.,, "Cavitation Inside Enlarged and Real-size Transparent injector nozzles and its Effect on Near-zozzle Spray Formation,," *Droplet Impact Phenomena & Spray Investigation Workshop,,* Bergamo, Italy, May 2012.

[57]   Kim S., Yan Y., Nouri J.M. and Arcoumanis C.,, "Effects of intake flow and coolant temperature on the spatial fuel distribution in a direct-injection gasoline engine by PLIF technique.," *Journal of Fuel, In Press, 2013..*

[58]   Arcoumanis, C., M. Badami, H. Flora and M. Gavaises,, "Cavitation in real size multi-hole diesel injector nozzles.," *Transactions Journal of Engines, SAE paper 2000-01-1249, SAE Transactions, 2000. 109(3): p. 1485-1500..*

[59]   Soteriou, C.C.E., M. Smith and R.J. Andrews., "Cavitation Hydraulic Flip and Atomization in Direct Injection Diesel Sprays,," *IMechE. in IMechE. 1993. London..*

[60]   Roth, H., Gavaises M. and Arcoumanis C.,, "Cavitation Initiation, Its Development and Link with Flow Turbulence in Diesel Injector Nozzles.," *Transactions Journal of Engines, SAE paper 2002-01-0214, SAE Transactions, 2002. 111(3): p. 561-580..*

[61]   Giannadakis, E., M. Gavaises and A. Theodorakakos., "The Influence of Variable Fuel Properties in High-Pressure Diesel Injectors," *SAE 2009-01-0832. 2009..*

[62]   Mitroglou, N., Gavaises, M., Nouri, J. M. & Arcoumanis, C. (2011)., "Cavitation inside Enlarged and real-size fully transparent injector nozzles and its effect on near nozzle spray formation.," *Droplet Impact Phenomena and Spray Investigations Workshop 2011.*

[63]   Arcoumanis, C., S. Golwin, and J. W. Kim. , "Effect of Tumble Strength on Combustion and Exhaust Emissions in a Single-Cylinder, Four-Valve Spark-Ignition Engine.," *Transactions Journal of Engines, SAE paper 981044, 1998, 107.*

[64]   Arcoumanis, C., M. Badami, H. Flora, and M. Gavaises., "Cavitation in real size multi-hole diesel injector nozzles.," *SAE Technical Paper 2000-01-1249, 2000,..*

[65]   Payri, F., V. Bermu´dez, R. Payri, and F. J. Salvador. , "The influence of cavitation on the internal flow and the spray characteristics in diesel injection nozzles, SAE technical papers, 2003, 83, 419.".

[66]   Lefebvre, Atomisation & Spray, Taylor & Francis Group, 2017.

[67]   Bonhoeffer B., Kwade A. , and Juhnke M., "Impact of Formulation Properties and Process Parameters on the Dispensing and Depositioning of Drug Nanosuspensions Using Micro-Valve Technology.," *Journal of Pharmaceutical Sciences. 2017, 106(4): p. 1102-1110.*

[68]   Mishra, Y. N. (2018)., "Droplet size, concentration, and temperature mapping in sprays using SLIPI-based technique," PhD Thesis, Lund University, 2018.

[69]   Tropea, Yarin, Foss, Collision Phenomena in liquids and solid, Cambridge University Press, 2017.

[70]   D. Kim, O. Desjardins, M. Herrmann AND P. Moin, "Toward two-phase simulation of the primary breakup of a round liquid jet by a coaxial flow of gas," *Center for Turbulence Research, Annual Research Briefs 2006.*

[71]   Rotz, PhD Thesis, Experimental Investigation of Spray characteristics and ignition processes of large two-stroke engines, 2015.

[72]   Haenlein, A.,, Disintegration of a liquid jet, NACA TN 659, 1932..

[73]   Miesse C., "Correlation of Experimental Data on the Disintegration of Liquid Jets," *Industrial & Engineering Chemistry,,* pp. 47(9):1690–1701, Sept. 1955..

[74]   Cyril Mauger, Loic Meez, Marc Michard, Marc Michard, Alexandre Azouzi, Stephane Valette, "Shadowgraph, Schlieren and interferometry in a 2D cavitating channel flow," *Experiments in Fluids,* no. DOI 10.1007/s00348-012-1404-3, 2012.

[75]   Hult, J., Simmank, P., Matlock, S., Mayer, S., Falgout Z., Linne M., "Interior flow and near-nozzle spray development in a marine-engine diesel fuel injector," *Experiment in Fluids,* vol. 57, no. 4, pp. 1-19, 2016.

[76]   Arthur H. Lefebvre, Vincent G. McDonell, Atomisation and Sprays, London: Taylor & Francis, 2017.

[77]   Mark Linne, "Imaging in the optically dense regions of a spray: A review of developing techniques," *Progress in Energy and Combustion Science,* 2013.

[78]   Berrocal E., Multiple Light scattering in optical Diagnostics of Dense Sprays, PhD Thesis, 2006.

[79]   Berrocal E., "Multiple scattering of light in optical diagnostics of dense sprays and other complex turbid media," *PhD Thesis,* 2006.

[80]   V. I. Kostylev, "Scattering Fundamentals," *Bistatic Radar Principles Practice,* p. 193–223, 2007.

[81]   https://www.artium.com/pdi-theory-of-operation.

[82]   Garreutto, D., "Cycle-Resolved flow Characterisitcs Within a Screw Compressor," *PhD Thesis.*

[83]   Phase Doppler Particle Analyser, Source: Dantec, [Online]. Available: www.dantecdynamics.com.

[84]   BSA Flow Software, Dantec Dynamics, [Online]. Available: https://www.dantecdynamics.com/solutions-applications/solutions/spray-and-particle/phase-doppler-anemometry-pda/.

[85]   Mirshahi, M., Yan, Y. and Nouri, J.M.. Journal of Physics: Conference Series,, *Influence of cavitation on near nozzle exit spray.,* pp. 656(1). doi:10.1088/1742-6596/656/1/012093., (2015).

[86]   Nouri, J.M., Whitelaw, J.H., & Yianneskis, M. (1988), "A refractive index matching technique for solid/liquid flows.," *In Laser Anemometry in Fluid Mechanics. 3, pp. 335-340..*

[87]   [Online]. Available: https://www.arri.com/en/lighting/daylight/m-series/m18.

[88]   Rewse-Davies, Zander, Near Nozzle Phenomena of Gasoline Direct Injection Sprays, City University London, 2015.

[89]   Mitroglou, N., Nouri J. M. , Gavaises M. , and Arcoumanis C., "Spray characteristics of a multi-hole injector for direct-injection gasoline engines.," *International Journal of Engine Research,* vol. 7, p. 255, 2005,.

[90]   M. Mirshahi, "Effect of injection pressure and duration in the multihole gasoline injector, Masters Thesis".

[91]   Simón, Fausto, Vicente R. Bermúdez, & José ,, 2010.

[92]   Hiroyasu & Aray, 1990, [Online].

[93]   Hardalupas, Y., Taylor, A, M. K. P, and Whitelaw, J. H, , 1992. Characteristics of the spray from a Diesel injector, ., *Int. J. Multiphase Flow,,* vol. 18, pp. 159-179,.

[94]   Nouri, J.M., Whitelaw J. H.,, "Spray characteristics of a gasoline direct injector with short durations of injection," *Exp. Fluids,,* vol. 31, pp. 377-383, 2001..

[95]   Yanta W.J., Smith R.A. (1973). Naval Ordonance Laboratory,, "Turbulence measurements with a laser Doppler velocimeter.," *Report NOLTR 73 - 94, White Oak, Silver Spring, CA, USA..*

[96]   Befrui B. i, Aye A. , Bossi A. ,Markle L. E., and Varble D. L., "ECN GDi Spray G: Coupled LES Jet Primary Breakup - Lagrangian Spray Simulation and Comparison with Data," *ILASS Americas 28th Annual Conference on Liquid Atomization and Spray Systems, Dearborn, MI, May 2016.*

[97]   Hellmann, Robin, "Towards design optimization of high-pressure gasoline injectors using Genetic Algorithm coupled with Computational Fluid Dynamics," *ILASS 2017.*

[98]   Hellmann R., Jochmann P., Leick P., Georg Stapf K., "Multi-objective optimization of high-pressure gasoline injector nozzles using Genetic Algorithms coupled with Computational Fluid Dynamics (CFD): exploiting the manufactural design space," *ILASS July 2018.*

[99]   "Renewables 2019 - Global status reports," [Online]. Available: https://www.ren21.net/wp-content/uploads/2019/05/gsr_2019_full_report_en.pdf.

[100]   "Gasoline direct injection by market," [Online]. Available: https://www.variantmarketresearch.com/report-categories/automotive/gasoline-direct-injection-market.

[101]   [Online]. Available: https://www.ucl.ac.uk/medical-physics-biomedical-engineering/sites/medical-physics/files/how-the-method-works.pdf.

[102]   "Emissions in the automotive sector," [Online]. Available: https://ec.europa.eu/growth/sectors/automotive/environment-protection/emissions_en.

[103]   "The 123,000 MPH Plasma engine that could finally take astronauts to Mars," [Online]. Available: http://www.popsci.com/technology/article/2010-10/123000-mph-plasma-engine-could-finally-take-astronauts-mars. [Accessed 23 10 2019].

[104]   European Environment Agency, "Progress of EU transport sector towards its environment and climate objectives," Nov 2018. [Online]. Available: https://www.eea.europa.eu/themes/transport/term/term-briefing-2018.

[105]   International Energy Agency, "Renewables 2019," [Online]. Available: https://www.ren21.net/wp-content/uploads/2019/05/gsr_2019_full_report_en.pdf.

[106]   Organisation for Economic Cooperation & Development, , "OECD Environmental Outlook to 2050," Organisation for Economic, [Online]. Available: https://www.oecd.org/env/cc/49082173.pdf.

[107]   Air Quality Expert Group, , "Non-Exhaust Emissions from Road Traffic," [Online]. Available: https://uk-air.defra.gov.uk/assets/documents/reports/cat09/1907101151_20190709_Non_Exhaust_Emissions_typeset_Final.pdf.

[108]   P. Yin J A., "Diurnal cloud cycle biases in climate," *Nat Commun,* vol. 8, p. 2969, 2017.

[109]   American Chemical Society, , "It's water vapor, not the CO2,," [Online]. Available: https://www.acs.org/content/acs/en/climatescience/climatesciencenarratives/its-water-vapor-not-the-co2.html.

[110]   European Environmental Agency, [Online]. Available: https://www.eea.europa.eu/data-and-maps/daviz/change-of-co2-eq-emissions-2#tab-dashboard-01.

[111]   European Environmental Agency, "Greenhouse gas emissions from transport in
        the EU," [Online]. Available: https://www.eea.europa.eu/data-and-
        maps/indicators/transport-emissions-of-greenhouse-gases/transport-emissions-
        of-greenhouse-gases-11.

[112]   Bauer D , Chaves H , Arcoumanis C , "Measurements of void fraction distribution in
        cavitating pipe flow using x-ray CT," *Measurement Science & Technology,* no.
        doi:10.1088/0957-0233/23/5/055302, p. 23, 2012.

[113]   BP report 2018, [Online]. Available:
        https://www.bp.com/en/global/corporate/energy-economics/energy-
        outlook/demand-by-sector/transport.html.

[114]   BP. Statistical review of world energy. BP Magazine, [Online]. Available:
        https://www.bp.com/en/global/corporate/energy-economics/statistical-review-
        of-world-energy.html.

[115]   International Energy Agency, "CO2 emission from combustion of fuels," 2019.
        [Online]. Available:
        https://webstore.iea.org/download/direct/2505?fileName=CO2_Emissions_from_
        Fuel_Combustion_2019_Overview.pdf.

[116]   European Environment Agency, "How do different sectors and processes
        contribute to emissions of the main air pollutants?," [Online]. Available:
        https://www.eea.europa.eu/data-and-maps/daviz/share-of-eea-33-emissions-
        5#tab-chart_1.

[117]   European Environment Agency, "Air pollutant emissions data viewer (Gothenburg
        Protocol, LRTAP Convention) 1990-2017," [Online]. Available:
        https://www.eea.europa.eu/data-and-maps/dashboards/air-pollutant-emissions-
        data-viewer-2.

[118]   Environmental Protection Agency, "Global Greenhouse Gas Emissions Data,"
        [Online]. Available: https://www.epa.gov/ghgemissions/global-greenhouse-gas-
        emissions-data.

[119]   Environmental Protection Agency, [Online]. Available: https://www.epa.gov/.

[120]   European Automobile manufacturers Association, , "The Automobile Pocket Guide
        2019 - 2020," [Online]. Available: file:///C:/Users/milad.mirshahi/Dropbox/1%20-
        %20Literature%20review/Reports/Car%20industry/ACEA_Pocket_Guide_2019-
        2020.pdf.

[121]   Fahim A., " VIsualisation of fuel spray characteristics from a stepped nozzle
        injector at varying injector pressure and duration," *MEng Final Year Project,.*

[122]   International Transport Forum, , "Is Low-Carbon Road Freight Possible," [Online].
        Available: https://www.itf-oecd.org/low-carbon-road-freight.

[123]   Sims R., R. Schaeffer, F. Creutzig, X. Cruz-Núñez, M. D'Agosto, D. Dimitriu, M. J.
        Figueroa Meza, L. Fulton, S. Kobayashi, O. Lah, A. McKinnon, P. Newman, M.
        Ouyang, J. J. Schauer, D. Sperling, and G. Tiwari,, "International Panel on Climate
        Change, Assessment Report 5: Mitigation for Climate Change," 2014. [Online].
        Available:
        https://www.ipcc.ch/site/assets/uploads/2018/02/ipcc_wg3_ar5_full.pdf.

[124]   Barkeley, Jon, [Online]. Available:
        https://www.economist.com/leaders/2017/08/12/the-death-of-the-internal-
        combustion-engine.

[125]   Khan, M., J. Helie, M. Gorokhovski, A. Wood, G. Wigley, J. Kashdan, J. Dumas, M.
        Mojtabi, and P. Guibert, "Numerical Analysis of Multihole Gasoline Direct Injection
        Sprays.," *International Conference on Liquid Atomisation and Spray Systems,*
        Heidelberg, Germany, 02/09/2012.

[126]   Grigoratos T, Gustafsson M, Eriksson O and Martini G., "Experimental
        investigation of tread wear and particle emission from tyres with different
        treadwear marking.," *Atmos Environ,* vol. 182, pp. 200-212, 2018.

[127]   Seoksu Moon, Tianyun Li, Kiyotaka Sato, Hideaki Yokohata, "Governing
        parameters and dynamics of turbulent spray atomization from modern GDI
        injectors," *Energy,* vol. 127, pp. 89-100, 2017.

[128]   Moon S., Liu Z. , Gao J. , Dufresne E. , Fezzaa K., Wang J., "Ultrafast X-ray Phase-
        Contrast Imaging of High-Speed Fuel Sprays from a Two-Hole Diesel Nozzle," *ILASS*

Americas, 22nd Annual Conference on Liquid Atomization and Spray Systems,, May 2010.

[129]   Volkswagen: The scandal explained, [Online]. Available: https://www.bbc.co.uk/news/business-34324772.

[130]   Bizhan B., "Analytical Optimization of Delphi GDi Fuel Injection Systems," *Vienna Motor Symposium,* 2015.

[131]   Financial Times, "Carmakers wrestle with diesel's decline," [Online]. Available: https://www.ft.com/content/6162bf96-65bd-11e9-b809-6f0d2f5705f6.

[132]   "CO_2 emission performance standards for cars and vans (2020 onwards)," European Commision, [Online]. Available: https://ec.europa.eu/clima/policies/transport/vehicles/regulation_en#tab-0-0.

[133]   International Council on Clean Transportation, "Explanation of the true real-world passenger vehicle emissions rating system," [Online]. Available: https://theicct.org/sites/default/files/publications/TRUE_explanation_technical_20180604.pdf.

[134]   Kalghatgi G., "Is it really the end of internal combustion engines and petroleum in transport?," *Applied Energy,* vol. 225, pp. 965-974, 2018.

[135]   Kim, D., Desjardins O. , Herrmann M. , and Moin P, "Toward two-phase simulation of the primary breakup of a round liquid jet by a coaxial flow of gas In Center for".

[136]   Endrizzi M., "X-ray phase-contrast imaging," *Nuclear Inst. and Methods in Physics Research, A,* no. 878, pp. 88-98, 2018.

[137]   Endrizzi M., "X-ray phase-contrast imaging," *Nuclear Inst. and Methods in Physics Research, A,* no. 878, pp. 88-98, 2018.

[138]   Mitroglou, N., Gavaises M., Arcoumanis C., "Spray stability from VCO and a new diesel nozzle design concept," *CAV 2012,* p. pp. 279, Berkley, USA, 07/07/2012,.

[139]   Nouri J.M., Mitroglou, N., Yan Y. and Arcoumanis C.,, "Internal flow and cavitation in a multi-hole injector for gasoline direct injection engines.," *SAE 2007-01-1405 April 2007..*

Appendices

10.1 Appendice 1 – Temporal and Velocity graphs

In this section the temporal velocity graphs are presented at different z values and for different y locations in each z location. The analysis of for each z location is similar to the analysis given for z=1 at section 7.4.1 .

10.1.1 Temporal velocity graphs at z = 2.5mm, x=-0.5mm along y axis for duration of 2ms

a) y=-2.4mm

b) y=-2.1mm

c) y=-1.8mm

d) y=-1.5mm

e) y=-1.2mm

f) y=-0.9mm

g) y=-0.6mm

h) y=-0.4mm

Figure 10-1 Temporal variation of average axial velocity over a time window of 0.05ms at z = 2.5mm, x=-0.5mm and at different y locations for 100 bar injection pressure and 2ms injection duration.

10.1.2 Temporal velocity graphs at z =5mm, x=-2.3mm along y axis for duration of 2ms

a) y=-3mm

b) y=-2.55mm

c) y=-2.1mm

d) y=-1.75mm

e) y=-1.3mm

f) y=-0.85mm

g) y=-0.4mm

h) y= 0mm
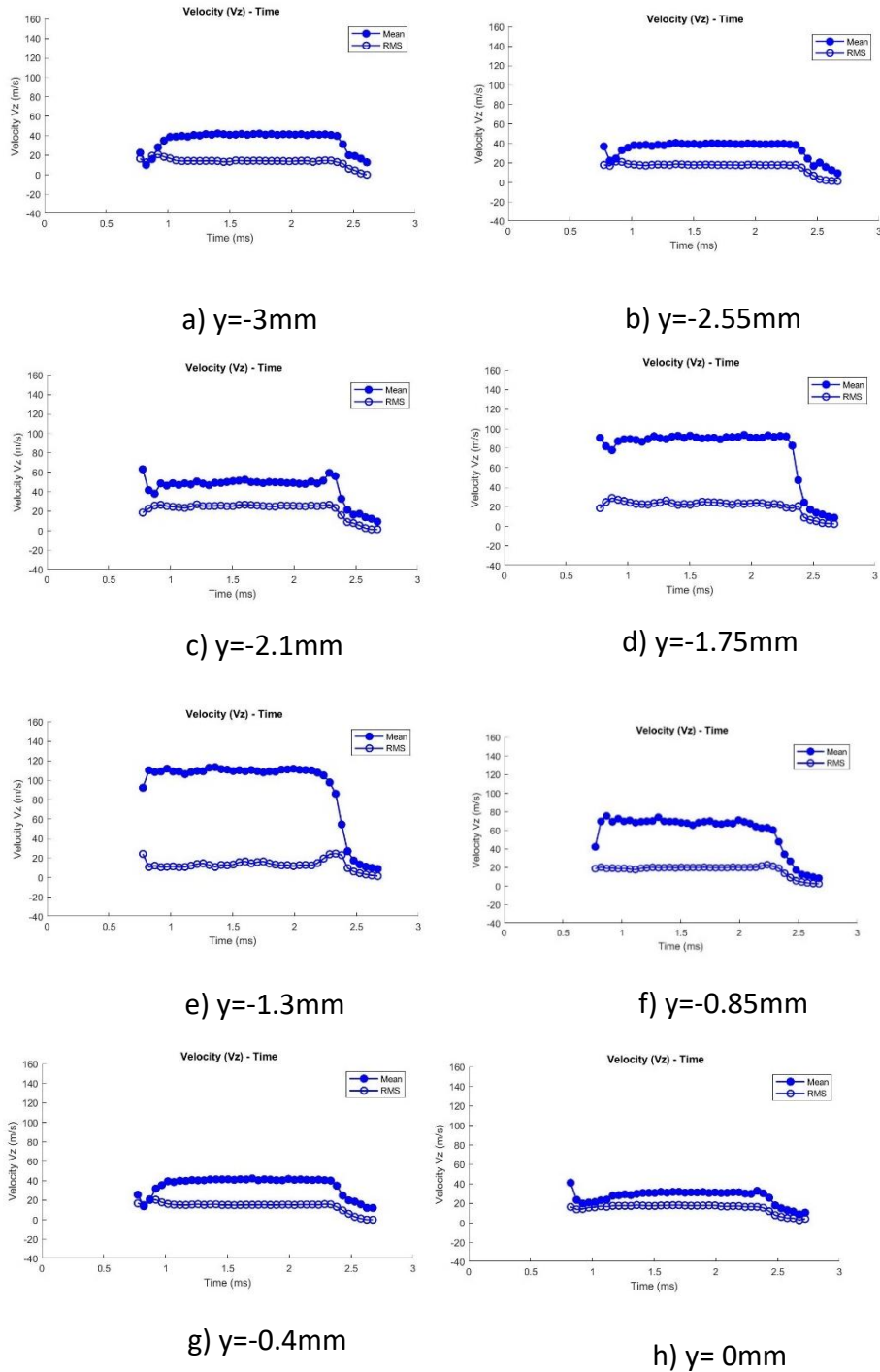
Figure 10-2 Temporal variation of average axial velocity over a time window of 0.05ms at z = 5mm, x=-2.3mm and at different y locations for 100 bar injection pressure and 2ms injection duration.

10.1.3 Temporal velocity graphs at z =10mm, x=-3.4mm along y axis for duration of 2ms

a) y=-3.5mm

b) y=-2.9mm

c) y=-2.3mm

d) y=-1.7mm

e) y=-1.1mm

f) y=-0.5mm

g) y=0.1mm

h) y=0.5mm
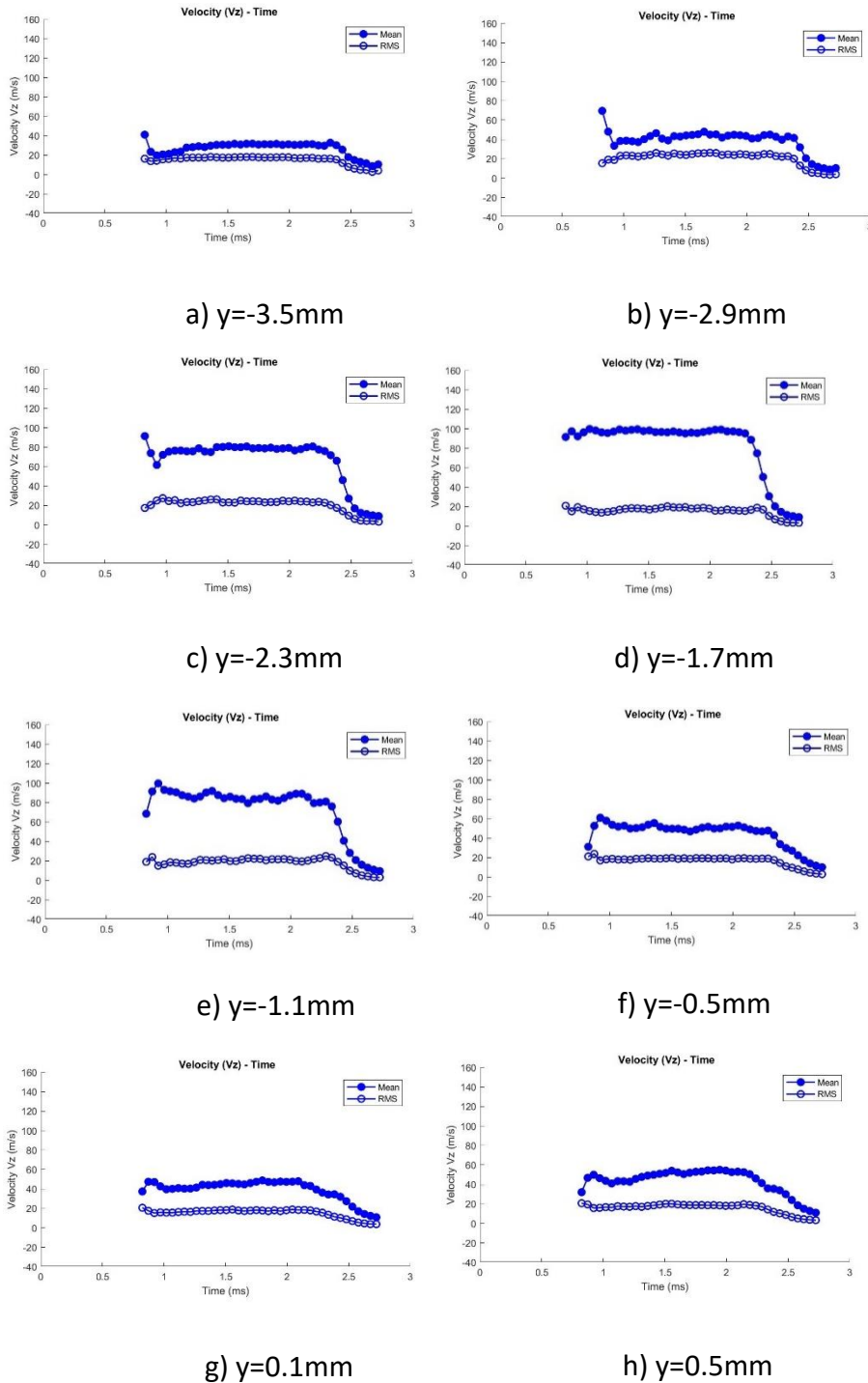
Figure 10-3 Temporal variation of average axial velocity over a time window of 0.05ms at z = 10mm, x=-3.4mm and at different y locations for 100 bar injection pressure and 2ms injection duration.

10.1.4 Temporal velocity graphs at z =20mm, x=-4.6mm along y axis for duration of 2ms
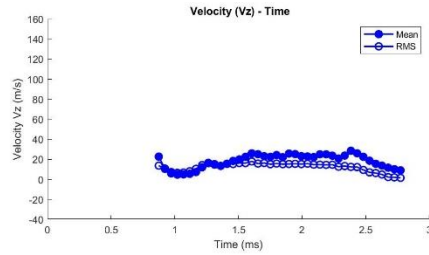
a) y=-6.5mm
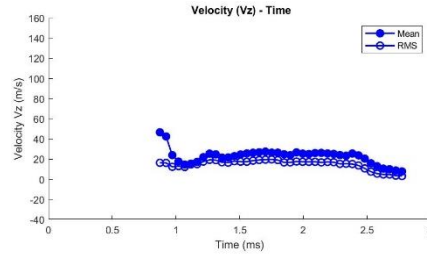
b) y=-5.3mm
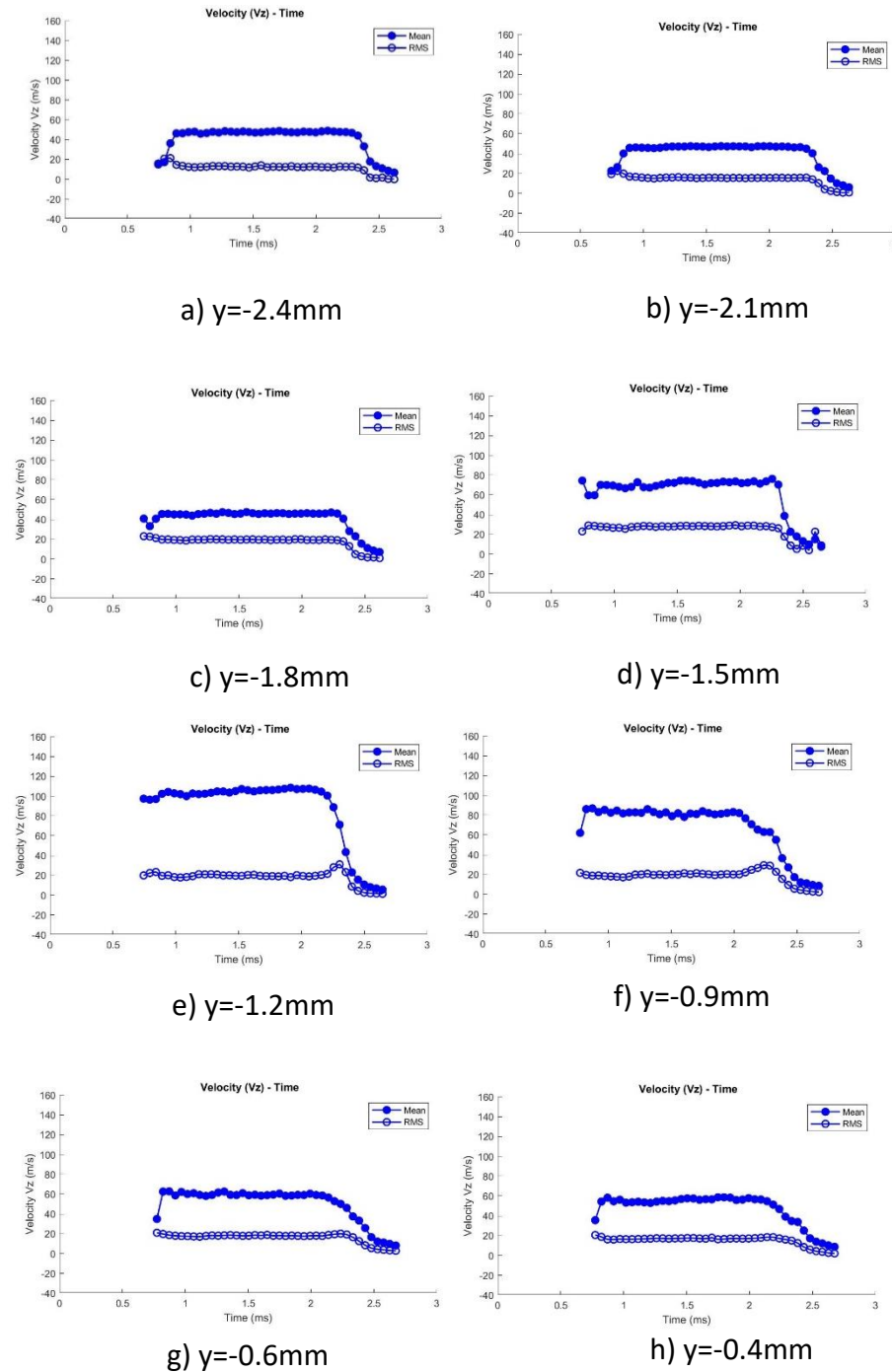
c) y=-4.1mm
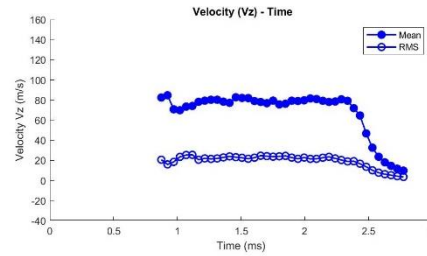
d) y=-2.9mm
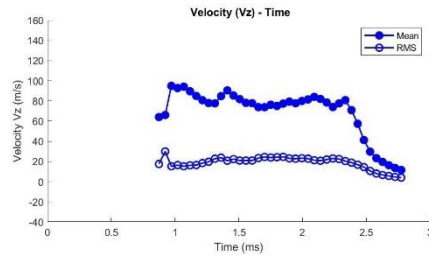
e) y=-1.7mm
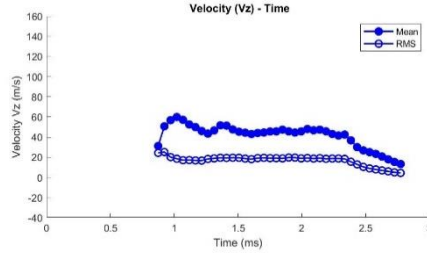
f) y=-0.5mm
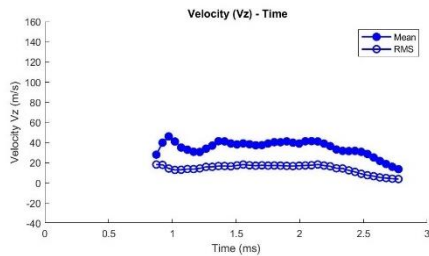
g) y=0.7mm
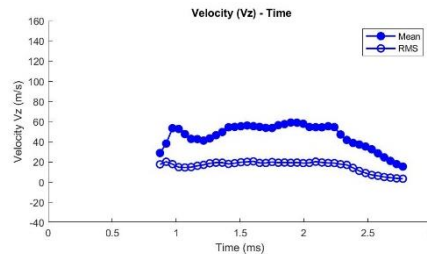
h) y=1.5

Figure 10-4 Temporal variation of average axial velocity over a time window of 0.05ms at z = 20mm, x=-4.6mm and at different y locations for 100 bar injection pressure and 2ms injection duration.

In this section the temporal mean droplet diameter graphs are presented at different z values and for different y locations in each z location. The analysis of for each z location is similar to the analysis given for z=1 at section 7.2.2 .

10.1.5 Temporal velocity graphs at z = 2.5mm, x=-0.5mm along y axis for duration of 2ms

a) y=-2.4mm

b) y=-2.1mm

c) y=-1.8mm

d) y=-1.5mm

e) y=-1.2mm

f) y=-0.9mm

g) y=-0.6mm

h) y=-0.4mm
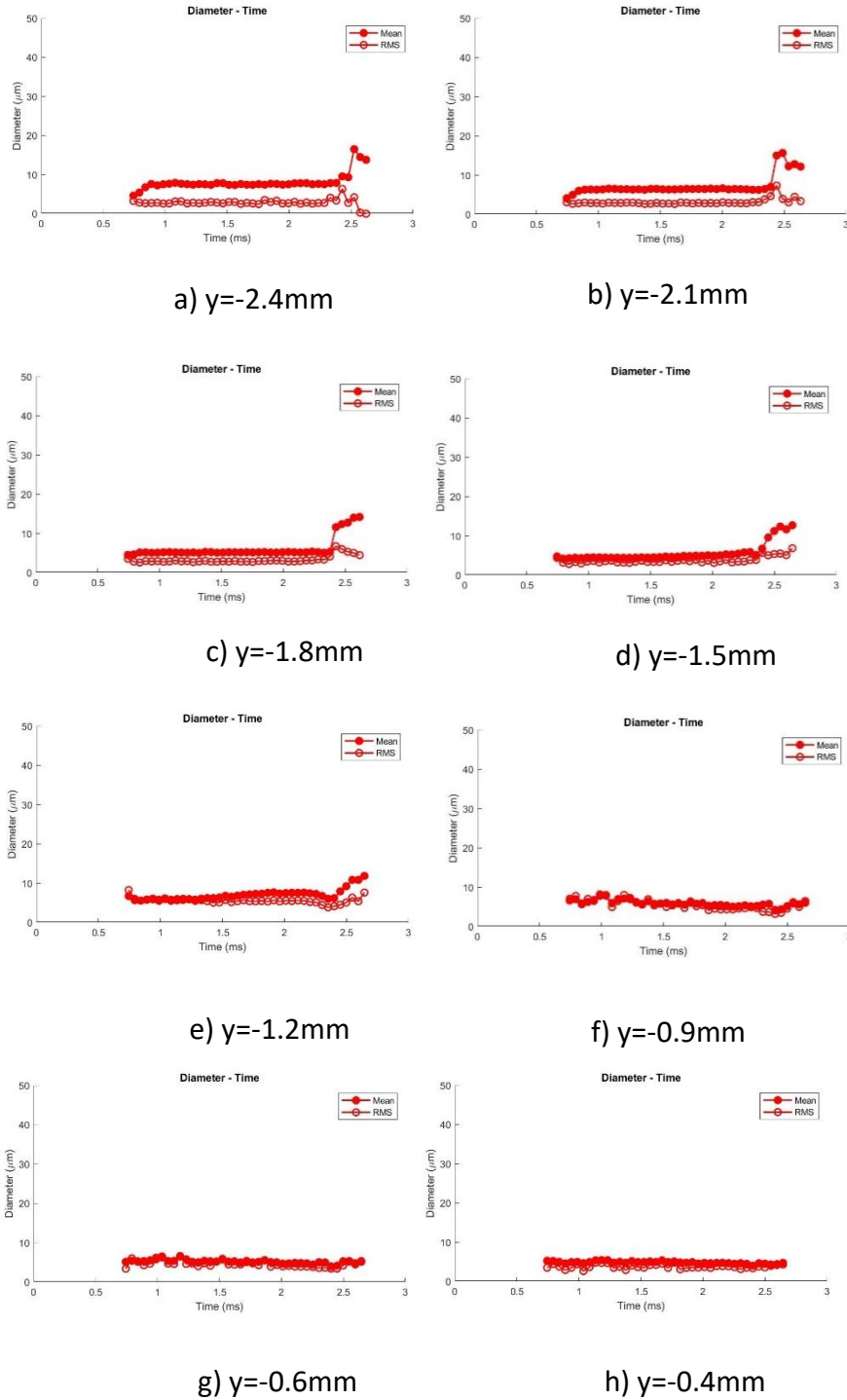
Figure 10-5 Temporal variation of average mean diameter over a time window of 0.05ms at z = 2.5mm, x=-0.5mm and at different y locations for 100 bar injection pressure and 2ms injection duration.

10.1.6 Temporal mean diameter graphs at z =5mm, x=-2.3mm along y axis for duration of 2ms
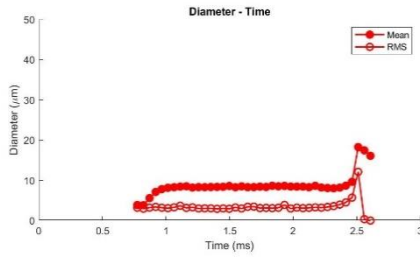
a) y=-3mm
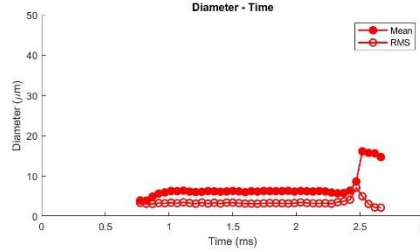
b) y=-2.55mm
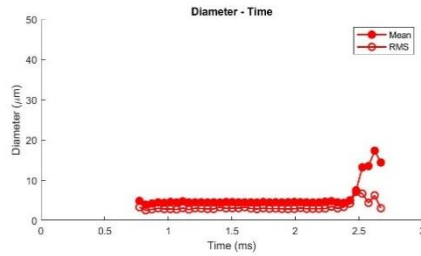
c) y=-2.1mm
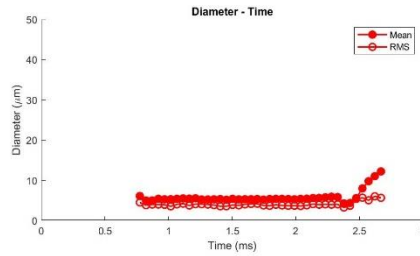
d) y=-1.75mm
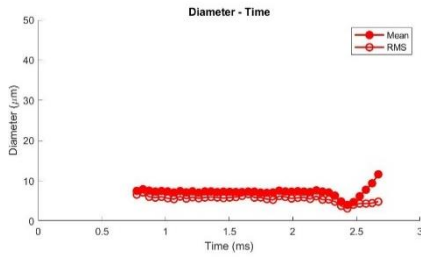
e) y=-1.3mm
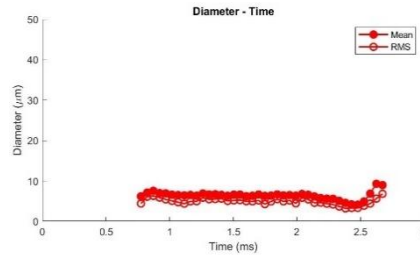
f) y=-0.85mm
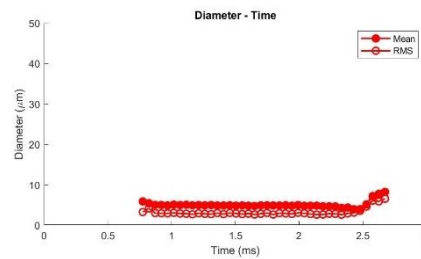
g) y=-0.4mm
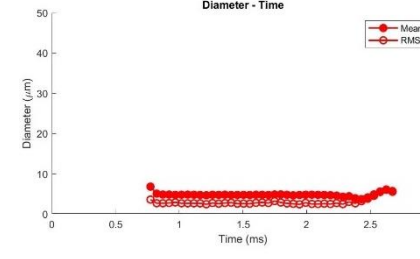
h) y= 0mm

Figure 10-6 Temporal variation of average mean diameter over a time window of 0.05ms at z = 5mm, x=-2.3mm and at different y locations for 100 bar injection pressure and 2ms injection duration.

329

10.1.7 Temporal mean diameter graphs at z =10mm, x=-3.4mm along y axis for duration of 2ms

a) y=-3.5mm

b) y=-2.9mm

c) y=-2.3mm

d) y=-1.7mm

e) y=-1.1mm

f) y=-0.5mm

g) y=0.1mm

h) y=0.5mm
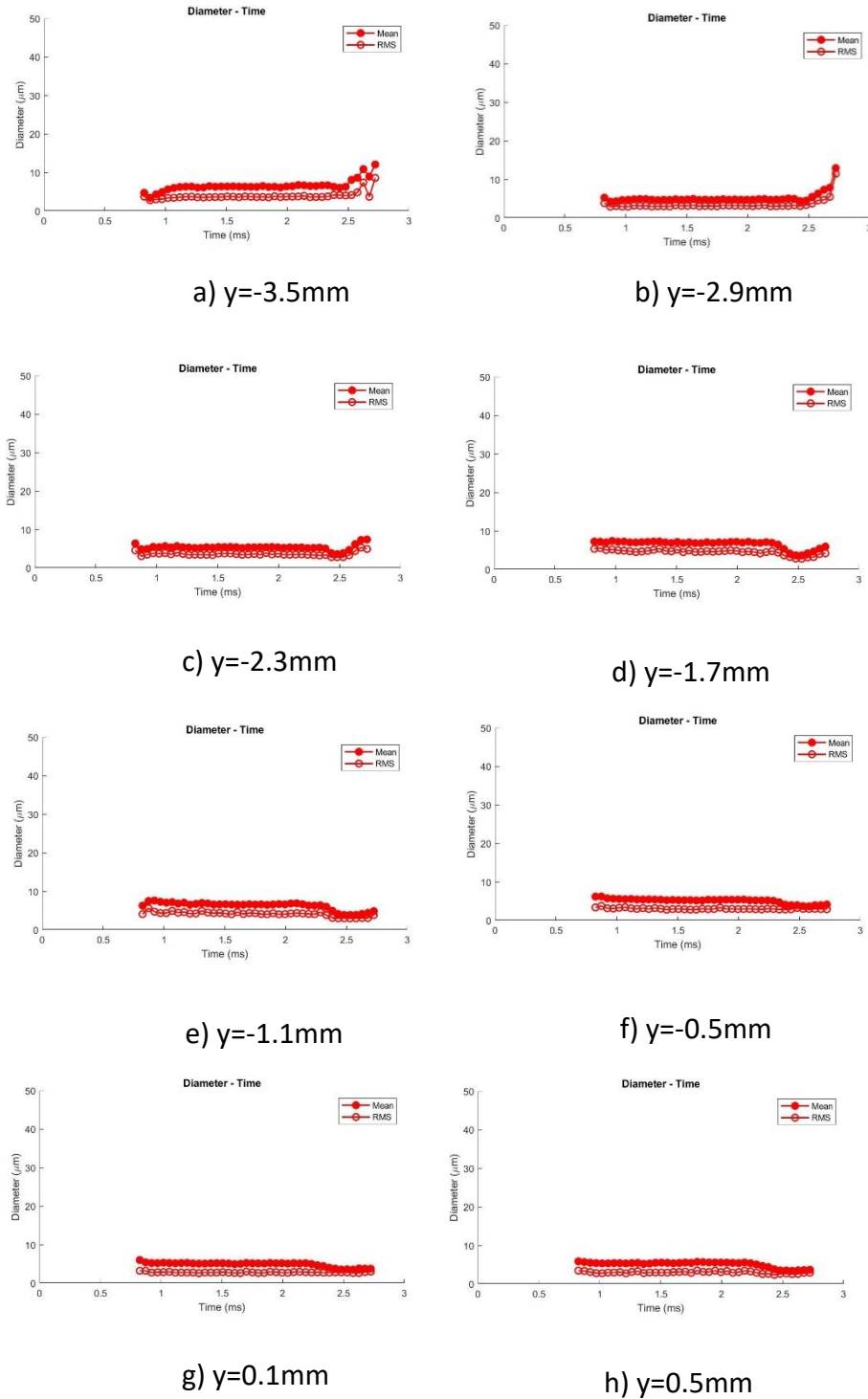
Figure 10-7 Temporal variation of average mean diameter over a time window of 0.05ms at z = 10mm, x=-3.4mm and at different y locations for 100 bar injection pressure and 2ms injection duration.

10.1.8 Temporal mean diameter graphs at z =20mm, x=-4.6mm along y axis for duration of 2ms

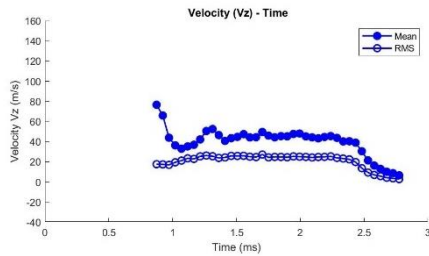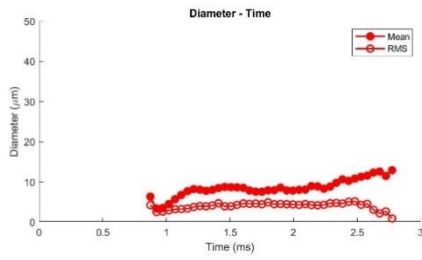a) y=-6.5mm
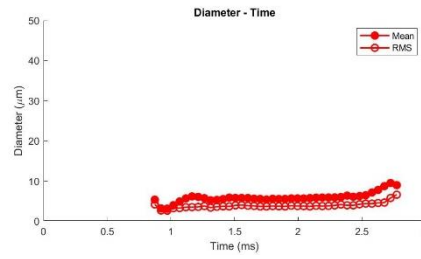
b) y=-5.3mm
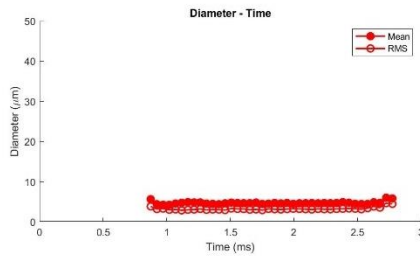
c) y=-4.1mm
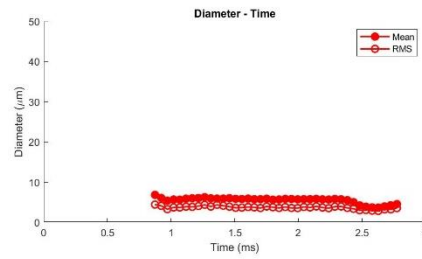
d) y=-2.9mm
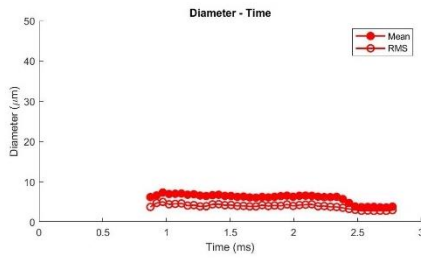
e) y=-1.7mm
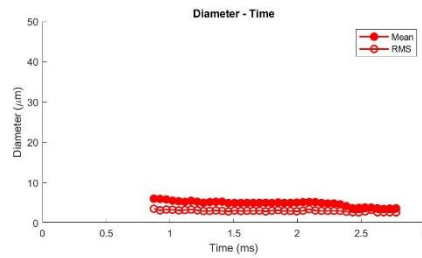
f) y=-0.5mm
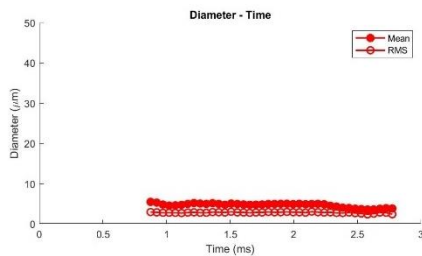
g) y=0.7mm
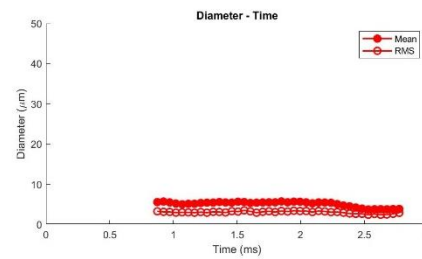
h) y=1.5

Figure 10-8 Temporal variation of average mean diameter over a time window of 0.05ms at z = 20mm, x=-4.6mm and at different y locations for 100 bar injection

10.2 Appendice 2 – Figures for superimposing the velocity countor plot

a) z=1mm

b) z=2.5mm

c) z=5mm

d) z=10mm
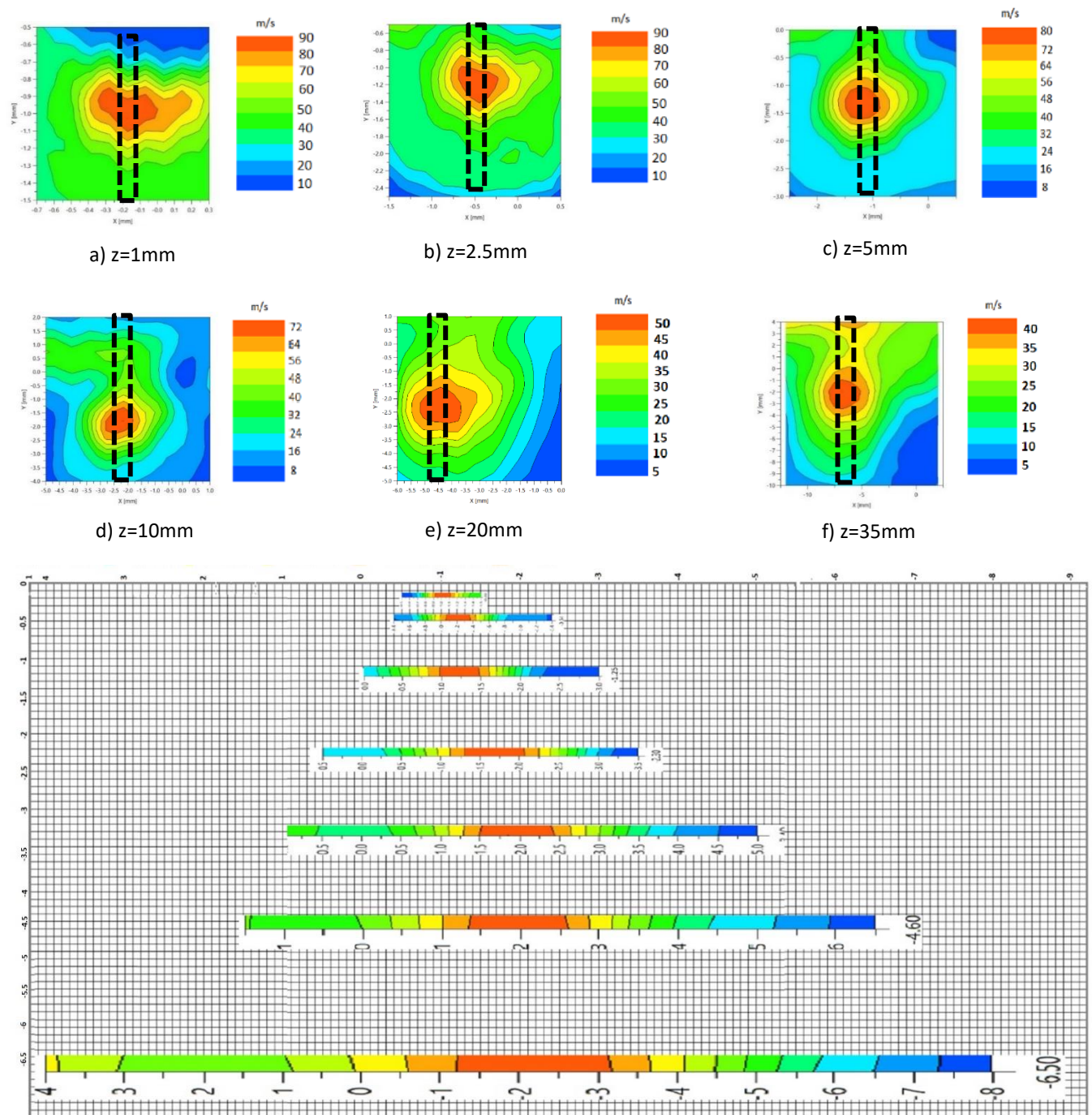
e) z=20mm

f) z=35mm

Figure 10-9 Superimposition of the velocity contour plots for the very fine grid measurement. The contour plots from top to bottom are shown in the scale paper and the velocity legends are given in page: Z=1mm, Z=2.5mm, Z=5mm, Z=10mm, Z=15mm, Z=20mm, Z=35mm

10.3 Appendice 3 - Matlab code for LDV and PDA measurements

```matlab
-----------------------------------
City University Of London
Milad Mirshahi
2018
---------------------------------------
nw=40;          % (double)number of windowing frames for
calculation of mean of velocity over time
xl=3;            % (double) limit x-axis

para=[0.8 1 1.4 1.6 1.9 2.1 0.8 2.1] ;        % (double) 3
pair of time window for calculation of spatial mean ;   %
(double) number of points to execute the code

ReturnPoint=21;
AlongX=0;    % (double) along x or along y

x1=-0.2; x2=-0.2; gridX=.05;   % (all double) minimum
maximum and grid length along x
y1=-1.5; y2=-0.5; gridY=.05;    % (all double)  minimum
maximum and grid length along y

radialPositionX=x1:gridX:x2;      % (all double) grid
generation fo x (only one number in case of along y
measurement)
radialPositionY=y1:gridY:y2;   % (all double) grid
generation for y (only one number in case of along x
measurement)


if AlongX==1
  radialPosition=  radialPositionX;  % (double)
else
  radialPosition=  radialPositionY;   % (double)
end



%--------------- Identify read Folder------------------
folder1=pwd; %  (character) Identify current folder path
and put it in folder1 for example when we are looking at
data in Z1 folder the value is:
```

```matlab
% folder1 = C:\Users\OneDrive - City, University of
London\4 - PDA\My Flow Projects\Export - Doc\Z1\Z_1___X_-
0.2_0.05___Y_-1.5_-0.5_0.05

%--------------   Identify write Folders------------------

filter=3; % double)

folder2=[folder1,'\LDA',num2str(filter)];  % (character)
define the path of folder LDA3
% (which has been created manualy in windows before in the
main folder)
% for writing velocity graphs into it
% here folder 2 = C:\Users\OneDrive - City, University of
London\4 -
% PDA\My Flow Projects\Export -
% Doc\Z1\Z_1___X_-0.2_0.05___Y_-1.5_-0.5_0.05\LDA3

folder3=[folder1,'\D',num2str(filter)];  % Character)
%define the path of folder D3
% (which has been created before in the main folder)
% for writing diametr graphs into it
%here folder3 =C:\Users\OneDrive - City, University of
London\4 -
%PDA\My Flow Projects\Export -
%Doc\Z1\Z_1___X_-0.2_0.05___Y_-1.5_-0.5_0.05\D3

folder4=[folder1,'\SMD',num2str(filter)];  % Character)
%define the path of folder SMD3
% (which has been created before in the main folder)
% for writing SMD graphs into it
%Here folder 4= C:\Users\OneDrive - City, University of
London\4 -
%PDA\My Flow Projects\Export -
%Doc\Z1\Z_1___X_-0.2_0.05___Y_-1.5_-0.5_0.05\SMD3

folder5=[folder1,'\Weber',num2str(filter)];  % Character)
%define the path of folder SMD3
% (which has been created before in the main folder)
% for writing SMD graphs into it
%Here folder 4= C:\Users\OneDrive - City, University of
London\4 -
%PDA\My Flow Projects\Export -
```

```
%Doc\Z1\Z_1___X_-0.2_0.05___Y_-1.5_-0.5_0.05\SMD3

folder6=[folder1,'\LDA+D',num2str(filter)];  % Character)
%define the path of folder LDA+D3
% (which has been created before in the main folder)
% for writing velocity diametr graphs into it
%Here folder 5= C:\Users\OneDrive - City, University of
London\4 -
%PDA\My Flow Projects\Export -
%Doc\Z1\Z_1___X_-0.2_0.05___Y_-1.5_-0.5_0.05\LDA+D3

folder7=[folder1,'\D+SMD',num2str(filter)];  % Character)
%define the path of folder D+SMD3
% (which has been created before in the main folder)
% for writing velocity diametr graphs into it
%Here folder 5= C:\Users\Mina\OneDrive - City, University
of London\4 -
%PDA\My Flow Projects\Export -
%Doc\Z1\Z_1___X_-0.2_0.05___Y_-1.5_-0.5_0.05\D+SMD3

% ------------------- Read Z (height) of the folder as an
input for function LDA3--------------
filelist   = dir(pwd);    % (structure) % Lists all the
files including text,excel,matlab, etc ) in the current
folder it has columns and each column could be char or
double etc
name       = {filelist.name};   % (cell) Create a cell
'name' which is the name column extracted from
% matrix of filelist which each element is the name of the
files
% in the current folder
str=name{1,10};  % (char) create str as the file name of
text file here it is:
% 100 bar profile _ -110___Z_1___X_-0.2_0.05___Y_-1.5_-
0.5_0.05__CV72ms_VS195 - SNR2-S1000 -G6-
LV4_SU100k_SV10k_Pos14.txt
newStr = extractBefore(str,"_Pos");  % (char) this create
the string from start of str up to _Pos which is :
% 100 bar profile _ -110___Z_1___X_-0.2_0.05___Y_-1.5_-
0.5_0.05__CV72ms_VS195 - SNR2-S1000 -G6-LV4_SU100k_SV10k
ET=extractAfter(extractBefore(extractAfter(folder1,"Doc\"),
"\"),"Z");   % (char) reads height here it is 1mm which is
```

```matlab
% string value of the number that appears after z in the
grandparent folder of the current directory
zz=str2double(ET)/100;  % (double)change z height from
string to number and divide by 100 which is here 1/100 =
0.01 for Z1




%------------------- Reading data from each text files i=1
to 42 and creating dataset z(i) of all the points --------
----------
for i=1:42
filename = [newStr,'_Pos', num2str(i) ,'.txt'] ; % creates
a variable which is like below where i goes from 1 to 42 in
the loop for example when i is 1 it creates
% filename = 100 bar profile _
% -110___Z_1___X_-0.2_0.05___Y_-1.5_-0.5_0.05__CV72ms_VS195
- SNR2-S1000
% -G6-LV4_SU100k_SV10k_Pos1.txt  or  _......pos2.txt when
i=2
full=fullfile(folder1,filename); %creates the full path +
name of the text file for example when i is 1 it creates
% % full = C:\Users\Mina\OneDrive - City, University of
London\4 - PDA\My Flow Projects\Export - Doc\Z1\Z_1___X_-
0.2_0.05___Y_-1.5_-0.5_0.05\100 bar profile _ -
110___Z_1___X_-0.2_0.05___Y_-1.5_-0.5_0.05__CV72ms_VS195 -
SNR2-S1000 -G6-LV4_SU100k_SV10k_Pos1.txt
z{i}=readtable(full);  % z is 1x42 matrix in which each
element is a table which has information of the text files
for all the positions from 1 to 42, for example z(1)=z(1,1)
has information of the text file .....pos1.text ,
end




%---------------------- Temporal Mean & RMS Velocity
Analysis ----------------------------
% Calculation and plotting of mean & RMS velocity graphs
(if needed using the filteration method which might not be
used) and drawing
% for 42 different graphs and saving them in LDA3 folder
```

```matlab
for i=1:42
mat=table2array(z{i});    %  mat is a 100000x9 array of the
text file i of z(i) which means it does not have the title
of the table but it has 100000 rows and 9 columns
% the rows are measured instance for 1 particle and the
columns are "AT [ms]","TT [us]","LDA1 [m/s]","U12
[deg]","U13 [deg]","D [um]","AT{2} [ms]","TT{2}
[us]","LDA4{2} [m/s]",


[VzMeanii(i),VzStdii(i),VzMeanmm(i),VzStdmm(i),VzMeanff(i),
VzStdff(i),VzMeantt(i),VzStdtt(i)]=LDA3(mat,zz,nw,xl,para);
% (1x1 double) temporal mean of the velocity for time
window of para1 and para2 at position i will be calculated
(42 positions) using function
LDA3(matrix_data,Z,n,xl,param) which has these inputs:
% mat=is the array of the table of data (the list of
arrival time table)
% nn=40;        is number of the windowing
%  xl=3;        is the limit of x-axis
% para=[t1 t2, ...] is the start and end of averaging
window
%the output meanV_pos(i) is one of the outputs of function
LDA3

basefile=num2str(i);  % creates a string of the number of
file which is from 1 to 42 for figure output of LDA3
function
fullname=fullfile(folder2,basefile); % Here fullname will
be C:\Users\Mina\OneDrive - City, University of London\4 -
% PDA\My Flow Projects\Export -
% Doc\Z1\Z_1___X_-0.2_0.05___Y_-1.5_-0.5_0.05\LDA3\1   or
\2 or ... depend
% on i value
savefig(fullname)
%saveas(gcf,fullname,'pdf')
saveas(gcf,fullname,'jpeg')
end
close all


%---------------Spatial Velocity Analysis-----------------
--
```

```matlab
% Draw velocity profile (mean and RMS) as a function of
position in LDA3 folder ----
% here VzMean(i) is LDAmean(i) and VzStd(i) is LDAstd (i)


figure(1)
plot(radialPosition,VzMeanii(1:ReturnPoint),'-
o','color','b','LineWidth',1.5,'MarkerSize',7,...
    'MarkerEdgeColor','b',...
    'MarkerFaceColor','b')
title('Velocity Vz - Position along y axis ')
xlabel('position along y axis (mm)');
ylabel('Velocity Vz (m/s)');
ylim([0 160])
hold on
plot(radialPosition,VzStdii(1:ReturnPoint),'-
o','color','b','LineWidth',1.5,'MarkerSize',7,...
    'MarkerEdgeColor','b')
legend('Mean','RMS')
fullnamev=fullfile(folder2,'V-y at 1');
savefig(fullnamev)
saveas(gcf,fullnamev,'jpeg');

figure(2)
plot(radialPosition,VzMeanmm(1:ReturnPoint),'-
o','color','b','LineWidth',1.5,'MarkerSize',7,...
    'MarkerEdgeColor','b',...
    'MarkerFaceColor','b')
title('Velocity Vz - Position along y axis ')
xlabel('position along y axis (mm)');
ylabel('Velocity Vz (m/s)');
ylim([0 160])
hold on
plot(radialPosition,VzStdmm(1:ReturnPoint),'-
o','color','b','LineWidth',1.5,'MarkerSize',7,...
    'MarkerEdgeColor','b')
legend('Mean','RMS')
fullnamev=fullfile(folder2,'V-y at t=1-5');
savefig(fullnamev)
saveas(gcf,fullnamev,'jpeg')

figure(3)
```

338

```matlab
plot(radialPosition,VzMeanff(1:ReturnPoint),'-
o','color','b','LineWidth',1.5,'MarkerSize',7,...
    'MarkerEdgeColor','b',...
    'MarkerFaceColor','b')
title('Velocity Vz - Position along y axis ')
xlabel('position along y axis (mm)');
ylabel('Velocity Vz (m/s)');
ylim([0 160])
hold on
plot(radialPosition,VzStdff(1:ReturnPoint),'-
o','color','b','LineWidth',1.5,'MarkerSize',7,...
    'MarkerEdgeColor','b')
legend('Mean','RMS')
fullnamev=fullfile(folder2,'V-y at t=2');
savefig(fullnamev)
saveas(gcf,fullnamev,'jpeg')

figure(4)
plot(radialPosition,VzMeantt(1:ReturnPoint),'-
o','color','b','LineWidth',1.5,'MarkerSize',7,...
    'MarkerEdgeColor','b',...
    'MarkerFaceColor','b')
title('Velocity Vz - Position along y axis ')
xlabel('position along y axis (mm)');
ylabel('Velocity Vz (m/s)');
ylim([0 160])
hold on
plot(radialPosition,VzStdtt(1:ReturnPoint),'-
o','color','b','LineWidth',1.5,'MarkerSize',7,...
    'MarkerEdgeColor','b')
legend('Mean','RMS')
fullnamev=fullfile(folder2,'V-y 1 to 2');
savefig(fullnamev)
saveas(gcf,fullnamev,'jpeg')
%-------------------Temporal Diameter Analysis-----------
----------------------------

% calculation of mean diameters using the filteration
method and drawing
% 42 different graphs in D3 folder out of which 21 of them
are filtered for
% later post processing
```

```matlab
for i=1:42
mat=table2array(z{i});

%-----Filteration of the end of injection data
% if i==11
%     inx=find(mat(:,3)>40);
%     mat=mat(inx,:);
% elseif i==12
%     inx=find(mat(:,3)>50);
%     mat=mat(inx,:);
%
% end
% %-----end of filteration--------


[DMeanii(i),Dstdii(i),DMeanmm(i),Dstdmm(i),DMeanff(i),Dstdf
f(i),DMeantt(i),Dstdtt(i)]=D3(mat,zz,nw,xl,para);   % call
function D3(matrix_data,Z,n,xl,param)
basefileD=num2str(i);
fullname=fullfile(folder3,basefileD);
savefig(fullname)
%saveas(gcf,fullname,'pdf')
saveas(gcf,fullname,'jpeg')
end
close all


%-----------------Spatial Diameter Analysis----------------
-----
% Draw two Diemeter profile plot (mean and RMS) as a
function of position in 'D3' folder here Dmean_pos(i) is
Dmean(i) which is one of the uotput of function D3

figure(1)
plot(radialPosition,DMeanii(1:ReturnPoint),'-
o','color','r','LineWidth',1.5,'MarkerSize',7,...
    'MarkerEdgeColor','r',...
    'MarkerFaceColor','r')
title('Diameter - Position along y axis')
xlabel('Position along y axis (mm)');
ylabel('Diameter (\mum)');
ylim([0 20]);
```

```matlab
hold on
plot(radialPosition,Dstdii(1:ReturnPoint),'-
o','color','r','LineWidth',1.5,'MarkerSize',7,...
    'MarkerEdgeColor','r')
legend('Mean','RMS');
fullnamev=fullfile(folder3,'D-y at t=1');
savefig(fullnamev)
saveas(gcf,fullnamev,'jpeg')

figure(2)
plot(radialPosition,DMeanmm(1:ReturnPoint),'-
o','color','r','LineWidth',1.5,'MarkerSize',7,...
    'MarkerEdgeColor','r',...
    'MarkerFaceColor','r')
title('Diameter - Position along y axis')
xlabel('Position along y axis (mm)');
ylabel('Diameter (\mum)');
ylim([0 20]);
hold on
plot(radialPosition,Dstdmm(1:ReturnPoint),'-
o','color','r','LineWidth',1.5,'MarkerSize',7,...
    'MarkerEdgeColor','r')
legend('Mean','RMS');
fullnamev=fullfile(folder3,'D-y at t=1-5');
savefig(fullnamev)
saveas(gcf,fullnamev,'jpeg')

figure(3)
plot(radialPosition,DMeanff(1:ReturnPoint),'-
o','color','r','LineWidth',1.5,'MarkerSize',7,...
    'MarkerEdgeColor','r',...
    'MarkerFaceColor','r')
title('Diameter - Position along y axis')
xlabel('Position along y axis (mm)');
ylabel('Diameter (\mum)');
ylim([0 20]);
hold on
plot(radialPosition,Dstdff(1:ReturnPoint),'-
o','color','r','LineWidth',1.5,'MarkerSize',7,...
    'MarkerEdgeColor','r')
legend('Mean','RMS');
fullnamev=fullfile(folder3,'D-y at t=2');
```

```matlab
savefig(fullnamev)
saveas(gcf,fullnamev,'jpeg')

figure(4)
plot(radialPosition,DMeantt(1:ReturnPoint),'-
o','color','r','LineWidth',1.5,'MarkerSize',7,...
    'MarkerEdgeColor','r',...
    'MarkerFaceColor','r')
title('Diameter - Position along y axis')
xlabel('Position along y axis (mm)');
ylabel('Diameter (\mum)');
ylim([0 20]);
hold on
plot(radialPosition,Dstdii(1:ReturnPoint),'-
o','color','r','LineWidth',1.5,'MarkerSize',7,...
    'MarkerEdgeColor','r')
legend('Mean','RMS');
fullnamev=fullfile(folder3,'D-y 1 to 2');
savefig(fullnamev)
saveas(gcf,fullnamev,'jpeg')

%-------------------Sauter Mean Dimater Analysis---------
------------------------------

% calculation of SMD for
% 42 different graphs in SMD3 folder out of which 21 of
them are chosen for
% later post processing

for i=1:42
mat=table2array(z{i});

[SauterMeanDii(i),SauterMeanDmm(i),SauterMeanDff(i),SauterM
eanDtt(i)]=SMD3(mat,zz,nw,xl,para);   % call function
SMD3(matrix_data,Z,n,xl,param)
basefileD=num2str(i);
fullname=fullfile(folder4,basefileD);
savefig(fullname)
%saveas(gcf,fullname,'pdf')
saveas(gcf,fullname,'jpeg')
end
close all
```

```matlab
% Draw  SMD profile as a function of position in 'SMD3'
folder here SauterMeanDii(i) is SauterMeanDi(i) which is
one of the uotput of function SMD3

figure(1)
plot(radialPosition,SauterMeanDii(1:ReturnPoint),'-
o','color','r','LineWidth',1.5,'MarkerSize',7,...
    'MarkerEdgeColor','r',...
    'MarkerFaceColor','r')
title('Sauter Mean Diameter - Position along y axis')
xlabel('Position along y axis (mm)');
ylabel('Sauter Mean Diameter (\mum)');
ylim([0 60]);
fullnamev=fullfile(folder4,'SMD-y at t=1');
savefig(fullnamev)
saveas(gcf,fullnamev,'jpeg')

figure(2)
plot(radialPosition,SauterMeanDmm(1:ReturnPoint),'-
o','color','r','LineWidth',1.5,'MarkerSize',7,...
    'MarkerEdgeColor','r',...
    'MarkerFaceColor','r')
title('Sauter Mean Diameter - Position along y axis')
xlabel('Position along y axis (mm)');
ylabel('Sauter Mean Diameter (\mum)');
ylim([0 60]);
fullnamev=fullfile(folder4,'SMD-y at t=1-5');
savefig(fullnamev)
saveas(gcf,fullnamev,'jpeg')

figure(3)
plot(radialPosition,SauterMeanDff(1:ReturnPoint),'-
o','color','r','LineWidth',1.5,'MarkerSize',7,...
    'MarkerEdgeColor','r',...
    'MarkerFaceColor','r')
title('Sauter Mean Diameter - Position along y axis')
xlabel('Position along y axis (mm)');
ylabel('Sauter Mean Diameter (\mum)');
ylim([0 60]);
fullnamev=fullfile(folder4,'SMD-y at t=2');
savefig(fullnamev)
saveas(gcf,fullnamev,'jpeg')
```

```matlab
figure(4)
plot(radialPosition,SauterMeanDtt(1:ReturnPoint),'-
o','color','r','LineWidth',1.5,'MarkerSize',7,...
    'MarkerEdgeColor','r',...
    'MarkerFaceColor','r')
title('Sauter Mean Diameter - Position along y axis')
xlabel('Position along y axis (mm)');
ylabel('Sauter Mean Diameter (\mum)');
ylim([0 60]);
fullnamev=fullfile(folder4,'SMD-y 1 to 2');
savefig(fullnamev)
saveas(gcf,fullnamev,'jpeg')


%-------------------Weber Number Analysis----------------
-----------------------

% calculation of Weber number for 42 different graphs in
Weber3 folder out of which 21 of them are chosen for
% later post processing

for i=1:42
mat=table2array(z{i});

[Weberi(i),Weberm(i),Weberf(i),Webert(i)]=Weber3(mat,zz,nw,
xl,para);    % call function SMD3(matrix_data,Z,n,xl,param)
basefileD=num2str(i);
fullname=fullfile(folder5,basefileD);
savefig(fullname)
%saveas(gcf,fullname,'pdf')
saveas(gcf,fullname,'jpeg')
end
close all

% Draw Weber profile as a function of position in 'Weber3'
folder here Weber(i) is Webernumber(i) which is one of the
uotput of function SMD3

figure(1)
plot(radialPosition,Weberi(1:ReturnPoint),'-
o','color','r','LineWidth',1.5,'MarkerSize',7,...
    'MarkerEdgeColor','r',...
    'MarkerFaceColor','r')
```

```matlab
title('Weber Number - Position along y axis')
xlabel('Position along y axis (mm)');
ylabel('Weber Number');
ylim([0 40]);
fullnamev=fullfile(folder5,'We-y at t=1');
savefig(fullnamev)
saveas(gcf,fullnamev,'jpeg')

figure(2)
plot(radialPosition,Weberm(1:ReturnPoint),'-
o','color','r','LineWidth',1.5,'MarkerSize',7,...
    'MarkerEdgeColor','r',...
    'MarkerFaceColor','r')
title('Weber Number - Position along y axis')
xlabel('Position along y axis (mm)');
ylabel('Weber Number');
ylim([0 40]);
fullnamev=fullfile(folder5,'We-y at t=1-5');
savefig(fullnamev)
saveas(gcf,fullnamev,'jpeg')

figure(3)
plot(radialPosition,Weberf(1:ReturnPoint),'-
o','color','r','LineWidth',1.5,'MarkerSize',7,...
    'MarkerEdgeColor','r',...
    'MarkerFaceColor','r')
title('Weber Number - Position along y axis')
xlabel('Position along y axis (mm)');
ylabel('Weber Number');
ylim([0 40]);
fullnamev=fullfile(folder5,'We-y at t=2');
savefig(fullnamev)
saveas(gcf,fullnamev,'jpeg')

figure(4)
plot(radialPosition,Webert(1:ReturnPoint),'-
o','color','r','LineWidth',1.5,'MarkerSize',7,...
    'MarkerEdgeColor','r',...
    'MarkerFaceColor','r')
title('Weber Number - Position along y axis')
xlabel('Position along y axis (mm)');
ylabel('Weber Number');
```

```matlab
ylim([0 40]);
fullnamev=fullfile(folder5,'We-y 1 to 2');
savefig(fullnamev)
saveas(gcf,fullnamev,'jpeg')




%-------------------V VS D Graph--------------------------
----------------------

figure(5)
yyaxis left
title('Velocity (Vz) & Diameter - Position along y axis')
plot(radialPosition,VzMeanii(1:ReturnPoint),'-
o','color','b','LineWidth',1.5,'MarkerSize',7,...
    'MarkerEdgeColor','b','MarkerFaceColor','b')
ylabel('Velocity Vz (m/s)')
xlabel('Position along y axis (mm)')
ylim([0 160])
hold on
plot(radialPosition,VzStdii(1:ReturnPoint),'-
o','color','b','LineWidth',1.5,'MarkerSize',7,...
    'MarkerEdgeColor','b')
yyaxis right
plot(radialPosition,DMeanii(1:ReturnPoint),'-
o','color','r','LineWidth',1.5,'MarkerSize',7,...
    'MarkerEdgeColor','r','MarkerFaceColor','r')
ylabel('Diameter (\mum)')
ylim([0 50])
% hold on
% plot(radialPosition,Dstdii(1:ReturnPoint),'-
o','color','r','LineWidth',1.5,'MarkerSize',7,...
%     'MarkerEdgeColor','r')
% legend('Mean Velocity (Vz)','RMS Velocity (Vz)','Mean
Diameter','RMS Diameter')
legend('Mean Velocity (Vz)','RMS Velocity (Vz)','Mean
Diameter')
fullnamef=fullfile(folder6,'V vs D at t=1');
savefig(fullnamef)
saveas(gcf,fullnamef,'jpeg')


figure(6)
```

```matlab
yyaxis left
title('Velocity (Vz) & Diameter - Position along y axis')
plot(radialPosition,VzMeanmm(1:ReturnPoint),'-
o','color','b','LineWidth',1.5,'MarkerSize',7,...
    'MarkerEdgeColor','b','MarkerFaceColor','b')
ylabel('Velocity Vz (m/s)')
xlabel('Position along y axis (mm)')
ylim([0 160])
hold on
plot(radialPosition,VzStdmm(1:ReturnPoint),'-
o','color','b','LineWidth',1.5,'MarkerSize',7,...
    'MarkerEdgeColor','b')
yyaxis right
plot(radialPosition,DMeanmm(1:ReturnPoint),'-
o','color','r','LineWidth',1.5,'MarkerSize',7,...
    'MarkerEdgeColor','r','MarkerFaceColor','r')
ylabel('Diameter (\mum)')
ylim([0 50])
% hold on
% plot(radialPosition,Dstdmm(1:ReturnPoint),'-
o','color','r','LineWidth',1.5,'MarkerSize',7,...
%     'MarkerEdgeColor','r')
% legend('Mean Velocity (Vz)','RMS Velocity (Vz)','Mean
Diameter','RMS Diameter')
legend('Mean Velocity (Vz)','RMS Velocity (Vz)','Mean
Diameter')
fullnamef=fullfile(folder6,'V vs D at t=1-5');
savefig(fullnamef)
saveas(gcf,fullnamef,'jpeg')


figure(7)
yyaxis left
title('Velocity (Vz) & Diameter - Position along y axis')
plot(radialPosition,VzMeanff(1:ReturnPoint),'-
o','color','b','LineWidth',1.5,'MarkerSize',7,...
    'MarkerEdgeColor','b','MarkerFaceColor','b')
ylabel('Velocity Vz (m/s)')
xlabel('Position along y axis (mm)')
ylim([0 160])
hold on
```

```matlab
plot(radialPosition,VzStdff(1:ReturnPoint),'-
o','color','b','LineWidth',1.5,'MarkerSize',7,...
    'MarkerEdgeColor','b')
yyaxis right
plot(radialPosition,DMeanff(1:ReturnPoint),'-
o','color','r','LineWidth',1.5,'MarkerSize',7,...
    'MarkerEdgeColor','r','MarkerFaceColor','r')
ylabel('Diameter (\mum)')
ylim([0 50])
% hold on
% plot(radialPosition,Dstdff(1:ReturnPoint),'-
o','color','r','LineWidth',1.5,'MarkerSize',7,...
%     'MarkerEdgeColor','r')
% legend('Mean Velocity (Vz)','RMS Velocity (Vz)','Mean
Diameter','RMS Diameter')
legend('Mean Velocity (Vz)','RMS Velocity (Vz)','Mean
Diameter')
fullnamef=fullfile(folder6,'V vs D at t=2');
savefig(fullnamef)
saveas(gcf,fullnamef,'jpeg')

figure(8)
yyaxis left
title('Velocity (Vz) & Diameter - Position along y axis')
plot(radialPosition,VzMeantt(1:ReturnPoint),'-
o','color','b','LineWidth',1.5,'MarkerSize',7,...
    'MarkerEdgeColor','b','MarkerFaceColor','b')
ylabel('Velocity Vz (m/s)')
xlabel('Position along y axis (mm)')
ylim([0 160])
hold on
plot(radialPosition,VzStdtt(1:ReturnPoint),'-
o','color','b','LineWidth',1.5,'MarkerSize',7,...
    'MarkerEdgeColor','b')
yyaxis right
plot(radialPosition,DMeantt(1:ReturnPoint),'-
o','color','r','LineWidth',1.5,'MarkerSize',7,...
    'MarkerEdgeColor','r','MarkerFaceColor','r')
ylabel('Diameter (\mum)')
ylim([0 50])
% hold on
```

```matlab
% plot(radialPosition,Dstdtt(1:ReturnPoint),'-
o','color','r','LineWidth',1.5,'MarkerSize',7,...
%      'MarkerEdgeColor','r')
% legend('Mean Velocity (Vz)','RMS Velocity (Vz)','Mean
Diameter','RMS Diameter')
legend('Mean Velocity (Vz)','RMS Velocity (Vz)','Mean
Diameter')
fullnamef=fullfile(folder6,'V vs D 1 to 2');
savefig(fullnamef)
saveas(gcf,fullnamef,'jpeg')


%-------------------D VS SMD Graph---------------------
-----------------------

figure(9)
yyaxis left
title('Mean Diameter & Sauter Mean Diameter - Position
along y axis')
plot(radialPosition,DMeanii(1:ReturnPoint),'-
o','color','b','LineWidth',1.5,'MarkerSize',7,...
    'MarkerEdgeColor','b','MarkerFaceColor','b')
ylabel('Mean Diameter (\mum)')
xlabel('Position along y axis (mm)')
ylim([0 60])
yyaxis right
plot(radialPosition,SauterMeanDii(1:ReturnPoint),'-
o','color','r','LineWidth',1.5,'MarkerSize',7,...
    'MarkerEdgeColor','r','MarkerFaceColor','r')
ylabel('Sauter Mean Diameter (\mum)')
ylim([0 60])
legend('Mean Diameter (\mum)','SMD (\mum)')
fullnamef=fullfile(folder6,'D vs SMD at t=1');
savefig(fullnamef)
saveas(gcf,fullnamef,'jpeg')


figure(10)
yyaxis left
title('Mean Diameter & Sauter Mean Diameter - Position
along y axis')
plot(radialPosition,DMeanmm(1:ReturnPoint),'-
o','color','b','LineWidth',1.5,'MarkerSize',7,...
```

```matlab
    'MarkerEdgeColor','b','MarkerFaceColor','b')
ylabel('Mean Diameter (\mum)')
xlabel('Position along y axis (mm)')
ylim([0 60])
yyaxis right
plot(radialPosition,SauterMeanDmm(1:ReturnPoint),'-
o','color','r','LineWidth',1.5,'MarkerSize',7,...
    'MarkerEdgeColor','r','MarkerFaceColor','r')
ylabel('Sauter Mean Diameter (\mum)')
ylim([0 60])
legend('Mean Diameter (\mum)','SMD (\mum)')
fullnamef=fullfile(folder6,'D vs SMD at t=1-5');
savefig(fullnamef)
saveas(gcf,fullnamef,'jpeg')

figure(11)
yyaxis left
title('Mean Diameter & Sauter Mean Diameter - Position
along y axis')
plot(radialPosition,DMeanff(1:ReturnPoint),'-
o','color','b','LineWidth',1.5,'MarkerSize',7,...
    'MarkerEdgeColor','b','MarkerFaceColor','b')
ylabel('Mean Diameter (\mum)')
xlabel('Position along y axis (mm)')
ylim([0 60])
yyaxis right
plot(radialPosition,SauterMeanDff(1:ReturnPoint),'-
o','color','r','LineWidth',1.5,'MarkerSize',7,...
    'MarkerEdgeColor','r','MarkerFaceColor','r')
ylabel('Sauter Mean Diameter (\mum)')
ylim([0 60])
legend('Mean Diameter (\mum)','SMD (\mum)')
fullnamef=fullfile(folder6,'D vs SMD at t=2');
savefig(fullnamef)
saveas(gcf,fullnamef,'jpeg')

figure(12)
yyaxis left
title('Mean Diameter & Sauter Mean Diameter - Position
along y axis')
plot(radialPosition,DMeantt(1:ReturnPoint),'-
o','color','b','LineWidth',1.5,'MarkerSize',7,...
```

```matlab
    'MarkerEdgeColor','b','MarkerFaceColor','b')
ylabel('Mean Diameter (\mum)')
xlabel('Position along y axis (mm)')
ylim([0 60])
yyaxis right
plot(radialPosition,SauterMeanDtt(1:ReturnPoint),'-
o','color','r','LineWidth',1.5,'MarkerSize',7,...
    'MarkerEdgeColor','r','MarkerFaceColor','r')
ylabel('Sauter Mean Diameter (\mum)')
ylim([0 60])
legend('Mean Diameter (\mum)','SMD (\mum)')
fullnamef=fullfile(folder6,'D vs SMD 1 to 2');
savefig(fullnamef)
saveas(gcf,fullnamef,'jpeg')

%--------------------V VS SMD Graph----------------------
------------------------

figure(13)
yyaxis left
title('Velocity (Vz) & Sauter Mean Diameter - Position
along y axis')
plot(radialPosition,VzMeanii(1:ReturnPoint),'-
o','color','b','LineWidth',1.5,'MarkerSize',7,...
    'MarkerEdgeColor','b','MarkerFaceColor','b')
ylabel('Velocity (Vz) (m/s)')
xlabel('Position along y axis (mm)')
ylim([0 160])
yyaxis right
plot(radialPosition,SauterMeanDii(1:ReturnPoint),'-
o','color','r','LineWidth',1.5,'MarkerSize',7,...
    'MarkerEdgeColor','r','MarkerFaceColor','r')
ylabel('Sauter Mean Diameter (\mum)')
ylim([0 60])
legend('Velocity (Vz)','SMD')
fullnamef=fullfile(folder6,'V vs SMD at t=1');
savefig(fullnamef)
saveas(gcf,fullnamef,'jpeg')

figure(14)
yyaxis left
```

```matlab
title('Velocity (Vz) & Sauter Mean Diameter - Position
along y axis')
plot(radialPosition,VzMeanmm(1:ReturnPoint),'-
o','color','b','LineWidth',1.5,'MarkerSize',7,...
    'MarkerEdgeColor','b','MarkerFaceColor','b')
ylabel('Velocity (Vz) (m/s)')
xlabel('Position along y axis (mm)')
ylim([0 160])
yyaxis right
plot(radialPosition,SauterMeanDmm(1:ReturnPoint),'-
o','color','r','LineWidth',1.5,'MarkerSize',7,...
    'MarkerEdgeColor','r','MarkerFaceColor','r')
ylabel('Sauter Mean Diameter (\mum)')
ylim([0 60])
legend('Velocity (Vz)','SMD')
fullnamef=fullfile(folder6,'V vs SMD at t=1-5');
savefig(fullnamef)
saveas(gcf,fullnamef,'jpeg')

figure(15)
yyaxis left
title('Velocity (Vz) & Sauter Mean Diameter - Position
along y axis')
plot(radialPosition,VzMeanff(1:ReturnPoint),'-
o','color','b','LineWidth',1.5,'MarkerSize',7,...
    'MarkerEdgeColor','b','MarkerFaceColor','b')
ylabel('Velocity (Vz) (m/s)')
xlabel('Position along y axis (mm)')
ylim([0 160])
yyaxis right
plot(radialPosition,SauterMeanDff(1:ReturnPoint),'-
o','color','r','LineWidth',1.5,'MarkerSize',7,...
    'MarkerEdgeColor','r','MarkerFaceColor','r')
ylabel('Sauter Mean Diameter (\mum)')
ylim([0 60])
legend('Velocity (Vz)','SMD')
fullnamef=fullfile(folder6,'V vs SMD at t=2');
savefig(fullnamef)
saveas(gcf,fullnamef,'jpeg')

figure(16)
yyaxis left
```

```matlab
title('Velocity (Vz) & Sauter Mean Diameter - Position
along y axis')
plot(radialPosition,VzMeantt(1:ReturnPoint),'-
o','color','b','LineWidth',1.5,'MarkerSize',7,...
    'MarkerEdgeColor','b','MarkerFaceColor','b')
ylabel('Velocity (Vz) (m/s)')
xlabel('Position along y axis (mm)')
ylim([0 160])
yyaxis right
plot(radialPosition,SauterMeanDtt(1:ReturnPoint),'-
o','color','r','LineWidth',1.5,'MarkerSize',7,...
    'MarkerEdgeColor','r','MarkerFaceColor','r')
ylabel('Sauter Mean Diameter (\mum)')
ylim([0 60])
legend('Velocity (Vz)','SMD')
fullnamef=fullfile(folder6,'V vs SMD 1 to 2');
savefig(fullnamef)
saveas(gcf,fullnamef,'jpeg')

%-------------------Simultaneous D and SMD---------------
-------------------------------
for i=1:42
mat=table2array(z{i});

%-----


[b(i)]=DSMD3(mat,zz,nw,xl,para);    % call function
DSMD3(matrix_data,Z,n,xl,param)
basefileD=num2str(i);
fullname=fullfile(folder7,basefileD);
savefig(fullname)
%saveas(gcf,fullname,'pdf')
saveas(gcf,fullname,'jpeg')
end
```

10.4 Appendice 4 - Matlab code for mean and standdard deviation calculation for spray

```matlab
-----------------------------------
City University Of London
Milad Mirshahi
2018
-----------------------------------

folder1='C:\Users\Milad\OneDrive - City, University of
London\3 - Image processing - Spray\3 hole-
shadowgraphy\X5_AP4_P100b_Dur2_FR40k_SS2m_R384-
320_A0deg_N200_10_V2';
 IMG = cell(151, 1) ;

  for k = 1 : 50
      if 0<k && k<10
          l=['00',num2str(k)];
      elseif k>=10 && k<100
          l=['0',num2str(k)];
      elseif k<=100
          l=num2str(k);
      end
 filename = ['X5_AP4_P100b_Dur2_FR40k_SS2m_R384-
320_A0deg_N200_10_V2000',l,'.jpg'];
full=fullfile(folder1,filename);
IMG{k}=imread(filename);
 end
 x=306; y=148; %noghteye maximum std
 sumImage=[];
 thisImage=[];
 lastImages=50;
 firstImage=1;
 numberofImage=lastImages-firstImage+1;
for k = firstImage : lastImages
  thisImage = double(IMG{k}); % Or whatever...
  [rows columns numberOfColorBands] = size(thisImage);
  % First do a check for matching rows, columns, and number
of color channels.  Then:
  if k == firstImage
```

```matlab
      sumImage = thisImage;
    else
      sumImage = sumImage + thisImage;
    end
end
meanImage = floor(sumImage / numberofImage);
figure()
imshow(meanImage,[])

for i=1:320
    for j=1:384
for k =  firstImage : lastImages
  thisImage = double(IMG{k}); % Or whatever...
  thisnumber(k-firstImage+1,1)=thisImage(i,j);
if i==x && j==y
 Keep=thisnumber;
end
end
    stdPic(i,j)=std(thisnumber);
    meanPic(i,j)=mean(thisnumber);
    end

end
figure()
plot (Keep)
stdpicF=floor(stdPic);
figure()
imshow(stdpicF,[])

L=50;
Fs=40000
Y = fft(Keep);
P2 = abs(Y/L);
P1 = P2(1:L/2+1)
P1(2:end-1) = 2*P1(2:end-1);
f = Fs*(0:(L/2))/L;
plot(f,P1)

colormap jet
figure()
meanPicF=floor(meanPic);
imshow(meanPic,[])
```